

https://dspace.org/

Fragmentation of the isoscalar giant quadrupole resonance in low mass 12 -< A -> 40 nuclei and 2+ level density in 40Ca from high energy-resolution (p,p') scattering at 200 MeV

Usman, Iyabo Tinuola

2010-03-15T12:05:51Z
http://hdl.handle.net/10539/7686

Downloaded from a DSpace repository. https://dspace.org/

Fragmentation of the Isoscalar Giant Quadrupole Resonance in low mass $12 \leq A \leq 40$ nuclei and 2^+ level density in ^{40}Ca from high energy-resolution (p,p$'$) scattering at 200 MeV

Iyabo Tinuola Usman

A thesis submitted to the Faculty of Science,
University of the Witwatersrand, Johannesburg, in fulfilment of the
requirements for the degree of
Doctor of Philosophy

Johannesburg, 2009

Declaration

I, the undersigned, hereby declare that the work contained in this thesis is my own original work. It is being submitted for the Degree of Doctor of Philosophy in the University of the Witwatersrand, Johannesburg. It has not previously in its entirety or in part been submitted for any degree or examination in any other University.

....

Signature Date

Abstract

The Isoscalar Giant Quadrupole Resonance (ISGQR) in low-mass nuclei has been investigated in high energy-resolution experiments using proton inelastic scattering at $E_{\mathrm{p}} = 200$ MeV. The measurements extend and complete the investigation already undertaken for medium and heavy-mass nuclei using the K600 magnetic spectrometer and a proton beam from the K200 Separated Sector Cyclotron (SSC) facility of iThemba LABS, South Africa. In the present work the nuclei ^{12}C, ^{27}Al, ^{28}Si and ^{40}Ca were studied by measuring excitation energy spectra in the region of the ISGQR ($10 \leq E_{\mathrm{x}} \leq 30$ MeV) for scattering angles below, at and above the maximum of the ISGQR.

It is already known that the ISGQR in low-mass nuclei is highly fragmented from the investigations using a variety of nuclear probes. Various theoretical calculations have confirmed the fragmentation of the ISGQR in this region of the periodic table and the present data are compared to state-of-the-art Second Random Phase Approximation (SRPA) predictions for ^{28}Si and ^{40}Ca. In order to do this, characteristic energy scales were extracted from both the experimental data and theoretical predictions using the relatively new application of Wavelet Analysis. For this purpose a new, physically realistic, Complex Lorentzian mother wavelet was developed, thus allowing the giant resonance to be viewed as overlaping Lorentzian functions of various energy width Γ. The different energy scales could be investigated for ^{40}Ca directly using a technique to reconstruct the measured excitation energy spectrum from coefficients gen-

erated by the Continuous Wavelet Transform (CWT) in the two dimensional wavelet energy scale *versus* excitation energy plot. It should be noted that no fine structure was found in the measured ^{12}C data but only confirmation of broad structures seen in previous investigations.

Quantitative analyses were carried on the ^{40}Ca and ^{28}Si data using the recently developed Semblance Analysis technique in order to extract information about the level of correlation that exists between the experimental data and the theoretical predictions. This was extended to the comparison of different probes exciting the region of the ISGQR in ^{28}Si and to the one-proton different ^{28}Si,^{27}Al(p,p$'$) and ^{90}Zr,^{89}Y(p,p$'$) experimental data. Here, the higher positive correlation found in medium-mass nuclei indicates the compactness of $1p$-$1h$ states in comparison to low-mass nuclei in which fragmentation causes the $E2$ strength to be spread over a much larger excitation energy region of about 10 MeV.

In addition, quasi-free knockout calculations were performed using the Distorted Wave Impulse Approximation (DWIA) in order to measure the extent of contributions from the ^{40}Ca(p,2p) and ^{40}Ca(p,pn) reactions as background to the measured ^{40}Ca(p,p$'$). This aided in the extraction of 2^+ level density for ^{40}Ca in which any instrumental background and contributions from other multipoles were determined by the model independent Discrete Wavelet Transform (DWT). Fluctuation analysis techniques were used in the extraction of experimental 2^+ level density in ^{40}Ca and comparisons are made with the phenomenological Back Shifted Fermi Gas (BSFG) model predictions and calculations of the Hartree-Fock Bogoluibov (HFB) microscopic model.

Dedication

This work is dedicated to my lovely daughters

Maryam and Mardiyat

Acknowledgements

Firstly, I would like to acknowledge the full support of my supervisor Prof. John Carter, who has contributed in all ways, finacially, morally, scientifically and spiritually, towards the success of this work. My appreciation also goes to Dr. Retief Neveling, my co-supervisor, who has devoted most of his time towards the success of this work. He has contributed greatly in experimental work a well as in making sure that the THREEDEE code works perfectly for me to do the calculation, Dankie. Thank you also for sparing your time to take me shoping at anytime while at iThemba LABS, though Sanri might have better plan for those evenings for both of you.

The availability of Top-up financial assistance from iThemba LABS through the NRF has helped me during the course of the programme. Also, support from WITS through the Bradlow and Post-graduate Merit Award Scholarships for the period of my PhD program are appreciated.

Scientifically, I would like to acknowledge the contributions from these important people:

Prof. Dr. Peter von Neumann-Cosel who have given me an opportunity to make a research visit to Technische Universitaet Darmstadt under support from DFG funding, Germany. Thanks for your useful ideas and suggestions in applying level density into my work.

Prof. Gordon Cooper of the School of Geosciences, WITS, for the timely discussion and suggestions for the Matlab code application of wavelet analysis in the data analysis.

Dr. Hiro Fujita (Post doctoral fellow WITS and iThemba LABS) for his contributions towards the use of CERN library code in the extraction of data during my stay at iThemba LABS.

Dr. Siegie Förtsch for his timely discussions and advice in the experimental and theoretical analysis.

Dr. Ricky Smit for making sure that all the experimental problems are solved and striving for background-free data.

Dr. Zinhle Buthelezi, my role-model and mentor, for given me inspirational advice and making me feel at home from so many weekend invitations spent with her, “Nyabonga ga kuulu”.

Yvonne Kheswa, our devoted target marker, for making sure that the targets used during the experiments are ready. Can you count how many shuttles we made together between J-Block and MRG Labs in the course of making calcium targets? “Nkosi“

Dr. Lowrie Conradie and the entire accelerator team, thanks for providing us good proton beams during the experimental weekends.

Ackowledgement also goes to Prof. Joao Rodrigues, the Head of the School of Physics, WITS, for his contributions towards the achievement of my goals. I will like to thank all the staff of the School of Physics for making life easy for me as an international student, ”Khealebogha”.

My fellow iThemba LABS post-graduate students: Sifiso, Paulus, Joel, Obed, Madiba, Buthaina, Justin, Taofiq and Daphey. Thank you for your cooperation and contributions in one way or the other towards the success of this work. I will like to thank fellow comrades at iThemba LABS like Tiro and Mpho (my flat-mate) for your support and encouragement.

I will also like to acknowledge my fellow post-graduate students at TU Darmstadt, Germany: Iryna, Olesky, Maksym, Abdul-rahman, Yuliya and Olena, some of you helped me for the first two weeks to pay for my lunch with your student cards in the Bistro, ”Dankie”.

My fellow Nigerian friends at WITS: Agatha, Okeke, Rasheed, Jimoh and Kayode, thank you for your friendly support. Also, I will like to thank Dr. Pedro (WITS School of Aeronautical, Industrial and Mechanical Engineering) and his family for their moral and spiritual support.

I will not forget Carter's family, Nicky, Leigh-ann and Amy, thanks for everyday love that you always give me anytime I visit your home. I felt like am with my child anytime I play with Amy. Thanks for the gifts and cards. May God continue to be with you.

To my brothers: Wale Ojetimi, Kola Ojetimi, Deji Ojetimi and Hakeem Ojetimi, and my sisters: Ibironke and Mosun, I am saying thank you very much for your support and encouragement throughout the course of my studies. May God almighty reward you abundantly.

Appreciation to my husband, Ali Usman, for his support during those hard times. Thank you a lot.

My daughters, Maryam and Mardiyat, thank you for being patient with me throughout the period of my studies, without your mum by your sides. I pray that God will give me the strength to make it up to you.

If not God,.....

Contents

Declaration **ii**

Abstract **iv**

Acknowledgements **viii**

List of Figures **xxv**

List of Tables **xxv**

1 Introduction **1**

2 Theoretical Considerations **9**

2.1 Excitation and decay of nuclear giant resonances 10

2.1.1 Width and decay of giant resonances 10

2.2 Transitions to the ISGQR and inelastic hadron scattering 15

2.2.1 Distorted Wave Born Approximation (DWBA) of inelastic scattering 18

2.2.2 Distorted Wave Impulse Approximation (DWIA) of Quasi-free knockout 21

2.3 Theoretical interpretation of giant resonances and their fine structure 23

2.3.1 ISGQR strengths in the Second Random Phase Approximation (SRPA) 24

2.3.2 SRPA Formalism 25
2.4 Tools for extracting characteristic energy scales 26
2.4.1 Fourier Transform 28
2.4.1.1 Discrete Fourier transform 28
2.4.1.2 Periodogram 28
2.4.1.3 Power Spectrum 29
2.4.2 Wavelet Analysis 30
2.4.2.1 Theory of wavelet 30
2.4.2.2 Continuous Wavelet Transform (CWT) 31
2.4.2.3 Semblance and Dot product analysis 34
2.4.2.4 Discrete wavelet transform (DWT) 35
2.5 Extraction of Level Densities 36
2.5.1 Level density models 37
2.5.1.1 Back-Shifted Fermi Gas (BSFG) model 39
2.5.1.2 Hartree-Fock-Bogoliubov (HFB) model 41
2.5.2 Fluctuation Analysis 42
2.5.2.1 Assumptions 42
2.5.2.2 Procedure 44

3 Experiments and Data Extraction 47

3.1 Separated Sector Cyclotron 48
3.2 K600 Magnetic Spectrometer 50
3.2.1 Ion Optical Characteristics of the K600 Magnetic Spectrometer 53
3.2.2 Focal-Plane Detector Package 55
3.3 Dispersion Matching Techniques 56
3.3.1 Faintbeam method 58
3.4 Targets 58
3.5 Experimental Procedure 60
3.5.1 High Energy-resolution 66

3.6 Data Acquisition System and Electronics 67
3.7 Data Extraction 69
3.7.1 Particle Identification 71
3.7.2 VDC data processing 73
3.7.3 Energy calibration 78
3.8 Experimental Cross-sections 80
3.8.1 Error Analysis 81
3.9 VDC Efficiency 81

4 Results, Analysis and Discussion 83

4.1 Spin-filter effects 84
4.2 Experimental results for measured spectra: ^{40}Ca, ^{28}Si, ^{27}Al and ^{12}C 85
4.3 SRPA $E2$ strength functions for ^{40}Ca and ^{28}Si 92
4.4 Extraction of characteristic energy scales: Experimental and Theoretical results 95
4.4.1 Application of Wavelet analysis 95
4.4.2 Experimental energy scales 97
4.4.3 Application of Fourier transform 103
4.4.4 Comparison of experimental and theoretical energy scales using wavelet analysis 104
4.5 Continuous Wavelet Transform spectrum reconstruction 107
4.5.1 Discussion of spectrum reconstruction results 115
4.6 Application of Semblance analysis 116
4.6.1 Comparison of ^{40}Ca and ^{28}Si experimental data with $E2$ strength predictions 117
4.6.2 Fragmentation of E2 strength in ^{28}Si 120
4.6.3 Semblance analysis for one-proton-different nuclei: ^{28}Si, ^{27}Al(p,p$'$) and ^{90}Zr, ^{89}Y(p,p$'$) experiment 130

4.7 Quasi-free - scattering background contributions for ^{40}Ca(p,p′) 134
4.8 Level density of 2^+ states in ^{40}Ca 142
4.8.1 DWT analysis and background determination 143
4.8.2 Extraction of 2^+ level density in ^{40}Ca 146
4.8.2.1 2^+ level density in ^{40}Ca via quasi-free background subtraction 152
4.8.3 Discussion of extracted 2^+ level densities for ^{40}Ca 153

5 Conclusions **158**

Bibliography **171**

List of Figures

2.1 Excitation of nuclear giant resonances illustrating the isoscalar and isovector electric and magnetic resonances [Ito05]. 11

2.2 Microscopic description of giant resonances in the closed shell nucleus ^{90}Zr [She04]. 11

2.3 Schematic representation of the the formation of fine structure by the mixture of strength fluctuations on multiple energy scales [Ric81]. 13

2.4 Schematic representation of the width of the collective 1p-1h state into a direct component $\Gamma\uparrow$ and a spreading component $\Gamma\downarrow$ of a giant resonance [Wou87]. Note that in principle the intermediate states can also decay as indicated by $\Gamma\downarrow\uparrow$. 14

2.5 Inelastic α-particle scattering spectra at 120 MeV on ^{24}Mg, ^{26}Mg, ^{28}Si and ^{40}Ca taken at $\theta_{\mathrm{Lab}} = 18^{\circ}$. The shape of the continuum is indicated by the dashed line. The arrows are located at the excitation energy $65A^{-\frac{1}{3}}$ which is within the excitation energy range of the ISGQR (taken from [Bor81]). 17

2.6 Illustration of the principles of wavelet analysis and wavelet families. Real ($k = 5$, see Eq. (2.30)) and Complex Morlet ($f_c = 1$, $f_b = 1$, see Eq.(2.31)) wavelets are the products of cosine and Gaussian functions. The Biorthogonal 3.9 wavelet has an antisymmetrical shape but no analytical expression. Complex Lorentzian ($f_c = 2\Gamma$, $f_b = 2$, see Eq.(2.32) and Sect. 4.4.1) wavelets is a continuous sum of Lorentzians plus Gaussian envelope. The real parts are shown as solid line and the imaginary parts are in dashed lines. 32

3.1 The layout of Separated Sector Cyclotron facility of iThemba LABS. Positions 1 to 5 indicate the locations of halo monitors. . 49

3.2 The layout of the K600 Magnetic Spectrometer showing its main components and the focal plane detector package. The K600 is positioned at 11° in this figure. 51

3.3 The internal beamstop for measurements at angles $7° < \theta_{K600} < 21°$ as viewed from the target ladder. The entrance to the K600 is visible on the left of the beamstop. 53

3.4 Schematic ion trajectories of a beam and a magnetic spectrometer under different beam transport conditions. The left-hand side (a) shows the situation when achromatic beam transportation is used while the the right-hand side (b) indicates the situation when lateral dispersion matching is realised. 57

3.5 The three faintbeam meshes, shown here before installation between the ECR ion source and the SPC2 injector cyclotron. The mesh on the left attenuates the beam by a factor of 100 and the two meshes on the right attenuates by a factor of 10000. 59

3.6 A position spectrum showing a prominent beam halo peak at the low momentum (right hand) side. 63

3.7 (a) A focal plane position spectrum for an empty target for bad beam halo conditions at 1.8 nA beam current taking for 15 minutes. (b) A focal plane position spectrum for an empty target under a good beam halo conditions at 3 nA beam current taking for 4 minutes. 63
3.8 (a) Beam loss monitor spectrum showing bad halo conditions. The countrate is shown as a function of time. Note the countrate above 30 Hz for the BLM in the vault (green line). (b) All the five beam loss monitor spectra showing overall good halo conditions. Note the beam loss monitor countrates were below 10 Hz. 65
3.9 The Hatanaka viewer shown in the in-beam position. The viewer is positioned 45° with respect to the beam. The beam direction is from left to right. 66
3.10 Event trigger and timing electronics for the K600 Magnetic Spectrometer. 68
3.11 Flow chart illustrating the offline data analysis algorithm. 70
3.12 Proton identification using the focal plane ΔE-ΔE spectrum. Other events (γ) seen are also indicated. 72
3.13 (a) Particle identification in paddle 1. (b) Particle identification in paddle 2. Note that the black line indicates all events, the red line indicates good events in X1, X2 and Y (i.e. Event ID = 0), and the green line indicates the software gates for good events used in the analysis. 73
3.14 TOF gates used in particle identification. Note that the black line indicates all events, the red line indicates good events in X1, X2 and Y (i.e. Event ID = 0), and the green line indicates the software in gates for good events used in the analysis. 74

3.15 Average drift time spectrum for the X1 wire chamber. The two lines with arrows illustrate the range of gate settings for minimum and maximum valid TDC drift time values on the horizontal axis. 75

3.16 The reconstructed lookup-table after setting gates on good events. Note that the vertical axis represents the drift distance (signal-wire to Al-plane spacing) divided into 1000 channels while the horizontal axis represents the drift time (channels). 76

3.17 A diagram showing the multislot collimator used for horizontal angle calibration. Note that all measurements are in mm. 77

3.18 (a) Focal plane scattering angle with red line representing the gated good events spectrum. (b) Target scattering angle with red line representing the gated good events spectrum. Note the seven peaks correspond to the holes on the multislot collimator used during the experiments. 77

3.19 Angle calibration at different focal plane positions. The top figure represents the focal plane position (horizontal axis) versus θ_{tgt} (vertical axis) while the bottom figure represents the focal plane position versus θ_{fp} for good events in ^{40}Ca at $\theta_{\mathrm{K600}} = 11^{\circ}$. It can be seen that all the peaks in the top figure are aligned on the appropriate angle. 78

3.20 Momentum calibration curve of ^{40}Ca spectra at different angles and momentum settings using a second order polynomial fitting. Note that the K600 momentum setting for 7° and 11° was 198 MeV while that of 15° was 202 MeV. 79

4.1 Angular distributions for DWBA inelastic proton scattering on ^{40}Ca for $L = 0$, 2, 3, and 4 excitations at $E_{\mathrm{p}} = 200$ MeV. 85

4.2 Excitation energy spectrum for ^{40}Ca at scattering angles of θ_{Lab} = 7°, 11° and 15°. Note the maximum of the ISGQR is at θ_{Lab} = 11°. 86
4.3 Excitation energy spectrum for ^{28}Si at a scattering angle of θ_{Lab} = 12° the maximum of the ISGQR. 86
4.4 Excitation energy spectra for ^{27}Al at scattering angles of θ_{Lab} = 12° and 17°. Note that the maximum of the ISGQR is at θ_{Lab} = 12°. 87
4.5 Excitation energy spectra for ^{12}C at scattering angles of θ_{Lab} = 13° and 20°. Note that the maximum of the ISGQR is at θ_{Lab} = 13°. 87
4.6 Excitation energy spectra for ^{208}Pb, ^{120}Sn, ^{90}Zr, ^{58}Ni, ^{40}Ca, ^{28}Si and ^{27}Al at scattering angles corresponding to the maximum of ISGQR. 90
4.7 Experimental cross-section for ^{40}Ca(p,p′) at θ_{Lab} = 11° for E_{p} = 200 MeV. 91
4.8 SRPA $E2$ strength distribution for ^{40}Ca folded with a FWHM = 38 keV Gauss function in order to make a direct comparison to the experimental data. 94
4.9 SRPA $E2$ strength distribution for ^{28}Si folded with a FWHM = 38 keV Gauss function in order to make a direct comparison to the experimental data. 94
4.10 Wavelet analysis results for ^{208}Pb using the Complex Morlet mother wavelet (left hand side) and the Complex Lorentzian mother wavelet (right hand side). Note that blue indicates negative values and red positive values. 96

4.11 Energy spectra for target nuclei ^{40}Ca, ^{28}Si and ^{27}Al shown in the upper part of each diagram for each nucleus at the maximum of the ISGQR. The corresponding real part of the wavelet coefficients determined using the Complex Lorentzian mother wavelet are shown underneath each spectrum. The left hand side shows larger scales while the right hand side shows the presence of smaller intermediate scales below 2 MeV. 98

4.12 Power spectra of ^{40}Ca at different scattering angles, $\theta_{\rm Lab} = 7^\circ$, 11° and 15°. The maximum of the ISGQR corresponds to $\theta_{\rm Lab} = 11^\circ$. 99

4.13 Power spectra of ^{28}Si at the scattering angle $\theta_{\rm Lab} = 12^\circ$ for maximum of the ISGQR. 100

4.14 Power spectra of ^{27}Al at different scattering angles $\theta_{\rm Lab} = 12^\circ$ and 17°. The maximum of the ISGQR corresponds to $\theta_{\rm Lab} = 12^\circ$. 100

4.15 Power spectra of ^{40}Ca at $\theta_{\rm Lab} = 11^\circ$ scattering angle and the SRPA theoretical prediction. 105

4.16 Power spectra of ^{28}Si at$\theta_{\rm Lab} = 12^\circ$ scattering angle and the SRPA theoretical prediction. 105

4.17 *Upper*: Class III energy scale showing the reconstruction of ^{40}Ca at $\theta_{\rm Lab} = 11^\circ$ indicated with a black line; *Middle*: Sum of the real coefficients between the limits shown in the coefficients plot; *Lower*: The region of largest energy scale between 4.9 MeV and 10 MeV indicated on the plot of real coefficients produced using the Complex Lorentzian mother wavelet. 109

4.18 *Upper*: Class III energy scale showing the reconstruction of ^{40}Ca at $\theta_{\mathrm{Lab}} = 11^{\circ}$ after adding the summed coefficients of Fig. 4.17 indicated with a black line; *Middle*: Sum of the real coefficients between the limits shown in the coefficient plot; *Lower*:The region of second largest energy scale between 1.36 MeV and 4.9 MeV indicated on the plot of real coefficients produced using the Complex Lorentzian mother wavelet. 110

4.19 *Upper*: Class III energy scale showing the reconstruction of ^{40}Ca at $\theta_{\mathrm{Lab}} = 11^{\circ}$ after adding the summed coefficients of Figs. 4.17 and 4.18 indicated with a black line; *Middle*: Sum of the real coefficients between the limits shown in the coefficient plot; *Lower*:The region of second largest energy scale between 700 keV and 1.36 MeV indicated on the plot of real coefficients produced using the Complex Lorentzian mother wavelet. 111

4.20 *Upper*: Class II energy scale showing the reconstruction of ^{40}Ca at $\theta_{\mathrm{Lab}} = 11^{\circ}$ after adding the summed coefficients of Fig. 4.17 and Fig. 4.18 indicated with a black line, *Middle*: Sum of the real coefficients between the limits shown in the plot; *Lower*: The region of medium energy scale between 330 kev and 700 keV indicated on the plot of real coefficients produced using the Complex Lorentzian mother wavelet. 112

4.21 *Upper*: Class I energy scale showing the reconstruction of ^{40}Ca at $\theta_{\mathrm{Lab}} = 11^{\circ}$ after adding the summed Class II coefficients of Fig. 4.20 and the summed Class III coefficients of Fig. 4.17 and Fig. 4.18 indicated with a black line; *Middle*: Sum of the real coefficients between the limits shown in the plot; *Lower*: The region of small energy scale between 180 keV and 330 keV indicated on the plot of real coefficients produced using the Complex Lorentzian mother wavelet. 113

4.22 *Upper*: Class I energy scale showing the reconstruction of ^{40}Ca at $\theta_{\mathrm{Lab}} = 11^{\circ}$ after adding the summed coefficients of Fig. 4.21, Class II coefficients of Fig. 4.20 and the summed Class III coefficients of Fig. 4.17 and Fig. 4.18 indicated with a black line; *Middle*: Sum of the real coefficients between the limits shown in the plot; *Lower*: The region of small energy scale between 110 keV and 180 keV indicated on the plot of real coefficients produced using the Complex Lorentzian mother wavelet. 114

4.23 Energy spectra of ^{40}Ca at 11° scattering angle (green line) and the theoretical predictions of SRPA (blue line) showing the extracted energy scales by applying the Complex Lorentzian mother wavelet. The bottom two parts represent the Semblance and Dot product analysis for a quantitative correspondence between the experimental data and the theoretical predictions. . . 118

4.24 Energy spectra of ^{28}Si at 12° scattering angle (green line) and the theoretical predictions of SRPA (blue line) showing the extracted energy scales by applying the Complex Lorentzian mother wavelet. The bottom two parts represent the Semblance and Dot product analysis for a quantitative correspondence between the experimental data and the theoretical predictions. . . 119

4.25 Excitation energy spectra for ^{28}Si ISGQR excited using different probes. ^{28}Si(p,p$'$) present data, ^{28}Si(α, α') [Bor81], ^{28}Si(e,e$'$) [Fri81], ^{24}Mg(α, γ_o) [Kuh83] and ^{27}Al(p,γ_o) [Sin65]. 121

4.26 Semblance and Dot product results for ^{28}Si(p,p$'$) (present data) and ^{28}Si(α, α') from [Bor81] for comparison of the ISGQR scales emerging from different selectivities. 122

4.27 Semblance and Dot product results for ^{28}Si(p,p$'$) (present data) and ^{28}Si(e,e$'$) from [Fri81] for comparison of the ISGQR scales emerging from different selectivities. 123

4.28 Semblance and Dot product results for ^{28}Si(p,p′) (present data) and ^{24}Mg(α, γ_o) from [Kuh83] for comparison of the ISGQR scales emerging from different selectivities. 124
4.29 Semblance and Dot product results for ^{28}Si(p,p′) (present data) and ^{27}Al(p,γ) from [Sin65] for comparison of the ISGQR scales emerging from different selectivities. 125
4.30 Power spectra from the semblance analysis on ^{28}Si(p,p′) (solid line) with ^{28}Si(α, α'), ^{28}Si(e,e′), ^{24}Mg(α, γ_o) and ^{27}Al(p,γ_o) for comparison of the ISGQR scales emerging from different selectivities. In each case the power spectrum is normalised to maximum of unity. 129
4.31 Semblance and Dot product results for the ^{28}Si(p,p′) (green line) and ^{27}Al(p,p′) (blue line) experimental data for comparison of the ISGQR scales emerging from one-nucleon-difference nuclei. Real part of the complex Lorentzian mother wavelet coefficients is depicted below each of the data. 132
4.32 Semblance and Dot product results for the ^{90}Zr(p,p′) (green line) and ^{89}Y(p,p′) (blue line) experimental data for comparison of the ISGQR scales emerging from one-nucleon-difference nuclei. Real part of the complex Lorentzian mother wavelet coefficients is depicted below each of the data. 133
4.33 Angle integrated continuum quasi-free cross-sections for the reaction ^{40}Ca(p,p′p) at incident energy of 200 MeV and scattering angle of 11° calculated for the $1d_{3/2}$, $2s_{1/2}$ and $1d_{5/2}$ proton states. 139
4.34 Continuum quasi-free cross-sections for the reaction ^{40}Ca(p,p′n) at incident energy of 200 MeV and scattering angle of 11° calculated for the $1d_{3/2}$, $2s_{1/2}$ and $1d_{5/2}$ neutron states. 139

4.35 The curves are results of the DWIA calculations for quasi-free background contributions from both proton and neutron indicated as QF background for ^{40}Ca(p,p′) at $\theta_{\rm Lab}$ =11° as indicated in Figs. 4.33 and 4.34. 140
4.36 Quasi-free background contribution (dashed-line) for ^{40}Ca at $\theta_{\rm Lab} = 11°$ as indicated in Fig. 4.35. 140
4.37 Quasi-free background contribution for ^{40}Ca at $\theta_{\rm Lab} = 15°$. . . . 141
4.38 Quasi-free background contribution for ^{40}Ca at $\theta_{\rm Lab} = 7°$. 141
4.39 Decomposition of the excitation energy spectrum of ^{40}Ca(p,p′) reaction measured at $E_{\rm p} = 200$ MeV for $\theta_{\rm Lab} = 11°$ into approximations and details. 145
4.40 from top to bottom: Experimental ^{40}Ca(p,p′) spectrum including background obtained with the use of discrete wavelet transform, smoothed spectra $g(E_{\rm x})$ and $g_{>}(E_{\rm x})$, stationary fluctuating spectrum d$(E_{\rm x})$ obtained by dividing the two smoothed spectra, autocorrelation functions from experimental (solid line) and theoretical (dashed line) method. 147
4.41 DWT (A10) background for ^{40}Ca(p,p′) at $\theta_{\rm Lab} = 11°$. 149
4.42 Extracted level density (solid line) of 2^+ states for ^{40}Ca(p,p′) at $\theta_{\rm Lab} = 11°$ compared to BSFG (dashed line) and HFB (dotted line) model predictions after using DWT (A10) background subtraction as shown in Figs. 4.39, 4.40 and 4.41. 149
4.43 DWT (A10) background for ^{40}Ca(p,p′) at $\theta_{\rm Lab} = 15°$. 150
4.44 Extracted level density (solid line) of 2^+ states for ^{40}Ca(p,p′) at $\theta_{\rm Lab} = 15°$ compared to BSFG (dashed line) and HFB (dotted line) model predictions after using DWT (A10) background subtraction as shown in Fig. 4.43. 150
4.45 DWT (A10) background for ^{40}Ca(p,p′) at $\theta_{\rm Lab} = 7°$. 151

4.46 Extracted level density (solid line) of 2^+ states for ^{40}Ca(p,p′) at $\theta_{\mathrm{Lab}} = 7^\circ$ compared to BSFG (dashed line) and HFB (dotted line) model predictions after using DWT (A10) background subtraction as shown in Fig. 4.45. 151

4.47 DWT (A10) background for the quasi-free subtracted spectrum ^{40}Ca(p,p′) at $\theta_{\mathrm{Lab}} = 11^\circ$. See Fig. 4.36 for the quasi-free background. 154

4.48 Extracted level density (solid line) of 2^+ states for ^{40}Ca(p,p′) at $\theta_{\mathrm{Lab}} = 11^\circ$ compared to BSFG (dashed line) and HFB (dotted line) model predictions after using quasi-free and DWT (A10) background subtraction as shown in Fig. 4.47. 154

4.49 DWT (A10) background for the quasi-free subtracted spectrum ^{40}Ca(p,p′) at $\theta_{\mathrm{Lab}} = 15^\circ$. See Fig. 4.37 for the quasi-free background. 155

4.50 Extracted level density (solid line) of 2^+ states for ^{40}Ca(p,p′) at $\theta_{\mathrm{Lab}} = 15^\circ$ compared to BSFG (dashed line) and HFB (dotted line) model predictions after using quasi-free and DWT (A10) background subtraction as shown in Fig. 4.49. 155

4.51 DWT (A10) background for the quasi-free subtracted spectrum ^{40}Ca(p,p′) at $\theta_{\mathrm{Lab}} = 7^\circ$. See Fig. 4.38 for the quasi-free background. 156

4.52 Extracted level density (solid line) of 2^+ states for ^{40}Ca(p,p′) at $\theta_{\mathrm{Lab}} = 7^\circ$ compared to BSFG (dashed line) and HFB (dotted line) model predictions after using quasi-free and DWT (A10) background subtraction as shown in Fig. 4.51. 156

4.53 Extracted level density (solid line) of 2^+ states for ^{40}Ca(p,p′) averaged over $\theta_{\mathrm{Lab}} = 11^\circ$ and $\theta_{\mathrm{Lab}} = 15^\circ$ compared to BSFG (dashed line) and HFB (dotted line) model predictions. 157

List of Tables

3.1 Technical specifications for the medium dispersion mode of K600 Magnetic Spectrometer. 54

3.2 A list of target nuclei investigated at the indicated angles at iThemba LABS. Note the bold scattering angle indicates the maximum of the ISGQR. 61

4.1 Summary of energy scales extracted for ^{40}Ca (CM = Complex Morlet, CL = Complex Lorentzian). Bold indicates the presence of a clearly identifiable scale. 102

4.2 Summary of energy scales extracted for ^{28}Si. 102

4.3 Summary of energy scales extracted for ^{27}Al. 102

4.4 Summary of energy scales extracted for ^{208}Pb, ^{120}Sn, ^{90}Zr and ^{58}Ni at the scattering angle corresponding to the maximum of the ISGQR. 102

4.5 Summary of energy scales observed for ^{40}Ca in comparison with microscopic SRPA calculations. Bold indicates the presence of a a clearly identifiable scale and columns indicate correspondence between scales (CL = Complex Lorentzian). 106

4.6 Summary of energy scales observed for ^{28}Si in comparison with microscopic SRPA calculations. Bold indicates the presence of a a clearly identifiable scale and columns indicate correspondence between scales (CL = Complex Lorentzian). 106

4.7 Energy-dependent optical potential parameters of Schwandt *et al.* [Sch82] used in the DWIA calculations for the p + ^{40}Ca as described in the text. Note that the potential strengths are in MeV, r and a in fm. 135

4.8 Energy-dependent optical potential parameters of Becchetti and Greenlees [Bec69] used in the DWIA calculation for the p + ^{39}K knockout channel in the energy range $0 < E_{\mathrm{p}} < 50$ MeV. Note that the potential strengths are in MeV, r and a in fm. 136

4.9 Energy-dependent optical potential parameter of Becchetti and Greenlees [Bec69] used in the DWIA calculation for the n + ^{39}Ca knockout channel in the energy range $0 < E_{\mathrm{n}} < 24$ MeV. Note that the potential strengths are in MeV, r and a in fm. . . 136

4.10 The principal quantum number, N, orbital angular momentum, L, and the total angular momentum,J, with binding energies and spectroscopic factors (S) of the three valence states of proton [Ant81] and neutron [Wat82] in ^{40}Ca. 137

4.11 List of parameters used in 2^+ level density extraction for ^{40}Ca. . 148

Chapter 1

Introduction

Giant resonances are elementary excitation modes of nuclei. Since giant resonances dominate the nuclear response at low excitation energies and low momentum transfer, their experimental and theoretical investigation constitutes a central topic in nuclear physics [Har00]. Giant resonances in nuclei were first discovered in 1937 by Bothe and Gentner [Bot37], who observed nuclear vibrations in the measurements of photon absorption using a source of 14 MeV. Ten years later these observations were confirmed by Baldwin and Klaiber [Bad47] with photons from a betratron. In 1948 Goldhaber and Teller [Gol48] interpreted these resonances, referred to as Isovector Giant Dipole Resonances (IVGDR), with a hydrodynamic model in which rigid proton and neutron fluids vibrate against each other, the restoring force coming from the surface energy. Steinwendel and Jensen [Ste50] further developed the model, considering compressible neutron and proton fluids vibrating in anti-phase in a common fixed sphere, the restoring force being associated with the volume symmetry energy.

In 1971, the Isoscalar Giant Quadrupole Resonance (ISGQR) was discovered in inelastic electron scattering by Pitthan and Walcher [Pit71] and in inelastic proton scattering by Lewis and Bertrand [Lew72]. Isoscalar Giant Monopole Resonances (ISGMR) were found later, their properties being closely related to

the compression modulus of nuclear matter. Following these, other resonances of higher multipolarities as well as the so-called magnetic giant resonances were investigated. The first microscopic basis for the description of giant resonances was the Random Phase Approximation (RPA), in which giant resonances appear as coherent superposition of one-particle one-hole ($1p$-$1h$) excitations in closed shell nuclei or two quasiparticle excitations in open shell nuclei [Spe91].

Typical probes for giant resonance studies include (1) γ-rays and electrons for the excitation of the IVGDR, (2) α-particles, protons and electrons for the excitation of the ISGMR and the ISGQR, and (3) the charge exchange reactions like (p,n), (n,p) or (^{3}He,t) for the Gamow-Teller (GT) resonance. These initial observations have blossomed into a bona fide subfield of nuclear physics, one that is pursued in nearly every major medium-energy nuclear physics facility throughout the world. Light ions such as protons, tritons, deuterons and alpha particles have been preferred for studying the nuclear structure and reaction mechanisms because they are relatively easy to accelerate. Each one of these light ions has some unique property that makes it useful for a certain type of study. For example, since both the spin and isospin of an alpha particle are zero, alpha-particle scattering is ideal for exciting a nucleus without changing the isospin. Proton inelastic scattering can be used to excite both isoscalar and isovector giant resonances due to its spin and isospin value of one-half.

In particular, ISGQR investigations in nuclei has been a most valuable field of study for decades. ISGQR studies became the centre of interest at iThemba LABS in the 1990's when coincidence experiments were performed on ^{40,48}Ca nuclei at the relatively-low proton beam energy of 100 MeV [Car98, Sch01, Car01] to investigate the ISGQR strength distribution. These experiments involved both local and international experts and made use of the K600 Magnetic Spectrometer. A coincidence experiment is a particularly attractive tool

for the study of giant resonances since it provides simultaneous access to the fundamental quantities defining a giant resonance like the strength (usually expressed as an exhaustion of model-independent Energy-Weighted Sum Rule (EWSR)) and its energy distribution, and the role of direct and statistical decay contributions to the damping of the giant resonances.

Some of the gross features of giant resonances such as centroid energies and collectivity, measured in terms of sum rules, have been studied and are well understood in microscopic models [Har00, Bor98]. Yet, the widths have not been fully understood due to the limitations in the experimental methods. Also, in recent years, high energy-resolution proton inelastic-scattering experiments revealed that giant resonances additionally carry fine structure. An early example of fine structure was seen in inelastic electron scattering experiments [Kuh81] investigating the giant quadrupole resonance in ^{208}Pb, carried out using the DALINAC electron accelerator of the TU Darmstadt, Germany. In addition, the fine structure of Gamow-Teller (GT) resonances in medium-heavy nuclei ($40 \leq A \leq 90$) has been investigated using the (^{3}He,t) reaction and the Grand-Raiden magnetic spectrometer of RCNP Osaka, Japan [Kal06]. Even so, the fine structure of giant resonances, which carries unique information on the underlying physical nature and the dominant decay mechanisms of the resonances, is still relatively unexplored topic especially in light nuclei ($A \leq 40$).

In the 1970's and early 1980's, investigations on the ISGQR using low-energy projectiles extracted information like the width, centroid and strength of the giant resonance for light nuclei with experiments such as (α, α') and (e, e') [Bor81, Zwa85, Lui85, Mos76, You78]. It was found that the strength is highly fragmented, completely intermingled with other multipole strength and little or no information on the fine structure and characteristic energy scales in these

nuclei could be obtained. This might be due to the low-energy scattering, selectivity of the beam used in carrying out these experiments and also low energy-resolution. Although measurements of inelastic alpha-particle scattering at high energy measurements would have been preferred for the investigation because of its isoscalar properties, this has been limited by constraints such as background and energy-resolution problems. Therefore, inelastic proton scattering has been chosen because of availability at intermediate energies up to about 200 MeV, suppressed peak to background ratio and because the technique of high energy-resolution measurements has been well developed. With the advent of high energy-resolution techniques using dispersion-matched proton beams and the K600 Magnetic Spectrometer of iThemba LABS, more insight could be gained into the nature of nuclei pertaining to damping mechanisms which lead to fine structure in nuclei across the periodic table.

A systematic study of heavy nuclei was undertaken using high energy-resolution inelastic proton scattering at $E_{\mathrm{p}} = 200$ MeV with the K600 Magnetic Spectrometer of iThemba LABS, utilising the selectivity of proton scattering to separate the isoscalar quadrupole mode from the monopole mode, which is not possible in electron scattering. In heavy nuclei the ISGMR is energetically separated from the ISGQR. Earlier it was shown for the example of the isoscalar giant quadrupole resonance in ^{208}Pb that the comparison between measurements using electrons and protons of about the same resolution ($\Delta E \simeq 50$ keV FWHM) revealed that the observed fluctuations are independent of the exciting probe [Kam97] and thus are physical in nature. The first experiments at iThemba LABS on the investigation of fine structure of the ISGQR were performed on heavy nuclei (^{208}Pb, ^{166}Er, ^{142}Nd, ^{120}Sn, ^{90}Zr) and a medium-heavy nucleus (^{58}Ni) in 2002. In order to make a global investigation across the periodic table, an experiment was proposed to extend the study to light nuclei specifically ^{40}Ca, ^{28}Si, ^{27}Al and ^{12}C in 2006. These sets of target nuclei

were chosen for this particular study because of their 0^+ ground state and even-even shell closure (except for ^{27}Al) and because they are stable and easy to work with at an incident energy of 200 MeV.

For better understanding of the experimentally observed data, a theoretical model prediction is very essential. The synthesis of such large quantities of diverse experimental information is the role of theoretical nuclear physics. Though nuclear models are very successful in correlating large amounts of experimental data, a unified, all-encompassing theory of nuclear structure and reaction have not yet been reached. That is why different theoretical models have been considered in explaining the most suitable results of the experimental data from heavy to light nuclei across the periodic table, partly because of the systematic dependence on shell structure (open or closed shell). With the increase in relevant model spaces there arises more computational problems, for example, in $A \leq 12$ nuclei an ab-initio method have been applicable, in $A \leq 60$ a shell-model approach have been used while in $A > 60$ approximations based on effective interactions have been applied. Different theoretical models such as the Quasiparticle Phonon Model (QPM), Random Phase Approximation (RPA), Second-RPA, Extended Time Dependent Hartree-Fock (ETDHF) and Extended Theory of Finite Fermi Systems (ETFFS), have been used for the microscopic description of the strength functions in nuclei in recent years. The crucial question now is the comparison of the calculations with experimental results. This comparison should test the applicability of forces which are thought to be universal for all the nuclei, and therefore yield information about the utility of these approaches for the description of the non-closed shell nuclei. The model that best described the $E2$ strength function in heavy and medium-heavy nuclei was the QPM [Sol92]. Likewise, the SRPA has been applied in the present study for the light nuclei in the case of ^{40}Ca and ^{28}Si because it involves calculations using a modern effective interaction constructed

on different ground state model spaces. In addition, SRPA is a self consistent model based on realistic effective nucleon-nucleon interaction up to $2p$-$2h$.

The choice of data analysis technique in characterising the fine structure remains a point of contention. One needs to find the unique technique that could resolve the position, width and localisation of the quantity in question. A variety of methods have been proposed to extract information on characteristic energy scales of the fine structure which include an entropy index method [Lac99, Lac00] and a multifractal analysis [Aib99] of the fluctuating strength function. Recently, an analysis based on continuous wavelet transform (CWT) has been shown to be most promising. A critical comparison of the different methods is discussed in [She08]. Both Wavelet and Fourier analysis techniques have been implemented in the analysis of the experimental data and the theoretical model predictions in this thesis. Moreover, work has been done on the development of a physically more-realistic Lorentzian mother wavelet which is compared with the results already obtained with the use of the Morlet type of wavelet [Usm06]. Therefore, an understanding of the decay modes, in particular the systematic behaviour of the escape width relative to the spreading width, is an essential ingredient for the complete description of the nuclear giant quadrupole resonance across the periodic table.

Another important aspect of proton inelastic scattering data with high energy-resolution is the use of it as a direct measurement of level densities even in the excitation energy region of giant resonances. Level densities are of fundamental interest not only as a test of the understanding of nuclear dynamics, but it also serves as a key ingredient of large reaction-network codes in modelling stellar energy production and nucleosynthesis. The phenomenon of fluctuating cross sections in compound nucleus reactions in the region of overlapping resonances was first studied theoretically in the early 1960's [Eri63] using the assumption

of random phases between the scattering amplitudes. In the higher excitation energy region, the levels still do not overlap but states are unresolved because of the limited energy resolution. Therefore, the extraction of level densities of the dominant 2^+ states will be considered especially in ^{40}Ca which lies between heavy and low mass nuclei. The level densities can be extracted by means of a fluctuation analysis [Mul82, Han90], provided the knockout contribution to the background cross-section can be estimated with reasonable accuracy. The (p,p′x) coincidence studies at iThemba LABS referred to earlier in this chapter, utilising the Distorted Wave Impulse Approximation (DWIA) calculations with the code THREEDEE, indicated that this process is understood well enough. The fluctuation analysis depends sensitively on assumptions about the background in the spectra. Identification of the knockout contribution is achieved by calculating the quasi-free knockout background contribution, and also in a model-independent way using a Discrete Wavelet Transform (DWT) of the spectra [Kal06, Kal07]. The results are then compared with theoretical values predicted from the Back Shifted Fermi Gas (BSFG) and Hartree-Fock-Bogoluibov (HFB) models.

High energy-resolution results obtained at intermediate proton beam energies, using a Magnetic Spectrometer in combination with dispersion matching techniques, provides the most suitable approach to study fine structure of the IS-GQR in nuclei. The necessary experimental techniques were recently discussed in [Fuj97] and are described in Chapter 3. With these techniques the possibility exists to perform (p,p′) experiments at forward angles with an energy resolution much better than the energy spread of the incident beam.

The layout of this thesis is as follows:

- Chapter 2 describes the theoretical considerations involved in the study

of isoscalar giant resonances and the quantities extracted like the fine structure of characteristic scales and level densities. This chapter also gives a short overview of the tools used in the extraction of the characteristic energy scales and the associated background subtraction. The novel wavelet analysis technique is presented.

- Chapter 3 presents the practical side of high-resolution experiments using the K600 Magnetic Spectrometer and gives a detailed account of the experimental procedure. Analysis of the raw data and extraction of physically relevant spectra is presented.

- Chapter 4 presents the results of the analysis of the experimental data and theoretical predictions and the application of wavelet and Fourier transform together with the extracted spin- and parity separated level densities results and discussion. The role of knockout contributions to the background calculated by DWIA is also presented.

- Chapter 5 deals with the conclusions.

Chapter 2

Theoretical Considerations

A general description of the excitation and decay of nuclear giant resonances is presented in Sect. 2.1, together with a discussion of the properties of the Isoscalar Giant Quadrupole Resonance (ISGQR), which is the main focus of this investigation. The population of the ISGQR transitions in inelastic hadron scattering reactions is described in Sect. 2.2 followed by determination of cross sections using the Distorted Wave Born Approximation (DWBA) in Sect. 2.2.1. The Distorted Wave Impulse Approximation (DWIA) presented in Sect. 2.2.2 is used for a better understanding of background contributions due to quasi-free knockout reaction. State-of-the-art calculations of the ISGQR excitation and damping within the Second-RPA model are then discussed in Sect. 2.3 together with its formalism. The mathematical tools required to extract characteristic energy scales from both the experimental data and the theoretical predictions are presented in Sect. 2.4. The tools encompass the use of the Fourier Transform and Wavelet Analysis. This model independent analysis will be used later to ascertain the correspondence between scales observed in the experimental data and the appearance of scales in the theoretical predictions, which in turn can be linked to specific damping processes of the ISGQR. This is followed by details concerning spin- and parity- dependent nuclear level-density extraction in Sect. 2.5.

2.1 Excitation and decay of nuclear giant resonances

Nuclear giant resonances are simple, collective, particle-hole excitations of the nucleus. Such resonances are elementary modes of nuclear excitation which involve the coherent motion of the nucleons in the nucleus. These oscillations are classified by their angular momentum as monopole ($L = 0$), dipole ($L = 1$), quadrupole ($L = 2$) etc. resonances [Ber79]. Each type is subdivided according to isospin (ΔT) and spin (ΔS) transfers as illustrated in Fig. 2.1. The isoscalar ($\Delta T = 0$) modes are vibrations in which neutrons and protons move in phase. Modes in which neutrons and protons move out of phase are called isovector ($\Delta T = 1$). Similar oscillations may take place in the spin space. Nucleons with spin-up and spin-down can move either as in phase ($\Delta S = 0$) modes or as out of phase ($\Delta S = 1$) modes.

Microscopically, collective modes are treated as small-amplitude vibrations around the ground state. These vibrations are described via the coherent overlap of many one particle-one hole excitations. A schematic representation of such a microscopic description for the Giant Dipole Resonance (GDR) and the Giant Quadrupole Resonance (GQR) for the example of ^{90}Zr is illustrated in Fig. 2.2, where ($1p$-$1h$) transitions contribute coherently to a dipole ($\Delta L = 1$) or to a quadrupole ($\Delta L = 2$) mode. Proton (arrows with solid circles) and neutron (arrows with open circles) ($1p$-$1h$) transitions below and above the Fermi level (ε_F) are shown.

2.1.1 Width and decay of giant resonances

Of the three parameters describing a giant resonance, the energy E, the width Γ and the strength S, the width is special and complex in the sense that its theoretical understanding requires the most complicated description. The

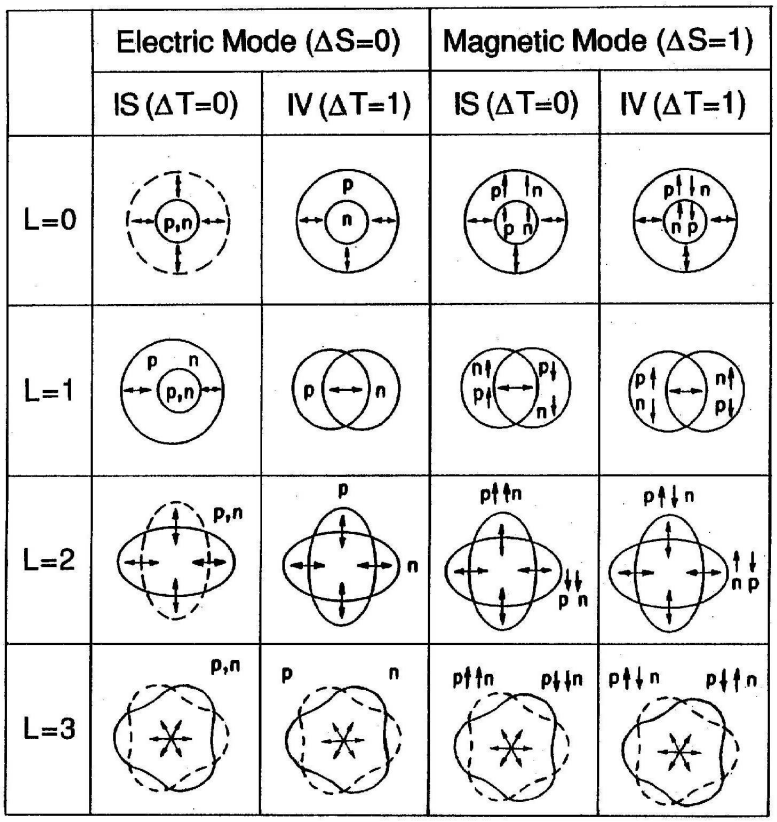

Figure 2.1: Excitation of nuclear giant resonances illustrating the isoscalar and isovector electric and magnetic resonances [Ito05].

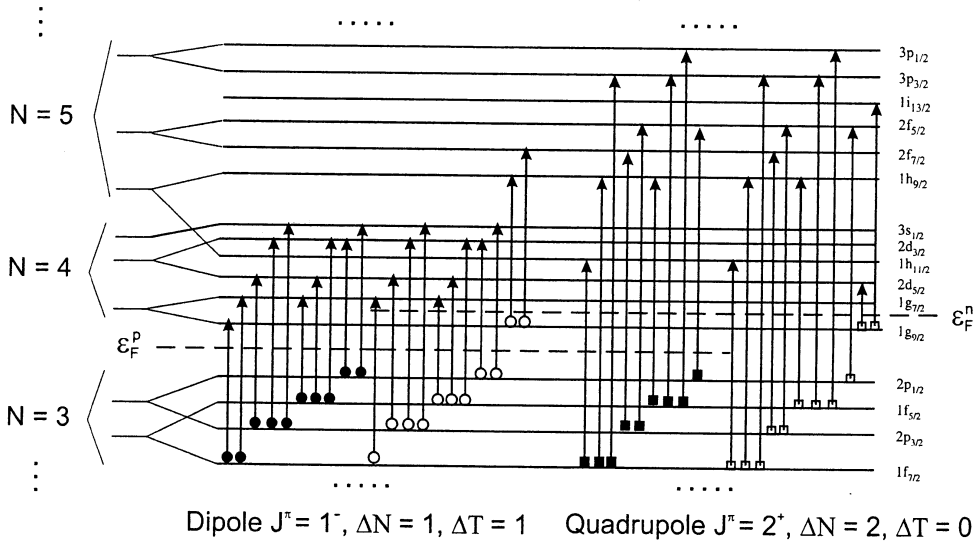

Figure 2.2: Microscopic description of giant resonances in the closed shell nucleus ^{90}Zr [She04].

strength distribution of the various giant resonances in spherical nuclei can be quantitatively described by a Lorentzian function with a width Γ. Only the centroid energy like the excitation energy $E_{\rm x}$ has been fitted as a smooth function of the mass number A. As a first approximation, the total width Γ can be written as

$$\Gamma = \Delta\Gamma + \Gamma\uparrow + \Gamma\downarrow, \tag{2.1}$$

where $\Gamma\uparrow$ is the escape width, $\Gamma\downarrow$ is the spreading width and $\Delta\Gamma$ is the Landau damping. Landau damping occurs because not all collective ($1p$-$1h$) strength, which acts as a doorway for the giant resonance, is necessarily concentrated in one single state but can be already appreciably fragmented. This is true for the higher multipole resonances and partly for the IVGDR.

The concept of the doorway picture describes the internal mixing that occurs through a hierarchy of couplings towards more and more degrees of freedom in the nucleus, starting from the two particle-two hole ($2p$-$2h$) states and ending with the np-nh states of the compound nucleus [Cas90, Rei94, Abe96]. The width of giant resonance can be represented with a Breit-Wigner distribution as shown in Fig. 2.3 [Ric81], in which the fine structure superimposes on the broad bump of the ISGQR. In this representation δE_1 denotes the escape width and δE_2 denotes the spreading width of giant resonance.

Giant resonances are located, in general, at excitation energies above the particle-decay threshold resulting in decay by particle emission. Although it should be noted that in a statistical decay process γ-decay may become dominant and, depending upon excitation energy, the average number of photons emitted may exceed the number of particles. However, because of the lower Coulomb barrier charged particles and neutrons are emitted by light nuclei

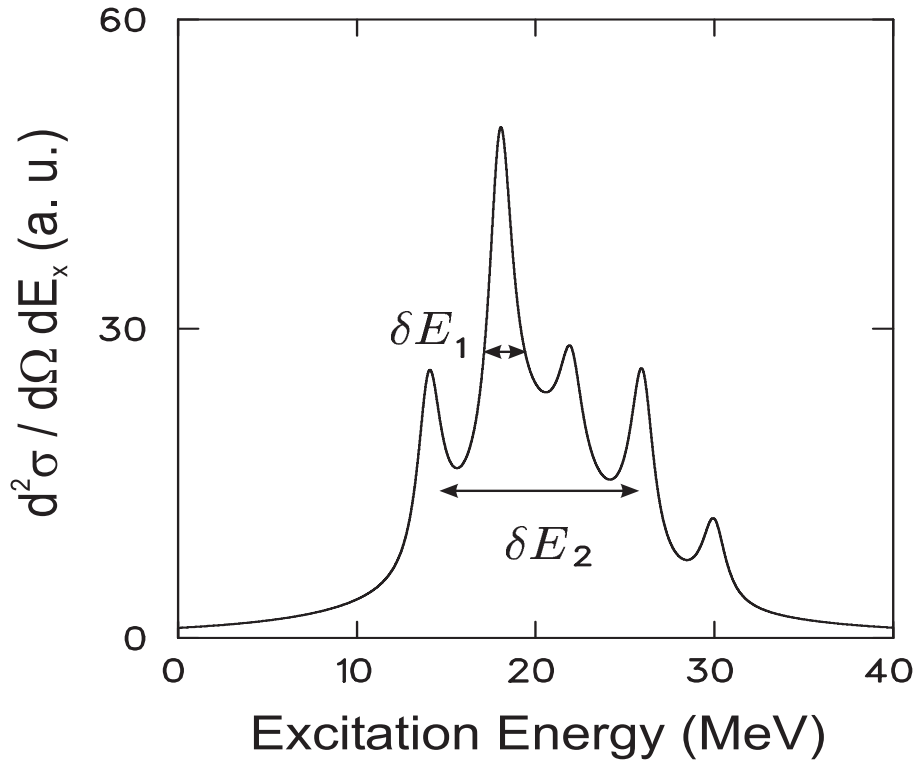

Figure 2.3: Schematic representation of the the formation of fine structure by the mixture of strength fluctuations on multiple energy scales [Ric81].

and only neutrons by heavier nuclei. Particle decay can occur through various processes as illustrated in Fig. 2.4. The coupling of the ($1p$-$1h$) state to the continuum gives rise to semi-direct decay into the hole states of the (A − 1) nucleus with a partial width $\Gamma\uparrow$, the escape width. If this process is the only one populating the hole state, then the relative population of these states would reflect the microscopic structure of the giant resonance. Also, the spreading width $\Gamma\downarrow$ arises as a result of the ($1p$-$1h$) doorway state which is mixed through the residual interaction with the more complicated and numerous ($2p$-$2h$) states that are present in the vicinity of the resonance.

One assumption often made is that the ($2p$-$2h$) states couple again to (3p-3h) ... (np-nh) states till finally a completely equilibrated system is reached. Particle decay can occur at each intermediate level. For a fully equilibrated system, the decay will be similar to that of a compound nucleus with the same

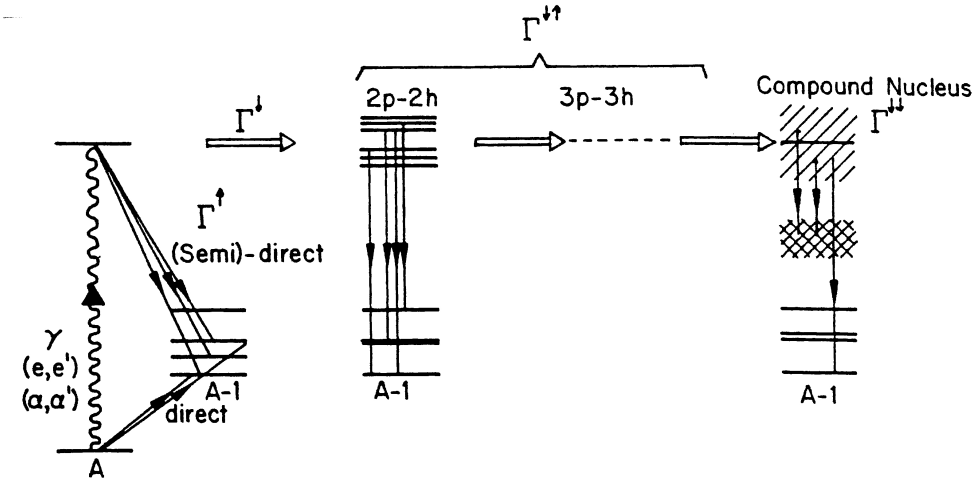

Figure 2.4: Schematic representation of the width of the collective 1p-1h state into a direct component $\Gamma\uparrow$ and a spreading component $\Gamma\downarrow$ of a giant resonance [Wou87]. Note that in principle the intermediate states can also decay as indicated by $\Gamma\downarrow\uparrow$.

excitation energy, spin and parity as the giant resonance. The total spreading width is given by

$$\Gamma\downarrow = \Gamma\downarrow\uparrow + \Gamma\downarrow\downarrow, \tag{2.2}$$

where $\Gamma\downarrow\uparrow$ is the partial width for pre-equilibrium decay and $\Gamma\downarrow\downarrow$ for statistical decay. In the case of the ISGQR it was found that, for a range of closed shell nuclei between ^{40}Ca and ^{208}Pb, damping into the doorway states (particle-hole + vibration) accounts for about 60% of the experimental width [Ber83].

From an experimental point of view one might try to distinguish gross and fine structure as well as intermediate structure ($2p$-$2h$), ($3p$-$3h$), *etc.* before reaching the final stage of the compound nucleus. From a theoretical point of view only two extremes, the primary doorway at the begining and the compound nucleus at the end of the (np-nh) hierarchy, are reasonably well understood

and detailed calculations on statistical decay are available for many nuclei.

2.2 Transitions to the ISGQR and inelastic hadron scattering

In a simple macroscopic picture an isoscalar giant quadrupole resonance can be described as a collective oscillation of the surface of a nucleus in which protons and neutrons move in phase. It is characterised by selection rules $\Delta L = 2$, $\Delta S = 0$ and $\Delta T = 0$, where L denotes the angular momentum, S denotes the spin and T is the isospin of the nucleons involved. The present study is based on the (p,p$'$) reaction in which the isoscalar quadrupole strengths, B($E2$), and the characteristic scales of the fine structure can be extracted from the data.

Inelastic hadron and electron scattering reactions at forward scattering angles have been extensively used as spectroscopic tools to map the ISGQR strength distribution. The most commonly used probe has been the (α, α') reaction [Zwa85, Ber81] since it selectively excites only isoscalar modes to first order due to its intrinsic properties. For example, for a $J^\pi = 0^+$ target nucleus the spin and parity of the state excited are given by ΔL and $(-1)^{\Delta L}$, respectively. As in the case of light nuclei, it was already clearly shown in [Zwa85] that a substantial amount of about 50% of the Energy Weighted Sum Rule (EWSR) for $E2$ strength in ^{40}Ca is present in the excitation energy region 10 - 16 MeV, being concentrated around $E_\mathrm{x} = 14$ MeV. While previous hadron scattering experiments on giant resonances almost exclusively used α-particles because of isospin selectivity, a proton inelastic-scattering measurement has recently demonstrated [She04] that proton scattering also provides a versatile tool for studies of structure in the continuum.

Figure 2.5 illustrates the results of (α, α') experiments demonstrating the prominent excitation of the ISGQR [Bor81] in light nuclei. Here, it should be noted that the continuum contribution underneath the giant resonance region has been drawn in just below the minima in the spectra as the dashed line. In contrast, however, in the present investigation a model independent analysis is presented for the determination of background in the continuum region (see Section 4.8.1). Additionally, contributions from the quasi-free scattering ^{40}Ca(p,2p)^{39}K and ^{40}Ca(p,pn)^{39}Ca reactions are calculated explicitly (see Section 4.7). With advancement in experimental techniques, more intrinsic structure can be found with high energy-resolution experiments at intermediate incident energies. It should, in particular, be noticed that as target mass increases the ISGQR becomes considerably more compact and moves to lower excitation energy.

In the (α, α') the reaction is predominantly surface-dominated and measures L transfer for the excited normal-parity states, and the isoscalar component of the projectile-nucleon force. The (e,e$'$) reaction gives reduced electromagnetic transition probabilities while the (p,p$'$) reaction is useful in probing various components of the effective interaction and testing microscopic wave-functions. Furthermore, the choice of the proton probe allows an independent test of ISGQR strengths deduced in electron and α-scattering experiments for the same reaction channel. This seems to question the models developed for the conversion of hadronic scattering cross section to transition strengths. Above all, the fine structure within the ISGQR can be investigated with better energy resolution in the (p,p$'$) than in inelastic α-particle scattering. Although proton scattering is more complicated since the excited states can be any of four modes, namely, isoscalar spin-flip and non-spin-flip and isovector spin-flip and non-spin-flip, a more sensitive quantity than a cross section can be determined from (p,p$'$) experiment. But there is a way to overcome this problem since the

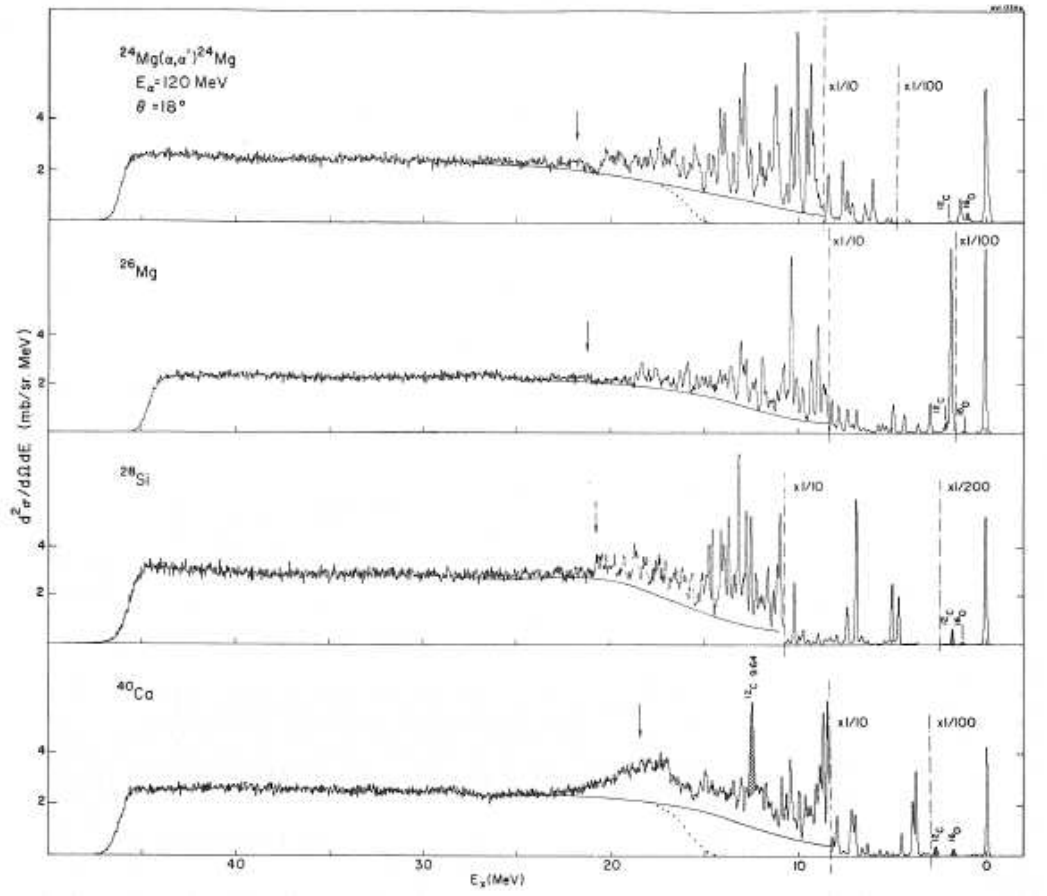

Figure 2.5: Inelastic α-particle scattering spectra at 120 MeV on ^{24}Mg, ^{26}Mg, ^{28}Si and ^{40}Ca taken at $\theta_{\mathrm{Lab}} = 18°$. The shape of the continuum is indicated by the dashed line. The arrows are located at the excitation energy $65A^{-\frac{1}{3}}$ which is within the excitation energy range of the ISGQR (taken from [Bor81]).

relative importance of the various excited modes can be estimated from the effective nucleon-nucleon interaction as deduced by Love and Franey [Lov81, Pet81].

The effective interaction between the projectile p and the i'th nucleon of the nucleus can be written as

$$V_{ip}\left(r_{ip}\right) = V^{C}\left(r_{ip}\right) + V^{LS}\left(r_{ip}\right)\vec{L}.\vec{S} + V^{T}\left(r_{ip}\right)S_{ip}\left(\hat{r}_{ip}\right), \qquad (2.3)$$

where $\vec{L}.\vec{S}$ and $\mathrm{S}_{ip}\left(\hat{r}_{ip}\right)$ are the usual spin-orbit and tensor operators. The cen-

tral interaction V^C, spin-orbit interaction V^{LS} and tensor interaction V^T, all depend on the momentum transfer and energy of the incident projectile. For the ISGQR to be selectively excited the V^C term must dominate. However, because of the large corrections due to the medium effects at low bombarding energies, the effective interactions used are energy dependent. Although experiments can be done at lower bombarding energies in which ISGQR cross-section is roughly independent of the incident energy, what is of concern is the more complex reaction mechanism and the possibility of background problems at these projectile energies. At intermediate energies ($100 < E < 400$ MeV/u), the effective interaction is taken to be the free nucleon-nucleon interaction [Won90]. At energies much lower than these values, the transit time of a nucleon through a nucleus is long enough that multiple scattering may happen frequently enough to complicate the reaction. At energies much higher than these values, good energy resolution is difficult to achieve and at the same time the increased production rates of pions and other particles make the condition unfavourable for studying nucleon-nucleus interaction. Therefore, it is clear to say that a proton energy of 200 MeV is sufficient enough for nucleon-nucleon interaction to occur in nuclei in order to achieve a dominant one-step reaction in the internal degrees-of-freedom of nuclei as well.

2.2.1 Distorted Wave Born Approximation (DWBA) of inelastic scattering

Distorted Wave Born Approximation (DWBA) is necessary due to its usefulness in generating distorted wave functions which were later implemented in the calculations involving the distorted wave impulse approximation and also in the spin-filter effects of various target nuclei. Inelastic scattering exciting collective states of the nuclei under investigation can be determined using the macroscopic collective-model within the DWBA, utilising prescriptions of the scattering process as described, for example, in [Sat72]. In general terms within

the DWBA, the two-body differential cross-section for the reaction $A(a,b)B$ can be expressed as

$$\frac{d\sigma\left(\theta\right)}{d\Omega}=\left(\frac{\mu_b}{2\pi\hbar^2}\right)^2\frac{v_b}{v_a}\frac{1}{(2J_A+1)(2s_a-1)}\sum_{M_AM_Bm_am_b}|T^{M_AM_Bm_am_b}|^2, \quad (2.4)$$

where μ is the reduced mass, v_a, v_b are the relative velocities of particles a and b for the entrance and exit channels, J is the orbital angular momentum, M_A and M_B are the masses of target and recoil nucleus and m_a and m_b are the masses of projectile and projectile related product, respectively. The transition amplitude, T, which describes the scattering reaction from an initial channel i to a final channel f for the reaction $A\left(a,b\right)B$ is given by

$$T=\int d^3r_b\int d^3r_a\chi^{(-)}(\vec{k}_f,\vec{r}_b)^*\langle bB|U|aA\rangle\chi^{(+)}(\vec{k}_i,\vec{r}_a), \quad (2.5)$$

where $\chi^{(+)}$ and $\chi^{(-)}$ are the distorted waves describing the relative motion before and after the collision, $\vec{r}_a$ and $\vec{r}_b$ are the relative coordinates for the systems (a,A) and (b,B) and the quantity $\langle bB|U|aA\rangle$ is the form factor which contains the nuclear structure information. The interaction potential U which depends on internal coordinates can be split into Coulomb and nuclear potential parts.

It should be noted that in this type of calculation, the cross-section with different normalisation can be applied depending upon whether it is an inelastic scattering or a particle transfer reaction. For the inelastic scattering $b=a'$ the inelastically scattered projectile and $B=A^*$ the excited target nucleus. The complex nuclear potential can then be written as

$$U\left(r\right)=V\left(r\right)+iW\left(r\right), \quad (2.6)$$

where $V(\mathrm{r})$ is the real part of the central potential which is responsible for elastic scattering and $W(\mathrm{r})$ is the imaginary part of the central potential and responsible for absorption of flux into non-elastic channels. The nuclear potential is complex because it is a short-range attractive interaction and represents the many-body interaction between colliding nuclei. Additionally, it contains terms to describe spin-orbit coupling and isospin dependence. A physically-realistic phenomenological potential often used is the Woods-Saxon potential. The optical potential used in the calculation of the distorted waves is parameterised as

$$\begin{aligned} U(r) = V_{\mathrm{C}}(r) - Vf_{\mathrm{o}}(r, R_{\mathrm{o}}, a_{\mathrm{o}}) - iWf_{\mathrm{w}}(r, R_{\mathrm{w}}, a_{\mathrm{w}}) \\ +4W_{\mathrm{d}}\, a_{\mathrm{w}} \frac{d}{dr} f_{\mathrm{w}}(r, R_{\mathrm{w}}, a_{\mathrm{w}}) \\ +\frac{2}{r}\left[V_{\mathrm{so}} \frac{d}{dr} f_{\mathrm{vso}}(r, R_{\mathrm{vso}}, a_{\mathrm{vso}})\right] \\ +\frac{2}{r}\left[iW_{\mathrm{so}} \frac{d}{dr} f_{\mathrm{wso}}(r, R_{\mathrm{wso}}, a_{\mathrm{wso}})\right] \overrightarrow{L}.\overrightarrow{\sigma}. \end{aligned} \tag{2.7}$$

The Coulomb potential $V_{\mathrm{C}}(r)$ is that from a uniformly charged sphere of radius $r_{\mathrm{oC}}A^{1/3}$. The quantities V_{so} and W_{so} are the corresponding real and imaginary strengths of the spin-orbit potential, W_{d} represents the imaginary surface potential and $\overrightarrow{L}$ and $\overrightarrow{\sigma}$ denotes the orbital and spin angular momentum of the incident nucleon. The geometry f has the usual Woods-Saxon shape given by

$$f(r, R_x, a_x) = \frac{1}{1 + exp[(r - R_x)/a_x]}, \tag{2.8}$$

with $R_x = r_{\mathrm{o}x}A^{1/3}$ and a_x the corresponding diffuseness parameter.

In first-order, DWBA inelastic scattering is treated as a one-step transition process which includes a collective form factor. In the collective model, it

is physically reasonable to expect the nuclear interaction to follow the shape of the nuclear surface. Thus, the spherically-symmetric optical potential is deformed by vibrations about a spherical mean of radius $R_{\rm o}$, or by rotations of a permanently deformed sphere of radius $R_{\rm o}$. Therefore, the collective form-factor can be described as a derivative of the interaction potential in the form

$$U(r) = U(r - R_{\rm o}) - \delta R \frac{d}{dr} U(r - R_{\rm o}). \tag{2.9}$$

In this expression, the second term represents the non-spherical part of the inelastic excitation where δ is the deformation length. It has been established that in a collective mode of excitation there exists a degree of correlation between the movements of individual nucleons. The strength of a collective excitation in the vibrational or rotational models is determined by the extent of departure from spherical state. In what follows, the deformation length for a rotational nuclei is given as

$$\delta_L = R_{\rm o}\beta_L^R = R_{\rm w}\beta_L^I \tag{2.10}$$

where $R_{\rm o}$ and $R_{\rm w}$ are the real and imaginary nuclear radii and β_L^R and β_L^I are the real and imaginary deformation parameters which depend on the multipolarity L of the state excited.

2.2.2 Distorted Wave Impulse Approximation (DWIA) of Quasi-free knockout

The Distorted Wave Impulse Approximation (DWIA) can be used to determine the contribution due to quasi-free proton and neutron knockout in the inclusive inelastic proton-scattering reaction. Such reactions contribute to the background underlying the isoscalar giant quadrupole resonances investigated.

In addition, determination of this background component should lead to a more reliable extraction of level density in the nuclear continuum.

In the DWIA, the three-body cross-section for a reaction $A(a, a'b)B$ can be written as

$$\frac{d^3\sigma}{d\Omega_{a'} d\Omega_b dE_{a'}} = SK \frac{d\sigma}{d\Omega_{a+b}} \sum_{\lambda} |T_{AB}^{L\lambda}|^2, \tag{2.11}$$

where S is the spectroscopic factor for the final state in B, K is a kinematic factor, and $d\sigma/d\Omega_{a+b}$ is a half-shell two-body cross section for $a+b$ scattering. The quantity $T^{L\lambda}$ is a distorted momentum distribution for a particle b bound to core B in target A with angular momentum L (projection λ) which can be written as [Cha98]

$$T_{AB}^{L\lambda} = \frac{1}{(2L+1)^{1/2}} \int \chi_{aB}^{(-)*}(\vec{k}_{aB}, \vec{r}) \chi_{bB}^{(-)*}(\vec{K}_{bB}, \vec{r}) \chi_{aA}^{(+)}(\vec{k}_{aA}, \gamma\vec{r}) \phi_{L\lambda}(\vec{r}) d\vec{r}. \tag{2.12}$$

In this expression $\gamma = \frac{B}{B+b}$, $\chi^{(\pm)}$ are distorted waves, and $\phi_{L\lambda}$ is the spatial part of the bound state wave-function of particle b. The quantities L and λ are the orbital angular momentum carried by b and its projection, respectively. In addition, the bound-state potential given by

$$V_{\mathrm{B}} = -V_{\mathrm{o}} f(r, R_{\mathrm{o}}, a_{\mathrm{o}}), \tag{2.13}$$

is also required in order to calculate the nuclear bound state wave-function. Three distorted waves are generated using the optical potential of Eq. (2.7) in Sect. 2.2.1. The two-body cross-section is then evaluated using an on shell amplitude interpolated from phase shifts for free $a+b$ scattering. This can be done

with two different prescriptions for the total energy, E. In the Final-Energy Prescription (FEP) approximation, E is taken to be the relative centre-of-mass energy of the emitted particles in the exit channel while in the Initial Energy Prescription (IEP) approximation, E is the relative centre-of-mass energy of the incident and struck particles in the entrance channel .

For inclusive studies, integration over the solid angle of the unobserved nucleon b gives

$$\frac{d^2\sigma}{d\Omega_{a'}dE_{a'}} = \int \frac{d^3\sigma}{d\Omega_{a'}d\Omega_b dE_{a'}} d\Omega_b. \tag{2.14}$$

It is assumed that the particle a' is observed after a quasi-free collision with particle b inside the nucleus A. Then particle b, which in the present case is either a proton or a neutron, remains undetected in the experiment.

2.3 Theoretical interpretation of giant resonances and their fine structure

The importance of the theoretical model of nuclear giant resonance excitation is to understand the origin and nature of the fine structure of the characteristic scales found in experiments by applying the most suitable microscopic models. A great deal of theoretical work has been directed towards the understanding of the origin of fine structure and damping mechanisms in light nuclei. Such models include Extended Theory of Finite Fermi Systems (ETFFS) [Kam97], Quasi-particle Phonon Model (QPM) [Sol92], Extended Time Dependent Hartree-Fock (ETDHF) [Lac01], Random Phase Approximation (RPA) [Bro64] and Second-RPA (SRPA) [Dro86]. The main focus of this study is on the low-mass region $A \leq 40$ for which the SRPA treatment has been applied

and is elaborated upon in Sect. 2.3.1. QPM is not so suited because of the underlying assumption of phonons as building blocks of low-energy structure is not well fulfilled in light nuclei. By way of example, the QPM has been proven to be most suitable for the description of strength distributions in heavy and medium-heavy nuclei [She04]. It is well known that the influence of the continuum on the total width is very important for more detailed problems such as the fine structure. Therefore, in order to explain giant resonance widths and the specific details of their strength distribution, including fine structure, it is necessary to take into account complex configurations as well as the single-particle continuum.

2.3.1 ISGQR strengths in the Second Random Phase Approximation (SRPA)

One of the methods of a microscopic calculation for the description of giant resonances or nuclear response is the Random Phase Approximation (RPA) [Bro64], in which giant resonances appear as a coherent superposition of one particle-one hole ($1p$-$1h$) excitations in closed-shell nuclei or two quasiparticle excitations in open-shell nuclei built on a correlated ground state. While it is well suited for the description of the mean energies and total transition probabilities, it fails to account for the energy distribution of the response function, for instance, the width of giant resonances. Thus, a theoretical prediction obtained in the framework of models that take coupling to complex degrees-of-freedom into consideration is essential.

An extension of the $1p$-$1h$ RPA by inclusion of $2p$-$2h$ excitations seems to be the most applicable candidate for incorporating damping effects which go beyond the mean-field description, and hence provides a more complete theory of small-amplitude collective motion. This was done within the framework of

Second Random-Phase Approximation (SRPA) [Dro86]. The approach is appropriate for the description of fine structure of giant resonances in light nuclei due to the fact that it improves the description of anharmonic effects and is also suited for incorporating higher-order effects in the ground state wave-function [Dro90]. The different contributions to the damping of the single-particle and collective response in light nuclei can be disentangled. In addition, SRPA has been used successfully for the description of damping of giant resonances in [Dro90, Yan83].

2.3.2 SRPA Formalism

The SRPA formalism of Yannouleas [Yan87] was used in analogy to RPA. Excited states $\mid \nu\rangle$ of energy $E_\nu = \hbar\omega_\nu$ with respect to the ground state $\mid 0\rangle$ given as

$$\mid \nu\rangle = Q^\dagger_\nu \mid 0\rangle, \tag{2.15}$$

are considered as combinations of $1p$-$1h$ and $2p$-$2h$ configurations. The corresponding creation operators $Q^\dagger_\nu$ are then written as

$$\begin{aligned} Q^\dagger_\nu \mid 0\rangle = \Sigma_{ph} X^\nu_{ph} O^\dagger_{ph} - \Sigma_{ph} Y^\nu_{ph} O_{ph} \\ +\Sigma_{p1h1p2h2} \chi^\nu_{p1h1p2h2} O^\dagger_{p1h1p2h2} \\ -\Sigma_{p1h1p2h2} \mathcal{Y}^\nu_{p1h1p2h2} O_{p1h1p2h2}, \end{aligned} \tag{2.16}$$

where $O^\dagger_{ph}$ creates a ph state and $O^\dagger_{php'h'}$ creates a $2p$-$2h$ state, such that

$$Q_\nu \mid 0\rangle = 0. \tag{2.17}$$

The SRPA ground state which is the vacuum of the annihilation operators

Q_ν, is approximated by the Hartree-Fock (HF) ground state. The forward $(X, \mathcal{X})$ and backward $(Y, \mathcal{Y})$ amplitudes are given by the SRPA equations in $ph \oplus 2p$-$2h$-space

$$\begin{pmatrix} A & \mathcal{A}_{12} & B & 0 \\ \mathcal{A}_{21} & \mathcal{A}_{22} & 0 & 0 \\ -B^* & 0 & -A^* & -\mathcal{A}_{12}^* \\ 0 & 0 & -\mathcal{A}_{21}^* & -\mathcal{A}_{22}^* \end{pmatrix} \begin{pmatrix} X^\nu \\ \mathcal{X}^\nu \\ Y^\nu \\ \mathcal{Y}^\nu \end{pmatrix} = \hbar\omega_\nu \begin{pmatrix} X^\nu \\ \mathcal{X}^\nu \\ Y^\nu \\ \mathcal{Y}^\nu \end{pmatrix}, \tag{2.18}$$

where A and B are usual RPA matrices, $\mathcal{A}_{12}$ describes the coupling between $1p$-$1h$ and $2p$-$2h$ states and $\mathcal{A}_{22}$ contains the $2p$-$2h$ states and their interactions. If the coupling among those states were neglected, then $\mathcal{A}_{22}$ is diagonal and its elements are equal to the unperturbed $2p$-$2h$ energies

$$[\mathcal{A}_{22}]_{p_1h_1p_2h_2,p_1'h_1'p_2'h_2'} = \delta_{p_1p_1'}\delta_{h_1h_1'}\delta_{p_1p_1'}\delta_{h_1h_1'}\left(e_{p_1} + e_{p_2} - e_{h_1} - e_{h_2}\right), \tag{2.19}$$

where e_i are the HF single-particle energies, respectively. Details of the calculation can be found in [Pap09].

2.4 Tools for extracting characteristic energy scales

A principal motivation why the characteristic energy scales are extracted is because of their usefulness in understanding the damping mechanisms present in nuclei across the periodic table, specifically as this work is focused on light nuclei. Fourier analysis as a signal processing tool has had extra-ordinary success in many different scientific fields. Typically, it is applied to a time-sequence

data set to determine dominant periodicities from the power spectrum extracted. However, a shortcoming of Fourier analysis is that scales cannot be identified directly in specific regions of the energy spectrum analysed. Hence, the need for developing an analysis technique that can extract both position and localisation of scales is required. Several approaches have been suggested for the extraction of these energy scales (see [She08] for a comprehensive discussion) but recently the use of Wavelet analysis was found to be the most efficient. Wavelet analysis of the input data set has an advantage over the Fourier transform in its ability to allow not only the "energy scales" of the input excitation energy spectrum to be determined but also the position of the scales within the energy spectrum.

The intrinsic scale of a particular wavelet basis function has a certain arbitrary character; it is chosen more for functional simplicity than any physical or mathematical characteristic of the wavelet. The conversion of a particular mother-wavelet scale can be achieved by relating it to the scale introduced by a Fourier transform [Tor98]. All scales can then be normalized to this "Fourier scale." A direct link between Fourier and intrinsic scale can be made for the case of the Complex Morlet wavelet, which should give identical scales while a constant factor of 0.813 can be used for a Real Morlet wavelet.

Continuous wavelet transform analysis using both the Real Morlet and Complex Morlet mother wavelets has been successfully applied [She04, Usm06]. Because of the physical nature of the scales suggested for the decay of giant resonances in nuclei [Har00], the use of a "wavelet scale," equivalent to the Fourier scale without any constant factor is preferred. Therefore, a newly developed Complex Lorentzian mother-wavelet has been applied since it represents the natural shape of a giant resonance (see Fig. 2.3) in form of the Breit-Wigner function and also gives the equivalent Fourier scale without any

constant factor.

2.4.1 Fourier Transform

The Fast Fourier Transform is a perfectly general mathematical transformation which was developed many years ago. This powerful tool relies on its ability to relate some very important pairs of physical variables, the most important of which are probably those of time and frequency. As such, it is possible to transform the present results obtained as a function of energy and express them either as a function of frequency or as a function of wavelength (1/frequency) in the corresponding energy units.

2.4.1.1 Discrete Fourier transform

Given an input data sequence of length N the Discrete Fourier Transform (DFT) is defined as $X(k)$ and is given by

$$X\left(k\right) = \sum_{n=1}^{N} x\left(n\right) exp\left(-2\pi i\right)\left(k-1\right)\left(\frac{n-1}{N}\right), \qquad 1 \leq k \leq N. \tag{2.20}$$

Here, *X(k)* are referred to as the Fourier coefficients or harmonics. Both $x(n)$ and $X(k)$ are, in general, complex. Also, the sequences $x(n)$ and $X(k)$ are referred to as time domain and frequency domain data, respectively. In principle, of course, there is no reason why $x(n)$ should be a sampled time series. The present case uses a signal which is a function of energy as the input data sequence.

2.4.1.2 Periodogram

The periodogram for a sequence $[X_1, \ldots, X_n]$ is given by the following formula:

$$S\left(e^{i\omega}\right) = \frac{1}{n}|\sum_{l=1}^{n} x_l e^{-i\omega l}|^2. \tag{2.21}$$

This expression forms an estimate of the power spectrum of the signal defined by the sequence $[X_1, \ldots, X_n]$. If the signal sequence is weighted by a window $[w_1, \ldots, w_n]$, then the weighted or modified periodogram is defined as [Wel67]

$$S\left(e^{i\omega}\right) = \frac{\frac{1}{n}|\sum_{l=1}^{n} x_l e^{-i\omega l}|^2}{\frac{1}{n}\sum_{l=1}^{n} x_l |w_l^2|}. \tag{2.22}$$

In either case, periodogram uses an n-point FFT to compute the power spectral density as $S\left(e^{i\omega}\right)/F$, where F is 2π when the sampling frequency was not supplied and f_s when the sampling frequency was supplied, with f_s as the given sampling frequency.

2.4.1.3 Power Spectrum

In the case of a time series the result of the Fourier transform is a complex vector. For a function $f(x)$ of quantity x that has a Fourier transform of the form $\hat{f}(k)$, the Fourier power spectrum $P_f(k)$ can be written as

$$P_f(k) = |\hat{f}(k)\hat{f}^*(k)|, \tag{2.23}$$

up to some normalisation of the spectrum. The absolute value of the complex vector is called the power P. Here, 1/frequency is used to obtain wavelength from an energy spectrum so as to provide a power spectrum against a characteristic scale in units of energy (keV or MeV).

2.4.2 Wavelet Analysis

Wavelet transforms have advantages over traditional Fourier transforms for representing functions that have discontinuities and sharp peaks. There are basically two classes of wavelet transform: Continuous Wavelet Transform (CWT) and Discrete Wavelet Transforms (DWT). Note that both CWT and DWT can be used to represent continuous-position spectra. CWT operates over every possible scale and translation whereas DWT uses a specific subset of scale and translation values or representation grid.

2.4.2.1 Theory of wavelet

Wavelet is defined as a series of functions $\psi_{a,b}(t)$ derived from a function $\psi(t)$ by dilation (scale) and translation (shift) [Gro84]

$$\psi_{a,b}(t) = \frac{1}{\sqrt{|a|}}\psi\left(\frac{t-b}{a}\right), \qquad a \neq 0, \qquad a, b \in R \tag{2.24}$$

where a is the scale parameter that controls the dilation, b is the shift parameter that controls the translation and $\psi(t)$ is the basis function of a wavelet. $\psi(t)$ is said to have n vanishing moments when it satisfies that [Mal92]

$$\int_{-\infty}^{+\infty} t^k \psi(t) dt = 0 \qquad \text{for} \qquad 0 \leq \text{k} < \text{n}. \tag{2.25}$$

A wavelet with n vanishing moments is orthogonal to polynomial of degree $n-1$, i.e. it can be used to suppress polynomial of degree $n-1$ through convolution. Therefore, a wavelet function with n vanishing moments can be written as the nth-order differentiation of a function $\theta(t)$ [Mal98]

$$\psi(t) = (-1)^n \frac{d^n \theta(t)}{dt^n}, \tag{2.26}$$

where $\theta(t)$ is a function with fast decay and whose integral is a non-zero con-

stant. With a wavelet function that has n vanishing moments, the transform can be given by [Mal98]

$$Wf(a,b) = f^{*}\psi_a(b) = f^{*}\left(a^n \frac{d^n\theta_a}{dt^n}\right)(b) = a^n \frac{d^n}{dt^n}\left(f^{*}\theta_a\right)(b), \tag{2.27}$$

where * denotes the operator of convolution, and $\psi_a(\mathrm{t}) = \frac{1}{a}\psi(\frac{t}{a})$, and $\theta_a(\mathrm{t}) = \frac{1}{a}\theta(\frac{t}{a})$. Therefore, the n'th-order derivative calculation of an analytical signal can be obtained through one wavelet transform by using a wavelet function with n vanishing moments.

A variety of wavelets provides a set of tools for performing many different tasks. It is found that wavelet transforms with commonly used wavelet functions can be regarded as a smoothing and a differentiation process. The number of vanishing moments of a wavelet indicates the order of the derivative that it will determine. It is important to note that the width and choice of the wavelet used affect the amount of the smoothing. Some examples of mother wavelets and their graphical representations are shown in Fig. 2.6.

2.4.2.2 Continuous Wavelet Transform (CWT)

The Continuous Wavelet Transform (CWT) is defined as the sum over all time of the signal multiplied by a scaled, shifted version of the wavelet function Ψ, which can be expressed as

$$C\left(a,b\right) = \int S(t)\frac{1}{\sqrt{a}}\Psi\left(\frac{t-b}{a}\right)dt, \tag{2.28}$$

where a is the scale and b is the position and are equivalent to δE and E_{x}, respectively, in the analysis of energy scale. By folding the original energy

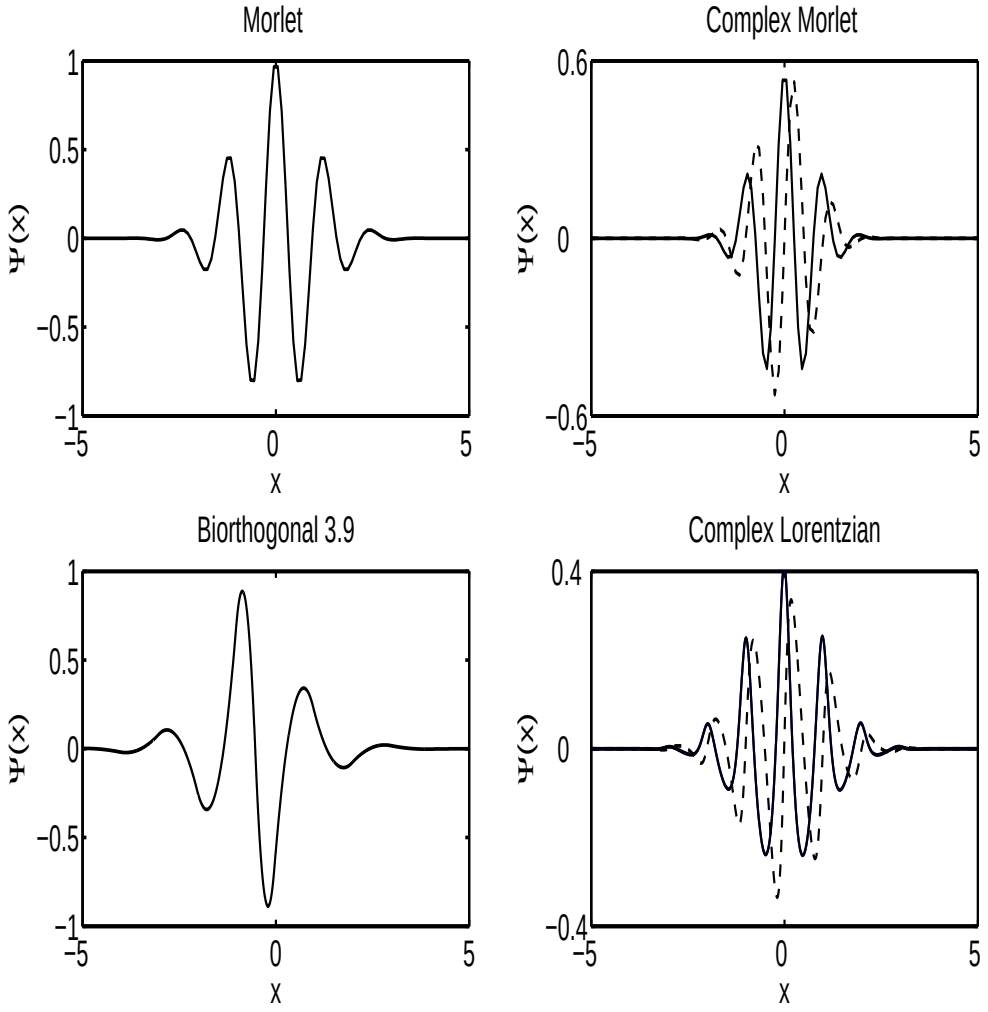

Figure 2.6: Illustration of the principles of wavelet analysis and wavelet families. Real ($k = 5$, see Eq. (2.30)) and Complex Morlet ($f_c = 1$, $f_b = 1$, see Eq.(2.31)) wavelets are the products of cosine and Gaussian functions. The Biorthogonal 3.9 wavelet has an antisymmetrical shape but no analytical expression. Complex Lorentzian ($f_c = 2\Gamma$, $f_b = 2$, see Eq.(2.32) and Sect. 4.4.1) wavelets is a continuous sum of Lorentzians plus Gaussian envelope. The real parts are shown as solid line and the imaginary parts are in dashed lines.

spectrum $\sigma(E)$ with a chosen wavelet function Ψ, the coefficients are obtained as

$$C\left(E_x, \delta E\right) = \frac{1}{\sqrt{\delta E}} \int \sigma\left(E\right) \Psi\left(\frac{E_x - E}{\delta E}\right) dE. \tag{2.29}$$

The parameters excitation energy E_x and bin size δE can be varied contin-

uously or in discrete steps j, where $\delta E = 2j$, $j = 1, 2, 3, \ldots$, and $E_{\mathrm{x}} = \delta E$. A variety of wavelets provide a set of tools for performing many different tasks. The choice of wavelet is made based on its mathematical properties among which are moments, compact support and the regularity of a signal (the number of times that it is continuously differentiable) [Mat06]. Complex wavelets produce a complex CWT analysis, allowing the phase of the result to be examined.

The Real Morlet wavelet is derived by taking a periodic wave and localising it with a Gaussian envelope and is expressed as

$$\Psi(x) = \frac{1}{\pi^{1/4}} cos(ikx)\, exp\left(-\frac{x^2}{2}\right). \tag{2.30}$$

The parameter k weighs the resolution in scales versus the resolution in localisation. In order to satisfy the admissibility conditions $k \leq 5$ must be fulfilled [Mat06]. In addition, the Complex Morlet wavelet is given by

$$\Psi(x) = \frac{1}{\sqrt{\pi} f_{\mathrm{b}}} exp(2\pi i f_{\mathrm{c}})\, exp\left(-\frac{x^2}{f_{\mathrm{b}}}\right), \tag{2.31}$$

where f_{c} is the wavelet centre frequency and f_{b} controls the wavelet band width. This has been used in the Semblance and Dot product analysis of Cooper *et al.* [Coo08]. The semblance analysis allows comparison to be made between data sets revealing common scales while the Dot product analysis produces a further refinement to compare large amplitude of scales between data sets.

The Complex Lorentzian mother wavelet would ideally be the sum of an infinite series of Lorentzian functions of width Γ and spacing f_{c} localised by a Gaussian

envelope. However, in practice it was found sufficient to sum on each side of the centre Lorentzian function only sixteen other Lorentzian functions. This can be written as

$$\Psi(x) = \sum_{n=-16}^{+16} \frac{\left(\frac{\Gamma}{2}\right)^2}{\left(x - (x_o + nf_c)\right)^2 + \left(\frac{\Gamma}{2}\right)^2} exp\frac{1}{2}\left(-\frac{x^2}{f_b}\right). \tag{2.32}$$

Here, the parameters x_o and Γ are the centre position and full-width at half-maximum (FWHM) of the Lorentzian function, respectively. The parameter f_c represents the spacing or wavelength of the wavelet. By setting $f_c = 2\Gamma$ there is an obvious similarity with the cosine function which was very successfully used in analysis using the Complex Morlet mother wavelet. In addition, the Complex Lorentzian wavelet scale is equivalent to the Fourier scale only if $f_c = 2\Gamma$. By varying the width of the Gaussian envelope f_b better localisation of wavelet scale can be achieved (see Sect. 4.4.1). Further it should be mentioned that spectrum reconstruction using CWT and Complex Lorentzian mother wavelet identifies half the wavelet scale as the width of the feature in the energy spectrum (see Sect. 4.5).

2.4.2.3 Semblance and Dot product analysis

The wavelet-based semblance S is given as

$$S = cos^n(\theta), \tag{2.33}$$

where n is an odd integer greater than zero, θ is the local phase (which can range between $-\pi$ and $+\pi$) given by

$$\theta = tan^{-1}\left(\Im(CWT_{1,2})/\Re(CWT_{1,2})\right) \tag{2.34}$$

and the cross-wavelet transform

$$CWT_{1,2} = CWT_1.CWT_2^*, \tag{2.35}$$

where $CWT_{1,2}$ is a complex quantity with CWT_1 as the continuous wavelet transform of dataset 1, and CWT_2 as the continuous wavelet transform of dataset 2 [Coo08]. The vector dot-product D of the two complex wavelet vectors can then be written as

$$D = cos^n(\theta)|CWT_{1,2}|, \tag{2.36}$$

respectively.

2.4.2.4 Discrete wavelet transform (DWT)

The discrete wavelet transform (DWT) is a more efficient way of representing data than the CWT, and as such is better suited to applications such as compression and filtering. A disadvantage of the DWT is that it is not shift-invariant i.e. the DWT of a signal and a shifted version of itself are not shifted version of each other. Another important fact is that the DWT is configured in powers of 2. From Eq. (2.28), if a and b assume only discrete values then from Eq. (2.29)

$$\delta E_k = 2^k \Delta \tag{2.37}$$

and

$$E_{xk} = k \cdot \delta E_k, \qquad k = 1, 2, \ldots, \tag{2.38}$$

where Δ is the bin size of the data. Here, the value of k specifies the number of significant sinusoidal oscillations within a Gaussian window.

The DWT is used to analyse or decompose signals and images. This process is called decomposition or analysis. The components can be assembled back into the original signal without loss of information. This process is called reconstruction or synthesis. The DWT breaks the data down into a sequence of approximations and details by using low-pass and high-pass filters (For more information on the application of this technique see [She08]). The mathematical manipulation that affects synthesis is called the inverse discrete wavelet transform. The process is repeated to yield a multilevel decomposition. This method will be used in the determination of background applicable to the extraction of level densities using the Biorthogonal (bior3.9) mother wavelet. Application of this method is presented in Sect. 4.8.1.

2.5 Extraction of Level Densities

Level density is one of the classical and fundamental quantities of the description of many-body systems. On the other hand, it is well known that through the statistical model of nuclear reactions, this fundamental quantity has a strong impact on the results of calculations and evaluations. This is particularly so for reaction cross-sections needed for many practical applications. Such applications include astrophysical calculations determining thermonuclear rates for nucleosynthesis [Ripl06] and in fission and fusion reactor design [Bha83]. Past developments have shown that it is difficult to satisfy both the accuracy and concise reflection of basic features of the level density behaviour simultaneously. In the spirit of the above, a model independent way of extracting experimental nuclear level densities that can be easily applied to the high energy-resolution data measured in this study is presented. The method involves the use of a fluctuation analysis with model-independent background subtraction incorporated. This type of analysis has been successfully applied recently to giant resonance data [Kal06, Kal07] whereby spin- and parity-

resolved level densities were extracted in the region of the Gamow-Teller (GT) resonances and magnetic quadrupole resonances, respectively. Furthermore, possible parity dependence of level densities extracted in the excitation energy region of giant resonances in light nuclei can be used as a testing ground for theoretical models of giant resonance excitation.

The interplay between giant resonances and the contribution of the background, instrumental and continuum, over the measured excitation energy region has been a problem in many nuclear physics experiments. In this particular analysis, the backgrounds due to the experimental uncertainties and contributions from other multipolarity giant resonances and quasi-free scattering are subtracted in the excitation region of interest. The shape of the background was determined in a model independent way using the Discrete Wavelet Transform (DWT) analysis technique. The method of background subtraction is discussed fully in Section 4.8.1. In addition, quasi-free scattering can be particularly strong in the excitation energy just above the particle threshold at forward scattering angles where the ISGQR is measured. As such, the contribution from (p,2p) and (p,pn) to the measured ^{40}Ca(p,p$'$) was calculated explicitly within the DWIA.

2.5.1 Level density models

Nuclear level densities are key ingredients of the statistical model calculations of nuclear reaction cross-sections. It is known that the density of states is too high at higher excitation energies for individual states to be identified, hence there is a need for level density determination in this region of excitation energy. The earliest theoretical work in the field of nuclear level densities dates back to the 1930's when the pioneering work of Bethe led to the development of the Fermi Gas model [Bet37]. An analytical form for the level density resulted from this work and it is this form that is normally fitted to experimental data

today. The density of states is the number of excited states per unit energy [Won90]. The density of states, ρ, according to the Fermi Gas model whereby nucleons are treated as noninteracting fermions in a nucleus is given as

$$\rho\left(E\right) = \frac{1}{12a^{1/4}E^{5/4}} exp\left(2\sqrt{aE}\right), \tag{2.39}$$

where E is the excitation energy and a represents the level density parameter. It is an important quantity in determining the rate of reactions taking place in a given energy region and in giving an approximate idea of the probability of finding a state at a given energy.

In an attempt to reproduce experimentally observed level spacings, a number of phenomenological modifications to Bethe's original expression were proposed, in particular to take into account shell and pairing effects. The so-called Back-Shifted Fermi Gas (BSFG) model which uses a simpler approach was proposed later [Gad68, Hui69, Von69]. It involves a two-parameter description in which both the ground-state energy correction, Δ, and the level density parameter, a, were fitted to the experimental data. The BSFG model formula is given as

$$\rho\left(E\right) = \frac{1}{12a^{\frac{1}{4}}\left(E-\Delta\right)^{\frac{5}{4}}} exp\left(2\sqrt{a\left(E-\Delta\right)}\right), \tag{2.40}$$

where both a and Δ are considered as free parameters. This two-parameter approach describes well the level density values over the whole range of excitation energies for light nuclei [Dil73, Kat70, Lu72]. For that mass range it turned out that the ground state position had to be back-shifted by an amount of 1-3 MeV in order to obtain good fits to the experimental data.

With an advancement in the computational and theoretical methods of calcu-

lating the level density, the Hartree-Fock Bogoliubov (HFB) plus Combinatorial model was proposed [Hil06]. This is an example of a microscopic model of level density calculation. There exists also the Hartree-Fock-Bardeen-Cooper-Schriffer (HFBCS) [Dem01] model. The most recent microscopic HFB plus Combinatorial model [Kon08] includes rotational and vibrational degrees-of-freedom combined with a combinatorial model for the occupation of single-particle states. This made the connection between the phenomenological level density approaches like BSFG and Constant Temperature models and a normalisation factor to the microscopic calculation was introduced. The calculations make a coherent use of nuclear structure properties determined within the deformed Skyrme-Hartree-Fock-Bogoliubov framework. One of the advantages of this approach is that it provides not only the energy and spin dependence of the level density, but also the parity dependence as well as the partial particle-hole level density that cannot be extracted in any satisfactory way from the statistical approach. In addition to the above named models, there are also Shell-Model Monte Carlo (SMMC) calculations [Alh07] which provides information on the spin dependence level densities.

2.5.1.1 Back-Shifted Fermi Gas (BSFG) model

The BSFG model has been successfully used to describe, amongst other things, neutron resonance densities and low-lying levels. The level density ρ described in terms of excitation energy E_{x} and spin J [Rau97, Egi05] can be written as

$$\rho\left(E_{\mathrm{x}}, J\right) = \frac{1}{2} F\left(E_{\mathrm{x}}, J\right) \rho\left(E_{\mathrm{x}}\right) \tag{2.41}$$

with

$$\rho\left(E_{\mathrm{x}}\right) = \frac{1}{\sqrt{2\pi}\sigma} \frac{\sqrt{\pi}}{12 a^{\frac{1}{4}}} \frac{exp\left(2\sqrt{a\left(E_{\mathrm{x}} - \delta\right)}\right)}{\left(E_{\mathrm{x}} - \delta\right)^{\frac{5}{4}}} \tag{2.42}$$

and

$$F(E_{\mathrm{x}}, J) = \frac{2J+1}{2\sigma^2} exp\left(\frac{-J\,(J+1)}{2\sigma^2}\right), \tag{2.43}$$

where $\sigma^2 = \dfrac{\Theta_{\mathrm{rigid}}}{\hbar^2}\sqrt{\dfrac{(E_{\mathrm{x}}-\delta)}{a}}$ = spin cutoff parameter,

$\Theta_{\mathrm{rigid}} = M_{\mathrm{exp}} A R^2$,

δ = the back-shift energy,

$R = r_{\mathrm{o}} A^{1/3}$ = the nuclear radius,

M_{exp} = the experimental mass of the nucleus,

a = the level density parameter and

A = the nuclear mass.

The pairing gap Δ is determined from differences in the binding energies of neighbouring nuclei, hence the back-shift is calculated by setting

$$\delta\,(Z,N) = \frac{1}{2}\left(\Delta_{\mathrm{n}}\,(Z,N) + \Delta_{\mathrm{p}}\,(Z,N)\right), \tag{2.44}$$

where $\Delta_{\mathrm{n}}\,(Z,N)$ and $\Delta_{\mathrm{p}}\,(Z,N)$ are neutron and proton separation energy, respectively. Also, the energy-dependent level density parameter a can be written as

$$a\,(E_{\mathrm{x}}, Z, N) = \widetilde{a}\,(A)\left(1 + C\,(Z,N)\,\frac{f(E_{\mathrm{x}}-\delta)}{E_{\mathrm{x}}-\delta}\right), \tag{2.45}$$

where $C = \delta - \Delta$ is called the microscopic energy correction, and

$$\widetilde{a}\,(A) = \alpha A + \beta A^{\frac{2}{3}} \tag{2.46}$$

$$f(E_{\mathrm{x}}-\delta) = 1 - exp\left(-\gamma\,(E_{\mathrm{x}}-\delta)\right). \tag{2.47}$$

The values of the free parameters α, β, and γ are determined by a fit to

experimental s-wave neutron resonance spacings of 272 nuclei at the neutron separation energy in [Rau97] and are given as $\alpha = 0.1337$, $\beta = -0.06571$, $\gamma = 0.04884$.

The cumulative number of levels as a function of excitation energy E_{x} is given by

$$N_{\mathrm{o}}\left(E_{\mathrm{x}}, J\right) = \int_{0}^{E_{\mathrm{x}}} \rho\left(E, J\right) dE. \tag{2.48}$$

Similarly, a relation for the mean level spacing $\langle D \rangle$ in the energy interval $\left[E_{\mathrm{x}}^{a}, E_{\mathrm{x}}^{b}\right]$ can be expressed as

$$\langle D \rangle = \frac{E_{\mathrm{x}}^{b} - E_{\mathrm{x}}^{a}}{N_{\mathrm{o}}\left(E_{\mathrm{x}}^{b}, J\right) - N_{\mathrm{o}}\left(E_{\mathrm{x}}^{a}, J\right)}. \tag{2.49}$$

2.5.1.2 Hartree-Fock-Bogoliubov (HFB) model

The Hartree-Fock-Bogoliubov (HFB) model is one of the microscopic class of level density determinations. Unlike phenomenological models, the microscopic HFB plus Combinatorial model [Hil06] predicts particle-hole level densities as a function of energy, spin and parity, taking collective behaviour of nuclei into account. The recent HFB calculations within the Skyrme framework is based on an effective interaction adjusted for nuclear masses and nuclear matter properties. This treats the shell effects, pairing correlations, deformation effects and collective excitations consistently for spherical and deformed nuclei. The results compare well with those of exact calculations. The predictions of spin- and parity-projected level densities even for N $\simeq$ Z nuclei at higher excitation energies where shell and pairing effects diminish can also be determined and are available in a tabular format for fixed excitation energies [Http]. The BSk13 force used is characterised by the following nuclear matter properties: energy per nucleon, a_{v}, at equilibrium in symmetric nuclear matter, the

corresponding density ρ_o, the isoscalar and isovector effective masses and the symmetry coefficient.

2.5.2 Fluctuation Analysis

Fluctuation analysis provides a method to determine the level densities of excited nuclei in the region of overlapping levels. It has been successfully applied in many nuclear experiments like β-delayed particle emission spectra [Jon76] and giant resonance spectra from electron scattering [Mul83] for the extraction of unresolved cross-sections. The motivation for carrying out this work is to acquire information on level densities in the excitation energy regions other than those close to the ground state (done by counting) or near the particle thresholds. Such data are generally scarce, in particular for specific J^π values. Level densities of a number of nuclei in the mass range $A = 20$ - 60 have been derived from cross section at excitation energies around 20 MeV [Bha83] through fluctuation analysis. The method used in the present study employs the autocorrelation function from [Han79] in order to obtain a measure of the cross-section fluctuations with respect to a stationary mean value. Below, the general formalism of fluctuation analysis and its underlying assumptions from an experimentalist's point of view are discussed explicitly.

2.5.2.1 Assumptions

In the reactions considered here the excitation energies of the ^{40}Ca in the region of the ISGQR are few MeV above the proton and neutron thresholds. The method discussed below is applicable in a region where $\langle\Gamma\rangle/\langle D\rangle \ll 1$ but $\langle D\rangle < \Delta E$. In the notation $\langle\Gamma\rangle$ represents the mean level width, $\langle D\rangle$ is the mean level spacing and ΔE is the experimental energy resolution. This is as opposed to the so-called Ericson fluctuations where $\langle\Gamma\rangle/\langle D\rangle \gg 1$.

The second assumption is the application of the Wigner distribution for the

nuclear level spacings $P_{\mathrm{W}}(s)$ and the Porter-Thomas distribution for the transition strengths $P_{\mathrm{PT}}(s)$ in a highly excited nucleus with strong fluctuation configuration mixing of levels with the same spin and parity. Wigner and Porter-Thomas distributions have been applied in the estimations of mean widths and resonance spacings explained in the calculation of nuclear reaction data [Ripl06]. It has been experimentally verified in the Nuclear Data ensemble to hold near thresholds using resonance data.

The probability for a certain spacing between adjacent states according to the Wigner distribution [Wig65] is

$$P_{\mathrm{W}}(s) = \frac{\pi s}{2} exp(-\frac{\pi s^2}{4}), \tag{2.50}$$

where

$$s = \frac{D}{\langle D \rangle} \tag{2.51}$$

and $\langle D \rangle$ is the mean value of the resonance spacing D. This distribution has a maximum around the mean value and shows so-called repulsion, *i.e.* a suppression at small distances between adjacent levels. The Porter-Thomas distribution [Por65] is given as

$$P_{\mathrm{PT}}(s) = \frac{1}{\sqrt{2\pi s}} exp(-\frac{s}{2}), \tag{2.52}$$

where

$$s = \frac{\Gamma}{\langle \Gamma \rangle}, \tag{2.53}$$

and $\langle \Gamma \rangle$ is the mean value of the level width Γ. This equation predicts that

weak transitions are more likely.

2.5.2.2 Procedure

The basic steps taken in the application of fluctuation analysis and the extraction of level densities from the present data are described here. The background is first subtracted from the measured experimental (p,p′) spectrum in the excitation energy range being investigated. This is then followed by smoothing of the background-subtracted spectrum using a Gaussian function with a width denoted by σ. This width is smaller than the experimental energy resolution ΔE in order to eliminate contributions of the fluctuations from counting statistics. The resulting spectrum is called $g\left(E_{\mathrm{x}}\right)$. Then the measured spectrum is again folded with a Gaussian of the width denoted by $\sigma_{>}$. This width is larger than the experimental energy resolution in order to remove gross structures in the resonance. The resulting spectrum is referred to as $g_{>}\left(E_{\mathrm{x}}\right)$ later. This spectrum defines the mean about which the original points fluctuate.

In order to remove the long-range correlations in the spectrum, the ratio of $g\left(E_{\mathrm{x}}\right)$ and $g_{>}\left(E_{\mathrm{x}}\right)$ is calculated and the resulting spectrum is called the stationary spectrum. Thus, the stationary spectrum fluctuates around unity and is given by

$$\langle d\left(E_{\mathrm{x}}\right)\rangle = \langle \frac{g\left(E_{\mathrm{x}}\right)}{g_{>}\left(E_{\mathrm{x}}\right)} \rangle = 1. \tag{2.54}$$

Here, the left and right-angle brackets indicate averaging over the energy interval where the level spacing is to be extracted.

The stationary spectrum is a direct measure of the local intensity fluctuations which can be expressed in terms of an autocorrelation function

$$C(\epsilon) = \langle d(E_x)\, d(E_x + \epsilon)\rangle, \tag{2.55}$$

where ϵ is the energy increment at excitation energy E_x and is a measure of spectral fluctuations with respect to a local mean value. The value $C(\epsilon = 0) - 1$ is known as the variance since

$$C(\epsilon = 0) - 1 = \frac{\langle d^2(E_x)\rangle - \langle d(E_x)\rangle^2}{\langle d(E_x)\rangle^2}. \tag{2.56}$$

This experimental autocorrelation function can be approximated by the analytical expression [Jon76]

$$C(\epsilon) = 1 + \frac{\alpha\langle D\rangle}{2\Delta E\sqrt{\pi}} \left\{ exp\left(-\frac{\epsilon^2}{4\Delta E^2}\right) + \frac{1}{y} exp\left(-\frac{\epsilon^2}{4\Delta E^2 y^2}\right)\right\} \times \left\{ -\sqrt{\frac{8}{1+y^2}} exp\left(-\frac{\epsilon^2}{4\Delta E^2(1+y^2)}\right)\right\}, \tag{2.57}$$

where

$$y = \frac{\sigma_>}{\sigma}. \tag{2.58}$$

The terms in curly brackets on the right hand side depend only on the experimental energy resolution ΔE and can be simplified as

$$C(\epsilon) - 1 = \frac{\alpha\langle D\rangle}{2\Delta E\sqrt{\pi}} f(\epsilon, \Delta E), \tag{2.59}$$

where the function $f(\epsilon, \Delta E)$ is normalised such that $f(\epsilon = 0) = 1$. It is important to note that in fluctuation analysis, the most stable results are obtained by setting $\sigma \simeq \frac{1}{2}\Delta E$ and $\sigma_> = (2.5 - 3.5)\sigma$. The quantity α is the

sum of the normalised variances of the assumed spacing and transition width distributions, and is given by

$$\alpha = \alpha_{\mathrm{W}} + \alpha_{\mathrm{PT}} = 0.273 + 2.0. \tag{2.60}$$

This is true only if states of the same spin and parity J^{π} are present in the spectrum, in this case 2^{+} states. Thus, one either assumes this condition experimentally utilising the selectivity of specific reactions or one has to correct for it. For example, application to mixed final states in heavy deformed odd-mass nuclei is discussed in [Hux99].

Chapter 3

Experiments and Data Extraction

The Isoscalar Giant Quadrupole Resonance (ISGQR) experiments on the investigation of the fine structure and characteristic energy scales in low-mass nuclei were carried out with proton beams delivered from the Separated Sector Cyclotron (SSC) of the iThemba Laboratory for Accelerator Based Sciences (iThemba LABS). The proton beams were dispersion-matched to the K600[1] Magnetic Spectrometer. This facility is situated near Somerset West in Cape Town. It is one of only a few existing laboratories in the world where such high energy-resolution inelastic proton scattering experiments can be carried out in the intermediate energy range.

In this chapter an overview of the experimental facilities and techniques used in these experiments will be discussed. The first section (Sect. 3.1) consists of a brief outline of the SSC as well as the injector cyclotron used for the experiments. Described in Sect. 3.2 is the detection of the inelastically scattered protons by the K600 Magnetic Spectrometer, which includes a description of

[1]The K-value for magnets is defined as $K = \frac{mE}{q^2}$ where m is the proton mass with charge q and E is the kinetic energy a magnetic device is designed for.

the general ion-optical specifications and functional features. In Sect. 3.2.2 the mechanical properties and basic functioning of the focal-plane detector package is described. Sect. 3.3 discusses the dispersion matching techniques for the realisation of high energy-resolution measurements. A brief discussion of targets used and the effect of target thickness on energy resolution follows in Sect. 3.4. This is followed by discussion of the experimental procedure in Sect. 3.5. The data acquisition system and the procedure followed in achieving high energy-resolution with minimum background is discussed in Sect. 3.6. Finally, the last section, Sect. 3.7, is devoted to the data extraction and analysis procedures employed with new data analysis software.

3.1 Separated Sector Cyclotron

The main facility which serves as the backbone to all other facilities at iThemba LABS is the K200 Separated Sector Cyclotron (SSC). This major facility delivers beams for radioactive isotope production, for proton and neutron therapy of cancer patients, as well as a wide range of beams, from light to heavy ions including a polarised light ion beam, for nuclear physics experimental purposes. The experimental facilities used in nuclear physics research include the gamma detector array AFRODITE, an electron spectrometer (which is about to be commissioned), the A-line nuclear reaction scattering chamber and the K600 magnetic spectrometer.

The layout of the accelerator infrastructure and beamlines is shown in Fig. 3.1. There are two injector cyclotrons where beams are produced and pre-accelerated, a K8 Solid Pole Cyclotron 1 (SPC1) with an internal ion source and K11 Solid Pole Cyclotron 2 (SPC2) with two external ion sources. Presently, three different types of ion sources are in use namely the Electron Cyclotron Resonance (ECR) ion source and the Polarised proton ion source which are both used

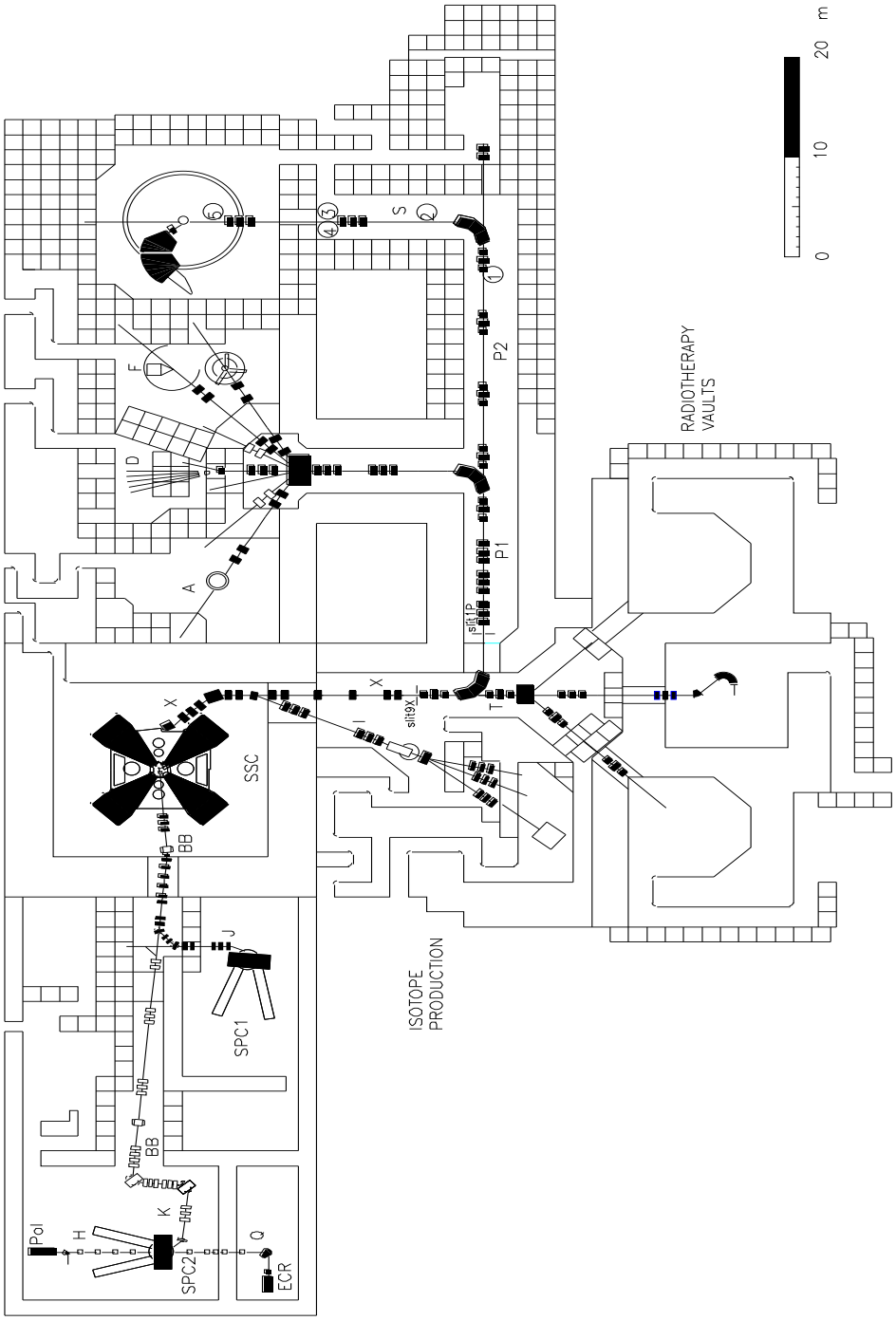

Figure 3.1: The layout of Separated Sector Cyclotron facility of iThemba LABS. Positions 1 to 5 indicate the locations of halo monitors.

with SPC2, and the Penning Ionisation Gauge (PIG) used for SPC1.

In the case of the ECR ion source, which was used for this particular experiment, proton beams are generated by dissociating hydrogen gas in a radio frequency (RF) field into hydrogen atoms which are accelerated by means of a pressure gradient. The pre-accelerated beam from SPC2 is injected into the SSC. For this experiment, a good quality proton beam is accelerated to an energy of 8.3 MeV at an RF frequency of 26 MHz in SPC2 and then to an energy of 200 MeV in the SSC. The beam was centred vertically by adjusting the different injection elements while the orbit pattern in the SSC was observed on movable harps. The injection beamline is equiped with klystron bunchers in order to reduce the energy spread which causes radial broadening of the beam and limits the beam separation between successive turns at the extraction radius of the cyclotron. The bunchers shorten the beam pulse length at the injection radius of the SSC. After extraction, the beam is guided through the high-energy beamlines, specifically the X, P and S lines (as can be identified in Fig. 3.1) which are equipped with sets of quadrupole and dipole magnets and slits for optimisation, to the K600 Magnetic Spectrometer. The beam dispersion is then matched to the spectrometer by properly adjusting the beam line elements. This will be discussed in more detail in Sect. 3.3.

3.2 K600 Magnetic Spectrometer

The experimental work was conducted using the K600 Magnetic Spectrometer of iThemba LABS which consists of five main elements, namely a quadrupole, two dipoles and two trim coils (K and H) as shown in Fig. 3.2. This QDD (quadrupole dipole dipole) spectrometer and its detection system are fully described in ref. [Nev08].

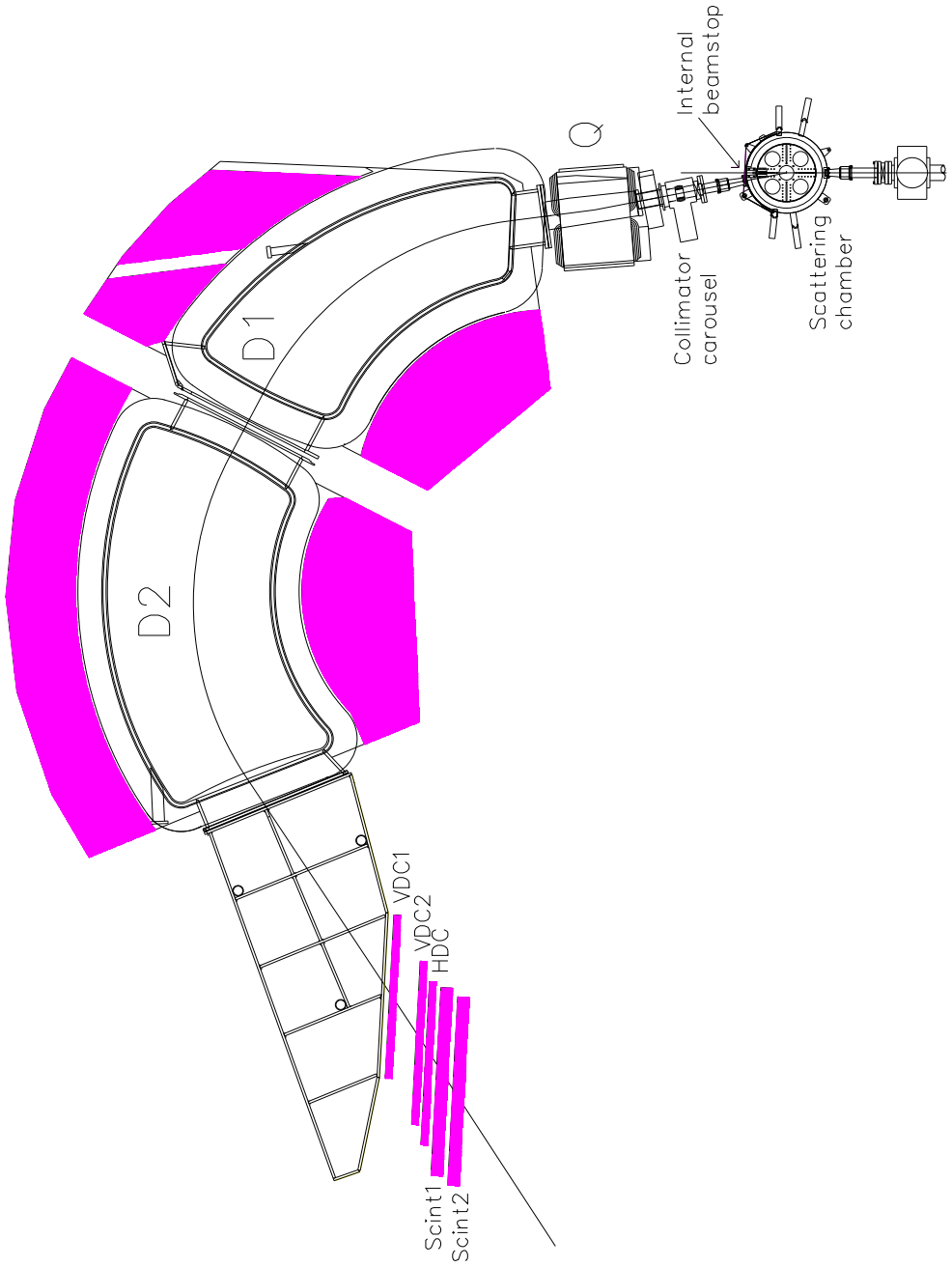

Figure 3.2: The layout of the K600 Magnetic Spectrometer showing its main components and the focal plane detector package. The K600 is positioned at 11° in this figure.

The collimator carousel, situated in front of the quadrupole magnet at a distance of 735.5 mm from the target centre, can hold 6 collimators. Situated at the turning axis of the spectrometer is the 524 mm diameter scattering chamber which houses the target ladder and a turntable on which detectors or an internal beam stop can be mounted. The target ladder consists of six target positions which in this experiment were filled with a combination of the following: an empty hole, ^{40}Ca, a beam viewer(ZnS), mylar (CH_2), ^{12}C, ^{28}Si and ^{27}Al of varied thicknesses. Behind the second dipole is the focal plane position-sensitive detector package. It can be positioned in one of the three dispersion mode focal planes: low, medium, and high dispersion with dispersion values 6.2 cm/%, 8.1 cm/% and 9.8 cm/%, respectively [Nev08]. For the present experiment, the spectrometer settings were optimized for the medium dispersion mode for protons of incident energy 200 MeV and covering an excitation energy range of approximately $E_{\mathrm{x}} = 6$ - 30 MeV. The required excitation energy range for each nucleus studied could be recorded within a single measurement, while at the same time providing sufficient energy resolution across the focal plane. It is important to note that the high energy-resolution capability of this facility is a pre-requisite for the analysis of the inelastically scattered protons of this study.

An internal beamstop, which is bolted onto the turntable, is used for measurements in the range $7^\circ < \theta_{\mathrm{K600}} < 21^\circ$ (see Fig. 3.3), while an external beamstop/Faraday cup is used for measurements with angles $\theta_{\mathrm{K600}} > 21^\circ$. The issue of background for small scattering angles approaching 7° is always problematic due to small angle scattering from the left hand side of the beamstop, which can lead to high countrate of the elastic peak in the focal plane detectors.

The Focal Plane Beamblocker, which is made up of a 60 mm thick movable

brass block, is situated in front of the Kapton exit windows of the K600 Spectrometer vacuum chamber. It can be positioned in front of either the high or medium dispersion planes depending on the mode being used in the experiment. It is used to shield some section of the focalplane detectors during experiments, for example the blocking of the elastic peak as its countrate is so high relative to the other states of interest.

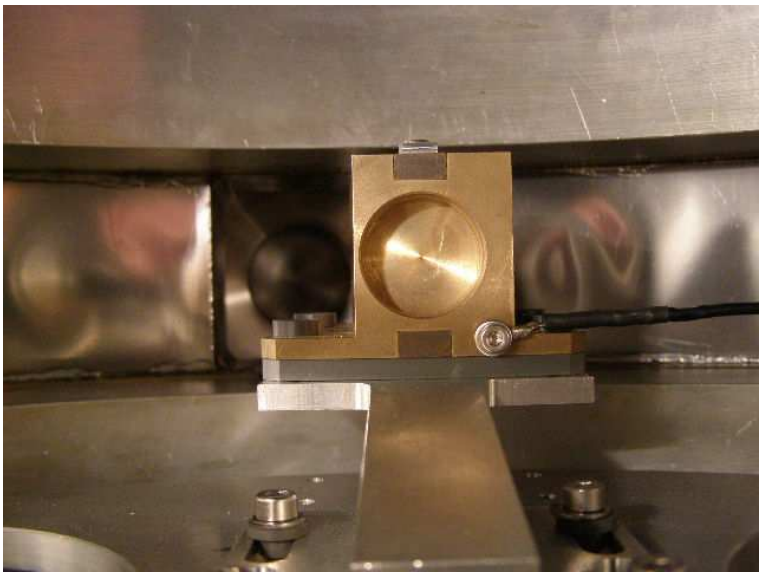

Figure 3.3: The internal beamstop for measurements at angles $7^\circ < \theta_{\mathrm{K600}} < 21^\circ$ as viewed from the target ladder. The entrance to the K600 is visible on the left of the beamstop.

3.2.1 Ion Optical Characteristics of the K600 Magnetic Spectrometer

The ion-optical properties of the K600 Magnetic Spectrometer are summarised in terms of its transfer coefficients. With the transfer coefficients the focalplane coordinates of the detected particles can be translated into the equivalent coordinates at the target position. The dipole magnets are used in achieving the dispersion of the incident flux of the charged particles entering the spectrometer. The H-coil is used for second order aberration corrections $\langle x|\theta^2\rangle$ while the K-coil is used for the first-order aberration corrections $\langle x|\theta\rangle$. The

Table 3.1: Technical specifications for the medium dispersion mode of K600 Magnetic Spectrometer.

Element	Value
Nominal bend radius	2.1 m
Nominal bend angle	115°
Dipole Field ratio	1
Maximum dipole field	1.64 T
Maximum magnetic rigidity	3.60 Tm
Momentum dispersion ($x\|\Delta$p/p)	8.1 cm/%
Energy dispersion for 200 MeV protons setting	42 keV/mm at 200 MeV
Momentum range, P_{max}/P_{min}	1.095
Resolving power, P/δP (with 0.6mm object width)	28000
Horizontal magnification at P_{max}	0.52
Vertical magnification at P_{max}	7.4
Tilting angle of focal plane w.r.t. central ray	35.75°
Horizontal VDC acceptance	78 cm
Vertical VDC acceptance	10 cm
Distance of target to back of collimator	735.5 mm
Maximum diameter collimator	63 mm
Maximum solid angle $\Delta\theta\Delta\Phi$	5.76 msr
Maximum vertical acceptance $\Delta\theta$	42.8 mrad, or ±2.45°
Maximum horizontal acceptance $\Delta\phi$	42.8 mrad, or ±2.45°

K600 has been designed to achieve a resolution of $(\delta p/p) \approx 10^{-4}$ over nearly the full momentum acceptance for a beam that is dispersion matched to the QDD spectrometer at the target position. The nominal ranges for both horizontal and vertical scattering angles, $\Delta\theta$ and $\Delta\phi$, are ±42.8 mr, yielding a relatively small solid angle acceptance of 5.76 msr which is defined by a collimator of inner diameter 63 mm. The momentum range accessible for a given fieldset is roughly -5% to 5% of the central momentum value. The design parameters associated with the medium dispersion focal plane of the spectrometer are listed in Table 3.1.

The optics are point-to-point ($\langle x \mid \theta \rangle = 0$) focussing in the horizontal plane, and point-to-parallel ($\langle \phi \mid \phi \rangle = 0$) focussing in the vertical plane. A well-defined

cycling procedure to set the magnetic fields of the dipoles was shown to be necessary to achieve a reproducible field. The entrance quadrupole operates in the vertical defocusing mode to reduce the required gap of the dipoles.

3.2.2 Focal-Plane Detector Package

The charged particles are detected by a detector system located in the focal plane of the K600 as shown in Fig. 3.2. It consists of three multi-wire drift chambers (MWDC) for position and angle measurements, and a pair of plastic scintillation detectors behind the MWDCs for particle identification and fast timing trigger purposes. The first two drift chambers, namely the Vertical Drift Chambers (VDC1 and 2), are used to determine the horizontal position in the focal plane while the Horizontal Drift Chamber (HDC) is used for vertical position determination. Note that the X-chambers are called Vertical Drift Chambers and the Y-chamber is called the Horizontal Drift Chamber due to the fact that the main drift direction of electrons is perpendicular to the signal wire plane in the VDC while the electrons drift in the plane of the signal wires in the HDC. The particle momentum is analysed by the VDC1 and VDC2-chambers with 198 vertical signal wires each oriented perpendicular to the dispersive direction. The HDC has 16 horizontal wires and is used to measure the vertical position of particles in the focal-plane. Two 25 μm thick mylar planes are used to isolate the interior of the MWDC from the atmosphere. The volume between the two cathode planes, which are made of 27 μm thick aluminium foil, is filled with gas mixture of 90% Ar and 10% CO_2. Electron drift velocities are of the order of 4-6 μm/sec which gives approximately 133 - 200 nsec drift-times for the 8 mm spacing between the High Voltage (HV) plane and the signal wire. The anode plane of the first VDC is placed such that it coincides with the real focal-plane of the magnetic spectrometer. With the position and horizontal angle information obtained from these chambers the position where a charged particle traversed the focal-

plane can be established by interpolation to a high degree of accuracy, thus providing accurate momentum information of such a particle.

Positioned just downstream from the drift chambers are two plastic scintillator detectors of dimension of 122 cm $\times$ 10.2 cm and different thicknesses 1.27 cm and 0.635 cm, respectively. These provide event trigger signals and aid in particle identification through $\Delta E - \Delta E$ particle identification spectra.

3.3 Dispersion Matching Techniques

Magnetic spectrometers are used in nuclear scattering experiments to extract high precision physics quantities like excitation energies of states, cross-sections and angular distributions. Dispersion matching techniques are used in order to exploit the full high resolution capability of a spectrometer in which the bending planes of the beamline and spectrometer are the same. The main aim of dispersion matching is to get the best possible spatial and scattering angle definition along the spectrometer focal plane.

At first achromatic focus at the target is achieved so that the position of the protons on the target is independent of momentum, that is $(x|\Delta \mathrm{p}/\mathrm{p}) = 0$. The beamspot is thus optimized to be as small as possible. It is also important that the horizontal and vertical slits at 9X in the X-line are used to constrain the beam object point to be as small as possible. After this procedure, the K and H coils can be tuned in order to get the appropriate kinematic correction for the particular target in use. Then the magnets from 9X downstream are changed to the dispersion matched settings. It is important to note that the last two quadrupoles in the S-line, Q5S and Q6S, are involved for the final fine tuning in order to ensure that the beam is dispersion matched to the K600.

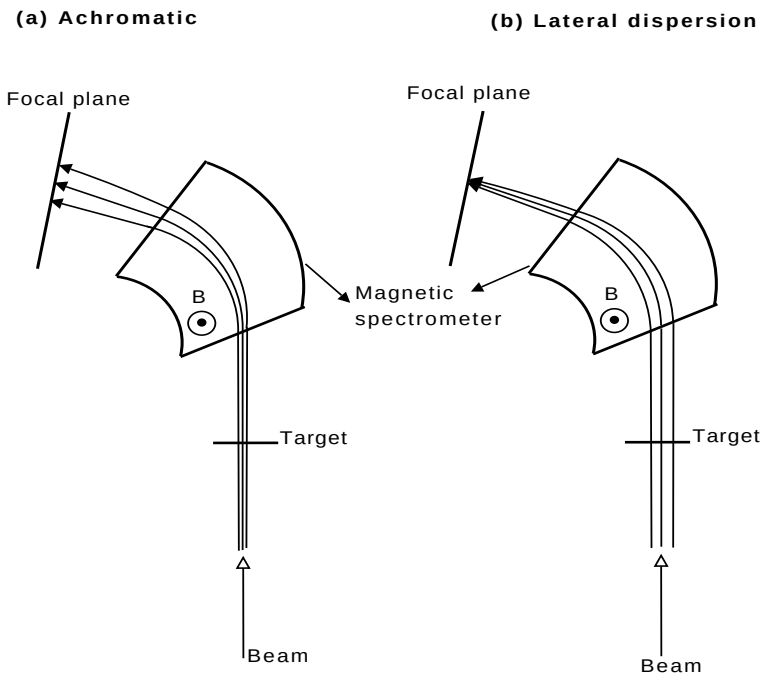

Figure 3.4: Schematic ion trajectories of a beam and a magnetic spectrometer under different beam transport conditions. The left-hand side (a) shows the situation when achromatic beam transportation is used while the the right-hand side (b) indicates the situation when lateral dispersion matching is realised.

Lateral dispersion matching is important for the realization of high momentum resolution [Fuj97, Mar83] and angular dispersion matching for high horizontal angle resolution [Fuj02]. The latter enables the precise determination of the scattering angles of particles in zero degree experiments. Lateral dispersion matching is shown schematically in Fig. 3.4. It should be noted that the angular dispersion matching was not used in this particular experiment.

Excellent event selectivity provided by this technique minimizes background sensitivity and simplifies analysis. Optimising the beamline dispersion and focus condition on target by tuning dipole and quadrupole elements of the beam tend to be complicated and time consuming. The high energy-resolution can be achieved if the accelerator, beam transport, and spectrometer form an achromatic system that focus the beam on the spectrometer focal plane.

3.3.1 Faintbeam method

There are three beam-attenuation or the so-called faintbeam meshes, as shown in Fig. 3.5, located between the ECR ion source and SPC2, which are used for the provision of "faintbeam". These meshes are used to reduce the number of protons in the beam by a factor of up to 10^6 without changing the beam profile or ion-optical characteristics of the beam. This gives a reasonably faintbeam that can be observed directly in the focal plane detectors of the K600 at 0°. The faintbeam method was initially conceived as a technique to help in achieving both lateral and angular dispersion matching for zero degree experiments, but it can also be use in non-zero degree experiments to check the quality of the achromatic beam by looking directly at the beam energy spread.

The use of faintbeam is possible only when SPC2 is in use together with the ECR ion source due to the fact that it accommodates an external ion source compared to SPC1 which has an internal ion source. The meshes are made of thin copper plates with very tiny holes and can reduce the beam going to SPC2 by a factor of ten, one hundred and one thousand, respectively. The mesh that attenuates the beam by a factor of 100 is listed as APP1 on the accelerator control system. The second mesh on the accelerator control system is listed as APP2 and it combines the factor 10 and factor 1000 meshes to attenuate the beam by a factor 10000.

3.4 Targets

There is a need for thin targets with high isotopic purity for many experiments in the field of nuclear physics. The thicknesses of these targets typically cover the range between 100 μg/cm^2 and a few mg/cm^2 for a surface of approximately 2 cm^2. Targets are prepared by using different methods based on the physical and chemical properties of the target elements. These methods

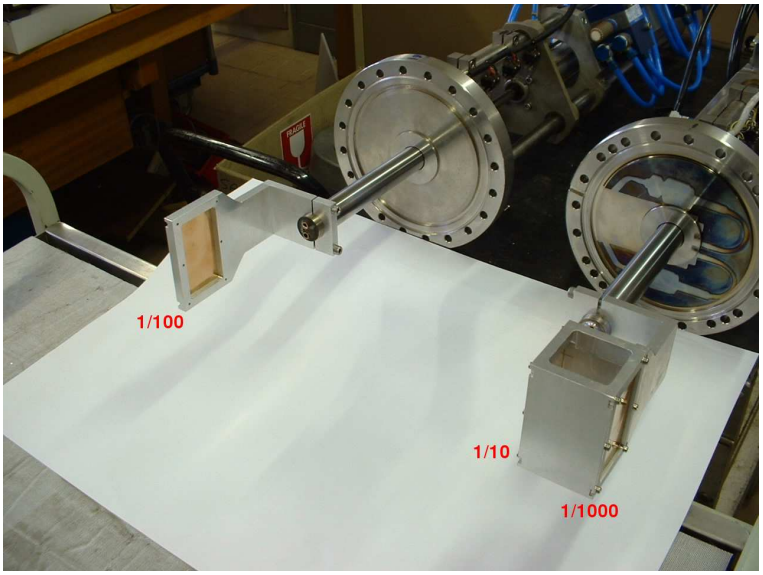

Figure 3.5: The three faintbeam meshes, shown here before installation between the ECR ion source and the SPC2 injector cyclotron. The mesh on the left attenuates the beam by a factor of 100 and the two meshes on the right attenuates by a factor of 10000.

include (1) resistive evaporation (2) electron beam deposition (3) mechanical rolling (4) ion beam and reactive sputtering and (5) electroplating. For more detail see ref. [Gre04]. The self supporting targets used during the experiments reported in this thesis are as follows: 3.5 mg/cm^2 thick ^{40}Ca, 0.232 mg/cm^2 thick ^{28}Si, 0.819 mg/cm^2 thick ^{27}Al and 1.052 mg/cm^2 thick ^{12}C. All of these targets were ordered from different vendors except the ^{40}Ca target, which was made at iThemba LABS. This was prepared by direct deposition using the vacuum evaporator present at the Material Research Group (MRG) Laboratory of iThemba LABS.

The setup used to manufacture the ^{40}Ca target was primitive compared to many other target laboratories. It did not have a thickness monitor and the liquid nitrogen for cooling the cold trap was fed manually through a funnel. Also, filament temperature control was not present. The primitive setup made it difficult to produce a target with the specified thickness required for the experiment. The oxidation of the ^{40}Ca in the presence of air presents a serious

problem in handling these thin targets. The technique of venting the bell-jar, where the ^{40}Ca target was manufactured, with argon gas retarded the oxidation process of the deposited calcium target. During the experiment, the target thickness was established to be 3.5 mg/cm^2 by using the faint beam and energy loss tables specific to the target material. The energy resolution of about 38 keV realised for ^{40}Ca data is worse than what was realised for the other targets due to increased straggling effects in the ^{40}Ca target, which is more than three times thicker than the others. Oxygen contamination of the calcium target was observed on the high momentum side of the spectra by comparing the kinematics of ^{16}O elastic peaks with the ^{40}Ca peaks during the experiment. It should be noted that contamination was minimal in the ISGQR region of ^{40}Ca.

3.5 Experimental Procedure

Target nuclei (^{40}Ca, ^{28}Si, ^{27}Al and ^{12}C) were bombarded with protons at an incident beam energy of 200 MeV over a period of three weekends. Table 3.2 summarises the targets and the different scattering angles at which measurements were performed. The scattering angles were selected to match the maximum of the cross sections for $\Delta L = 2$ excitations in the corresponding targets, thereby exciting predominantly the isoscalar giant quadrupole resonance (ISGQR) under investigation. Additionally, measurements were taken at angles above and below the maximum of the $\Delta L = 2$ angular distributions in order to estimate the effects of the mixing of different multipoles in the cross sections.

Prior to the main experimental period many preparations must be completed in order to ensure the smooth running of the experiment. This includes target preparation, the implementation of the autotrim procedure, checking the gas flow to the MWDC's, a scattering chamber vacuum test, MWDC's high

Table 3.2: A list of target nuclei investigated at the indicated angles at iThemba LABS. Note the bold scattering angle indicates the maximum of the ISGQR.

Target nuclei	Z	N	Target Thickness (mg/cm^2)	Lab Scattering Angle (°)
^{40}Ca	20	20	3.5	7, **11**, 15
^{28}Si	14	14	0.232	**12**
^{27}Al	13	14	0.819	**12**, 17
^{12}C	6	6	1.052	**13**, 20

voltage checks and also work on the trigger electronic circuit. The main experiment started with a field setting procedure using the values of electric currents for the Q, D1 and D2 magnets of the K600 settings obtained from the computer program SPEXCIT. All magnets were set according to a predetermined hysteresis curve or "degaussing cycle" to ensure that correct and reproducible field values were attained for each set point. The spectrometer was operated over a wide range of central momenta and the stability of the magnetic fields were monitored using nuclear magnetic resonance (NMR) probes installed in the dipole magnets. The faintbeam method was used to check the quality of the achromatic beam by looking directly at the beam energy spread. The intensity of the incoming beam, normally a few nA, is reduced by several orders of magnitude by the use of meshes as described in Sect. 3.3.1. This allows for the placement of the magnetic spectrometer at zero degrees to observe the incident beam directly with the focal-plane detector system. A circular brass collimator of inner diameter of 49 mm and lip thickness of 14mm, situated in front of the quadrupole magnets at a distance of 735.5 mm from the target centre, was used to define the solid angle of the spectrometer as $\Delta\theta\Delta\Phi = 3.48$ msr.

The energy resolution of proton scattering from heavy targets was optimised for the beam in achromatic mode in order to avoid kinematic effects. This

was realised by tuning the K and H coils and focusing the beam at slit 9X. A resolution of about 60 keV was achieved with an achromatic beam which was considered good enough for this experiment. A white tune spectrum was taken at 160 MeV with a ^{12}C target and 63 mm diameter collimator in order to check the responses in the TDC and preamp channels, and correct those channels that were not in a good condition. A white tune is a process whereby the whole focal plane is illuminated uniformly in order to check for the dead and/or misaligned TDC channels associated with wires in the MWDC's. This was followed by the dispersive mode tune where the beam dispersion was matched to that of the K600 magnetic spectrometer. Once good resolution was obtained, an energy calibration run was taken with the ^{12}C target. It is important to note that once the dispersion matching is achieved the K and H coil settings should not be changed so as to avoid a negative influence on the matching condition, and therefore the experimental resolution. This is because the matching condition depends on the matrix elements of the k600 magnetic field. Different coil settings will change the k600 matrix elements, and thus the required matching condition.

Data was typically acquired for one hour and was followed by a background measurement with an empty target frame, after which the next data run was started. Background from beam halo was monitored by Bergoz Beam Loss Monitors (BLM) placed at five strategic positions along the beam-line (see Fig. 3.1). The Bergoz BLM consists of two PIN-photodiodes mounted face-to-face to detect charged particles. It has an active area of 7.34 mm^2, can tolerate a maximum count rate of about 10 MHz and has a positive output TTL of 50 Ω. It was connected through the 50 Ω patch-panel to a level adapter (TTL input, NIM output) and CAMAC scaler.

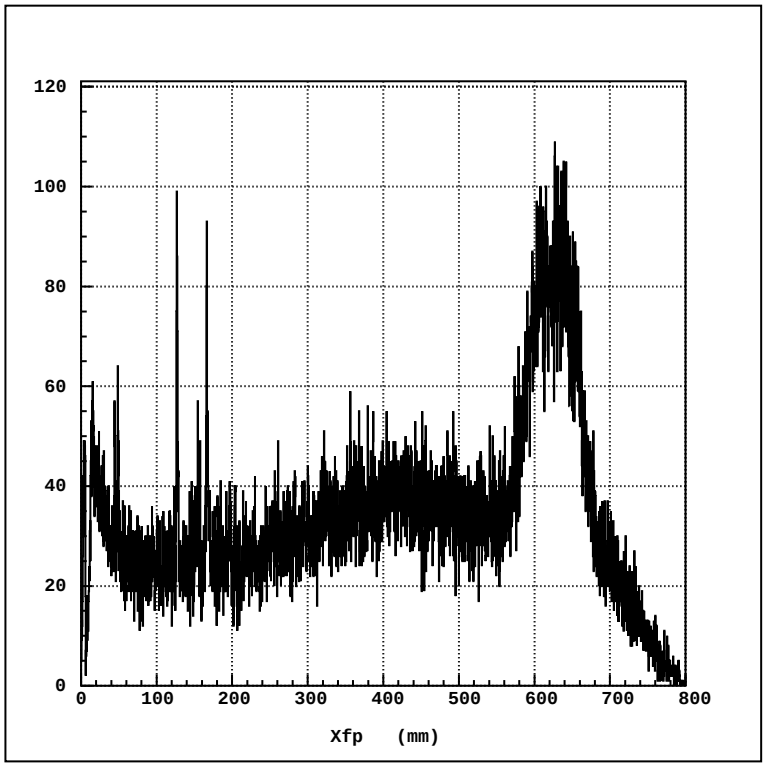

Figure 3.6: A position spectrum showing a prominent beam halo peak at the low momentum (right hand) side.

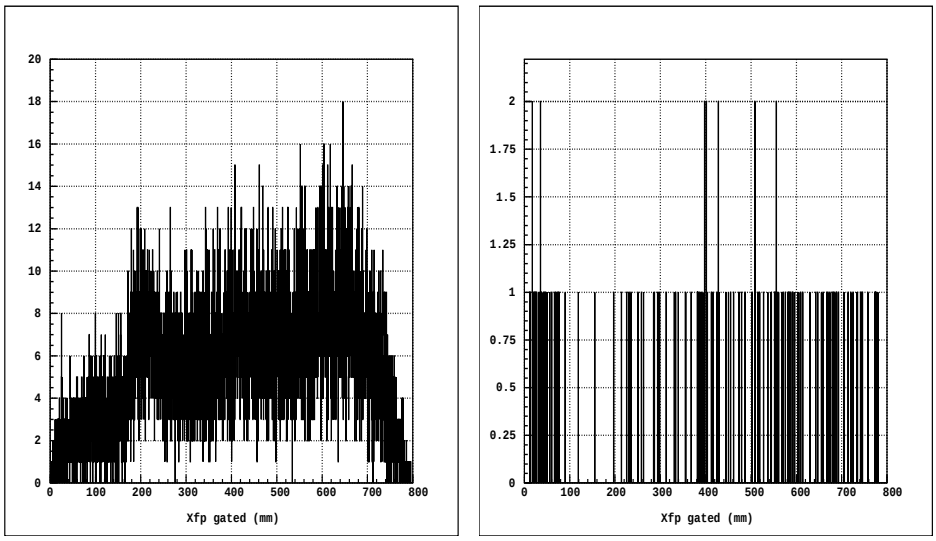

(a) (b)

Figure 3.7: (a) A focal plane position spectrum for an empty target for bad beam halo conditions at 1.8 nA beam current taking for 15 minutes. (b) A focal plane position spectrum for an empty target under a good beam halo conditions at 3 nA beam current taking for 4 minutes.

Information from these BLM's proved to be of great help to beam operators in diagnosing the cause for halo seen in the focal plane detectors. The first was positioned along the P-line between steerers STX 6P and STY 6P, followed by another one just after the last bending magnet B3P. The third and fourth were positioned at Q3S opposite each other on the S-line while the last one was inside the vault between steerers STY 3S and STX 3S (see Fig. 3.1).

An example of a bad halo position spectrum with the ^{40}Ca target and the spectrometer positioned at 7° is shown in Fig. 3.6. The broad halo peak in the low momentum (right hand) side of the position spectrum can be clearly seen. In order to measure precisely the effect of background contribution in the experiments, data taken with an empty target should clearly show the difference between a bad halo and a background free or clean spectrum. The beam was set up for minimum halo by comparing the count rate with the target in position to that obtained with an empty frame. An example of these spectra is shown in Fig 3.7. The beam loss monitor in the vault showed high countrate for bad halo conditions as can be seen in Fig. 3.8(a), where the green line represents the BLM in the vault. The situation where the beam loss monitors detect no halo events is shown in Fig. 3.8(b).

In addition to the normal harps used by the Accelerator Group for beam alignment purposes there are three beamviewers that consist of ZnS scintillating material and are used for checking the beam position. The first one, which is located just after the last quadrupole in the S-line (QS6) is a ZnS mesh and is called the Hatanaka viewer, shown in Fig. 3.9. Note that the standard harp at iThemba LABS cannot be used in this position since they are only useful at high beam currents of approximately 50 - 100 nAmp. Since the experiments do not require high currents (which can damage the target viewer) the need developed to replace the harp after Q6S with a fluorescent viewer. The second

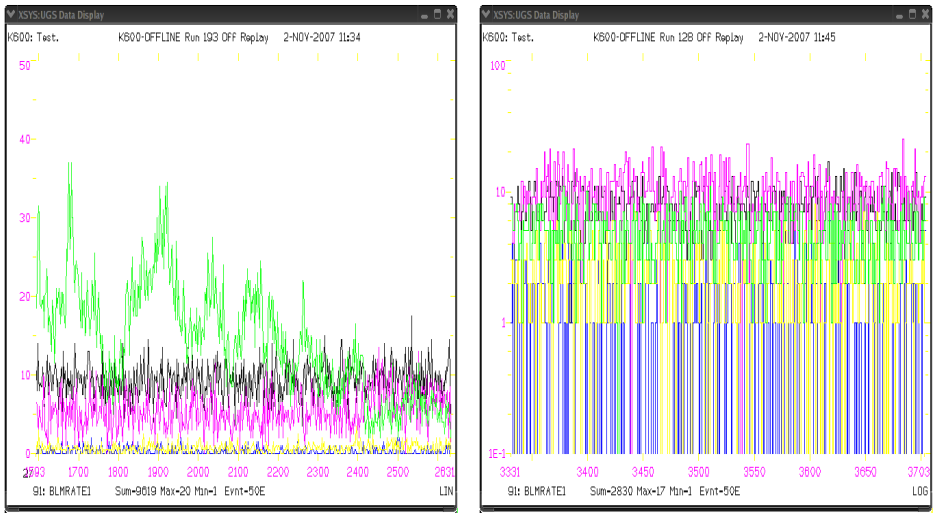

(a) (b)

Figure 3.8: (a) Beam loss monitor spectrum showing bad halo conditions. The countrate is shown as a function of time. Note the countrate above 30 Hz for the BLM in the vault (green line). (b) All the five beam loss monitor spectra showing overall good halo conditions. Note the beam loss monitor countrates were below 10 Hz.

ZnS viewer, a solid ZnS screen, is the standard beam-viewer (without an hole at the center, as in the case of the standard iThemba LABS target viewer) and it is placed at the target position. The last ZnS viewer is also a solid ZnS screen and is located in the zero-degree beam-line just before the zero-degree beam-dump. The Hatanaka viewer together with the ZnS target viewer are used to ensure that the beam alignment on the target is correct. Above all, the target viewer helps to monitor beam focusing conditions on target.

Whenever the halo count rate increased, the beam was realigned by adjusting steerers in the S and P-lines to obtain the smallest possible empty target count rate in the drift chambers. In some cases, all these steps had to be repeated iteratively to ensure a minimum contribution of the experimental background to the spectrum and provide the best possible resolution.

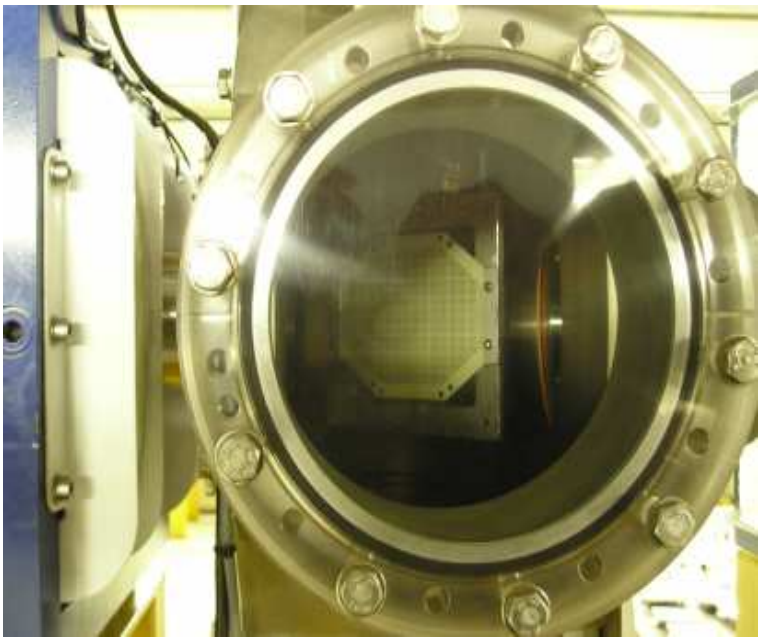

Figure 3.9: The Hatanaka viewer shown in the in-beam position. The viewer is positioned 45° with respect to the beam. The beam direction is from left to right.

Five measurements for angle calibration were taken with a multislot collimator at different magnetic field settings, covering the 10% momentum bite of the spectrometer, to determine the horizontal scattering angle. The procedure was repeated at each angle under investigation. The data was stored as event files on event disks available for offline data extraction and analysis.

3.5.1 High Energy-resolution

The resolution attainable with a magnetic spectrometer system depends upon several factors. Some of these factors are common to both the conventional and dispersive-beam techniques, while others apply only to the latter. The three main contributions to the spectrometer resolution are the angular kinematics broadening, target thickness and improper dispersion matching. The kinematic broadening owes its importance to the finite solid angle acceptance of the

spectrometer. The influence of target thickness effects on energy resolution is as a result of ionization losses which spread the energy distribution of the scattered beam.

The main goal in this particular inelastic proton scattering experiment was to achieve high energy-resolution of $\Delta E \leq 30$ keV. All the above mentioned factors contribute in one way or the other to the final realisation, but the implementation of dispersion matching techniques in particular aid in achieving this goal. A typical energy resolution of 38 keV has been achieved on ^{40}Ca and ^{12}C targets with beam currents in the range of 2-20 nA. With a thin ^{28}Si target, the best resolution achieved was 25 keV during the third weekend of the experiment due to the fact that it was a very thin target.

3.6 Data Acquisition System and Electronics

The main source of computing power was a VAX/VMS 4000 workstation, which was responsible for monitoring and storing the data, event by event on storage disks. Online analysis of the data was carried out using the XSYS analysis software [Pil89, Gou81].

The trigger signals were conducted via fast 50 Ω coaxial cables; these included signals from the PMTs of the two plastic scintillators. Fig. 3.10 shows a schematic of the trigger component of the K600 electronics. The particle trigger was formed by the coincidence of the plastic scintillators P1 and P2, since they have 100% efficiency for detecting heavy charged particles. Derived from this trigger signal were gates to the QDC's, start signals for the time-to-digital converters (TDC's) and an interrupt to the computer instructing it to log all the event information to disk. A relative time-of-flight (TOF) measurement used for particle identification (refer to Section 3.7.1) was generated with the

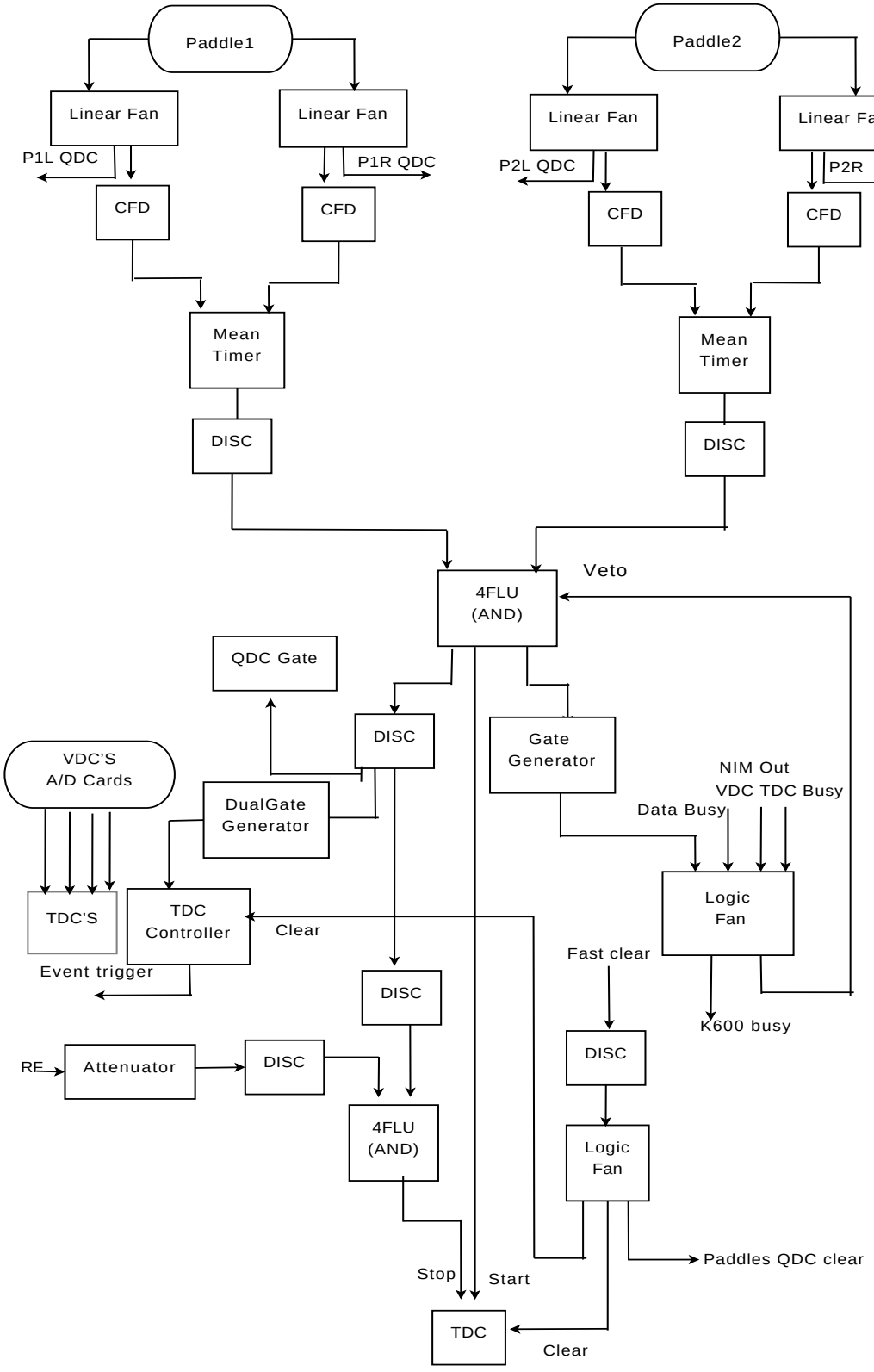

Figure 3.10: Event trigger and timing electronics for the K600 Magnetic Spectrometer.

electronic setup of Fig. 3.10. A TDC digitised the interval between a paddle coincidence signal and an SSC RF signal. In addition to the primary trigger electronics, several parallel coincidence circuits were maintained in order to determine the electronic and computer dead-times. Rates for each circuit were accumulated by scalers.

3.7 Data Extraction

Raw data in the form of event files created by the XSYS Data Acquisition (DAQ) system can be analysed offline. The offline analysis was performed using software written in C and developed at iThemba LABS by H. Fujita [Fuj07]. A schematic of the offline data processing algorithm is presented in Fig. 3.11 and can be summarised as follows:

- Plot the PMT outputs for the paddles and select good events.
- Obtain drift lengths from the corresponding TDC outputs for MWDC1 and MWDC2.
- Determine which events are good events.
- Check for all "Event-IDs" and continue if Event-ID = 0 (see Section 3.7.2).
- Perform ray-trace analysis for good events only and determine the position X1 in MWDC1 and X2 in MWDC2.
- Obtain Y information.
- From X1 and X2, deduce θ_{fp} angle.
- Reconstruct horizontal scattering angle θ_{tgt} from θ_{fp}.
- Construct $\mathrm{X_{fp}}$ corrections for high resolution (see Section 3.7.2).

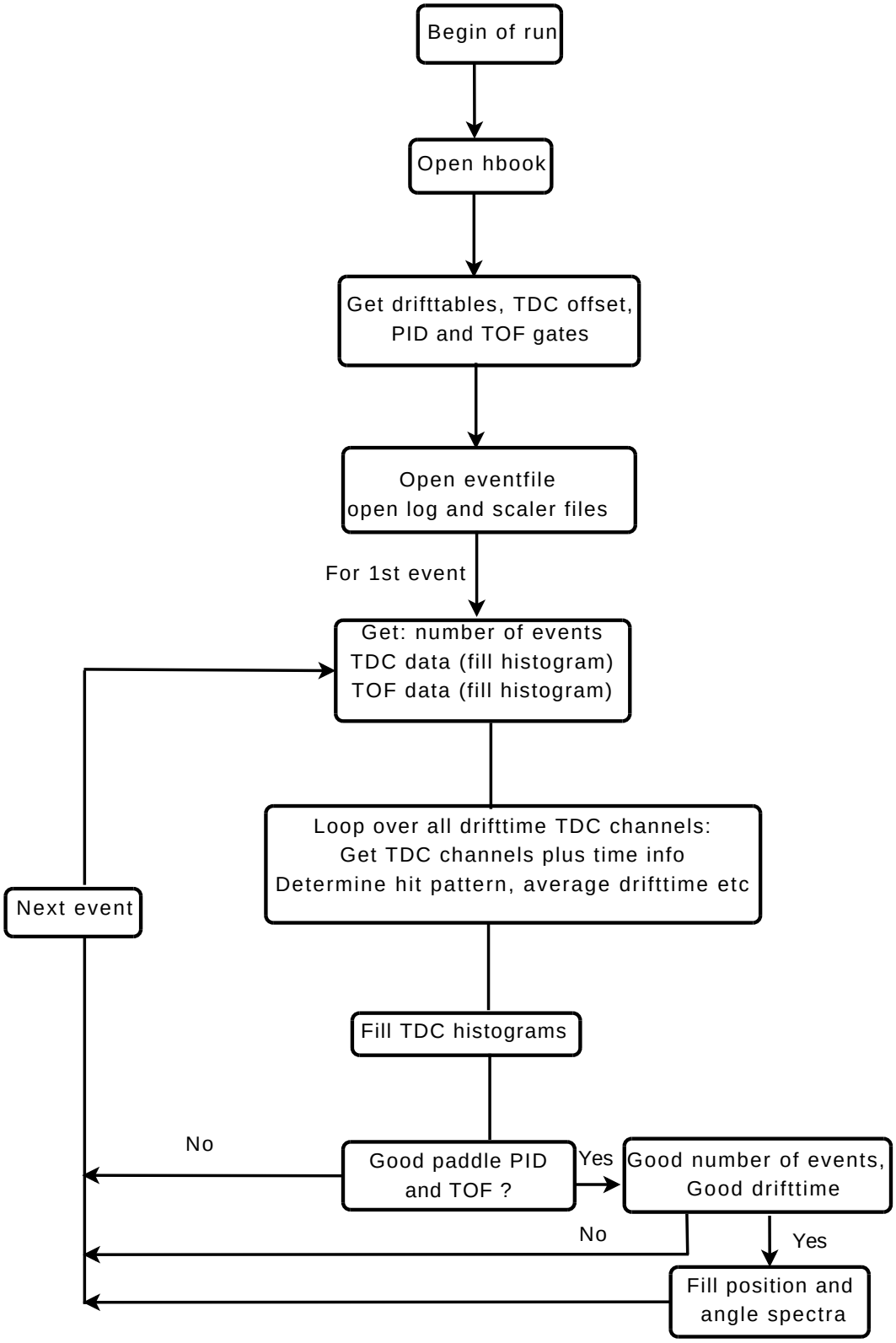

Figure 3.11: Flow chart illustrating the offline data analysis algorithm.

- Accumulate total number of good events and specific Event-ID's to evaluate detection efficiencies of each wire chambers.

- Fill histograms for all events.

The final spectra obtained after summing up all the data for a given target at each scattering angle are presented in Sect. 4.2.

3.7.1 Particle Identification

Particle identification is the process of using information left by a particle passing through a particle detector to identify the type of particle. This can help to reduce backgrounds. The magnetic setting of the K600 Spectrometer only helps in knowing the momentum (p) of the particle observed. No individual information concerning the particle's mass (m), energy (E) and/or charge (q), is provided, thus the need for particle identification. It is important to note that in this type of experiment other types of particles may contribute to the experimental yield and may be counted by the focal plane detectors. The process of particle identification relies on a measurement of the momentum in a tracking chamber combined with a measurement of energy loss in the plastic scintillators to determine the charged particle mass, and therefore, its identity. In addition, particle identification can be achieved by considering the time-of-flight (TOF) selection technique.

In the ΔE-ΔE spectrum, energy-loss of particles passing through the scintillator detectors depends on the type of particle and the kinetic energy of the particle. Taking the geometrical average of the signals from the two photomultiplier tubes on the ends of each scintillator eliminates the dependence of the pulse height on the position of the event along the length of the scintillator. Any particles other than protons were considered as background to this particular experiment and by setting a software gate on the protons as illustrated

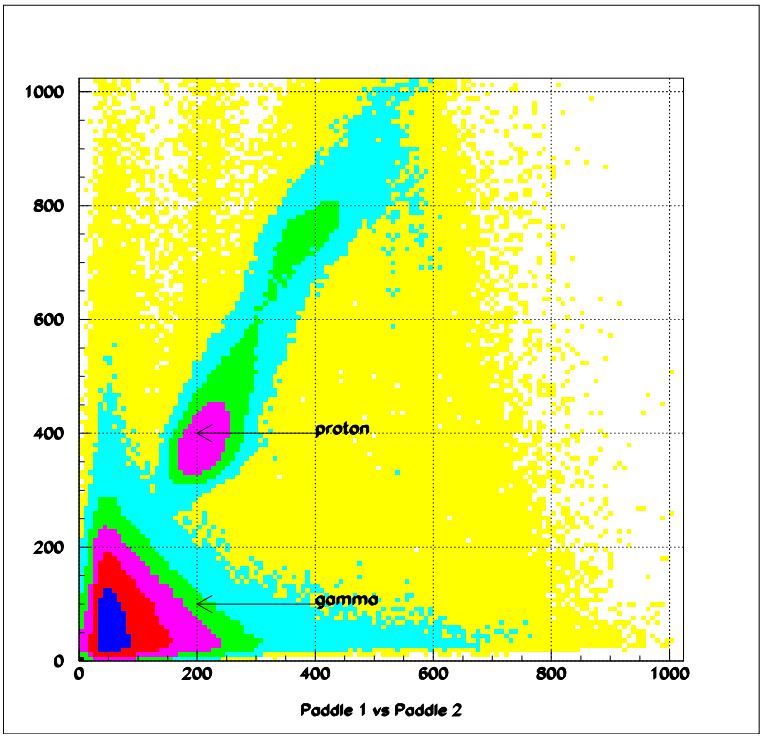

Figure 3.12: Proton identification using the focal plane ΔE-ΔE spectrum. Other events (γ) seen are also indicated.

by the indicated locus in Fig. 3.12 only protons can be selected, leaving out any contribution from other particles such as gammas (γ) originating from the target. An example of how protons are selected in the detectors pulse height spectra is shown in Fig. 3.13. Also indicated in Fig. 3.13 are the pulse height spectra due to software gates shown as the red and green lines on the averages of scintillator detectors 1 and 2 (also referred to as paddles 1 and 2). The gates are set to include good events only on both detectors with the green line.

The TOF is measured as the relative time elapsed between a coincident paddle signal and the radio-frequency (RF) signal from the SSC. In order to select the incoming particles through the TOF technique, a narrow cut is made in time which serves as a gate. The appropriate peak in the TOF spectrum is shown as green line in Fig. 3.14.

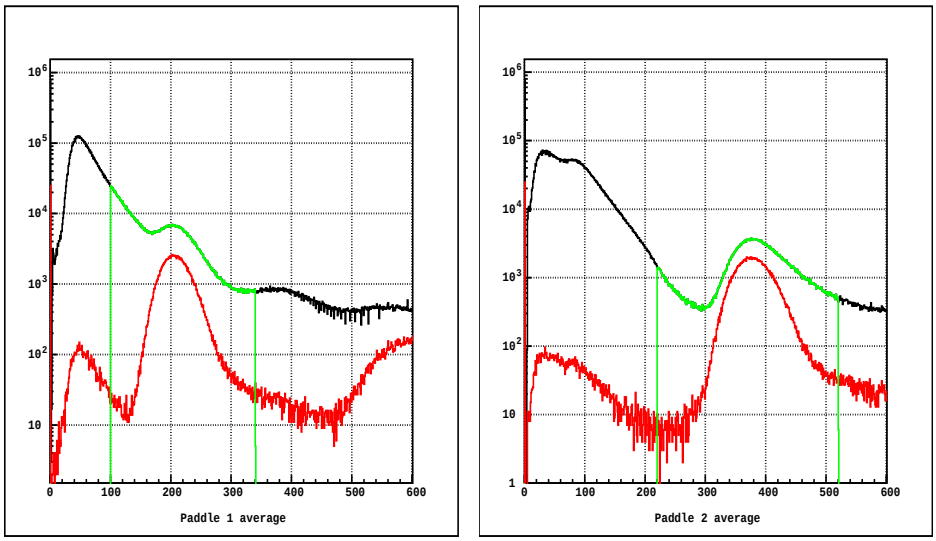

(a) (b)

Figure 3.13: (a) Particle identification in paddle 1. (b) Particle identification in paddle 2. Note that the black line indicates all events, the red line indicates good events in X1, X2 and Y (i.e. Event ID = 0), and the green line indicates the software gates for good events used in the analysis.

3.7.2 VDC data processing

As illustrated in Section 3.2.2, there is a focal-plane detector package situated behind the second dipole. This consists of three multi-wire drift chambers and a pair of plastic scintillation detectors shown in Fig. 3.2. Good events per drift chamber can be chosen if the following criteria are fulfilled:

- If at least 3 and less than 9 MWDC signal wires registered a hit.
- If both paddles are receiving signals.
- If the drift times associated with these events are within the range specified by the software gate.
- If the wires make a good group.

For all good VDC events, the position (X_{fp}) of a particle can be determined by an interpolation method. The drift times associated with these good events

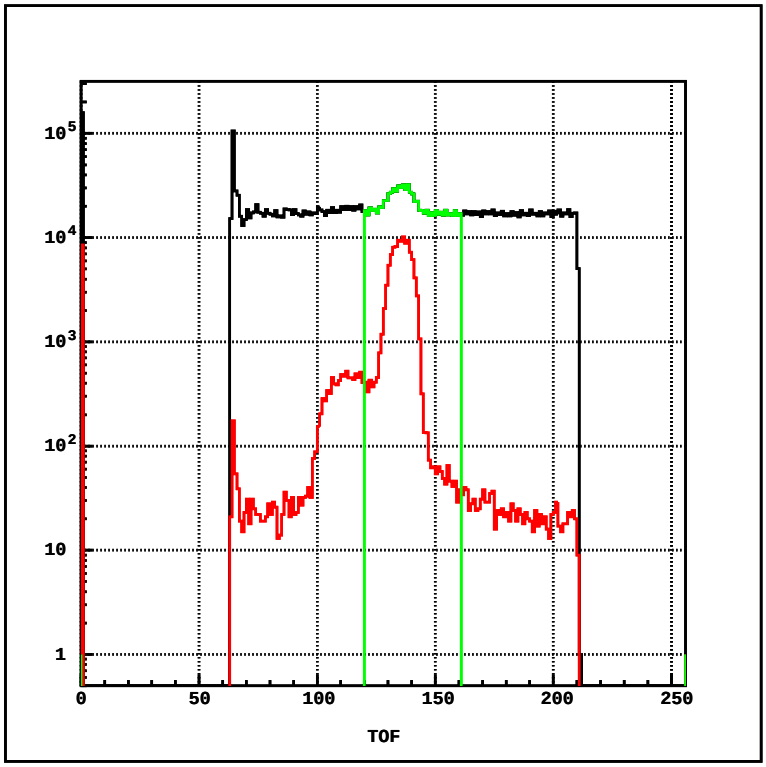

Figure 3.14: TOF gates used in particle identification. Note that the black line indicates all events, the red line indicates good events in X1, X2 and Y (i.e. Event ID = 0), and the green line indicates the software in gates for good events used in the analysis.

must be within the range specified by the software gate on the average drift time spectrum as shown in Fig. 3.15. The drift times have to be converted into drift distances by using the so-called look-up table. Prior to the data analysis, TDC offset corrections were made to ensure that the offsets on all TDC channels were similar. Figure 3.16 presents a look-up table after the correction. Once the drift distances are acquired, the position of the crossing point of the particle track in the focal plane along the dispersive direction is determined.

In an ideal spectrometer the position along the focal plane at which a particle is detected is directly related to its momentum. In practice, however, due to kinematic broadening, which is higher in light nuclei, the momentum can also depend on the angle of the particle trajectory. If the properties of the

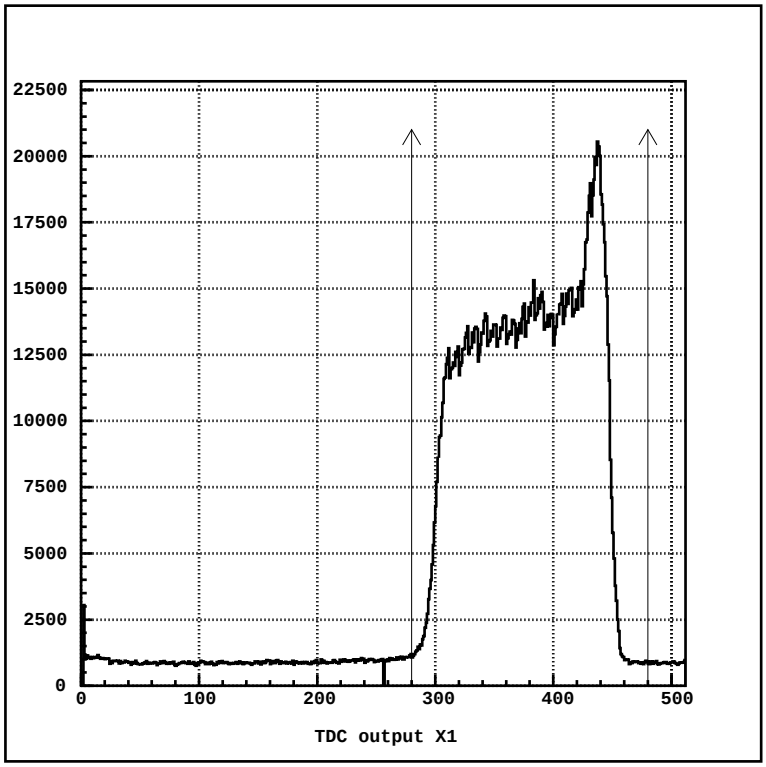

Figure 3.15: Average drift time spectrum for the X1 wire chamber. The two lines with arrows illustrate the range of gate settings for minimum and maximum valid TDC drift time values on the horizontal axis.

spectrometer are known, it is possible to correct the measured position if the angles at which a particle enters the spectrometer are determined. Hence angle reconstruction is a valuable tool. Scattering angle calibration also allows one to divide the $\pm 2^{\circ}$ acceptance of the K600 spectrometer into finer angular sections for angular correlation determination. In order to be able to reconstruct the target angle (θ_{tgt}) from the measured focal plane angle (θ_{fp}), measurements were performed in the (p,p$'$) experiments by using a multislot collimator shown in Fig. 3.17. The multislot collimator was positioned at 735.5 mm downstream from the target in the normal collimator position. There are seven slots each with an opening of 5 mm by 15 mm, enabling an exact definition of the scattering angle. Different peak positions were found in the position spectra $\mathrm{X_{fp}}$ from different spectrometer magnetic settings. Then the corresponding scattering angles are determined from the peaks found in the θ_{fp} spectra.

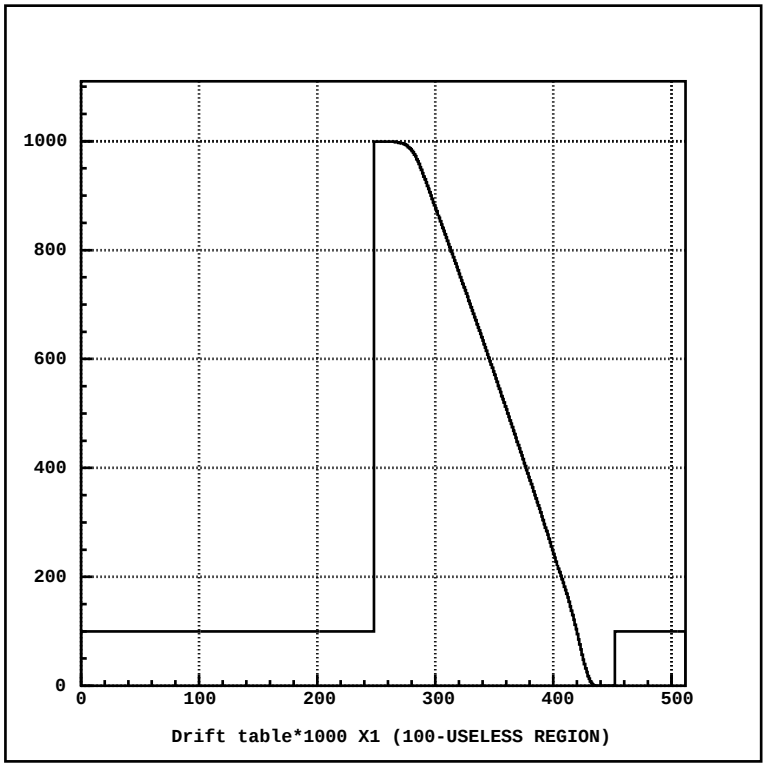

Figure 3.16: The reconstructed lookup-table after setting gates on good events. Note that the vertical axis represents the drift distance (signal-wire to Al-plane spacing) divided into 1000 channels while the horizontal axis represents the drift time (channels).

One should bear in mind that a positive focal plane angle corresponds to a negative target angle and vice versa. For a full spectrum, there appears seven peaks which correspond to the seven holes present in the multislot collimator.

Below is summarised the basic procedure on how the required parameters are determined for horizontal scattering angle reconstruction:

- Observe histogram 106, (θ_{fp}) similar to Fig. 3.18, and note the peak positions on the horizontal axis. This process is made easy by using a macro for gaussian fitting in order to get accurate position values.

- Determine the θ_{fp} for each of the peaks in the spectrum and record them in a tabular form with their corresponding θ_{tgt} values.

- Create a graph of θ_{fp} vs θ_{tgt} and at specific focalplane position ($\mathrm{X_{fp}}$),

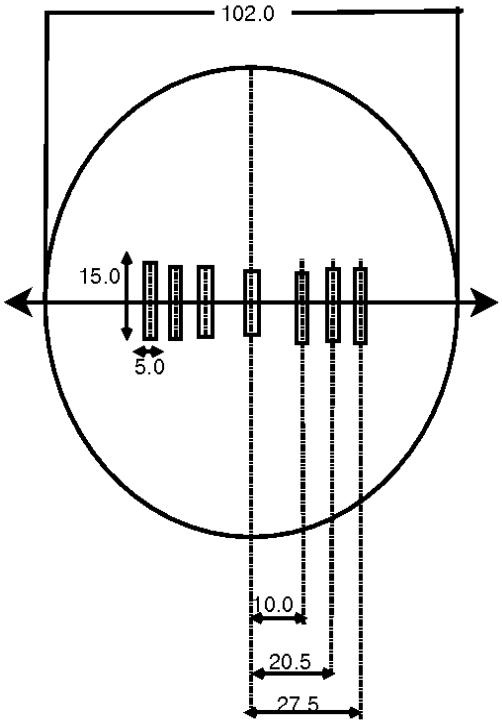

Figure 3.17: A diagram showing the multislot collimator used for horizontal angle calibration. Note that all measurements are in mm.

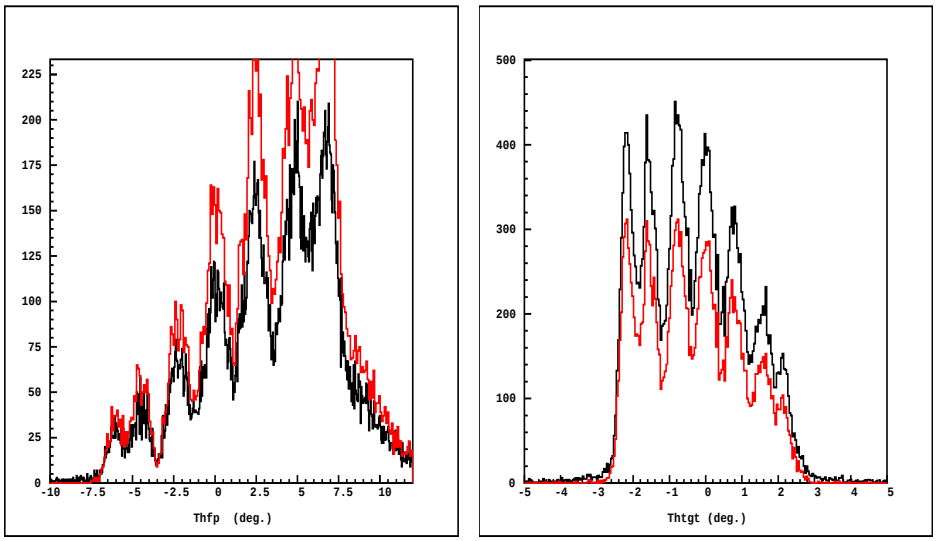

(a) (b)

Figure 3.18: (a) Focal plane scattering angle with red line representing the gated good events spectrum. (b) Target scattering angle with red line representing the gated good events spectrum. Note the seven peaks correspond to the holes on the multislot collimator used during the experiments.

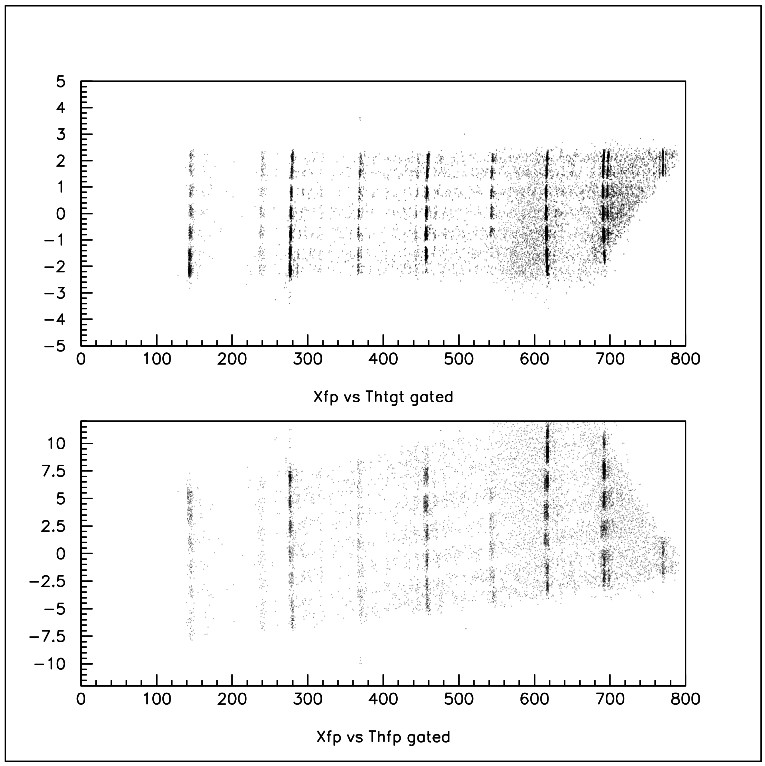

Figure 3.19: Angle calibration at different focal plane positions. The top figure represents the focal plane position (horizontal axis) versus $\theta_{\rm tgt}$ (vertical axis) while the bottom figure represents the focal plane position versus $\theta_{\rm fp}$ for good events in ^{40}Ca at $\theta_{\rm K600} = 11^{\circ}$. It can be seen that all the peaks in the top figure are aligned on the appropriate angle.

determine the function which converts focalplane angle ($\theta_{\rm fp}$) into target angle ($\theta_{\rm tgt}$) using a quadratic function

$$\theta_{\rm tgt} = A + B\theta_{\rm fp} + C(\theta_{\rm fp})^2. \tag{3.1}$$

- The same procedure is done at different $X_{\rm fp}$, which corresponds to a number of runs using the multislot collimator at different magnetic settings.

The resultant $X_{\rm fp}$ vs θ plot is shown in Fig. 3.19.

3.7.3 Energy calibration

Peak centroids were extracted from the position spectrum of the ^{40}Ca(p,p$\prime$) reaction via a Gaussian peak fitting program. The position of each peak iden-

tified in the X_{fp} spectrum was associated with a proton energy using kinematic calculations of the program KINMAT. Energy levels with the most accurate excitation energies listed in the recent table of isotopes were used as calibration lines to assign accurate energies to the known levels. The excitation energy uncertainties associated with these calibration lines increase from 0.2 keV for the low-lying levels to 1.2 keV for a resonance state around 10 MeV. The corresponding momenta were calculated using the relativistic conversion. Using these calibration lines a quadratic momentum versus focal plane position calibration curve was established via the the least squares fitting procedure. An example of the result is shown in Fig. 3.20 for the case of ^{40}Ca at 7°, 11° and 15°.

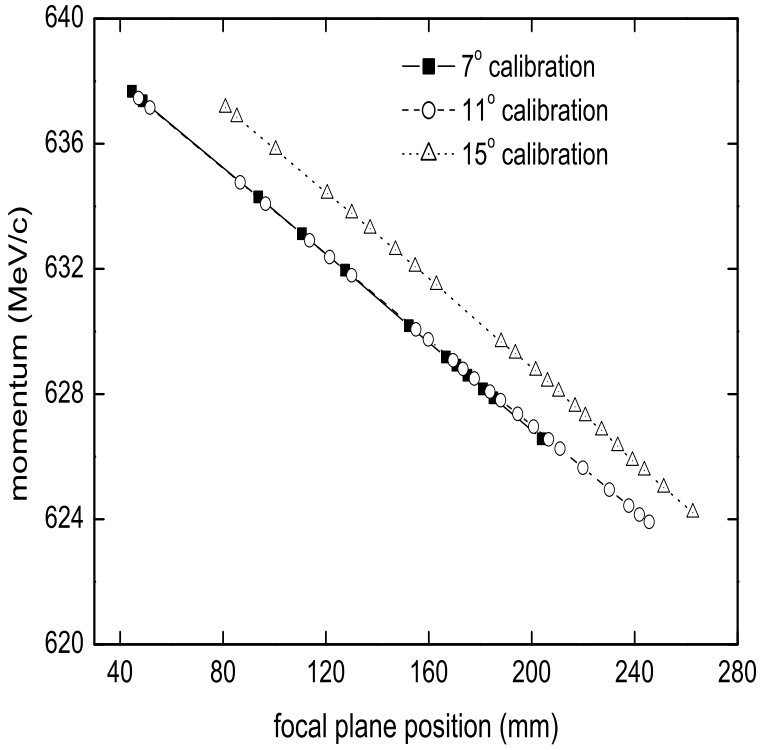

Figure 3.20: Momentum calibration curve of ^{40}Ca spectra at different angles and momentum settings using a second order polynomial fitting. Note that the K600 momentum setting for 7° and 11° was 198 MeV while that of 15° was 202 MeV.

3.8 Experimental Cross-sections

The experimental double differential cross-section of the inelastic proton scattering in units of mb/srMeV can be written as

$$\frac{d^2\sigma}{d\Omega dE} = \frac{10^{27} \cdot N_{\rm c}}{N_{\rm o} \cdot \rho \cdot D \cdot \Delta\Omega \cdot \Delta E \cdot \varepsilon}, \tag{3.2}$$

where

- $N_{\rm c}$ is the corrected number of counts in a bin,
- $N_{\rm o}$ is the total number of incident protons on the target,
- ρ is the number of target nuclei per unit area (in $\rm mb^{-1}$),
- D is an electronic dead time correction factor,
- $\Delta\Omega$ is the solid angle of the K600 in sr, and
- ΔE is energy bin size (in MeV),
- ε is the K600 VDC efficiency.

Cross-section results were generated for ^{40}Ca spectrum at scattering angles of 7°, 11° and 15°, respectively.

In Eq. 3.2 the number of incident protons is calculated by

$$N_{\rm o} = \frac{CI \cdot R \cdot 10^{-12}}{e}\ , \tag{3.3}$$

where

- CI is the scaler read-out of the current-integrator,
- R is the selected range (in nA) of the current integrator which represents 1000 counts/s for a full scale current read-out, and
- e is the proton electric charge (in coulomb).

The number of nuclei per unit area of the ^{40}Ca target is calculated from

$$\rho = \frac{\lambda_{\mathrm{T}} \cdot N_{\mathrm{A}}}{cos\frac{\theta_{\mathrm{T}}}{2} \cdot A} \ , \tag{3.4}$$

where

- λ_{T} is the target thickness (gcm^{-2}),
- N_{A} is Avogadro's number,
- θ_{T} is scattering angle of the target's normal with respect to the beam direction, and
- A is mass number.

The alive-time D of 0.9 and the energy bin size ΔE of 0.01 MeV were used in the calculation.

3.8.1 Error Analysis

The statistical error for the double differential cross-section is given by

$$\delta\left(\frac{d^2\sigma}{d\Omega dE}\right) = \frac{10^{27}.\sqrt{N_{\mathrm{c}}}}{N_{\mathrm{o}} \cdot \rho \cdot D \cdot \Delta\Omega \cdot \Delta E \cdot \varepsilon.} \tag{3.5}$$

The systematic error in the measured cross section values is mainly due to the uncertainty in the target thickness which is estimated to be less than 11% for the ^{40}Ca target. A similar systematic error is assumed for the other targets.

3.9 VDC Efficiency

The detection efficiency of the vertical drift chambers for charged particles is defined as

$$\text{efficiency}(\varepsilon) = \frac{\text{good events in X1, X2 and Y wires}}{(\text{good } + \text{ bad}) \text{ events in X1, X2 and Y wires}}. \tag{3.6}$$

Criteria for good events have been stated in Sect. 3.7.2. These events are the ones that are used in making a good spectrum of the scattered particles. The efficiency of each of the runs taken was calculated online from various analyser and scaler results. In this particular experiment, the average overall efficiency obtained varied between 88% and 94% for the X1 and X2 drift chambers.

Chapter 4

Results, Analysis and Discussion

This chapter presents the resulting extracted experimental data and seeks to obtain the correspondence with the theoretical predictions by applying the theoretical models and analysis tools detailed in Chapter 2. Section 4.1 deals with the results of the DWBA inelastic-scattering calculations, in particular for $L = 2$ angular distributions of the nuclei used during the experiments in order to choose suitable scattering angles for the measurement of the ISGQR for each nucleus. The experimental results are discussed in Sect. 4.2 followed by the theoretical results of the SRPA calculations in Sect. 4.3. Extraction of characteristic energy scales in the excitation energy region of the ISGQR in nuclei under investigation using wavelet analysis is presented for both the experimental data and the SRPA predictions in Sect. 4.4. This is followed in Sect. 4.5 by the reconstruction of the various energy-width features in the excitation energy region of the ISGQR using Continuous Wavelet Transform (CWT) analysis, in order to gain further insight into the nature of energy scales extracted for the case of ^{40}Ca. The characteristic energy scales of the ISGQR obtained in the experimental data compared to those obtained from the theoretical model calculations using the newly-developed Semblance and Dot product analysis techniques are presented in Sect. 4.6. Also presented in this section is the comparison of ^{28}Si proton inelastic scattering data with

other probes exciting the ISGQR and the semblance of one-proton difference nuclei in ^{28}Si,^{27}Al(p,p$'$) and ^{90}Zr,^{90}Y(p,p$'$) experiments. Section 4.7 presents the results of quasi-free scattering calculations in ^{40}Ca at the three scattering angles measured and is used later in the extraction of 2^+ level densities for ^{40}Ca. Finally, details concerning the extraction of experimental 2^+ level densities for ^{40}Ca using the model independent method of Discrete Wavelet Transform (DWT) background determination and their comparisons with theoretical model predictions are discussed in Sect. 4.8.

4.1 Spin-filter effects

Excitation of the ISGQR by inelastic scattering of protons at intermediate energies is strongly angle dependent. In order to identify suitable scattering angles at which measurements of excitation energy spectra should be taken, calculations were made of inelastic scattering within the DWBA using a collective form-factor (see Sect. 2.2.1). By way of example, Fig. 4.1 shows the results for ^{40}Ca for an $L = 2$ transfer together with other multipoles excited. Scattering angles of $\theta_{\rm Lab} = 7^\circ$, 11° and 15° were chosen for ^{40}Ca below, at and above the first maximum of the ISGQR, respectively. As in previous studies of the ISGQR [Car98, Car01], contributions to an underlying background from higher-order multipoles are expected to be present. In addition, for $L = 0$ a pronounced minimum can be seen at the first maximum of the ISGQR. Thus, the "spin-filter" effect can be taken advantage of in the selection of suitable scattering angles. Details of the optical potential used in the calculations are given later in Sect. 4.7 and a value of $\beta = 1$ was used (see Sect. 2.2.1). Similar calculations were performed for the other low-mass targets used in the present investigation. It should be noted that the position of the first maximum of the ISGQR moves to smaller scattering angles as target mass increases and can be identified as a diffraction effect.

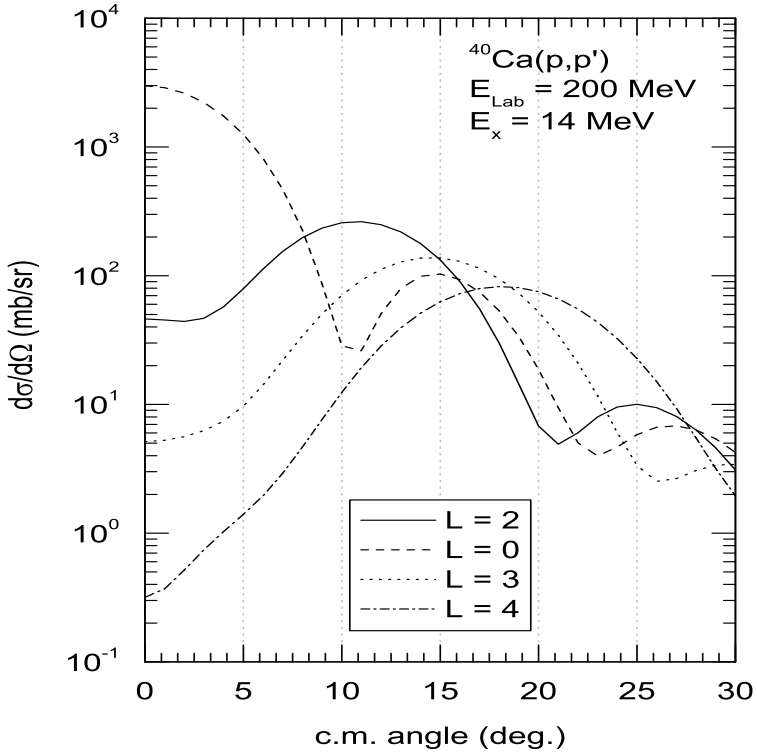

Figure 4.1: Angular distributions for DWBA inelastic proton scattering on ^{40}Ca for $L = 0$, 2, 3, and 4 excitations at $E_{\rm p} = 200$ MeV.

4.2 Experimental results for measured spectra: ^{40}Ca, ^{28}Si, ^{27}Al and ^{12}C

The results of the raw data analysis explained in Chapter 3 are presented here for the target nuclei ^{40}Ca, ^{28}Si, ^{27}Al and ^{12}C. Measured data for each of the target nuclei at the corresponding angles below, at and above the maximum of the ISGQR are shown in Figs. 4.2, 4.3, 4.4 and 4.5 for ^{40}Ca, ^{28}Si, ^{27}Al and ^{12}C, respectively. The full energy-bite of the K600 Magnetic Spectrometer, 6 $\leq E_{\rm x} \leq$ 30 MeV (see Sect. 3.5 for details) are presented for each of the target nuclei.

For ^{40}Ca, measurements were performed at three different scattering angles *viz.* $\theta_{\rm Lab} = 7^\circ$, 11° and 15° being below, at and above the maximum of the ISGQR, respectively, as illustrated in Fig. 4.2.

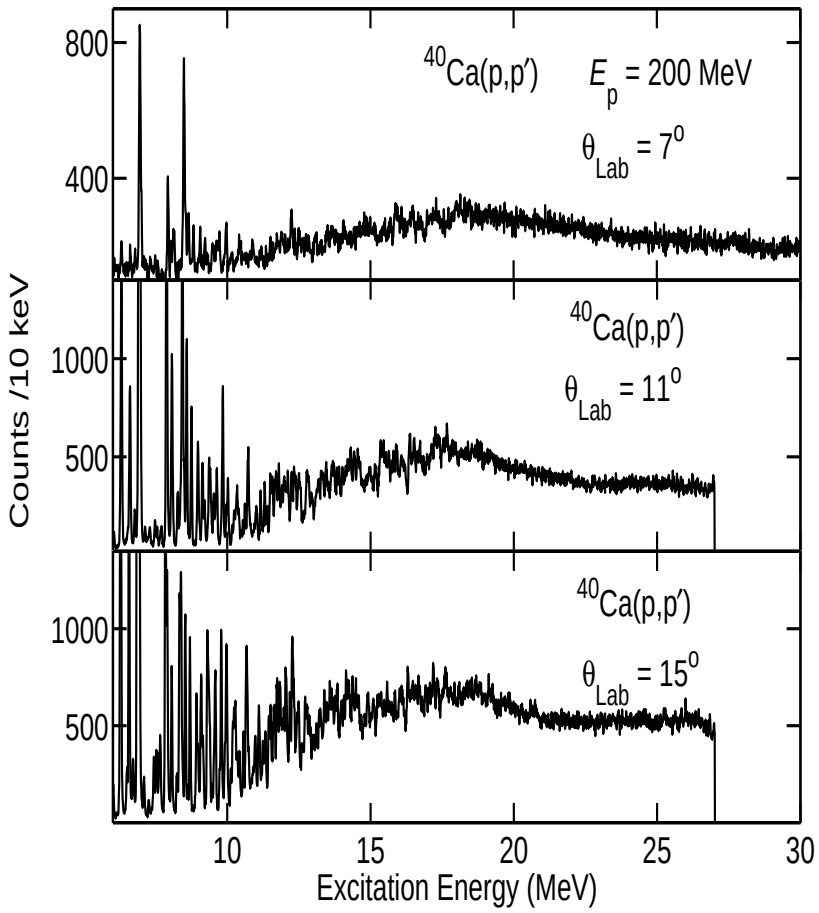

Figure 4.2: Excitation energy spectrum for ^{40}Ca at scattering angles of $\theta_{\rm Lab}$ = 7°, 11° and 15°. Note the maximum of the ISGQR is at θ_{Lab} = 11°.

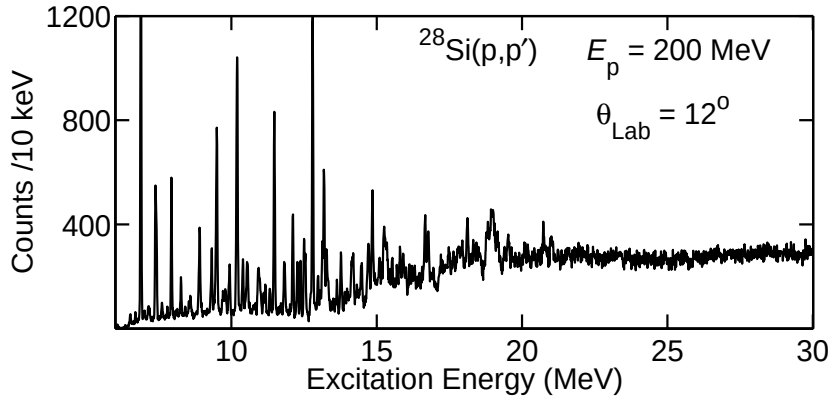

Figure 4.3: Excitation energy spectrum for ^{28}Si at a scattering angle of $\theta_{\rm Lab}$ = 12° the maximum of the ISGQR.

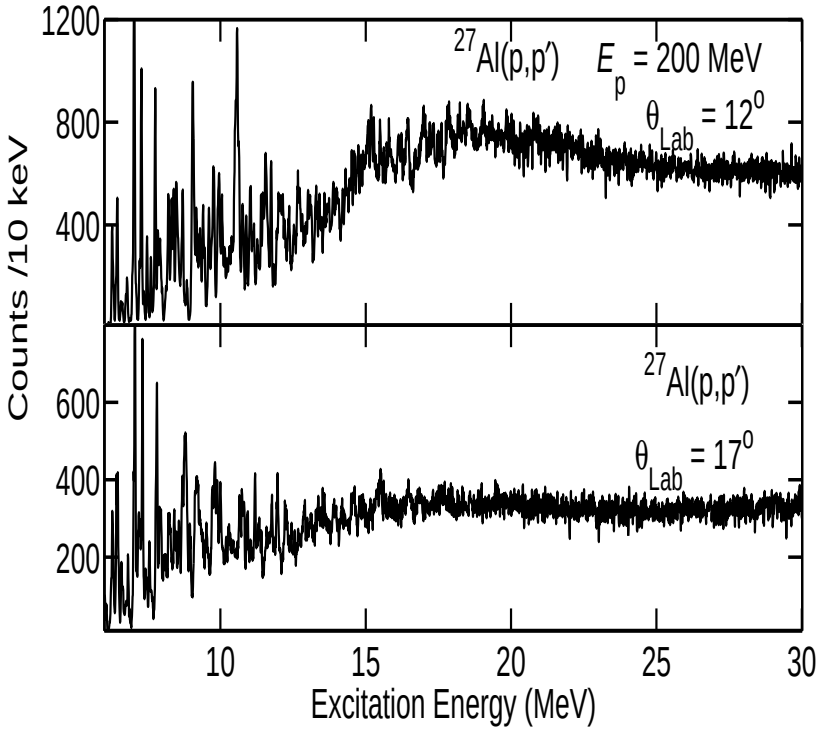

Figure 4.4: Excitation energy spectra for ^{27}Al at scattering angles of $\theta_{\rm Lab} = 12°$ and 17°. Note that the maximum of the ISGQR is at $\theta_{\rm Lab} = 12°$.

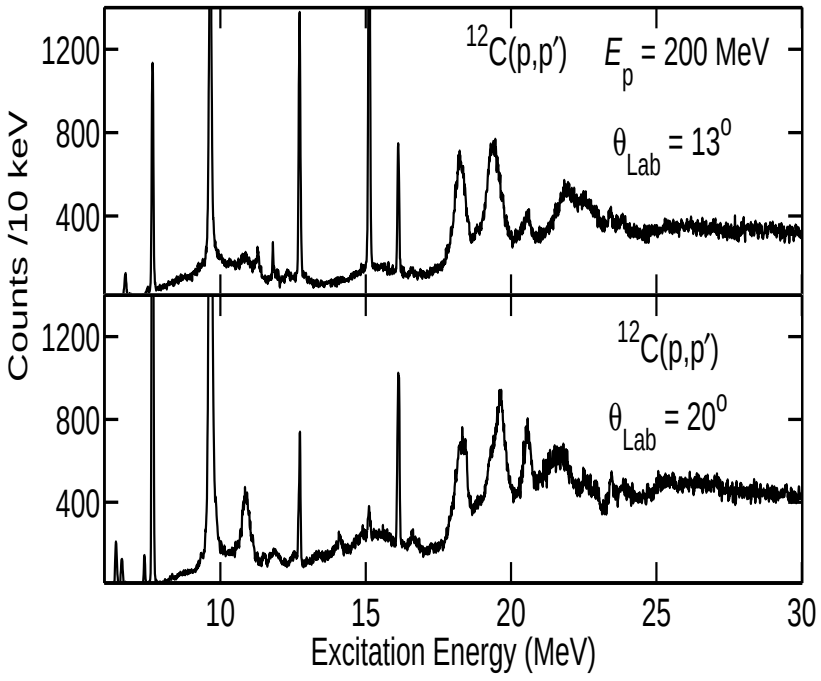

Figure 4.5: Excitation energy spectra for ^{12}C at scattering angles of $\theta_{\rm Lab} = 13°$ and 20°. Note that the maximum of the ISGQR is at $\theta_{\rm Lab} = 13°$.

Due to lack of beamtime, only one angle measurement could be performed for ^{28}Si at $\theta_{\mathrm{Lab}} = 12^{\circ}$ the ISGQR maximum (see Fig. 4.3). Two angle measurements were obtained at $\theta_{\mathrm{Lab}} = 12^{\circ}$ and 17° for ^{27}Al and likewise for ^{12}C at $\theta_{\mathrm{Lab}} = 13^{\circ}$ and 20° with the smaller angle corresponding to the maximum of the ISGQR. One can clearly identify discrete low-lying states below the respective proton and neutron thresholds in each of the target nuclei and above these levels fine structure can be observed in the region of the ISGQR, especially at scattering angles corresponding to the maximum of $\Delta L = 2$ in each nucleus except for ^{12}C. At the maximum of the ISGQR for each of the target nuclei, except for ^{12}C, *viz.* ^{40}Ca at $\theta_{\mathrm{Lab}} = 11^{\circ}$, ^{28}Si at 12° and ^{27}Al at 12°, the fine structure is well pronounced and each of the spectra displays very different specific details within the ISGQR region. Dealing with each target nucleus in turn:

^{40}Ca: The excitation energy spectra for ^{40}Ca between 6 and 30 MeV measured at three different scattering angles are presented in Fig. 4.2. The spectrum at $\theta_{\mathrm{Lab}} = 11^{\circ}$, which is the maximum of the ISGQR, appears as a broad feature with distinctive sub-structure and a mean energy of $E_{\mathrm{x}} \approx 18$ MeV and with a width of about 5 MeV consistent with the corresponding peak identified in Fig. 2.5 for (α, α') scattering. At the larger scattering angle of $\theta_{\mathrm{Lab}} = 15^{\circ}$ the overall structure is reduced in size and importance but it should be noticed that some of the distinctive fine structure still persists. At the smaller scattering angle $\theta_{\mathrm{Lab}} = 7^{\circ}$ the resonance still persists but centred $E_{\mathrm{x}} \approx 19$ MeV.

^{28}Si: The experimental data for ^{28}Si are unfortunately less extensive, with only a single spectrum at $\theta_{\mathrm{Lab}} = 12^{\circ}$ shown in Fig. 4.3, again corresponding to the maximum of the ISGQR. Here, a broad peak of width approximately 5 MeV is observed, being highly fragmented and centred around $E_{\mathrm{x}} =$ 19 MeV. This is consistent with the corresponding feature identified in Fig. 2.5 for (α, α') scattering from ^{28}Si.

^{27}Al: In the case of ^{27}Al two measurements were obtained, one for $\theta_{\mathrm{Lab}} = 12^{\circ}$ (at the maximum of the ISGQR) and the other one at the larger scattering angle $\theta_{\mathrm{Lab}} = 17^{\circ}$ as seen in Fig. 4.4. Again, a broad peak can be identified, about 5 MeV wide, being centred at $E_{\mathrm{x}} \approx 18$ MeV for the maximum of the ISGQR but becomes flat at the higher scattering angle.

^{12}C: Data for the lightest nucleus are shown in Fig. 4.5 for two angle measurements at $\theta_{\mathrm{Lab}} = 13^{\circ}$ and 20°. It should be noted that all the states seen in were previously known and do not belong to the ISGQR which is too fragmented [Rie78]. In addition, there is no clear signal of fine structure in the region of the ISGQR for both of the spectra measured. This might signal that such a light nucleus cannot support a high frequency collective mode.

For completeness, the present experimental results on low-mass nuclei were linked to the previously measured data for medium and heavy-mass nuclei. This is shown in Fig. 4.6 for the corresponding maxima of the ISGQR only. It can be seen from the overview that as the nuclear mass, A, increases the centroid of the ISGQR excitation energy region decreases and the resonance becomes more compact. This can be explained by the spacing of shell-model states which are squeezed together by a factor of approximately $A^{-1/3}$.

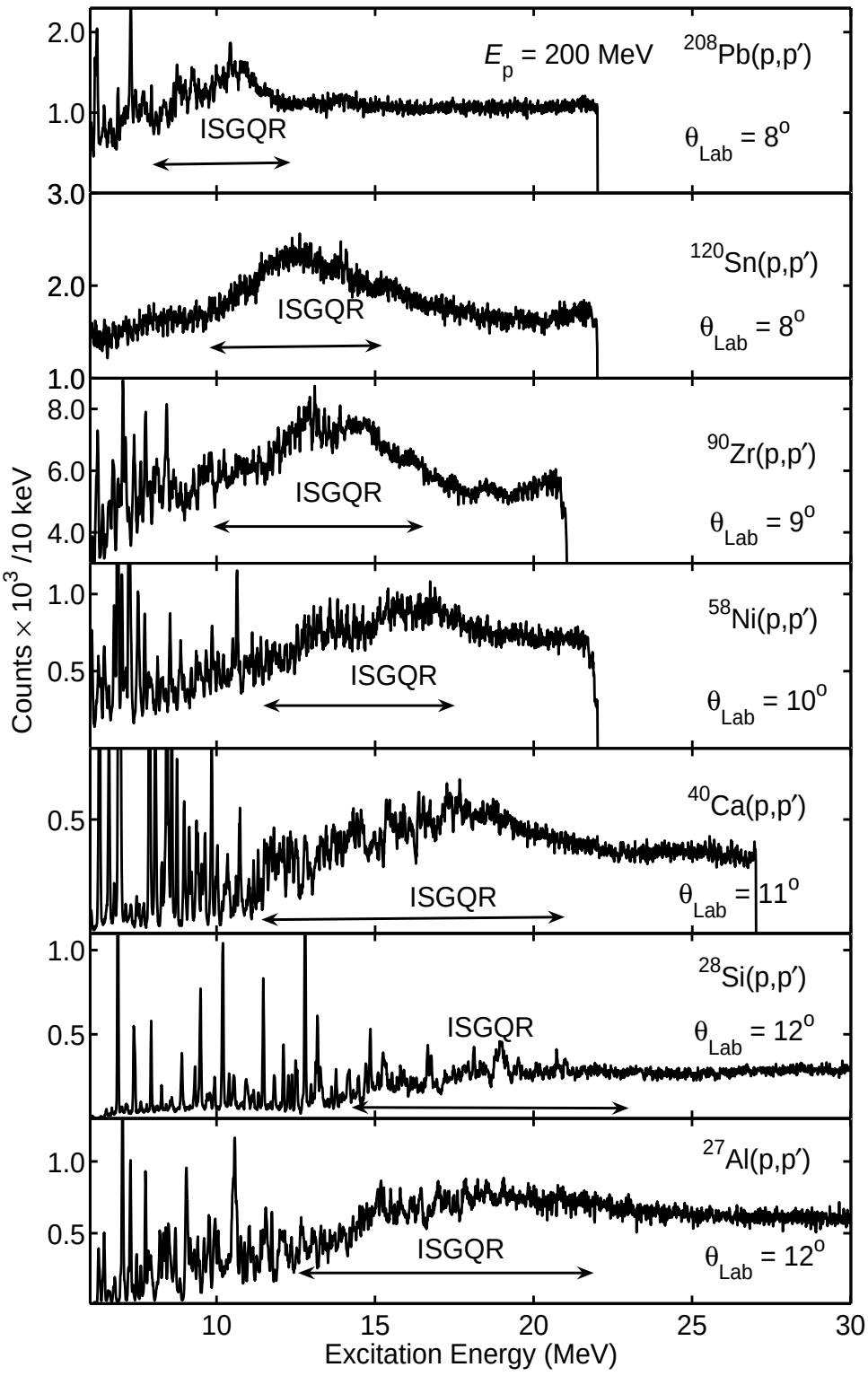

Figure 4.6: Excitation energy spectra for ^{208}Pb, ^{120}Sn, ^{90}Zr, ^{58}Ni, ^{40}Ca, ^{28}Si and ^{27}Al at scattering angles corresponding to the maximum of ISGQR.

In addition, absolute experimental cross-sections were determined for ^{40}Ca at the different scattering angles measured. These were calculated using the double differential cross-section equation (see Sect. 3.8) implementing the experimental parameters. This was done in order to make a direct comparison with the predictions of the quasi-free scattering calculations. For illustration, the ^{40}Ca(p,p′) cross-section measured at $\theta_{\rm Lab} = 11^\circ$ is shown in Fig. 4.7.

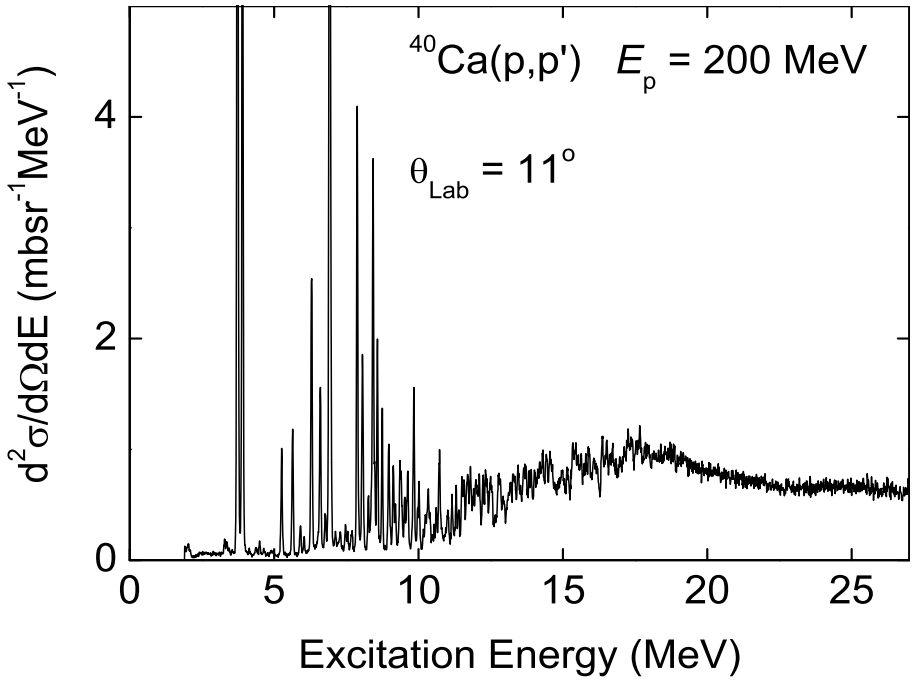

Figure 4.7: Experimental cross-section for ^{40}Ca(p,p′) at $\theta_{\rm Lab} = 11^\circ$ for $E_{\rm p} =$ 200 MeV.

4.3 SRPA $E2$ strength functions for ^{40}Ca and ^{28}Si

In order to compare the experimentally measured excitation energy spectra for ^{40}Ca and ^{28}Si in the region of the ISGQR, $E2$ strength functions were calculated using the SRPA formalism described in Sect. 2.3.1. The SRPA calculations were performed with an effective interaction derived with the Unitary Correlation Operator Method (UCOM) from the correlated Argonne V18 interaction, which is a realistic nucleon-nucleon interaction [Wir95] method described in [Rot05]. The correlated Argonne V18 is softer than (but phase-shift equivalent to) the original "bare" Argonne V18. All $1p$-$1h$ and $2p$-$2h$ states available in the model space were used. The largest model space used in the calculations was such that all single-particle states with orbital angular momentum, L, and node quantum numbers (n = 0, 1,...) up to nMax = 6 for ^{40}Ca and up to 12 for ^{28}Si were included [Pap09, Rot08]. No further energy truncation was imposed. The energy of the highest-lying $2p$-$2h$ 2^+ states used in this model space was around 250 MeV. For example, with nMax = 6 there were one million (more precisely, 1109818) $2p$-$2h$ states and 236 $1p$-$1h$ states included. Of course, only the lowest eigenvalues that are relevant for the description of the giant-resonance region were calculated.

In light nuclei, it is possible to compute giant resonance spectra by fully solving the SRPA equation. This is because the density of $2p$-$2h$ states is reasonably small. Therefore, in these calculations, special attention was paid to the effects of quantum coherence, noting that there is a strong cancelation between particle and hole decay amplitudes in ^{40}Ca and ^{28}Si. Also, in very light nuclei there is a strong asymmetry between hole decay and particle decay due to angular momentum conservation. With increasing mass number this asymmetry is reduced and hence the interference effects grow. Thus, very light nuclei are

dominated strongly by shell effects, such that most of the global arguments derived from bulk matter do not apply very well.

It should be noted that experimental spectra have a finite energy resolution while the SRPA model provides the strength of a number of discrete states. Therefore, in order to make direct comparison between experiment and theory, the calculated SRPA $E2$ strength was smoothed with a Gauss function of FWHM = 38 keV and put into a bin size of 10 keV. The results of this process are presented in Fig. 4.8 for ^{40}Ca. Here it can be seen that the centroid energy is situated around 18 MeV and the strength distribution shows considerable fine structure.

Since RPA is not suitable for ^{28}Si, shell model calculations can be reliably used at the Fermi surface in order to excite $L = 2$ states in the ISGQR region . The shell model is one of the fundamental frameworks for the nuclear many-body problem. In the conventional shell model calculation, the Hamiltonian matrix elements of the effective shell model interaction are calculated by a complete basis set in a given shell model space, and then diagonalised. This was done by determining the ground-state occupation numbers which is used as input in constructing the SPRA [Pap09]. Figure 4.9 presents the results of the SRPA theoretical model prediction for ^{28}Si. It can be seen that the ISGQR contributions are widely spread out and the resonance is highly fragmented.

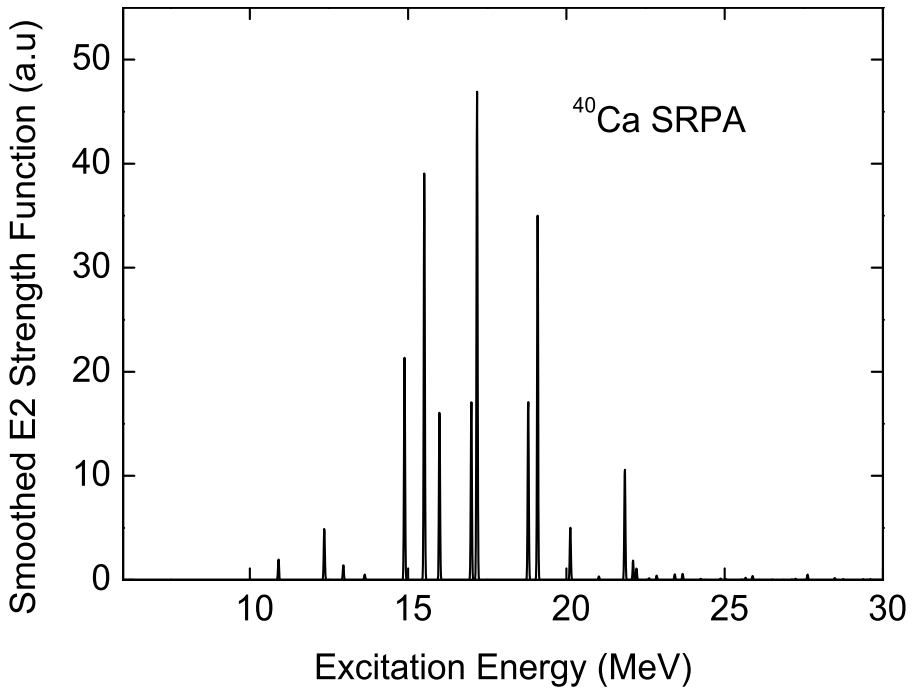

Figure 4.8: SRPA $E2$ strength distribution for ^{40}Ca folded with a FWHM = 38 keV Gauss function in order to make a direct comparison to the experimental data.

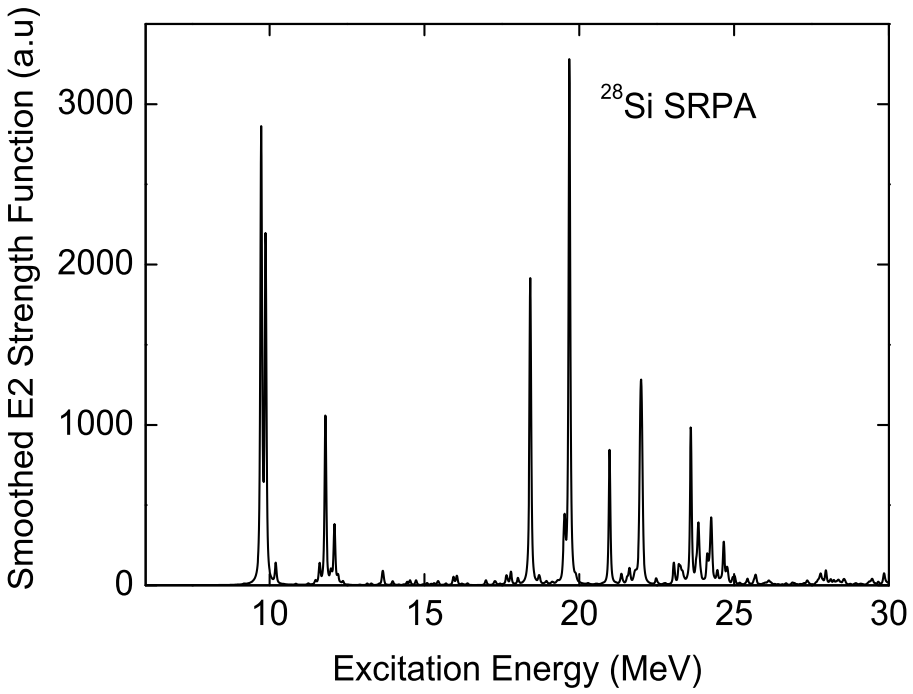

Figure 4.9: SRPA $E2$ strength distribution for ^{28}Si folded with a FWHM = 38 keV Gauss function in order to make a direct comparison to the experimental data.

4.4 Extraction of characteristic energy scales: Experimental and Theoretical results

One of the aims of this study was to extract characteristic energy scales from the excitation energy region of the ISGQR and to compare those scales to the ones obtained from the corresponding theoretical strength functions. In order to quantitatively investigate the observed structures, Fourier transform (see Sect. 2.4.1) and Wavelet analysis techniques (see Sect. 2.4.2) were implemented in the extraction of the energy scales.

4.4.1 Application of Wavelet analysis

Wavelet analysis of the data was accomplished using the Matlab programme [Mat06]. Details of the process have been given in Sect. 2.4.2. The choice of mother wavelet is motivated by the type of spectrum being fitted. In the case of giant nuclear resonances generally pictured as overlapping Lorentzian functions (see Fig. 2.3), a physically more-realistic mother wavelet was constructed as an infinite series of Lorentzian functions of width Γ and spacing 2Γ, localised by a Gaussian envelope (see Fig. 2.6). This is as opposed to the previous more conventional use of a Complex Morlet mother wavelet, being a cosine function localised by a Gaussian envelope (also shown in Fig. 2.6). It should be emphasised that input data preparation is absolutely essential in order to minimize end effects. In this case, the mean of the input data set is subtracted from the data set before applying the wavelet technique.

By way of example, results using both mother wavelets are given in Fig. 4.10 which shows the corresponding coefficient plots as wavelet scale *versus* excitation energy for the much studied ^{208}Pb(p,p$'$) [She04, She08, Lac00]. Note that in both cases the wavelet scale corresponds to the equivalent Fourier scale and that the real part of the complex wavelet coefficients is plotted.

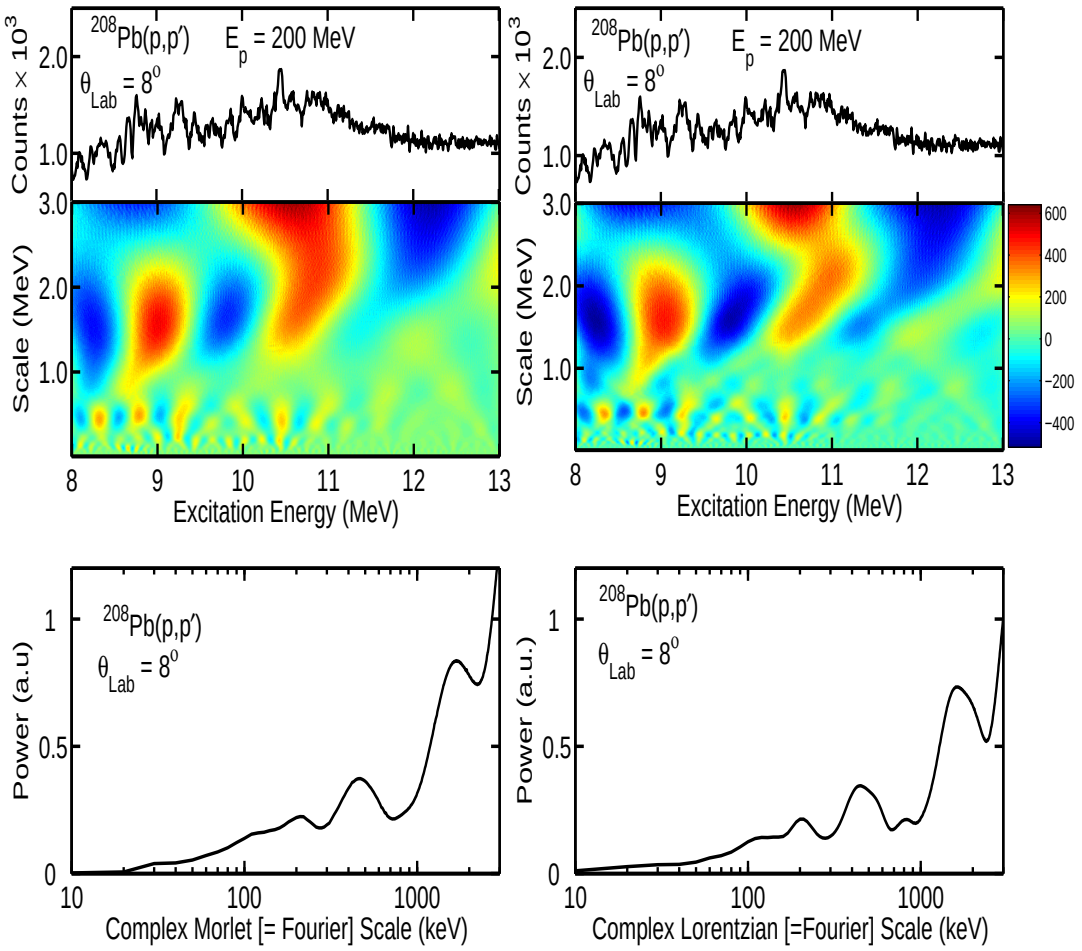

Figure 4.10: Wavelet analysis results for ^{208}Pb using the Complex Morlet mother wavelet (left hand side) and the Complex Lorentzian mother wavelet (right hand side). Note that blue indicates negative values and red positive values.

The corresponding power spectra (cf. Fourier analysis) are obtained from the absolute values of the coefficients summed onto the scale axis and are shown in the bottom part of Fig. 4.10. The width of the Gaussian envelope for the Complex Lorentzian was optimised ($f_{\mathrm{b}} = 2$, see Eq. (2.32)) such that a better localisation on the scale axis was achieved than for the previously Complex Morlet mother wavelet ($f_{\mathrm{b}} = 1$, see Eq. (2.31)) , producing clearer, better defined, wavelet coefficient plots (top right Fig. 4.10). Further, it can be seen from the power spectra that there is a better separation of scales and the

appearance of new weaker scales when using the Complex Lorentzian mother wavelet (bottom right Fig. 4.10).

4.4.2 Experimental energy scales

The Continuous Wavelet Transform (CWT) was applied to the region of each energy spectrum corresponding to the maximum of the ISGQR for the low-mass nuclei studied using the Complex Lorentzian mother wavelet. By plotting the real part of the complex coefficients on a two-dimension plot of scales *versus* excitation energy, the positions of the structures within the original energy spectrum can be identified. This is illustrated in Fig. 4.11 for each of the nuclei studied. The maximum scale was restricted to 5 MeV in order to show the detail in substructures existing at smaller energy scales. On inspection of the coefficient plots obtained from the wavelet analysis presented in Fig. 4.11, specific features at particular scales can be easily visualized.

In order to obtain the corresponding power spectrum for each nucleus the absolute values of the complex coefficients are summed across onto the scale axis. The resulting power spectra are shown as dashed line on the right hand side of Figs. 4.12, 4.13 and 4.14 for ^{40}Ca, ^{28}Si, and ^{27}Al, respectively. Dealing with each target nucleus in turn.

^{40}Ca: The dashed line on the right hand side of Fig. 4.12 corresponds to the power spectra obtained from a Wavelet analysis of the ^{40}Ca data. At θ_{Lab} = 11°, the maximum of the ISGQR, three peaks can be identified below a scale of 1 MeV. Above a scale of 1 MeV also three peaks can be identified at approximately 1 MeV, 2 MeV and 4 MeV which also persist at the other scattering angles. In addition, there are three different smaller scales existing below 1 MeV at θ_{Lab}= 7° which are not present at θ_{Lab} = 11° and θ_{Lab} = 15°. These additional scales might be due to the presence of other multipoles.

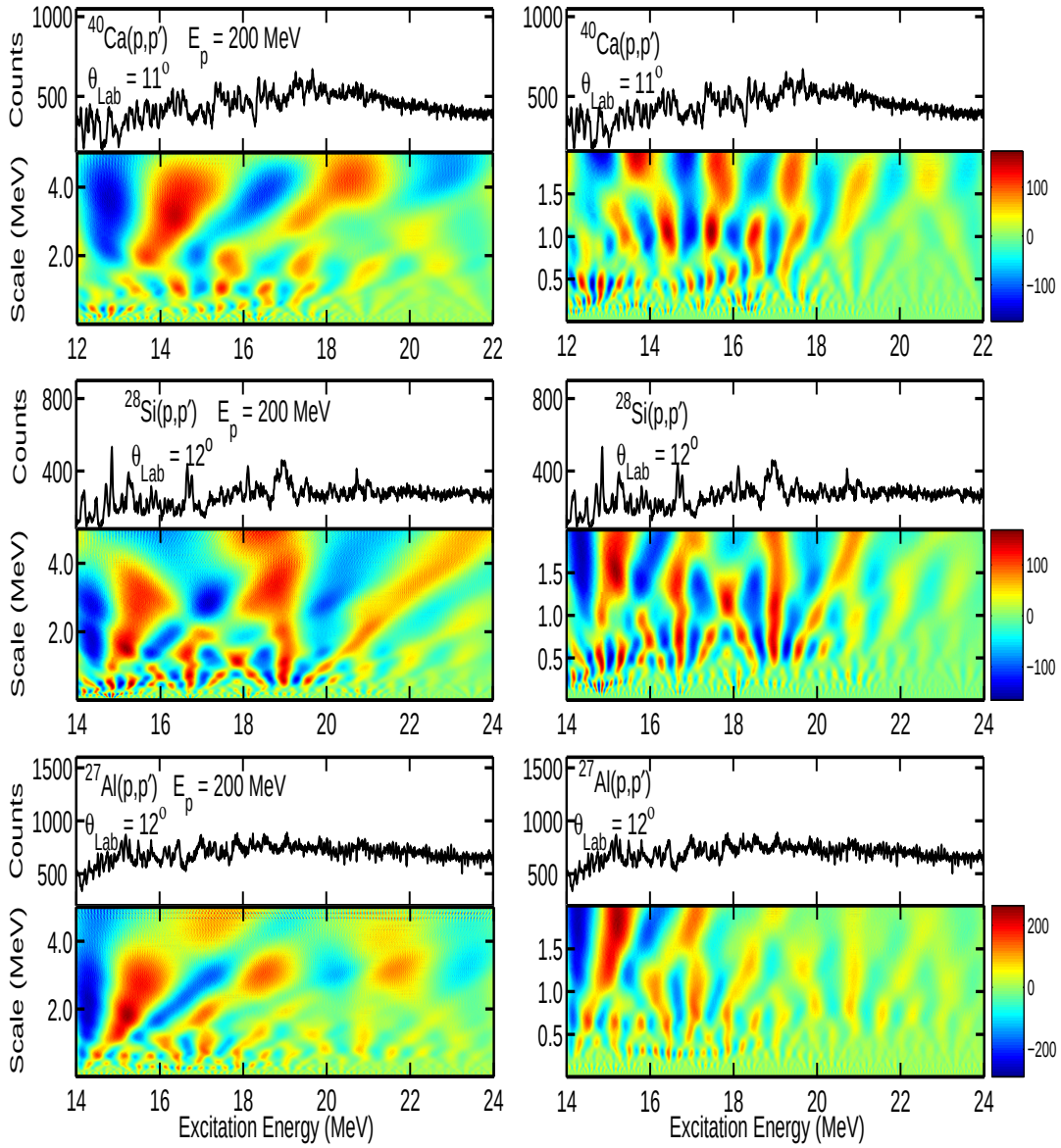

Figure 4.11: Energy spectra for target nuclei ^{40}Ca, ^{28}Si and ^{27}Al shown in the upper part of each diagram for each nucleus at the maximum of the ISGQR. The corresponding real part of the wavelet coefficients determined using the Complex Lorentzian mother wavelet are shown underneath each spectrum. The left hand side shows larger scales while the right hand side shows the presence of smaller intermediate scales below 2 MeV.

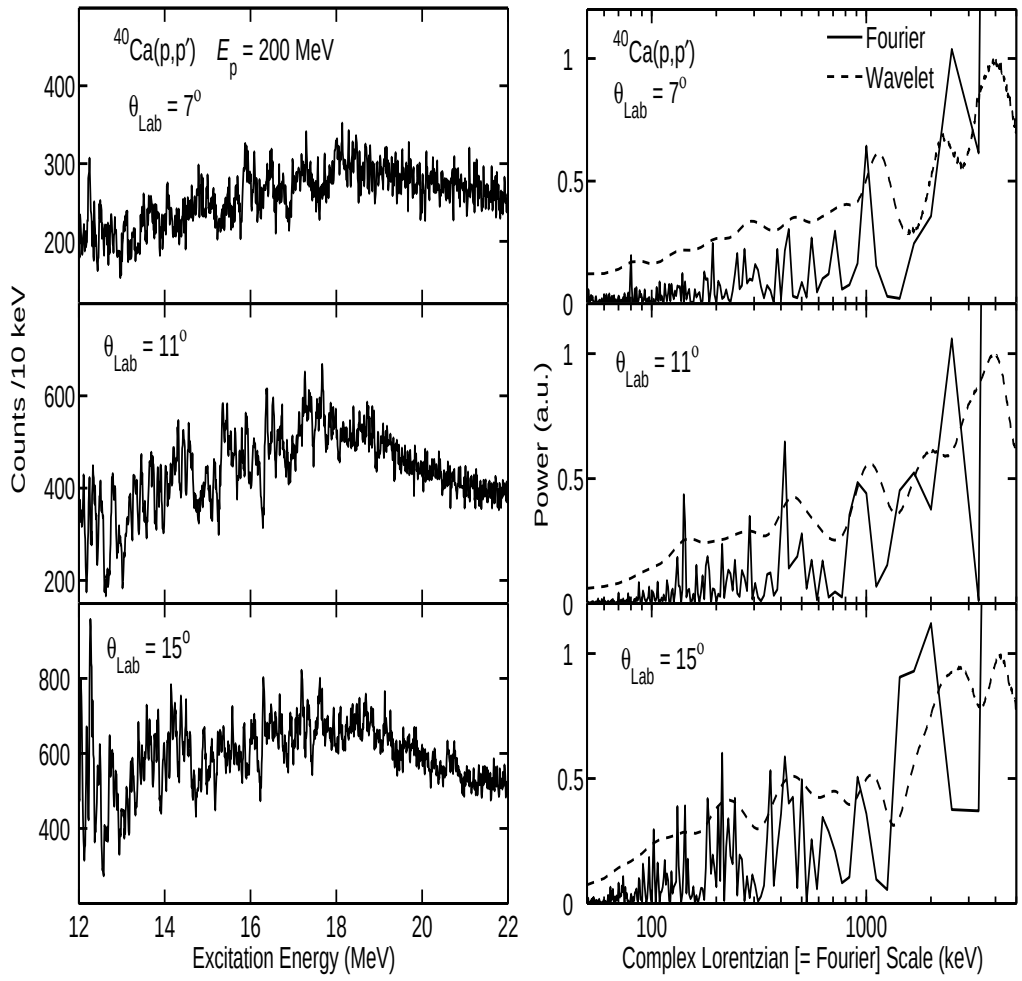

Figure 4.12: Power spectra of ^{40}Ca at different scattering angles, $\theta_{\rm Lab} = 7°$, 11° and 15°. The maximum of the ISGQR corresponds to $\theta_{\rm Lab} = 11°$.

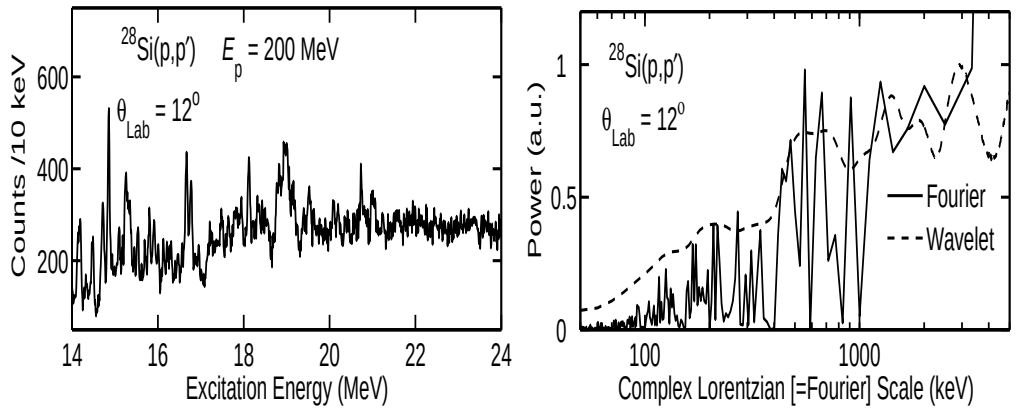

Figure 4.13: Power spectra of ^{28}Si at the scattering angle $\theta_{\rm Lab} = 12^\circ$ for maximum of the ISGQR.

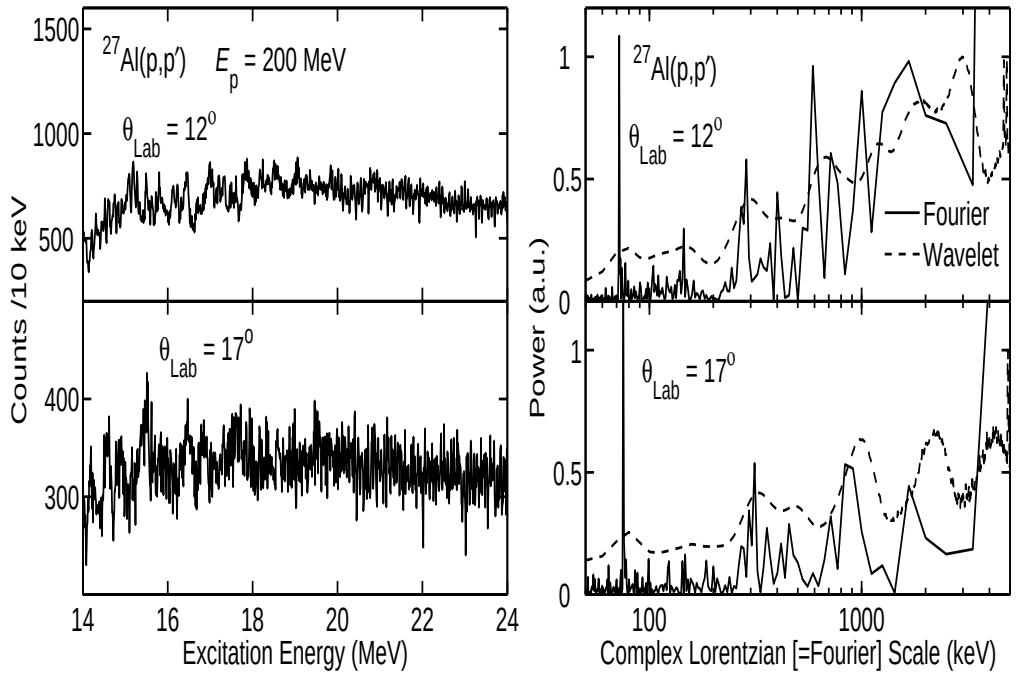

Figure 4.14: Power spectra of ^{27}Al at different scattering angles $\theta_{\rm Lab} = 12^\circ$ and 17°. The maximum of the ISGQR corresponds to $\theta_{\rm Lab} = 12^\circ$.

^{28}Si: The dashed line shown on the right hand side of Fig. 4.13 shows the wavelet power spectrum for ^{28}Si at $\theta_{\rm Lab}$= 12°, the maximum of the ISGQR. Below a scale of 1 MeV several peaks can be identified corresponding to the presence of substructures related to very light nuclei. Above a scale of 1 MeV three peaks can be identified between 1 and 3 MeV.

^{27}Al: The dashed line on the right hand side of Fig. 4.14 shows the power spectra for the ISGQR maximum at $\theta_{\rm Lab}$= 12° and at $\theta_{\rm Lab}$= 17°. Here again several peaks, though somewhat spread out, can be seen below a scale of 1 MeV. Two peaks can be found at a scale between 1 and 3 MeV at the two scattering angles measured.

A global analysis of all available experimental data reveals three classes [She04] of scales: all nuclei studied so far occupy a range, in the present analysis, of $\Delta E < 300$ keV, termed Class I, which includes the experimental energy resolution of the spectrum and reflects the fine structure present in each nucleus; Class II energy scales of range 300 keV $\leq \Delta E \leq$ 1000 keV which are called intermediate scales and vary strongly from nucleus to nucleus; Class III energy scales of range $\Delta E > 1$ MeV which identify the gross structure and total width of the ISGQR.

Following the above classification, the various prominent energy scales seen in the wavelet power spectra shown in Figs. 4.12, 4.13 and 4.14 have been extracted and tabulated in Tables 4.1, 4.2 and 4.3 for ^{40}Ca, ^{28}Si and ^{27}Al, respectively. Here, dominant i.e. prominent wavelet energy-scales are shown in bold. For ease of comparison, such scales are entered vertically down the tables. The various columns of Tables 4.1 to 4.3 contain the values of scales common to both the Complex Morlet and Complex Lorentzian wavelet analysis and link the persistence of that scale to different scattering angles.

Table 4.1: Summary of energy scales extracted for ^{40}Ca (CM = Complex Morlet, CL = Complex Lorentzian). Bold indicates the presence of a clearly identifiable scale.

^{40}Ca Angle	**Scale**	**Class I** $\Delta E < 300$ keV	**Class II** $300 \leq \Delta E \leq 1000$ keV	**Class III** $\Delta E \geq 1000$ keV
$\theta_{\mathrm{Lab}} = \mathbf{7^\circ}$	CM	140 290	490	**1150 2360 3900**
	CL	**80 140 200 290**	**470 800**	**1150 2280 4000**
$\theta_{\mathrm{Lab}} = \mathbf{11^\circ}$	CM	150 270	**460**	**1070 1980 3090**
	CL	**150 290**	**460**	**1050 1950 4000**
$\theta_{\mathrm{Lab}} = \mathbf{15^\circ}$	CM	140 **230**	**470** 720	1080 2570
	CL	**150 230**	**460** 700	**1060 2700 4100**

Table 4.2: Summary of energy scales extracted for ^{28}Si.

^{28}Si Angle	**Scale**	**Class I** $\Delta E < 300$ keV	**Class II** $300 \leq \Delta E \leq 1000$ keV	**Class III** $\Delta E \geq 1000$ keV
$\theta_{\mathrm{Lab}} = \mathbf{12^\circ}$	CM	130 **210**	**600**	1250 3030
	CL	**130 210**	**540 700**	**1410 1900 2940**

Table 4.3: Summary of energy scales extracted for ^{27}Al.

^{27}Al Angle	**Scale**	**Class I** $\Delta E < 300$ keV	**Class II** $300 \leq \Delta E \leq 1000$ keV	**Class III** $\Delta E \geq 1000$ keV
$\theta_{\mathrm{Lab}} = \mathbf{12^\circ}$	CM	**160**	330	**1180** 1860 **3130**
	CL	**80 150**	**300** 420 **670**	**1190 1880 3240**
$\theta_{\mathrm{Lab}} = \mathbf{17^\circ}$	CM	**80** 150	**330** 500	**1020 2300**
	CL	**80 150**	**330 490**	**1010 2280**

Table 4.4: Summary of energy scales extracted for ^{208}Pb, ^{120}Sn, ^{90}Zr and ^{58}Ni at the scattering angle corresponding to the maximum of the ISGQR.

Nucleus Angle	**Scale**	**Class I** $\Delta E < 300$ keV	**Class II** $300 \leq \Delta E \leq 1000$ keV	**Class III** $\Delta E \geq 1000$ keV
^{208}Pb	CM	**110 190**	**500**	**1690**
$\theta_{\mathrm{Lab}} = \mathbf{8^\circ}$	CL	60 **120 210**	**440 830**	**1640**
^{120}Sn	CM	**80 160**	**300** 800	**1300 1830**
$\theta_{\mathrm{Lab}} = \mathbf{8^\circ}$	CL	80 **160**	**310 480**	**1110 1520 2280**
^{90}Zr	CM	**160 270**	**600 900**	**2000**
$\theta_{\mathrm{Lab}} = \mathbf{9^\circ}$	CL	80 **160 260**	**700**	**1170 1820**
^{58}Ni	CM	**200**	**500**	**1340** 2050
$\theta_{\mathrm{Lab}} = \mathbf{10^\circ}$	CL	**140 200 270**	**400** 650 870	**1300 2160**

On revisiting the heavy and medium-mass nuclei, characteristic energy scales were again extracted for ^{208}Pb, ^{120}Sn, ^{90}Zr and ^{58}Ni at the scattering angle corresponding to the maximum of the ISGQR by applying both Complex Morlet and Complex Lorentzian mother wavelets. The results are presented in Table 4.4. It can be seen that additional scales responsible for fine structure can be extracted in the Class I region from the Complex Lorentzian results that were not present when using the Complex Morlet mother wavelet. In addition, also in the intermediate scale, Class II, more scales can be found in this region which are not present in Complex Morlet results. This shows the importance of the new mother wavelet in the extraction of energy scales, even for heavy nuclei.

4.4.3 Application of Fourier transform

In this section the regions corresponding to the maximum of the ISGQR in the measured experimental energy spectra for the light nuclei ^{40}Ca, ^{28}Si, and ^{27}Al are analysed using the Fourier Transform. Energy scales were extracted from the experimental data by applying the Fast Fourier Transform (FFT) of Eq. 2.20 as discussed in Sect. 2.4.1. The standard plot of power versus frequency is called a "periodogram" (see Sect. 2.4.1.2). However, since energy scales are of specific interest in the investigation, power spectra will be shown as power versus 1/frequency, yielding directly a wavelength or energy scale. The resulting periodograms are shown as solid lines on the right hand side of Figs. 4.12, 4.13 and 4.14 for ^{40}Ca, ^{28}Si, and ^{27}Al, respectively.

Details of the various power spectra produced after application of the Fast Fourier transform to the experimental data can now be examined. Dealing with each target nucleus in turn.

^{40}Ca: The resulting periodograms for the ^{40}Ca data taking at scattering angles

of $\theta_{\rm Lab}$= 7°, $\theta_{\rm Lab}$= 11° and $\theta_{\rm Lab}$= 15° are shown as solid lines on the right hand side of Fig. 4.12. At $\theta_{\rm Lab}$ = 11° (middle panel), corresponding to the maximum of the ISGQR, many peaks appear below 1 MeV which might be related to the fragmentation of scales present in light nuclei.

^{28}Si: The periodogram corresponding to ^{28}Si at the maximum of the ISGQR, $\theta_{\rm Lab}$ = 12°, is shown as solid line on the middle right hand side of Fig. 4.13. Here, many significant scales can be identified below 1 MeV reflecting the complexity and fragmentation of the ISGQR observed in the measured data. Scales greater than 1 MeV can be attributed to gross features within the excitation energy window.

^{27}Al: Data taken at the maximum of the ISGQR, $\theta_{\rm Lab}$= 12° and above, $\theta_{\rm Lab}$= 17°, for ^{27}Al have the resulting periodograms shown as solid lines on the right hand sides of Fig. 4.14. Here, various strong scales can be identified below 1 MeV, reaching as low as 70 keV. Also, the gross structure of the data again lies in scales above 1 MeV.

4.4.4 Comparison of experimental and theoretical energy scales using wavelet analysis

For a theoretical interpretation of different classes of scales observed in all the nuclei studied with the application of Wavelet analysis, microscopic calculations within the SRPA were performed for ^{40}Ca and ^{28}Si. The left hand side of Figs. 4.15 and 4.16 shows the outcome of $E2$ strength functions calculated within the SRPA while the right hand sides show their corresponding wavelet power spectra. A comparison of the theory with experimental data and a summary of results is presented in Tables 4.5 and 4.6. Dealing with each target nucleus in turn:

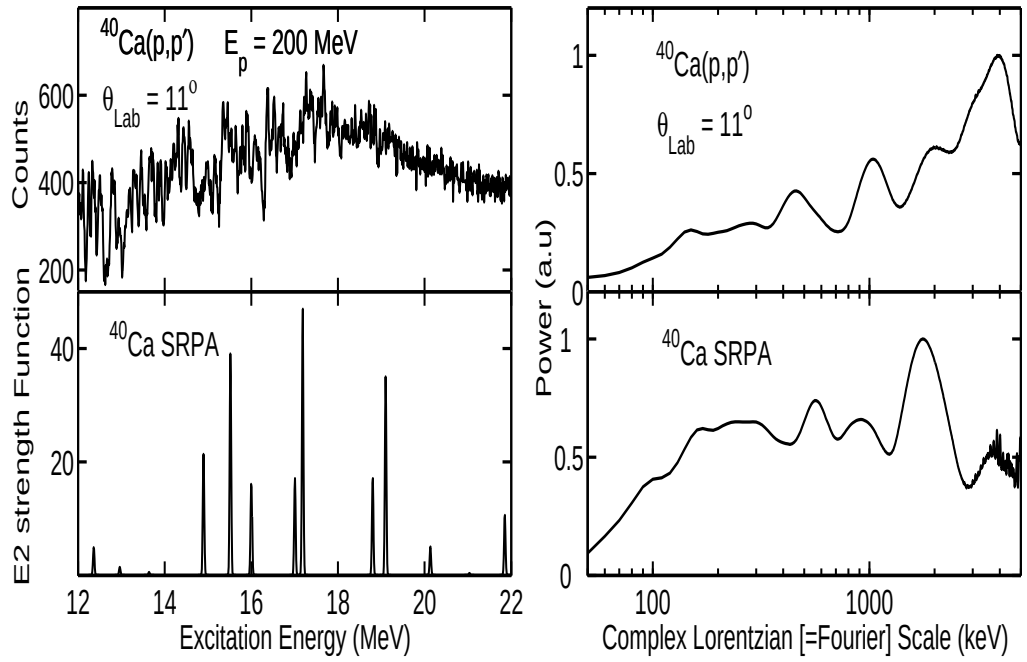

Figure 4.15: Power spectra of ^{40}Ca at $\theta_{\rm Lab} = 11^\circ$ scattering angle and the SRPA theoretical prediction.

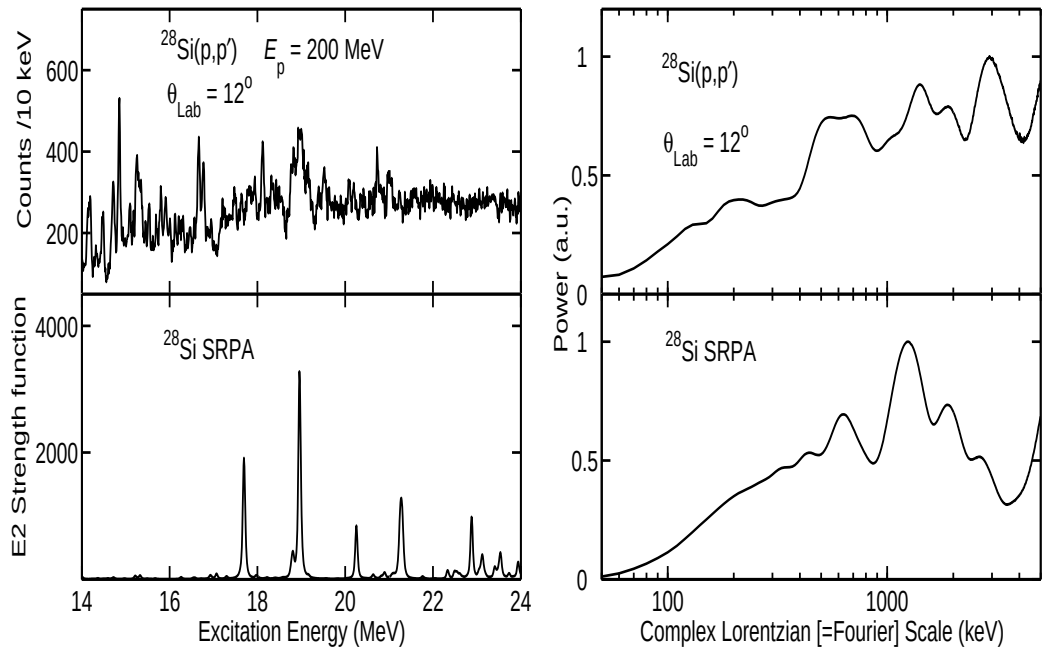

Figure 4.16: Power spectra of ^{28}Si at$\theta_{\rm Lab} = 12^\circ$ scattering angle and the SRPA theoretical prediction.

Table 4.5: Summary of energy scales observed for ^{40}Ca in comparison with microscopic SRPA calculations. Bold indicates the presence of a a clearly identifiable scale and columns indicate correspondence between scales (CL = Complex Lorentzian).

^{40}Ca	**Scale**	**Class I** $\Delta E < 300$ keV	**Class II** $300 \leq \Delta E \leq 1000$ keV	**Class III** $\Delta E \geq 1000$ keV
Expt	CL	**150 290**	**460 1050**	**1950 4000**
SRPA	CL	**100 170** 290	**560 910**	**1770 4000**

Table 4.6: Summary of energy scales observed for ^{28}Si in comparison with microscopic SRPA calculations. Bold indicates the presence of a a clearly identifiable scale and columns indicate correspondence between scales (CL = Complex Lorentzian).

^{28}Si	**Scale**	**Class I** $\Delta E < 300$ keV	**Class II** $300 \leq \Delta E \leq 1000$ keV	**Class III** $\Delta E \geq 1000$ keV
Expt	CL	**130 210**	**540 700**	**1410 1900 2940**
SRPA	CL		330 **440 630**	**1240 1890 2670**

^{40}Ca: Wavelet power spectra are shown on the right hand side of Fig. 4.15 for ^{40}Ca for the maximum of the ISGQR at $\theta_{\text{Lab}} = 11^\circ$ and the SRPA predictions. Extracted energy scales are presented in Table 4.5. A broad distribution of wavelet power can be seen for the experimental and SRPA but with the aid of the corresponding wavelet coefficient plots (see Fig. 4.11) energy scales can be more easily extracted. A Class I scale at approximately 150 and 290 keV can be identified in the experimental data which persist in the SRPA. An important Class II scale at approximately 500 keV can be identified in the experimental data and SRPA with the indication of another scale at approximately 900 keV in the SRPA. Large scale Class III structure can again be identified at approximately 2 MeV.

^{28}Si: The corresponding power spectra for ^{28}Si measured at the maximum of the ISGQR $\theta_{\text{Lab}} = 12^\circ$ and for the SRPA predictions are shown on the right hand side of Fig. 4.16. Extracted energy scales are presented in Table 4.6. Below 300 keV no specific feature can be observed in the

SRPA prediction but these scales can be extracted with the aid of the corresponding wavelet coefficient plots (see Fig. 4.11) for the experimental data. This shows that the substructures found in the experimental data can not be revealed by the SRPA predictions. Class II scales can be identified at approximately 300 and 700 keV and show a correspondence between the experiment and the SRPA. Large scale Class III structure is seen at approximately 1 MeV and 2 MeV in the experimental data with some correspondence seen in the SRPA predictions.

4.5 Continuous Wavelet Transform spectrum reconstruction

One of the basic problems which has to be solved for a full understanding of giant resonances is the origin of width. It is instructive, therefore, to perform reconstruction of the original experimentally-measured excitation energy spectrum in the region of ISGQR allowing more insight to be gained as to the nature of the different energy scales. The largest scales of Class III represent the overall width of the ISGQR while Classes II and I bring out specific finer details associated with the fragmentation and damping mechanisms of the ISGQR. Typical, though, in the case of Wavelet analysis the Discrete Wavelet Transform (DWT) has been used which allows an exact reconstruction, as does the Inverse Fourier Transform. The drawback here is that reconstruction for the DWT is constrained to powers of two within the energy scales. As an alternative, spectrum reconstruction has been developed from the Continuous Wavelet Transform (CWT), thus allowing a much greater flexibility to include only specific scales.

Specific features in the original excitation energy spectrum can be identified by inspection of the wavelet coefficients plot of energy scale *versus* excitation en-

ergy. Here, a red area corresponds to large positive coefficients and a blue area to large negative, indicating the position of a peak maximum and peak minimum, respectively. Reconstruction of a spectrum component can be achieved by summing the coefficients belonging to a certain energy scale down to the excitation energy axis. The resulting oscillatory structure around zero is then scaled back to the measured spectrum. In order to illustrate the procedure and by way of example this was done for the case of ^{40}Ca. Figure 4.17 shows the reconstruction for the largest scale in Class III at about 7 MeV. The range of summation of coefficients is indicated in the bottom part of Fig. 4.17 with the resulting sum of coefficients shown in the middle part of Fig. 4.17.

After scaling the summed coefficients up to the experimental spectrum a broad, single peak, shown by the black line is plotted over the original spectrum, blue line, in the top part of Fig. 4.17. The procedure is repeated for the successively smaller scales identified (see Table 4.1) in Figs. 4.18, 4.19, 4.20, 4.21 and 4.22, each time adding to all previously summed coefficients before scaling to the measured spectrum. Figure 4.22 shows the reconstruction for the smallest scale in Class I at 150 keV. Thus, by Fig. 4.22 a almost complete spectrum reconstruction is achieved using all of the coefficients indicated.

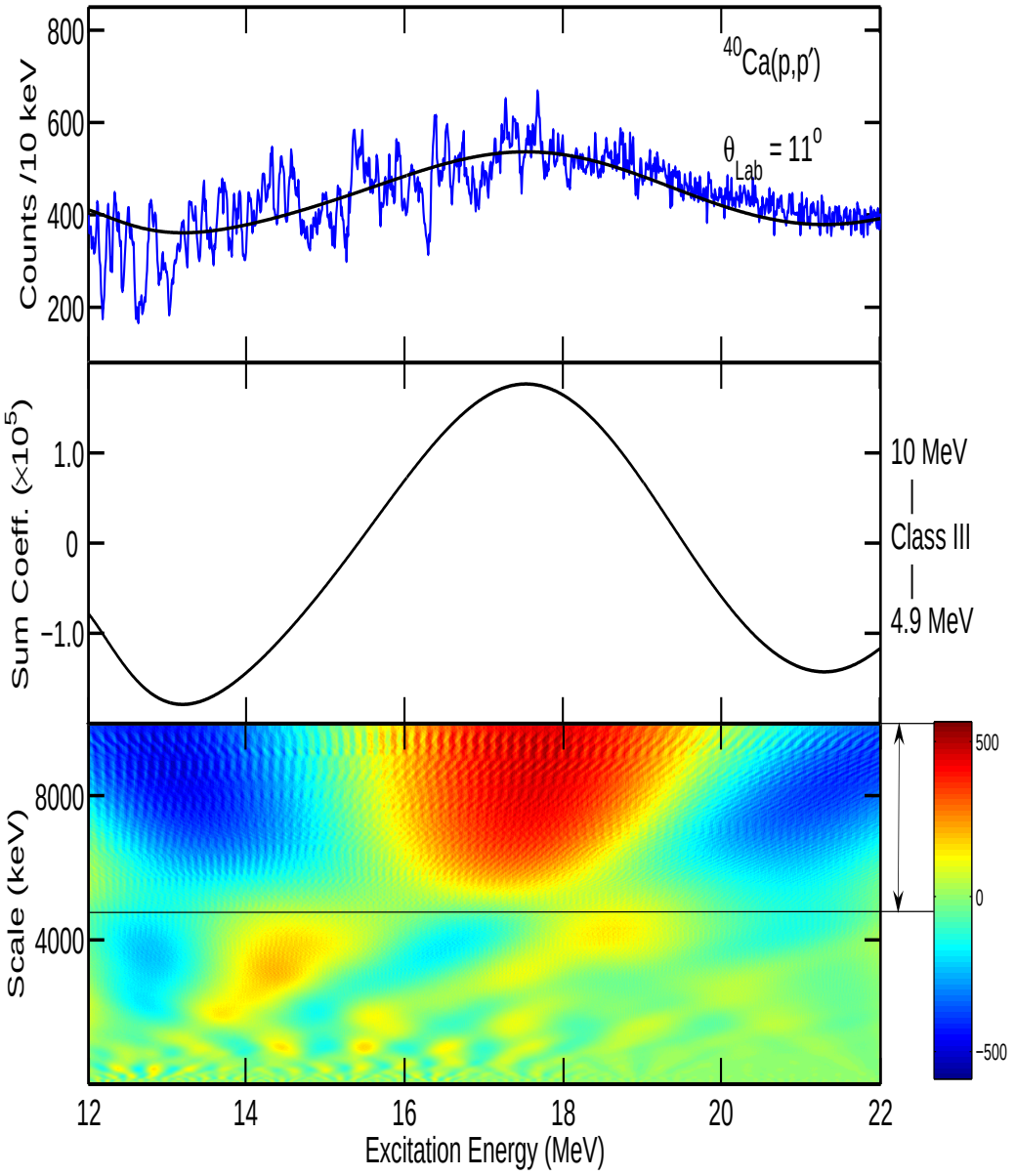

Figure 4.17: *Upper*: Class III energy scale showing the reconstruction of ^{40}Ca at $\theta_{\rm Lab} = 11^{\circ}$ indicated with a black line; *Middle*: Sum of the real coefficients between the limits shown in the coefficients plot; *Lower*: The region of largest energy scale between 4.9 MeV and 10 MeV indicated on the plot of real coefficients produced using the Complex Lorentzian mother wavelet.

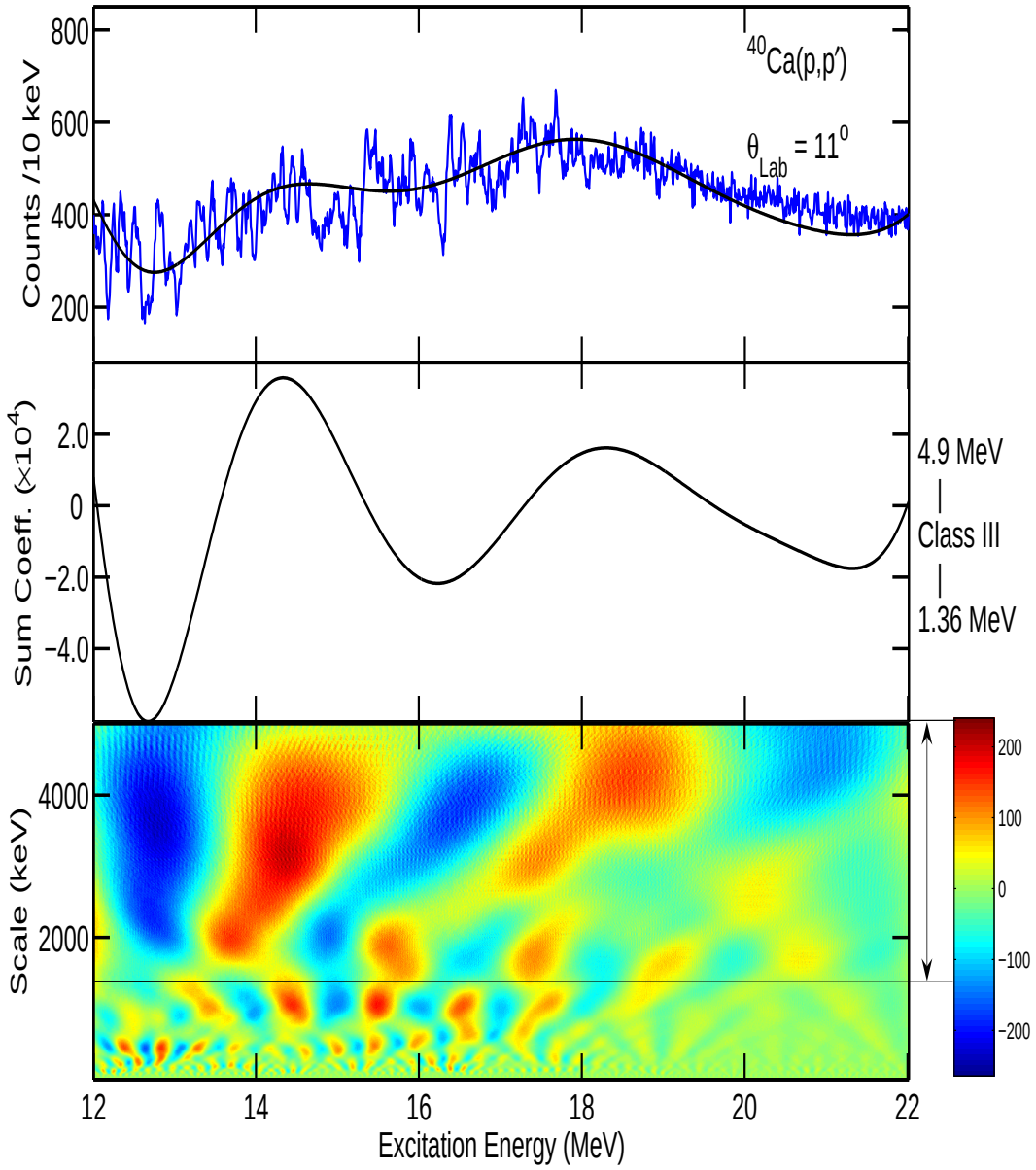

Figure 4.18: *Upper*: Class III energy scale showing the reconstruction of ^{40}Ca at $\theta_{\rm Lab} = 11^\circ$ after adding the summed coefficients of Fig. 4.17 indicated with a black line; *Middle*: Sum of the real coefficients between the limits shown in the coefficient plot; *Lower*:The region of second largest energy scale between 1.36 MeV and 4.9 MeV indicated on the plot of real coefficients produced using the Complex Lorentzian mother wavelet.

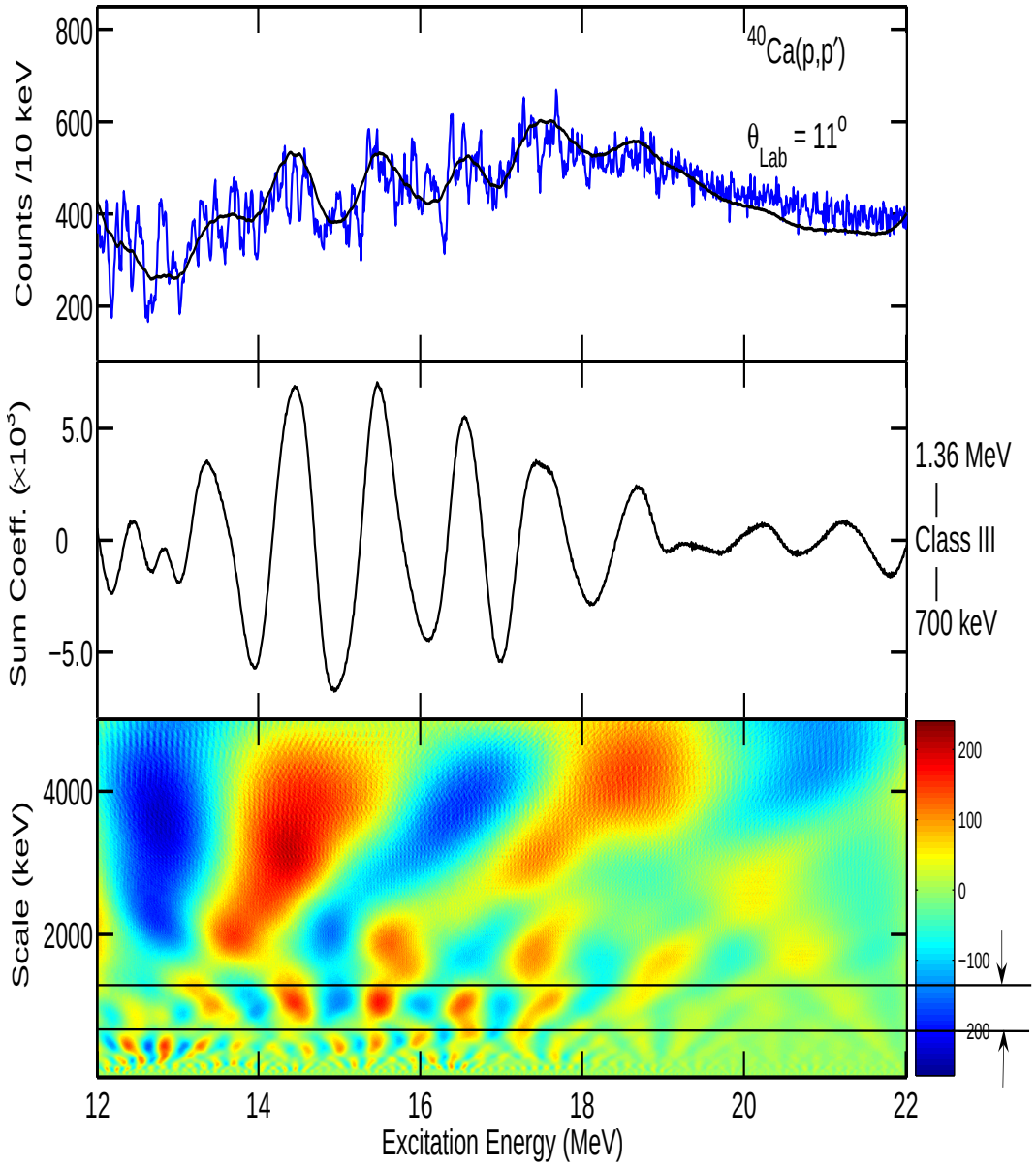

Figure 4.19: *Upper*: Class III energy scale showing the reconstruction of ^{40}Ca at $\theta_{\rm Lab} = 11^{\circ}$ after adding the summed coefficients of Figs. 4.17 and 4.18 indicated with a black line; *Middle*: Sum of the real coefficients between the limits shown in the coefficient plot; *Lower*:The region of second largest energy scale between 700 keV and 1.36 MeV indicated on the plot of real coefficients produced using the Complex Lorentzian mother wavelet.

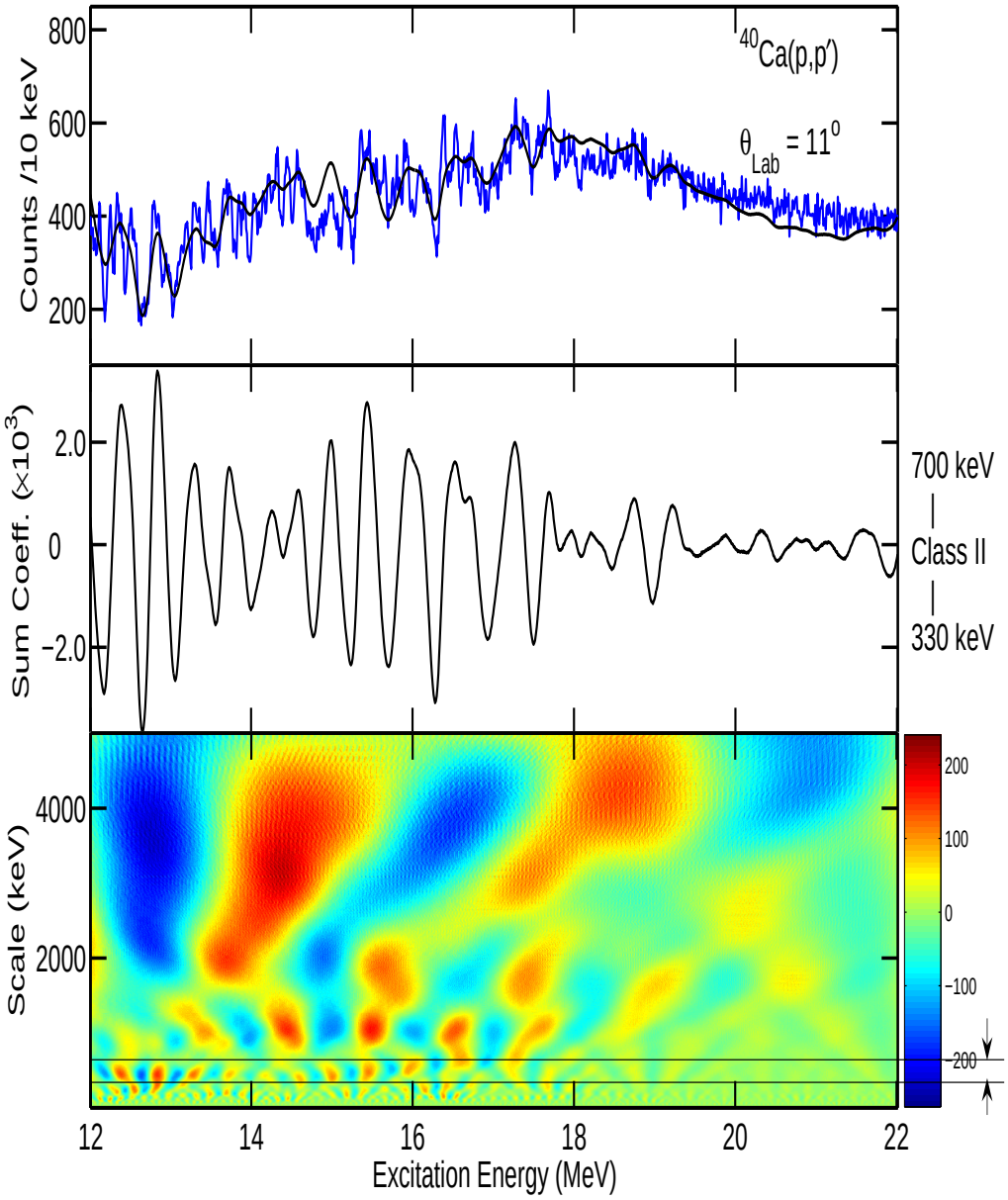

Figure 4.20: *Upper*: Class II energy scale showing the reconstruction of ^{40}Ca at $\theta_{\rm Lab} = 11^{\circ}$ after adding the summed coefficients of Fig. 4.17 and Fig. 4.18 indicated with a black line, *Middle*: Sum of the real coefficients between the limits shown in the plot; *Lower*: The region of medium energy scale between 330 kev and 700 keV indicated on the plot of real coefficients produced using the Complex Lorentzian mother wavelet.

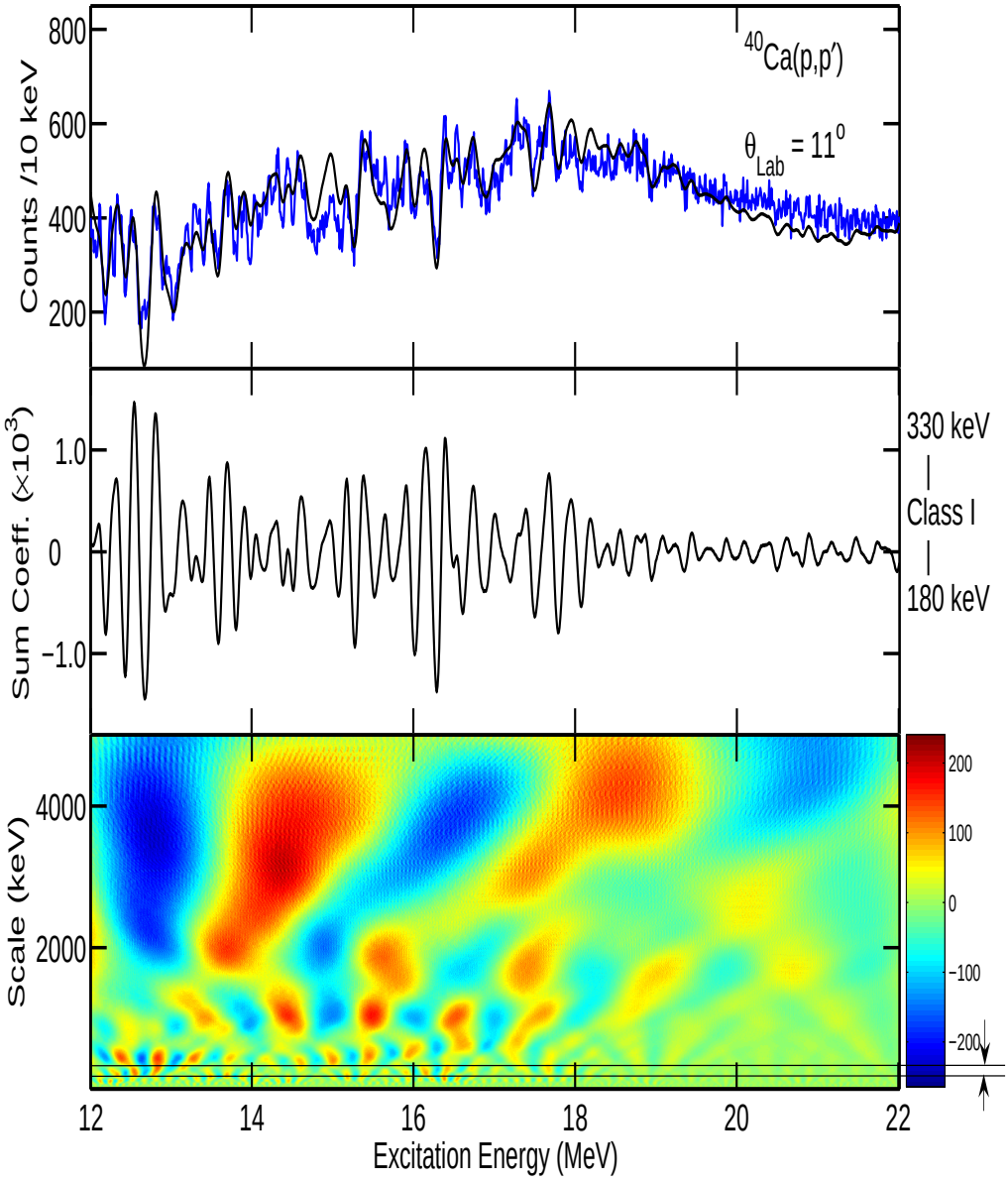

Figure 4.21: *Upper*: Class I energy scale showing the reconstruction of ^{40}Ca at $\theta_{\rm Lab} = 11^{\circ}$ after adding the summed Class II coefficients of Fig. 4.20 and the summed Class III coefficients of Fig. 4.17 and Fig. 4.18 indicated with a black line; *Middle*: Sum of the real coefficients between the limits shown in the plot; *Lower*: The region of small energy scale between 180 keV and 330 keV indicated on the plot of real coefficients produced using the Complex Lorentzian mother wavelet.

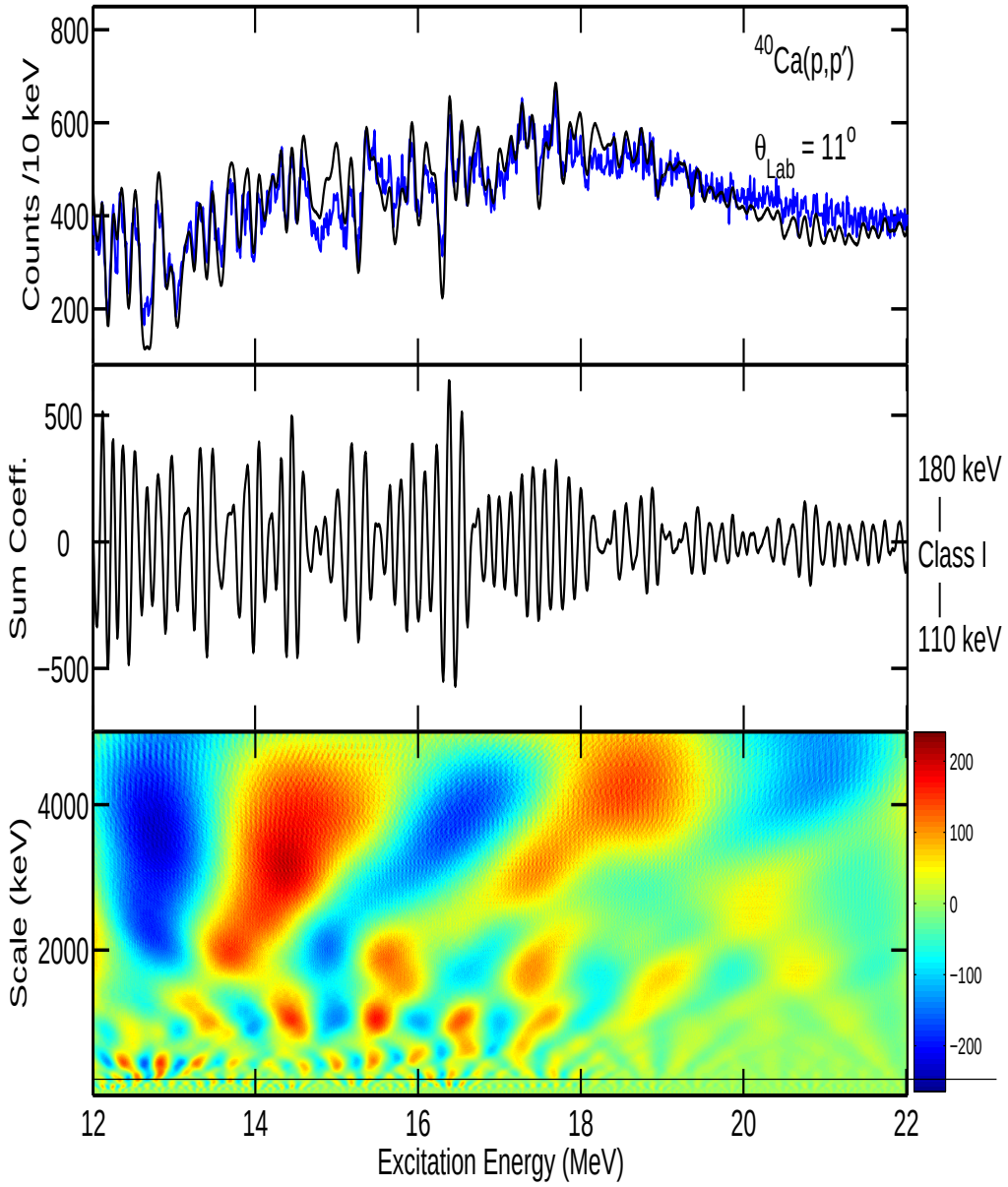

Figure 4.22: *Upper*: Class I energy scale showing the reconstruction of ^{40}Ca at $\theta_{\rm Lab} = 11°$ after adding the summed coefficients of Fig. 4.21, Class II coefficients of Fig. 4.20 and the summed Class III coefficients of Fig. 4.17 and Fig. 4.18 indicated with a black line; *Middle*: Sum of the real coefficients between the limits shown in the plot; *Lower*: The region of small energy scale between 110 keV and 180 keV indicated on the plot of real coefficients produced using the Complex Lorentzian mother wavelet.

4.5.1 Discussion of spectrum reconstruction results

Spectrum reconstruction allows further insight to be gained as to the importance of the various energy scales identified. Here it should be noted that because of the nature of the Complex Lorentzian mother wavelet used and the properties of the Lorentzian function, a wavelet scale identified yields a Lorentzian function feature in the energy spectrum with a FWHM equivalent to half of the value of the wavelet scale extracted (see Sect. 2.4.2.2). Dealing with each class of energy scale in turn.

Class III: The Class III energy scales are associated with the gross structure of the ISGQR and for ^{40}Ca span a range of approximately 1.0 MeV to 10.0 MeV as shown in Figs. 4.17, 4.18 and 4.19. Here, for the largest scale of 7 MeV with a range of CWT coefficients spanning 4.9 to 10.0 MeV (see bottom part of Fig. 4.17) the resulting single peak average through the experimental spectrum is shown in the top part of Fig. 4.17, displaying a width (FWHM) of the ISGQR in ^{40}Ca of approximately 4.5 MeV. A second smaller scale associated with Class III is identified in the bottom part of Fig. 4.18 with a range of 1.36 MeV to 4.9 MeV (see Table 4.1). This yields two smaller width peaks (each approximately 2.0 MeV wide) centred at an excitation energies of 14 and 18 MeV (see middle part of Fig. 4.18) and the smallest scale in Class III is shown in the bottom part of Fig. 4.19). When combined with the largest scale of Fig. 4.17 a good representation of the average structure of the experimental spectrum is seen in the top part of Fig. 4.19.

Class II: The intermediate energy scale known as Class II is presented in the bottom part of Fig. 4.20 within a range of 330 - 700 keV and it is centred at about 500 keV (see Table 4.1). This energy scale produces smaller width peaks each approximately 350 keV wide (see middle part of Fig. 4.20).

Class I: The same procedures apply to the Class I energy scales which are associated with the experimental energy resolution of the spectrum. This is illustrated in the bottom part of Figs. 4.21 and 4.22 within a range of 180 - 330 keV, centred at 290 keV and a range of 110 - 180 keV, centred at 150 keV (see Table 4.1). This yields a number of peaks of narrow width (see middle part of Figs. 4.21 and 4.22). When combined with the summed of Class III and Class II coefficients of Fig. 4.20 full reconstruction can be identified as shown in the top part of Fig. 4.22 with the black solid line.

In general, one can see that the use of CWT method of reconstruction allows a specific scale to be identified and the corresponding energy width and position in the excitation energy spectrum to be determined.

4.6 Application of Semblance analysis

Semblance analysis is a technique to determine the degree of correlation (both positive and negative) between two data sets [Coo08] which in the present case is a function of both energy scale and excitation energy. This approach uses information on the phase angles of the wavelet coefficients found, for example, for an experimental and corresponding theoretical data set and thus determines their level of correlation (see Section 2.4.2.3). The semblance can take on values between -1 and $+1$. A value of $+1$ implies perfect correlation, 0 implies no correlation, and -1 implies perfect anticorrelation. However, the disadvantage of lack of amplitude information lead to the further use of the Dot product. A Dot product is equivalent to the vector Dot product of the complex wavelet coefficients at each point in scale and excitation energy. This was considered a better option because it combines the phase information of Semblance with the amplitude information of the CWT coefficients in order to emphasise the larger amplitude components of the data sets. It also enables the

changing phase relationships of the two data sets to be visualised depending upon the importance of the feature (value of the coefficient). The results of the application of both Semblance and Dot product to various experimental and theoretical data sets are presented in Sect. 4.6.1, 4.6.2 and 4.6.3.

4.6.1 Comparison of ^{40}Ca and ^{28}Si experimental data with $E2$ strength predictions

Semblance and Dot product analysis were applied to the experimental data and the corresponding SRPA theoretical predictions for ^{40}Ca and ^{28}Si. The resulting two-dimensional spectra are shown at the bottom of Figs. 4.23 and 4.24 for ^{40}Ca and ^{28}Si, respectively. The quantitative correspondence between the experimental data and theoretical predictions can be observed in these plots. In ^{40}Ca, there exists a positive correlation of a broad red band in both the Semblance and Dot product results which span across the entire excitation energy range at energy scales between 1.4 and 2 MeV. In addition, there is a positive correlation for scales around 500 and 900 keV running through the excitation energy range between 14 and 18 MeV. The Dot product at the bottom of Fig. 4.23 emphasises those regions where both the experimental data and theoretical prediction has significant strength. It can also be seen to isolate significant regions of positive correlations better than the semblance results. There are, however, regions of poor or even negative correlation indicating the presence of other components e.g. different multipoles in the experimental data.

For the ^{28}Si Semblance and Dot product results of Fig. 4.24, the red area running through the excitation energy between 16 and 22 MeV corresponding to different wavelet scales between 1 and 3 MeV. The region of negative correlation, blue area, can be observed in particular for scales below 500 keV, which indicates the absence of small substructures in the SRPA predictions.

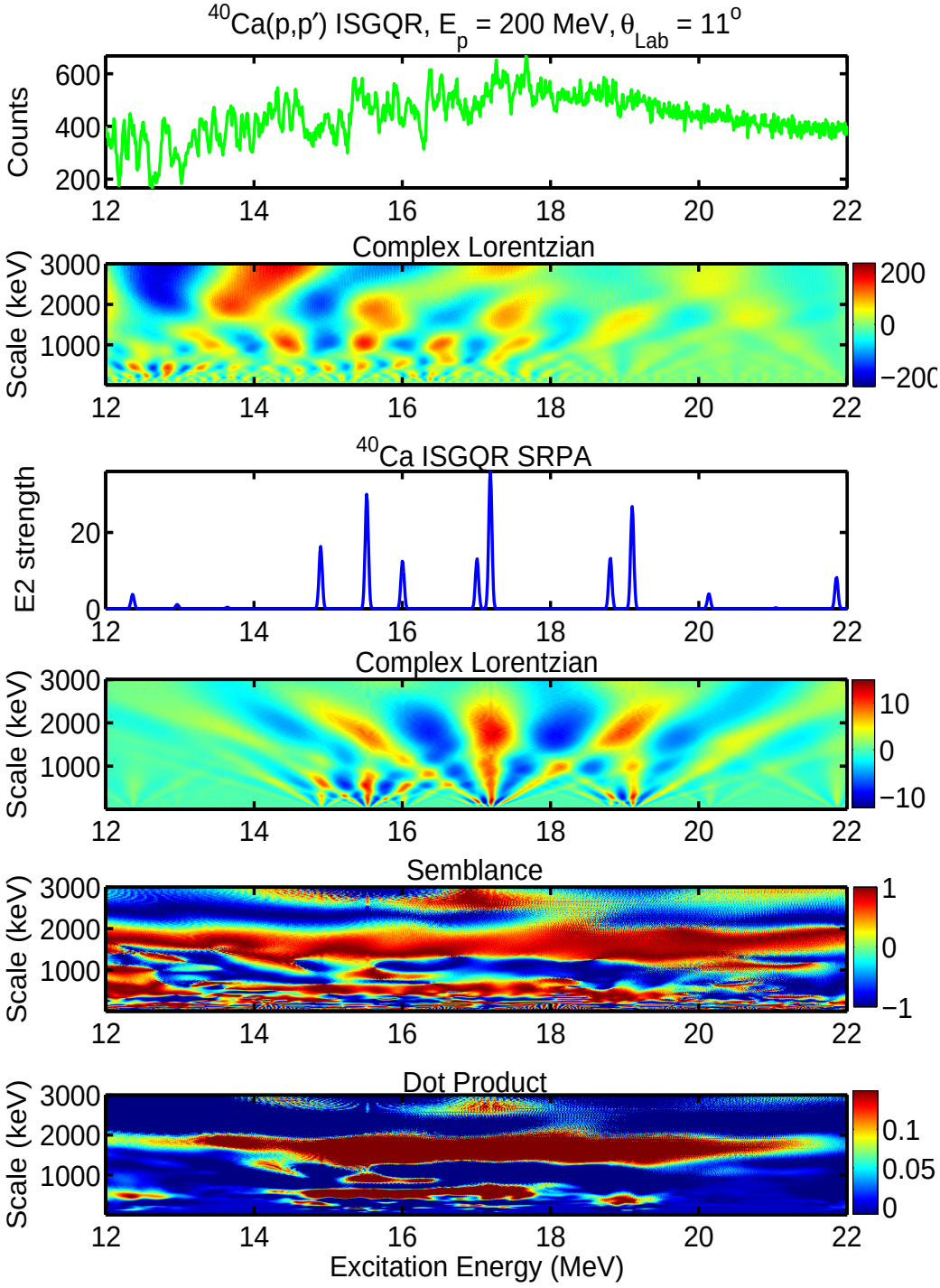

Figure 4.23: Energy spectra of ^{40}Ca at 11° scattering angle (green line) and the theoretical predictions of SRPA (blue line) showing the extracted energy scales by applying the Complex Lorentzian mother wavelet. The bottom two parts represent the Semblance and Dot product analysis for a quantitative correspondence between the experimental data and the theoretical predictions.

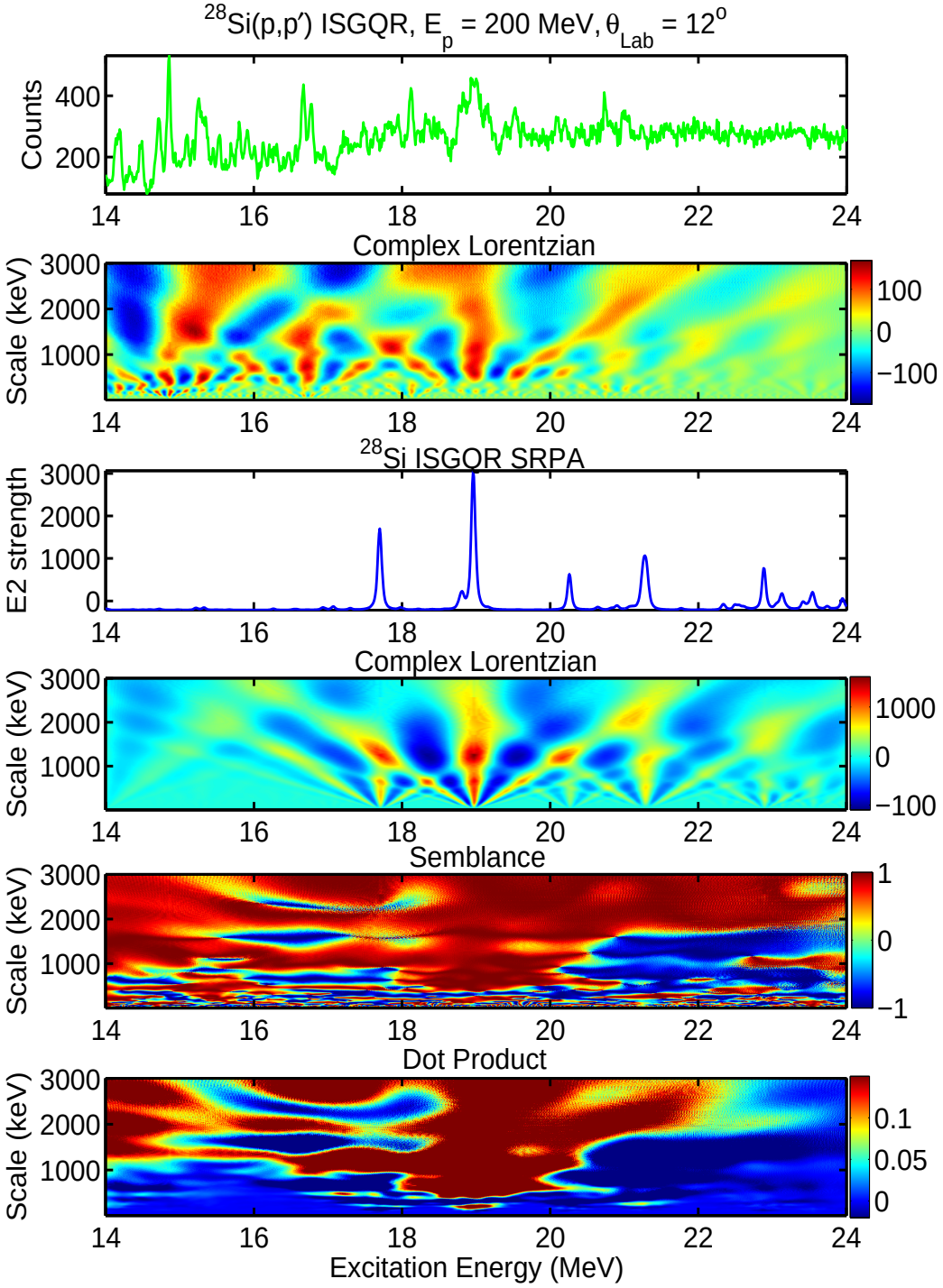

Figure 4.24: Energy spectra of ^{28}Si at 12° scattering angle (green line) and the theoretical predictions of SRPA (blue line) showing the extracted energy scales by applying the Complex Lorentzian mother wavelet. The bottom two parts represent the Semblance and Dot product analysis for a quantitative correspondence between the experimental data and the theoretical predictions.

4.6.2 Fragmentation of E2 strength in ^{28}Si

Strong, weak and electromagnetic interaction processes play an essential role in many different applications of nuclear physics. In this section, different probes with different selectivities are compared with (p,p$'$) data so as to understand the nature of the intermediate structures. In order to tackle the problem of structure and strength of giant resonances various experimental methods are needed. By putting the results from experiments using electromagnetic probes in which the exchange of virtual photons leads to negative parity, for example (e,e$'$), together with those from strongly interacting probes like (p,p$'$) and (α, α') into a common perspective, deep insight could be gained in their electric transitions and structures. Also, by considering the weakly interacting probes like (p,γ) and (α, γ), some information about the magnetic transitions could be ascertained. For example, a comparison between the spectra from the (e,e$'$) and (p,p$'$) reactions often give a qualitative hint on the nuclear structure aspect of the transition due to the fact that under the kinematic conditions of the (p,p$'$) experiment, the cross section is dominated by the spin-isospin dependent term in the effective interaction. A quantitative comparison between the results of different probes can be made with the use of Semblance and Dot product analysis to reveal the extent of similarity, or not, between measured excitation energy spectra.

In the case of *sd*-shell nuclei $A \leq 32$, extensive experimental investigations have been made of the fragmentation of the isoscalar giant quadrupole resonance. In particular, ^{28}Si has been particularly well studied. Resulting energy spectra are shown in Fig. 4.25 for the excitation of ^{28}Si using various different probes with the corresponding Semblance analysis results presented in Figs. 4.26, 4.27, 4.28 and 4.29.

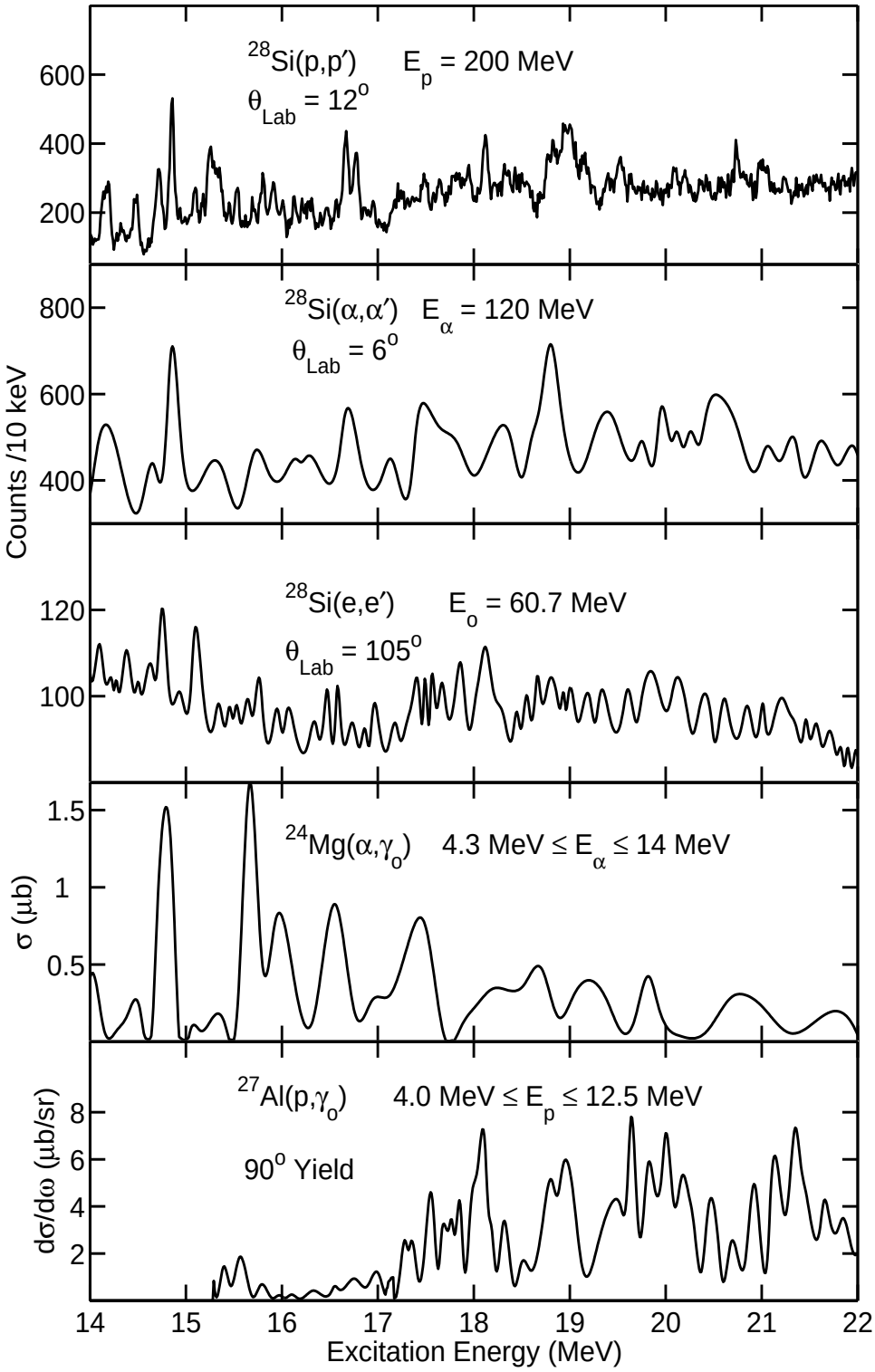

Figure 4.25: Excitation energy spectra for ^{28}Si ISGQR excited using different probes. ^{28}Si(p,p′) present data, ^{28}Si(α, α') [Bor81], ^{28}Si(e,e′) [Fri81], ^{24}Mg(α, γ_o) [Kuh83] and ^{27}Al(p,γ_o) [Sin65].

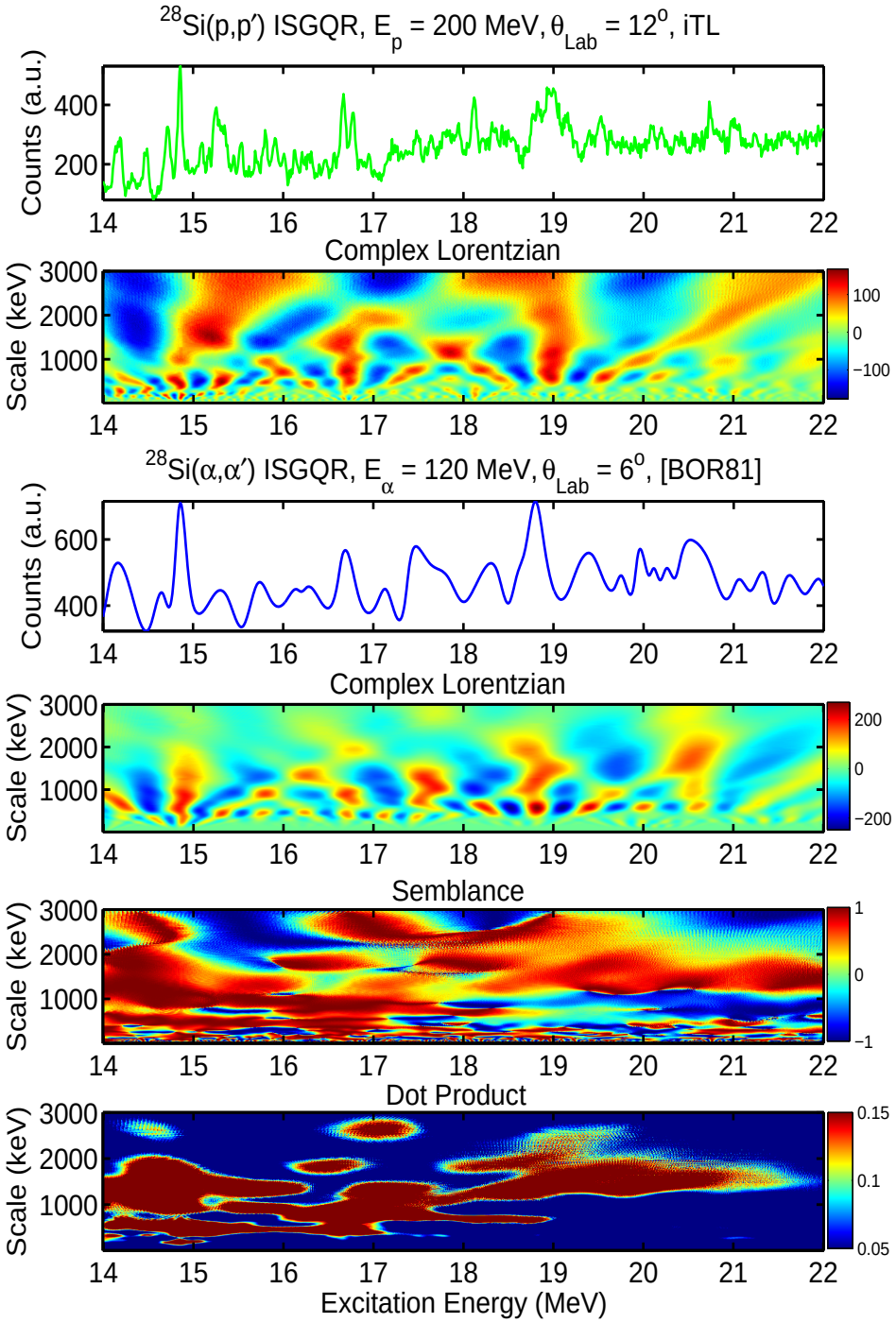

Figure 4.26: Semblance and Dot product results for ^{28}Si(p,p′) (present data) and ^{28}Si(α, α') from [Bor81] for comparison of the ISGQR scales emerging from different selectivities.

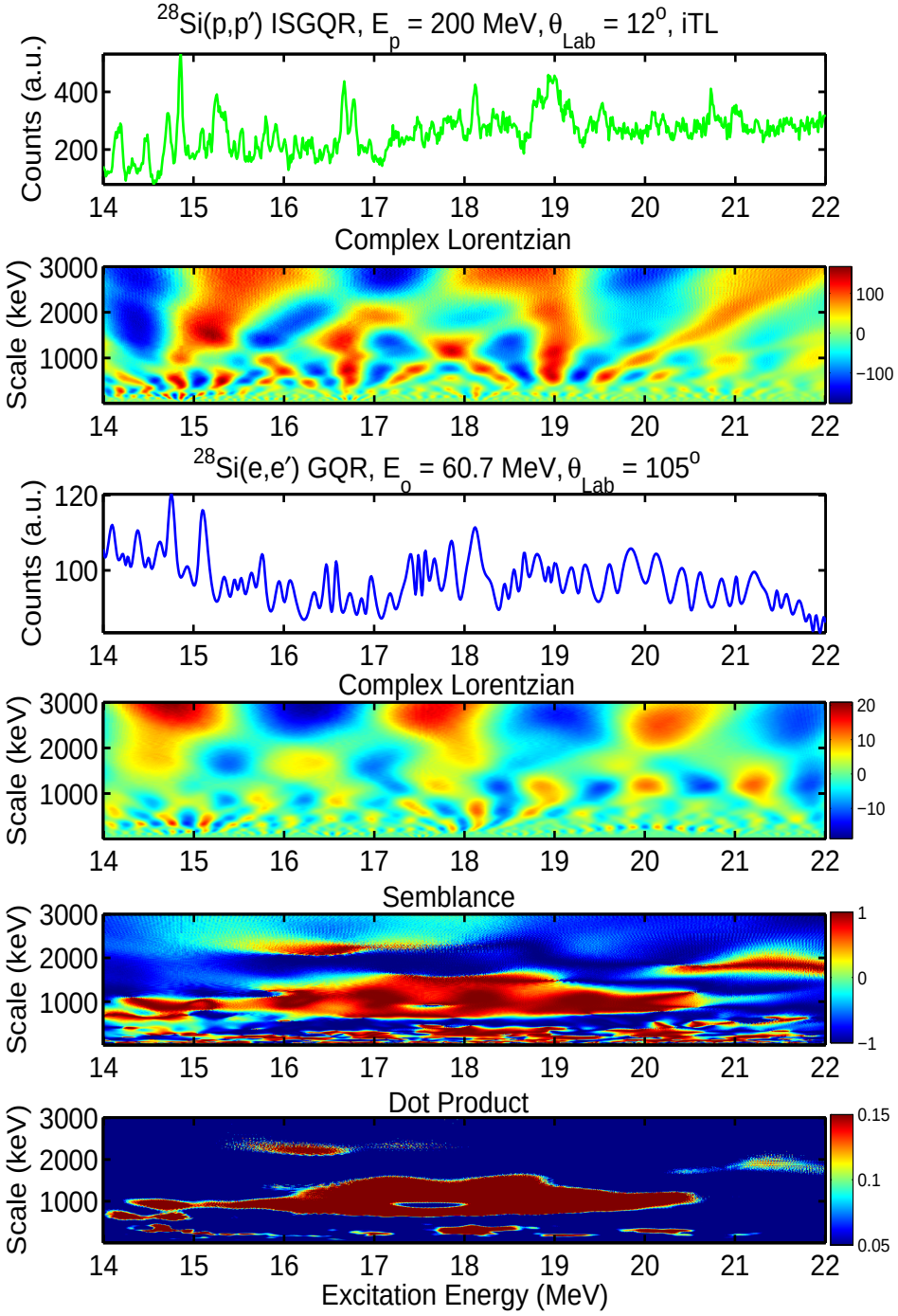

Figure 4.27: Semblance and Dot product results for ^{28}Si(p,p′) (present data) and ^{28}Si(e,e′) from [Fri81] for comparison of the ISGQR scales emerging from different selectivities.

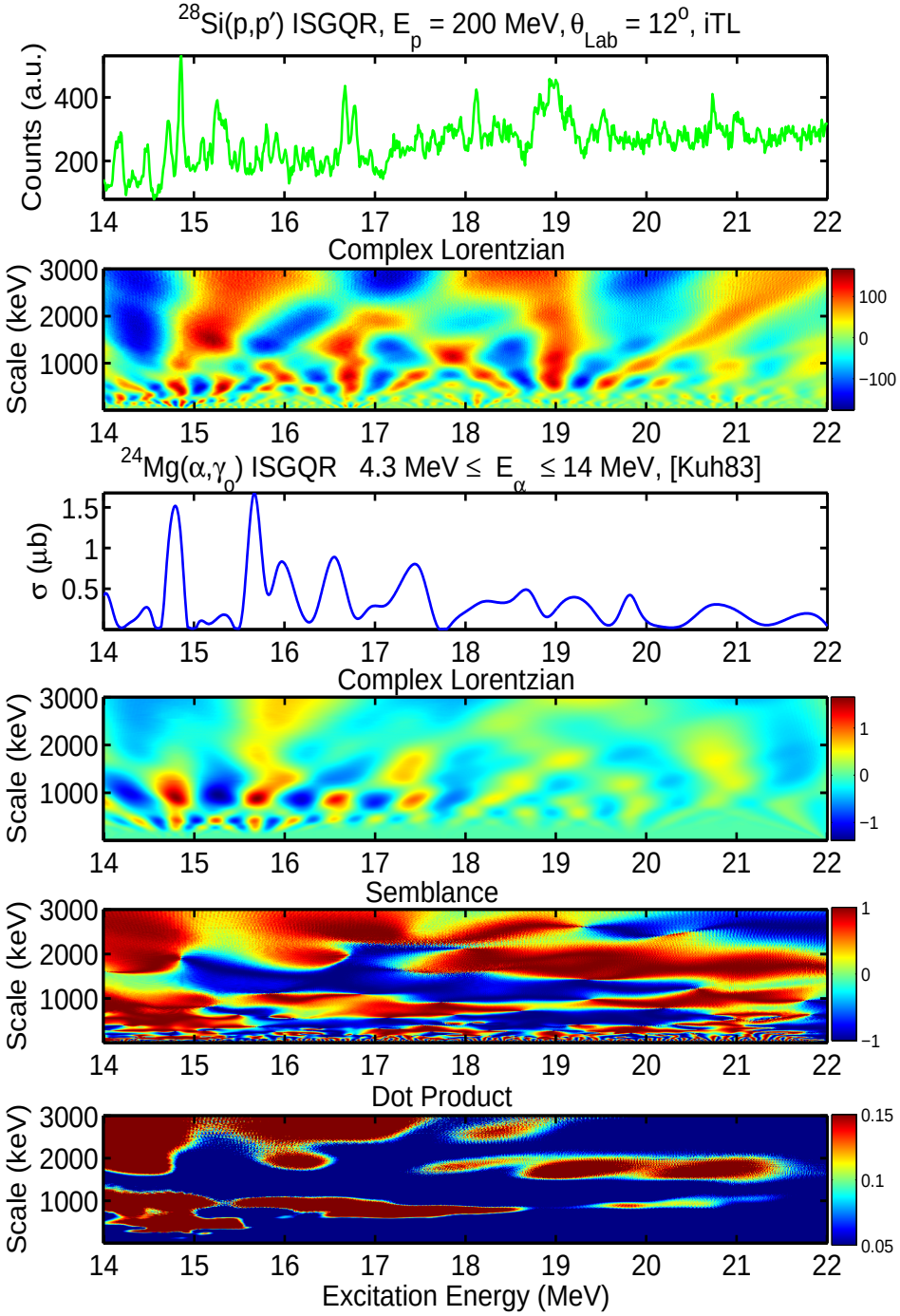

Figure 4.28: Semblance and Dot product results for ^{28}Si(p,p′) (present data) and ^{24}Mg(α, γ_o) from [Kuh83] for comparison of the ISGQR scales emerging from different selectivities.

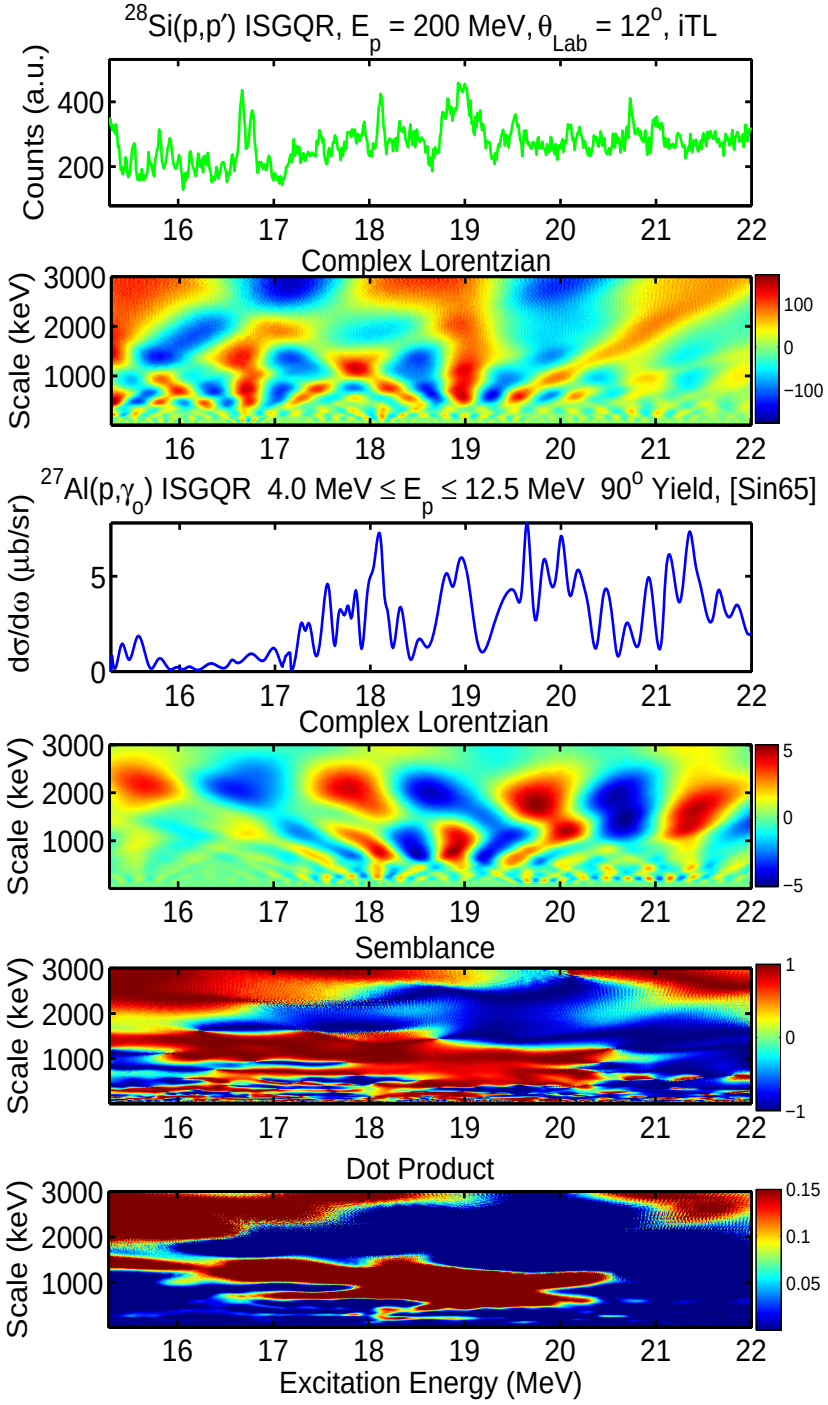

Figure 4.29: Semblance and Dot product results for ^{28}Si(p,p′) (present data) and ^{27}Al(p,γ) from [Sin65] for comparison of the ISGQR scales emerging from different selectivities.

Dealing with each comparison in turn:

^{28}Si(p,p′) and ^{28}Si(α, α'): A close correspondence is expected between the present ^{28}Si(p,p′) data at the maximum of the ISGQR and ^{28}Si(α, α') scattering. In a then high energy-resolution measurement (E_α = 120 MeV, FWHM = 125 keV) van der Borg *et al.* [Bor81] investigated $E2$ fragmentation for a variety of *sd*-shell nuclei. The resulting ^{28}Si(α, α') excitation energy spectrum at $\theta_{\rm Lab} = 6^\circ$ is shown in the second panel down of Fig. 4.25. Here, it should be noted that a shift of the ^{28}Si(α, α') data by 200 keV to larger excitation energies was required, due to the uncertainty in energy calibration of the experimental data, in order to match strong peaks in the ^{28}Si(p,p′) spectrum. This was also the case when comparison was made to ^{28}Si(e,e′) data by Friebel [Fri81]. Many of the states excited in ^{28}Si in the excitation energy range $14 \leq E_{\rm x} \leq 25$ were identified [Bor81] as $J^\pi = 2^+$ from angular distribution measurements and 24^{+7}_{-5}% of the $E2$ EWSR was reported for this region. In comparison, only 4.5% and 0.9 ± 0.6% was extracted for the $E0$ (T = 0) and $E3$ (T = 0) EWSR's, respectively. A direct comparison with the present ^{28}Si(p,p′) data at the maximum of the ISGQR is shown in Fig. 4.26. Here, it can be seen that there is an extensive positive correlation between the two data sets as indicated by the red areas of the Semblance and Dot Product plots.

^{28}Si(p,p′) and ^{28}Si(e,e′): Some correspondence can be expected between the present ^{28}Si(p,p′) data at the maximum of the ISGQR and ^{28}Si(e,e′) depending upon the kinematic conditions for the electron scattering measurement. Shown in Fig. 4.25 in the third panel down are the ^{28}Si(e,e′) results for $E_{\rm o}$ = 60.7 MeV at $\theta_{\rm Lab} = 105^\circ$ measured by the Darmstadt group [Fri81] with an energy resolution of ΔE = 50 keV (FWHM) but rebinned to 150 keV for comparison with hadronic scattering. For the kinematic conditions of the electron scattering, isoscalar and isovector

$E2$ strengths of Σ B($E2$,ΔT = 0)$\uparrow$ = 81 $\pm$ 21 fm^4 and Σ B($E2$,ΔT = 1)$\uparrow$ = 49 $\pm$ 13 fm^4, respectively, were extracted. Thus, there should exist a degree of correlation between the present ^{28}Si(p,p$'$) data and the electron scattering data but not to the same extent as for the previously discussed α-particle scattering data. This is confirmed in Fig. 4.27 where a very much more restricted red area is seen in the Semblance and Dot Product analysis in comparison to Fig. 4.26.

^{28}Si(p,p$'$) and ^{24}Mg(α, γ_o): An advantage of α-capture reactions is that $E2$ strength can be obtained with relatively background free. The presence of $E1$ decay from the Isovector Giant Dipole resonance (IVGDR) can be determined in a model independent way from angular distribution measurements. As such, the extracted $E2$ strength from ^{24}Mg(α, γ_o) is shown in the fourth panel down of Fig. 4.25 as measured by Kuhlmann *et al.* [Kuh83]. Here, the energy resolution of the data depends on the E_α step size which ranged from 150 keV to 340 keV, being equal to the thickness of the target used. Results of the Semblance analysis comparison with the present ^{28}Si(p,p$'$) data are shown in Fig. 4.28. As can be seen, there is a general correspondence for energy scales of approximately 1000 keV and 2000 keV below and above $E_x \approx 18$ MeV, respectively.

^{28}Si(p,p$'$) and ^{27}Al(p,γ_o): A final comparison with the present ^{28}Si(p,p$'$) is made with proton capture which predominantly excites the isovector giant dipole resonance. Data for ^{27}Al(p,γ_o) measured at 90° [Sin65] are shown in the bottom panel of Fig. 4.25. These data contain less than 1% $E2$ strength [Fri81] and are remarkably similar in structure to the ^{28}Si(e,e$'$) data of Friebel *et al.* [Fri81] (see above). As such, the Semblance and Dot Product results of Fig. 4.29 should be very similar to those of Fig. 4.27, which is indeed the case. A limited correlation exists for energy scales less than 1000 keV in the range $16 \leq E_x \leq 20$ MeV.

Power spectra from all the four probes considered here are presented in Fig. 4.30 where the solid line represents the power spectrum from ^{28}Si(p,p$'$) after projection of the two-dimensional spectrum shown in the second panel from the top of Figs. 4.26, 4.27, 4.28 and 4.29, onto the scale axis. The power spectrum from the other probe for comparison is indicated as a dashed line. It can be seen from the top panel of Fig. 4.30 that in ^{28}Si(α, α') power spectrum the four peaks between 400 keV and 2 MeV have corresponding peaks in the ^{28}Si(p,p$'$) power spectrum. This provides the same positive correlation as observed in Fig. 4.26. In the second panel down of Fig. 4.30 only two peaks around 600 keV and 2.8 MeV give a positive correspondence between ^{28}Si(p,p$'$) and ^{28}Si(e,e$'$) probes. The same type of structure can be observed in ^{24}Mg(α, γ_o) third panel down and ^{27}Al(p,γ_o) (bottom panel) power spectra with only two peaks in correspondence with ^{28}Si(p,p$'$) power spectrum but at different energy scales.

As a summary of the above, comparison of the wavelet power spectra resulting from different probes exciting ^{28}Si in the region of ISGQR clearly shows the correspondence between the present ^{28}Si(p,p$'$) data and previously measured ^{28}Si(α, α'). In the former case, kinematic conditions were specifically chosen to maximise excitation of the ISGQR in ^{28}Si. While in the former case, confirmation of the excitation of 2^+ states in ^{28}Si by (α, α') scattering was achieved by the measurement of angular distribution. Moreover, the $E2$ strength was confirmed to be highly fragmented over a reliably large excitation energy range 12 $\leq E_x \leq$ 22 MeV. Besides the good agreement of energy scales in the wavelet power spectra for (p,p$'$) and (α, α') scattering for ^{28}Si (top panel Fig. 4.30) the existence of this correspondence is seen for the fragmented $E2$ strength across nearly 10 MeV of excitation energy as seen in the semblance analysis of Fig. 4.26. On the other hand, the different selectivity of the other probes (e,e$'$), (α, γ_o), (p,γ_o) exciting ^{28}Si results in poor agreement of the corresponding wavelet power spectra with that of ^{28}Si(p,p$'$) (see Fig. 4.30) which is also

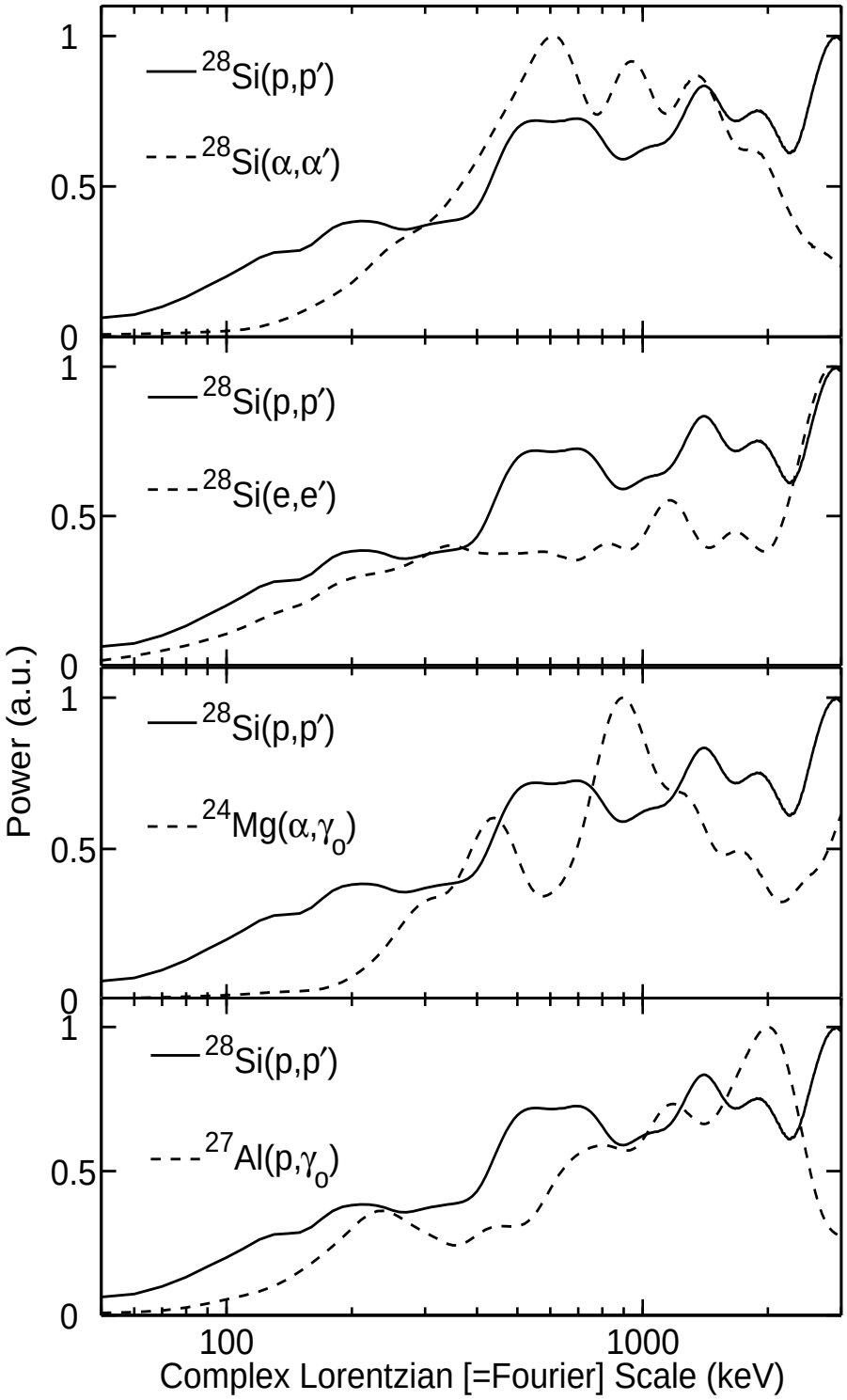

Figure 4.30: Power spectra from the semblance analysis on ^{28}Si(p,p′) (solid line) with ^{28}Si(α, α'), ^{28}Si(e,e′), ^{24}Mg(α, γ_o) and ^{27}Al(p,γ_o) for comparison of the ISGQR scales emerging from different selectivities. In each case the power spectrum is normalised to maximum of unity.

bourne out by the general lack of strong correlation coming out of the corresponding semblance analyses (see Figs. 4.27, 4.28 and 4.29). Here, the presence of other multipoles excited, in particular the IVGDR, tends to dominate as confirmed in the ^{27}Al(p,γ_o) data [Sin65] and despite $E2$ strength having been selected for in the case of ^{24}Mg(α, γ_o) [Kuh83].

4.6.3 Semblance analysis for one-proton-different nuclei: ^{28}Si, ^{27}Al(p,p′) and ^{90}Zr, ^{89}Y(p,p′) experiment

A comparison can be made between ^{28}Si, ^{27}Al(p,p′) and ^{90}Zr, ^{89}Y(p,p′) data using semblance analysis. These results are shown in Figs. 4.31 and 4.32 for the low mass and medium mass nuclei, respectively. As can be seen in Fig. 4.31 the semblance analysis for ^{28}Si, ^{27}Al(p,p′) shows a good correlation for energy scales below about 500 keV corresponding to a large amount of fine structure present for both experimental excitation energy spectra. However, the Dot product results (bottom panel Fig. 4.31) has large area indicating little correlation between the ISGQR regions of ^{28}Si and ^{27}Al. As previously discussed, for ^{28}Si the ISGQR is highly fragmented (see Fig. 4.13) and by removing one proton the corresponding $1p$-$1h$ $2\hbar\omega$ excitation of the ISGQR in ^{27}Al can be expected to be significantly different from ^{28}Si due to the restricted configuration available in the extreme single-particle shell model.

On the other hand, a comparison for ^{90}Zr, ^{89}Y(p,p′) shown in Fig. 4.32 yields significant correlation both for the Semblance and Dot product results as seen by the large red areas in the bottom panels of the figure. The prominent peak at approximately 13 MeV excitation energy in Yttrium (^{89}Y) energy spectrum shown in the third panel down of Fig. 4.32 is an Isobaric Analogue State (IAS) and does not belong to the ISGQR. By way of example the $1p$-$1h$ excitation of the ISGQR was presented in Fig. 2.2 where it can be seen that there is a large

configuration space available for $2\hbar\omega$ transitions [Har00]. A change of proton leading to ^{89}Y should, therefore, not influence too significantly the resulting ISGQR excitation. This is confirmed by the present analysis.

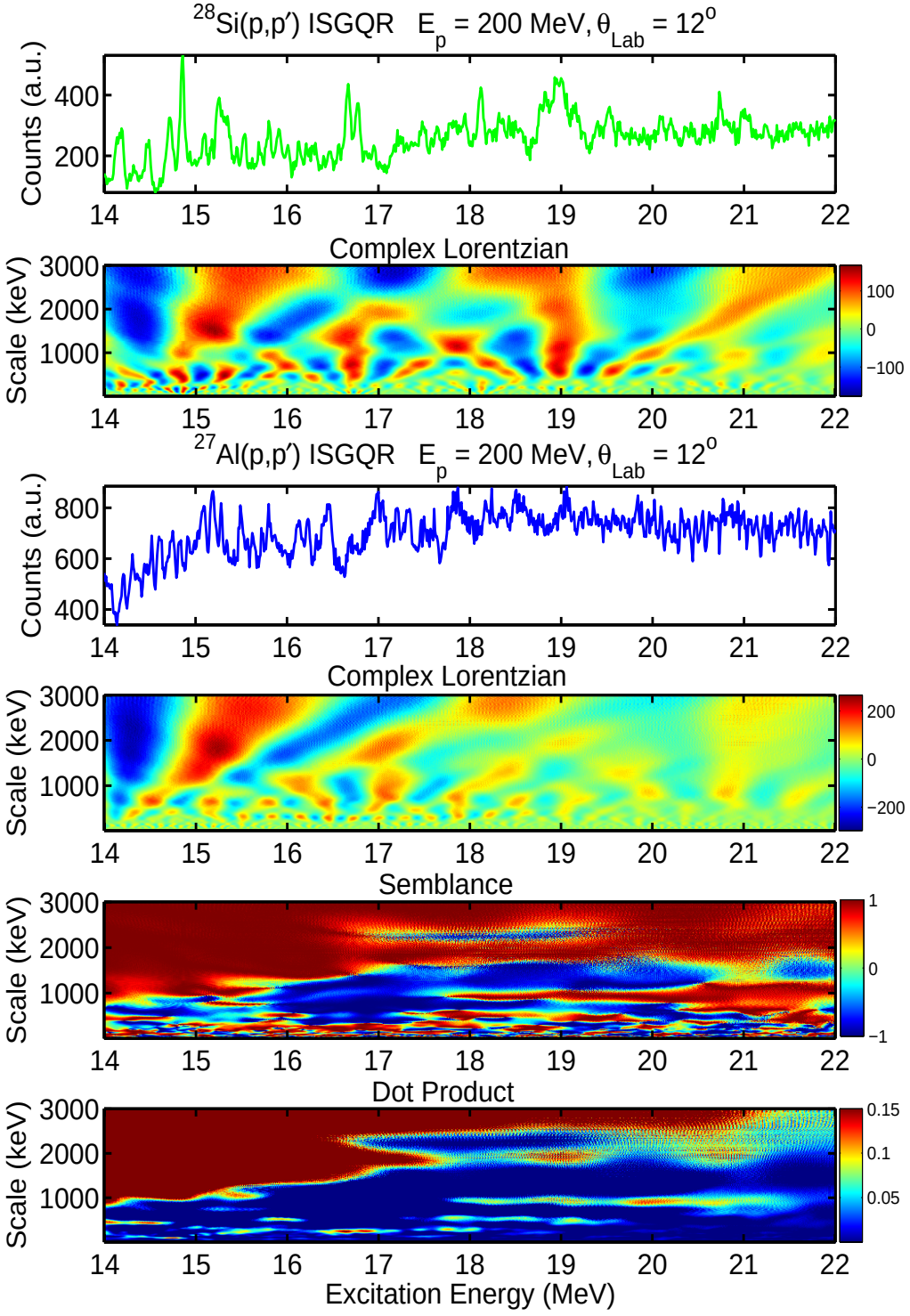

Figure 4.31: Semblance and Dot product results for the ^{28}Si(p,p′) (green line) and ^{27}Al(p,p′) (blue line) experimental data for comparison of the ISGQR scales emerging from one-nucleon-difference nuclei. Real part of the complex Lorentzian mother wavelet coefficients is depicted below each of the data.

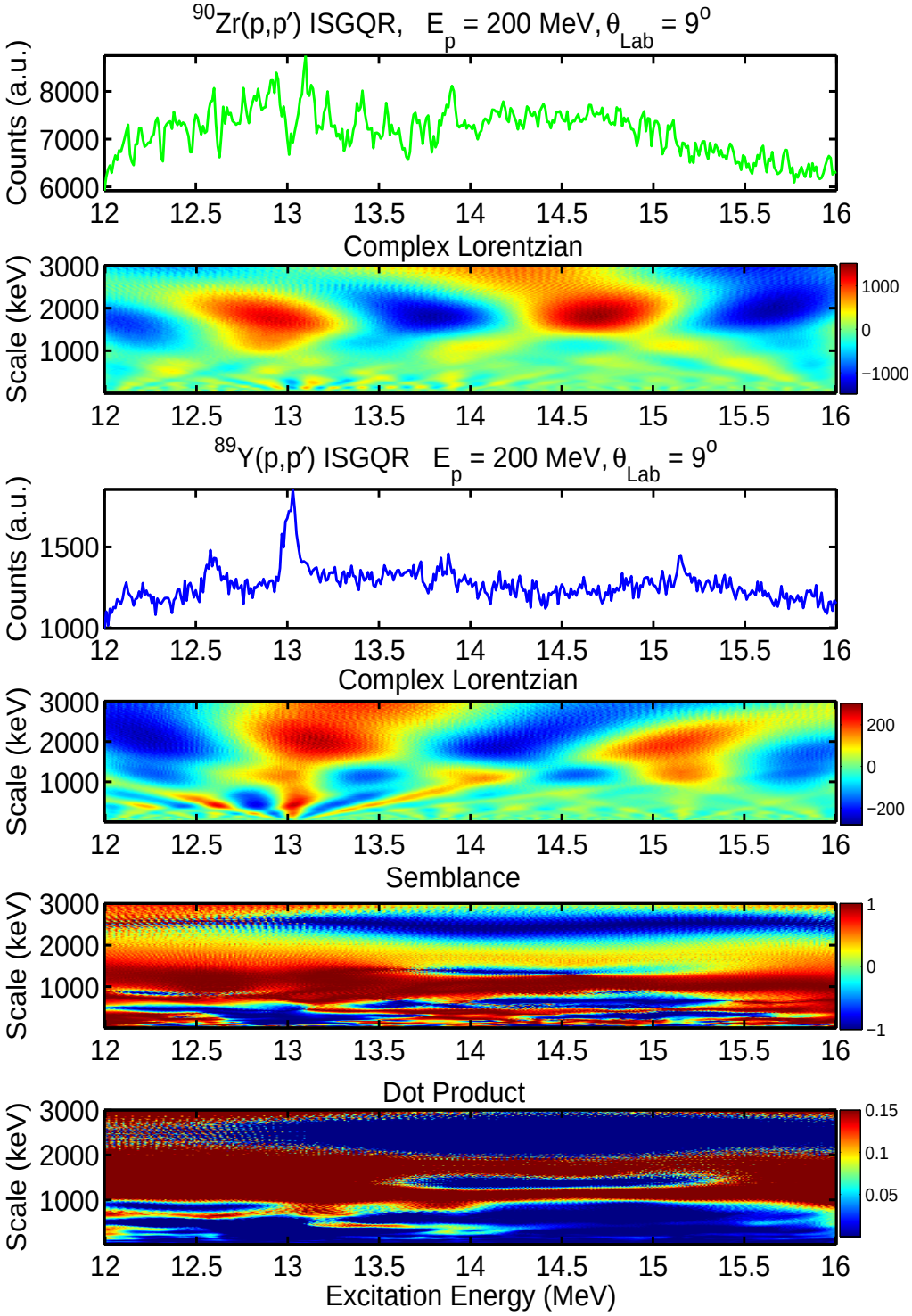

Figure 4.32: Semblance and Dot product results for the ^{90}Zr(p,p′) (green line) and ^{89}Y(p,p′) (blue line) experimental data for comparison of the ISGQR scales emerging from one-nucleon-difference nuclei. Real part of the complex Lorentzian mother wavelet coefficients is depicted below each of the data.

4.7 Quasi-free - scattering background contributions for ^{40}Ca(p,p′)

Details of the description for the calculation of the quasi-free - scattering background contributions due to the (p,2p) and (p,pn) processes are given in Sect. 2.2.2. The code THREEDEE [Cha98] was used for the calculation of quasi-free nucleon knockout in the reactions ^{40}Ca(p,2p)^{39}K and ^{40}Ca(p,pn)^{39}Ca at 200 MeV incident energy. Within the DWIA model an assumption is made of a simple quasi-free projectile-nucleon interaction. These calculations were done in order to investigate the strength of the quasi-free knockout contributions from protons and neutrons in the target nucleus ^{40}Ca, which could contribute significantly to the background in the continuum. This was prompted by very successful earlier studies of angular correlations for ^{40}Ca(p,p′p$_0$), ^{40}Ca(p,p′α_0) and ^{48}Ca(p,p′n$_0$) at E_p = 100 MeV [Sch01, Car01] also using the K600 Magnetic Spectrometer of iThemba LABS. In addition, since the excitation energy region of the ISGQR is expected to have contributions from other multipoles excited and possibly instrumental background, it was thought that the subtraction of a known quasi-free background would lead to a more reliable extraction of 2^+ level density for ^{40}Ca (see Sect. 4.8.2).

As a requirement, optical potential parameters are needed as input for generating distorted waves for the incoming proton and its subsequent quasi-free scattering as the outgoing proton. These have been parameterised by Schwandt *et al.* [Sch82] for medium to heavy-mass targets across the periodic table and are applicable to energy range $80 \leq E_\mathrm{p} \leq 180$ MeV. The corresponding energy-dependent optical potential parameters are listed in Table 4.7. Details of the optical potential used are given in Eq. (2.7) of Sect. 2.2.1.

Turning to the knockout channels, for the knockout proton the low-energy

Table 4.7: Energy-dependent optical potential parameters of Schwandt *et al.* [Sch82] used in the DWIA calculations for the p + ^{40}Ca as described in the text. Note that the potential strengths are in MeV, r and a in fm.

Potential Parameter	**p + ^{40}Ca** Description / Values
V	$105.5(1 - 0.1625\ \ln E_{\rm p}) + 16.5(N - Z)/A$
$r_{\rm o}$	$1.125 + 1.0 \times 10^{-3} E_{\rm p}$
$a_{\rm o}$	$0.675 + 3.1 \times 10^{-4} E_{\rm p}$
W	$6.6 + 2.73 \times 10^{-2}(E_{\rm p} - 80) + 3.87 \times 10^{-6}(E_{\rm p} - 80)^3$
$r_{\rm w}$	$1.65 - 2.4 \times 10^{-3} E_{\rm p}$
$a_{\rm w}$	$0.32 + 2.5 \times 10^{-3} E_{\rm p}$
$V_{\rm so}$	$19.0(1 - 0.166\ \ln E_{\rm p}) - 3.75(N - Z)/A$
$r_{\rm so}$	$0.920 + 0.0305 A^{1/3}$
$a_{\rm vso}$	$0.768 - 0.0012 E_{\rm p}$
$W_{\rm so}$	$7.5(1 - 0.248\ \ln E_{\rm p})$
$r_{\rm wso}$	$0.877 + 0.0360 A^{1/3}$
$a_{\rm wso}$	0.62
$r_{\rm oC}$	1.25

proton optical potential of Bechetti and Greenless [Bec69], applicable in the energy range $0 < E_{\rm p} < 50$ MeV, was employed while for the knockout neutron the low-energy neutron optical potential also from [Bec69], applicable in the energy range $0 < E_{\rm n} < 24$ MeV , was used. Values for the corresponding low-energy proton and neutron optical potentials are listed in Tables 4.8 and 4.9, respectively. Details of the form of the optical potential are given in Eq. (2.7) of Sect. 2.2.1. For the calculation of proton and neutron bound state wave-functions, the Wood-Saxon well radius and diffuseness parameters were taken from Elton and Swift [Elt67] ($r_{\rm o} = 1.3$ fm, $a = 0.6$ fm) with a spin-orbit strength, $V_{\rm so} = 12$ MeV. The depth of the Wood-Saxon well in which the bound state wave-functions are calculated was adjusted in order to reproduce the binding energies for the various hole states listed in Table 4.10, corresponding to the considered final states in ^{39}K and ^{39}Ca. The final relative nucleon-nucleon energy prescription (FEP) was used in the evaluation of cross sections (see Sect. 2.2.2).

Table 4.8: Energy-dependent optical potential parameters of Becchetti and Greenlees [Bec69] used in the DWIA calculation for the p + ^{39}K knockout channel in the energy range $0 < E_{\rm p} < 50$ MeV. Note that the potential strengths are in MeV, r and a in fm.

Potential Parameter	**p + ^{39}K** Description / Values
V	$54.0 - 0.32E_{\rm p} + 24.0(N-Z)/A + 0.4(Z/A)^{1/3}$
$r_{\rm o}$	1.17
$a_{\rm o}$	0.75
W	$0.22(E_{\rm p} - 80) - 2.7$
$r_{\rm w}$	1.32
$a_{\rm w}$	$0.51 + 0.7(N-Z)/A$
$V_{\rm so}$	6.2
$r_{\rm vso}$	1.01
$a_{\rm vso}$	0.75
$W_{\rm d}$	$11.8 - 0.25E_{\rm p} + 12(N-Z)/A$
$r_{\rm wd}$	1.32
$a_{\rm wd}$	$0.51 + 0.7(N-Z)/A$

Table 4.9: Energy-dependent optical potential parameter of Becchetti and Greenlees [Bec69] used in the DWIA calculation for the n + ^{39}Ca knockout channel in the energy range $0 < E_{\rm n} < 24$ MeV. Note that the potential strengths are in MeV, r and a in fm.

Potential Parameter	**n + ^{39}Ca** Description / Values
V	$56.3 - 0.32E_{\rm p} - 24.0(N-Z)/A$
$r_{\rm o}$	1.17
$a_{\rm o}$	0.75
W	$0.22E_{\rm p} - 1.56$
$r_{\rm w}$	1.26
$a_{\rm w}$	0.58
$V_{\rm so}$	6.2
$r_{\rm vso}$	1.01
$a_{\rm vso}$	0.75
$W_{\rm d}$	$13.0 - 0.25E_{\rm p} - 12(N-Z)/A$
$r_{\rm wd}$	0.0
$a_{\rm wd}$	1.0

Table 4.10: The principal quantum number, N, orbital angular momentum, L, and the total angular momentum,J, with binding energies and spectroscopic factors (S) of the three valence states of proton [Ant81] and neutron [Wat82] in ^{40}Ca.

State	***N***	***L***	***J***	**p + ^{39}K Proton** BE(MeV)	S	**n + ^{39}Ca Neutron** BE(MeV)	S
$1d_{3/2}$	1	2	3/2	8.33	3.7	15.6	4.0
$2s_{1/2}$	2	0	1/2	10.85	1.65	18.2	1.9
$1d_{5/2}$	1	2	5/2	15.07	4.96	21.9	6.0

In order to perform the integration over the kinematics of the knockout particle, certain conditions in choosing the angular range conformed to the symmetry of the solid angle and the determined momentum of the recoil nucleus were taken into consideration so as to achieve a pure quasi-free reaction. It should be noted that in this type of reaction the recoil momentum were chosen arbitrarily to be less than 200 MeV/c in order to find the corresponding primary angles at each proton energy. This was determined using kinematic calculations of the program QUASTA [Quasta] which performs kinematics for the three-body break-up where particles a' and b were observed and particle B recoils. The contributions due to the quasi-free process were later determined in terms of the sum of the cross section in $1d_{3/2}$, $2s_{1/2}$ and $1d_{5/2}$ states for both proton and neutron with known spectroscopic factors, S, taken from ref. [Ant81] for the protons and ref. [Wat82, Ahm84] for neutron states, except for the case of neutrons knocked out of $1d_{3/2}$ shell where the shell model limit of $S = 4.0$ was used. The calculations were performed within the range of excitation energy of 10 to 30 MeV for ^{40}Ca as measured in the experiment which corresponds to $E_{p'}$ of about 190 to 170 MeV, respectively. It is important to note that from previous calculations it was found that the contribution due to ^{40}Ca(p,p$'\alpha$) was very small. Present test calculations confirmed this and therefore (p,p$'\alpha$)

calculations were neglected.

For ^{40}Ca at 11° scattering angle, Figs. 4.33 and 4.34 show the results of quasi-free contributions due to (p,2p) and (p,pn) for the three states $1d_{3/2}$, $2s_{1/2}$ and $1d_{5/2}$ calculated. It should be emphasised that these have been weighted with their respective Spectroscopic Factor (S) as indicated in Table 4.10. By adding all the three components the total contribution is indicated as Sum in both figures. It can be seen that the strength of contributions from both protons and neutrons were almost the same. By adding the proton and neutron Sum cross-sections and multiplying by a factor of 2 due to symmetry in the angular range (see above), the resulting quasi-free background is shown in Fig. 4.35 as the dashed line. To indicate the strength of quasi-free background contribution, this is plotted together with the measured ^{40}Ca(p,p′) cross section in Fig. 4.36. By applying the above procedure to the other scattering angles, quasi-free background contributions were calculated for $\theta_{\mathrm{Lab}} = 15°$ and $\theta_{\mathrm{Lab}} = 7°$ and the results are presented in Figs. 4.37 and 4.38, respectively. It can be seen that the quasi-free contribution at $\theta_{\mathrm{Lab}} = 11°$ is quite significant in the excitation energy range 20 - 25 MeV while the quasi-free contribution above and below the maximum of the ISGQR for $\theta_{\mathrm{Lab}} = 15°$ and $\theta_{\mathrm{Lab}} = 7°$, respectively, is not as strong.

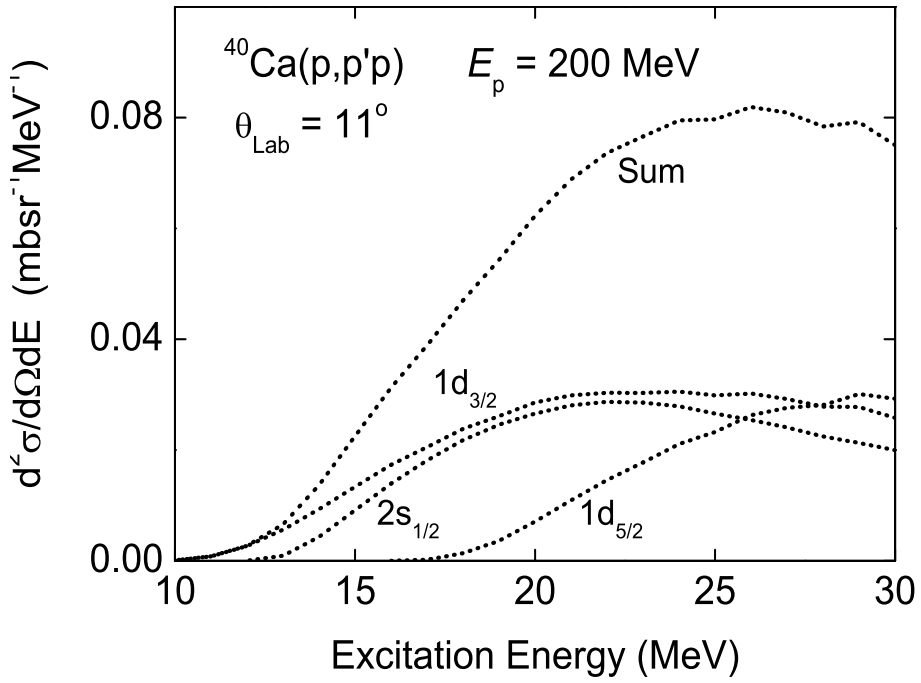

Figure 4.33: Angle integrated continuum quasi-free cross-sections for the reaction ^{40}Ca(p,p′p) at incident energy of 200 MeV and scattering angle of 11° calculated for the $1d_{3/2}$, $2s_{1/2}$ and $1d_{5/2}$ proton states.

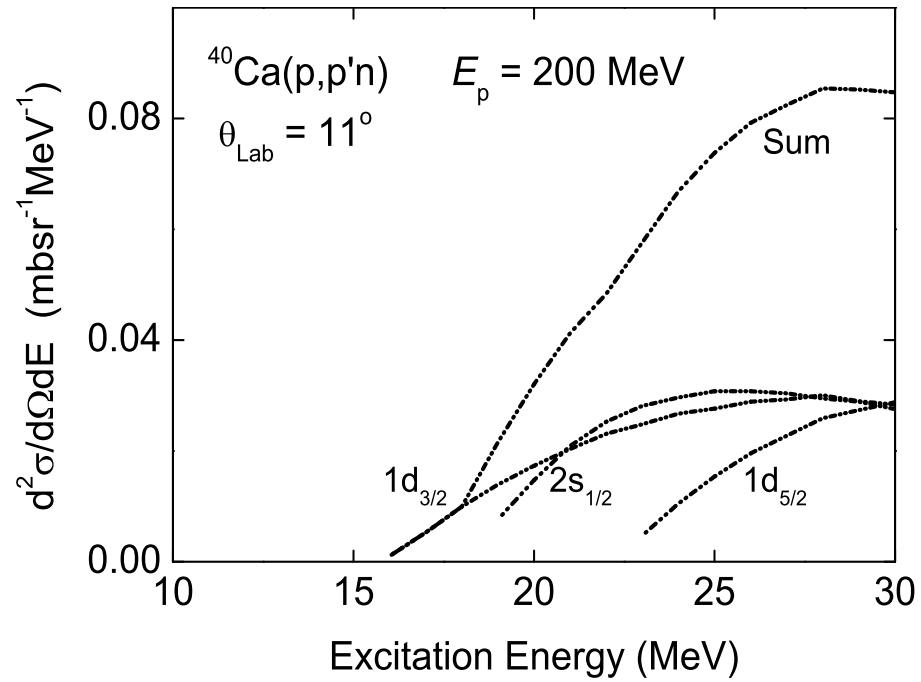

Figure 4.34: Continuum quasi-free cross-sections for the reaction ^{40}Ca(p,p′n) at incident energy of 200 MeV and scattering angle of 11° calculated for the $1d_{3/2}$, $2s_{1/2}$ and $1d_{5/2}$ neutron states.

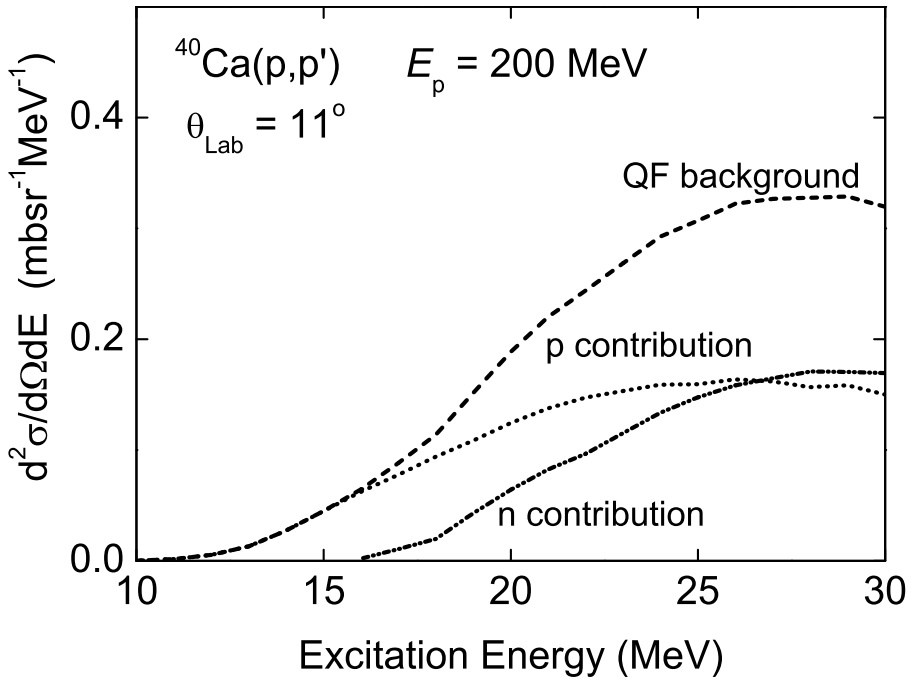

Figure 4.35: The curves are results of the DWIA calculations for quasi-free background contributions from both proton and neutron indicated as QF background for ^{40}Ca(p,p′) at $\theta_{\rm Lab}$ =11° as indicated in Figs. 4.33 and 4.34.

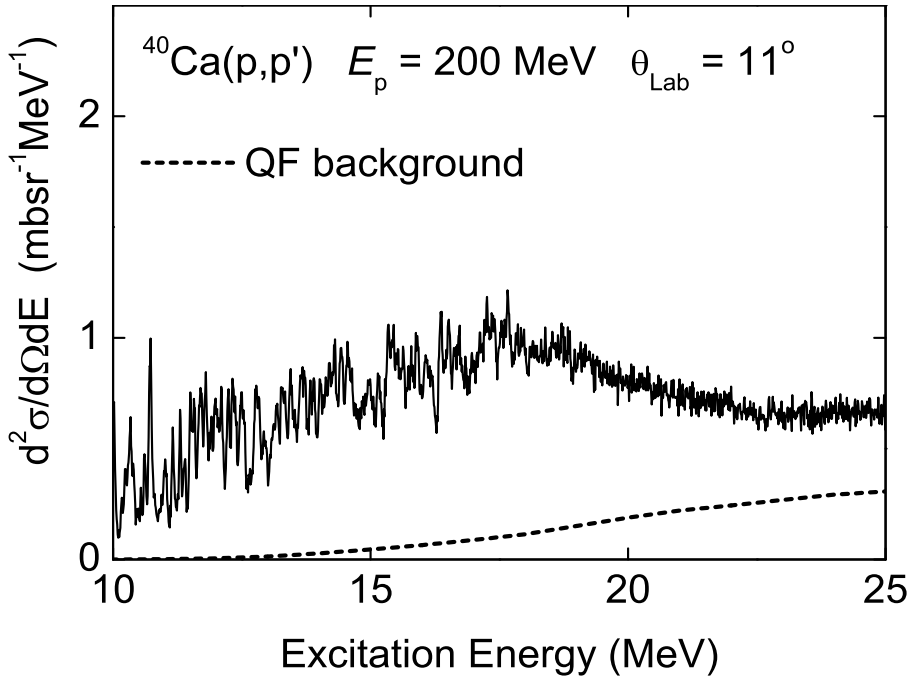

Figure 4.36: Quasi-free background contribution (dashed-line) for ^{40}Ca at $\theta_{\rm Lab}$ = 11° as indicated in Fig. 4.35.

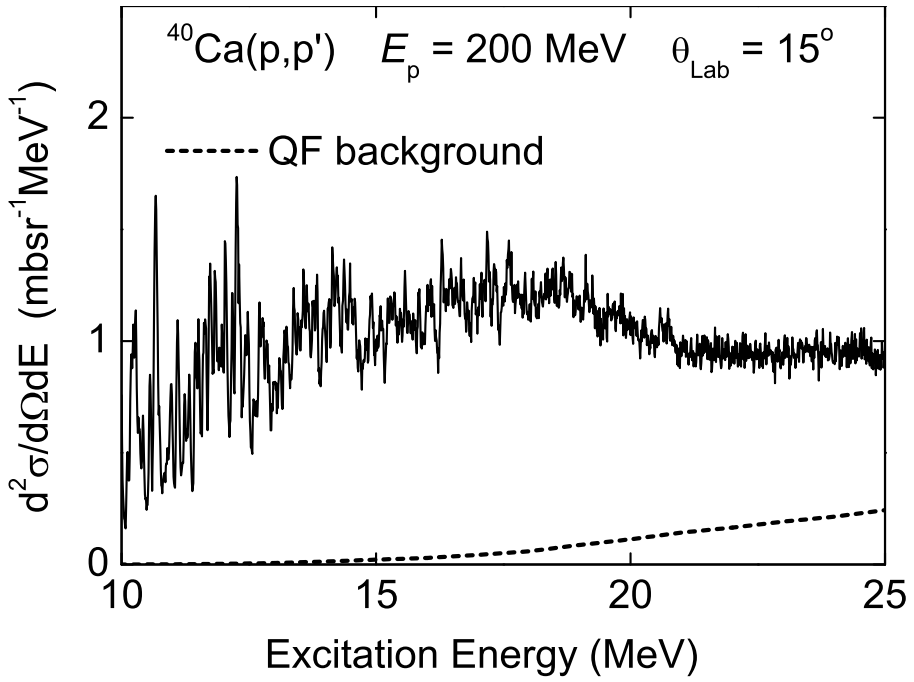

Figure 4.37: Quasi-free background contribution for ^{40}Ca at $\theta_{\mathrm{Lab}} = 15°$.

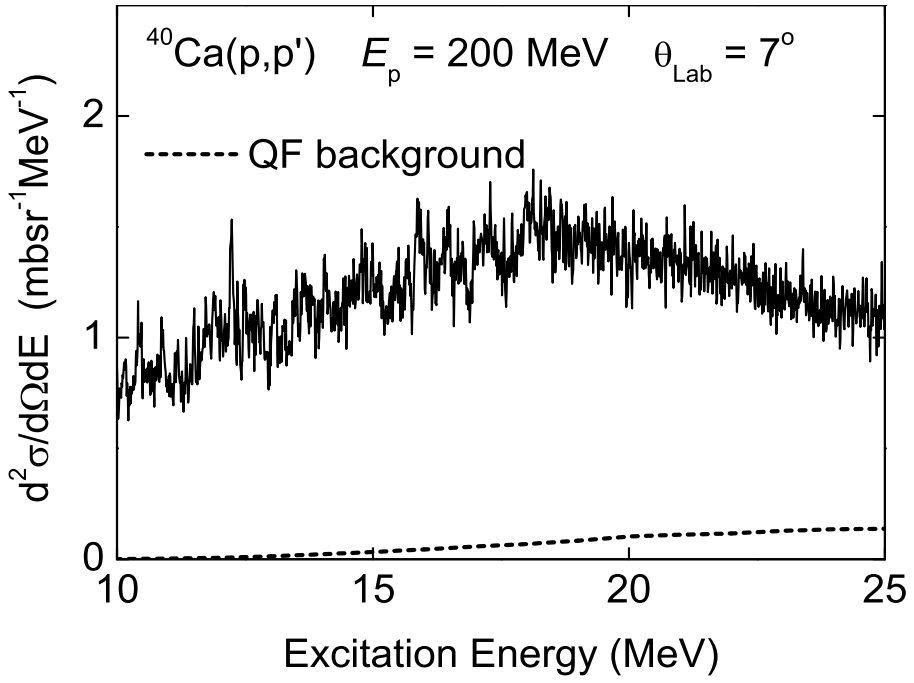

Figure 4.38: Quasi-free background contribution for ^{40}Ca at $\theta_{\mathrm{Lab}} = 7°$.

4.8 Level density of 2^+ states in ^{40}Ca

The basic research on nuclear level densities has been concerned with various phenomenological and microscopic models, their validation by comparison with measurements and the extraction of level density parameters from experimental data. In this section, the level density of 2^+ states in ^{40}Ca extracted by means of a self-consistent procedure based on a fluctuation analysis in the excitation energy interval between 10 and 20 MeV is discussed.

The method of extraction of level density was presented in Sect. 2.5.2 and from Eq. (2.57), the value of the autocorrelation function $(C(\epsilon) - 1)$ at $\epsilon = 0$, known as the variance of the stationary spectrum, is proportional to the mean level spacing $\langle D \rangle$. Thus, $\langle D \rangle$ can be extracted directly once the value of the variance is known. In turn, there are two different approaches possible in the extraction of mean level spacing.

- The background is required to be known so that one can extract the mean level spacing from the experimental autocorrelation function by using Eq. (2.57).
- The level density is assumed to be defined, *e.g.* calculated by a theoretical model, so that one can exactly determine the background by varying its shape in such a way that the experimental value $(C(\epsilon = 0) - 1)$ becomes equal to the theoretical value.

In the present case, an extraction of the level density was done with the first approach making use of the fact that the level density is an intrinsic feature of a nucleus.

The sources of background to the measured proton inelastic-scattering spectra can be grouped into three:

- instrumental background,
- background from other multipoles excited and
- background from quasi-free scattering contributions, especially (p,2p) and (p,pn). It should be noted that the background contribution of the (p,pα) reaction is very small [Sch01, Car01] when compared to the (p,2p) and (p,pn) reactions and thus it has been neglected.

Bearing in mind that instrumental background has been largely removed using software corrections during data analysis, all of the above mentioned background contributions can be accounted for using the Discrete Wavelet Transform (DWT) analysis described below in the region of ISGQR. In the case of the quasi-free contributions, the cross section can be determined with a high degree of accuracy within the DWIA formalism using known spectroscopic factors. Therefore, in this work two methods of background determination have been implemented. Firstly, in a model-independent way DWT analysis is used to account for all three background contributions. Secondly, quasi-free scattering calculations can be used to remove physical background, with DWT analysis then applied to remove the remaining physical background from other multipoles excited and any remaining instrumental background. The latter method should give a more precise determination of background since a relatively large contribution from quasi-free scattering has already been accounted for.

4.8.1 DWT analysis and background determination

Background as described above, in the region of the ISGQR, was determined using a model independent method based on the DWT decomposition. The background lines are smooth and can be well approximated by low-order polynomials. This allows to take advantage of the vanishing moments of wavelets

in which the Biorthogonal 3.9 wavelet family (see Sect. 2.4.2) is chosen due to the fact that it has suitable vanishing moments when applied to the form of background present in this analysis [Dau94]. In addition, if a function has a sufficient number of moments, then all non-resonant components are always found in the approximations, while details contain the information on the fluctuations. Thus, at some stage of the decomposition the approximation corresponds to the background and does not anymore carry information on the fine structure. This level depends on such parameters like the bin size or the total width of the resonance.

The cross-section data measured at the various scattering angles is then decomposed into approximations and details. In this the approximation that best fits the data was chosen as a background. It can be seen that the background lines are smooth and can be well approximated by the low-order polynomial due to the number of vanishing moments present in the type of DWT mother wavelet used. The bior3.9 has n = 3 vanishing moments which is sufficient enough to give the approximation in which all non-resonant components are found and this particular approximation carries no fine structure information and also gives the total width of the resonance. The result is shown in Fig. 4.39 for $\theta_{\mathrm{Lab}} = 11°$. As can be seen from this figure, the global shape of the ISGQR is given by A9 so the next approximation corresponds to the background which contains no information on the fine structure. Therefore, the chosen background A10 is considered to be a non-resonant contribution to the spectrum. A "fine tuning" of the background is then carried out by shifting the A10 in the vertical direction in order to satisfy the observation that the spectrum is background-free below the proton and neutron thresholds. After subtraction of the modified A10 a fluctuation analysis is performed on the spectrum.

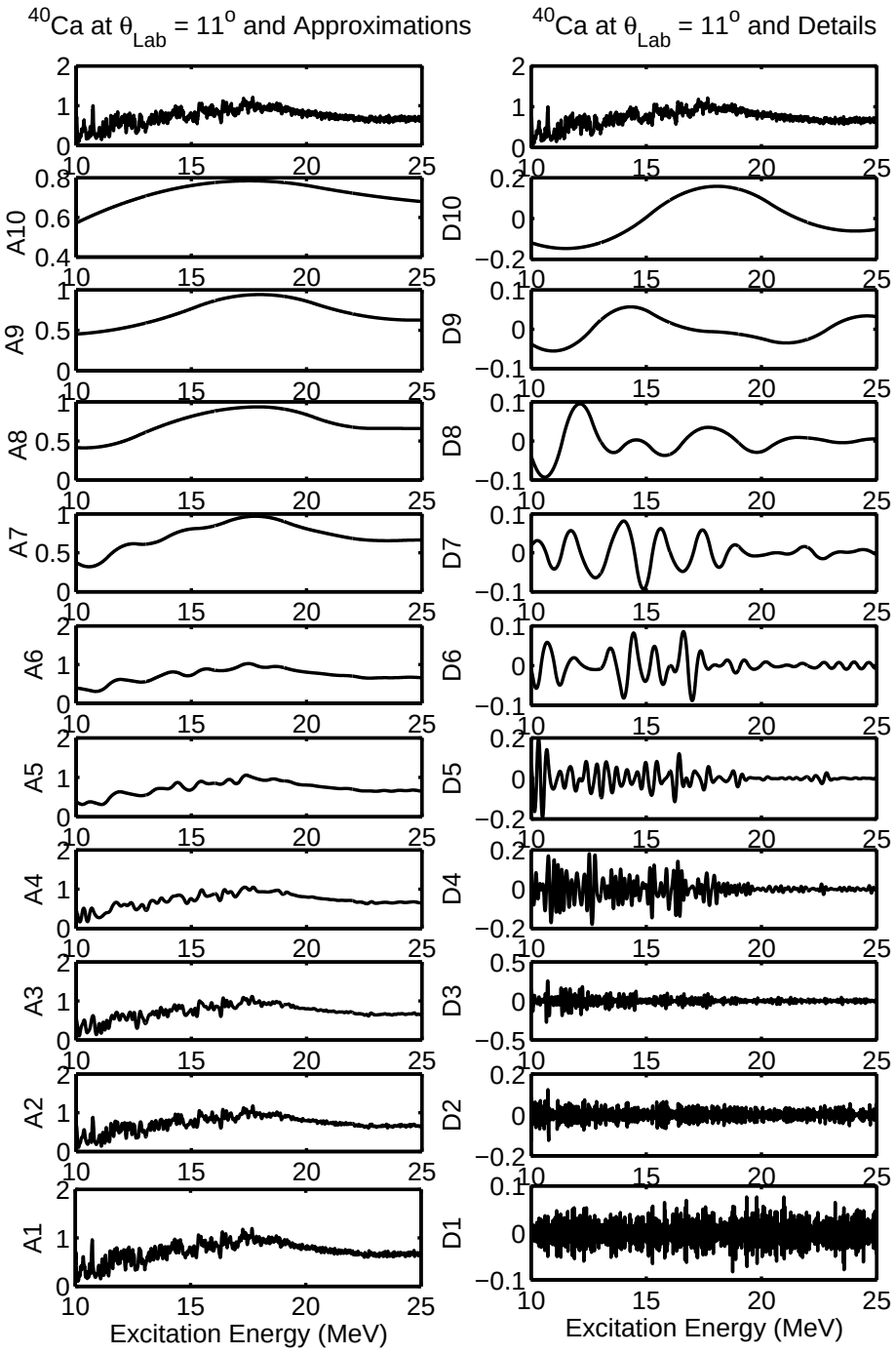

Figure 4.39: Decomposition of the excitation energy spectrum of ^{40}Ca(p,p$'$) reaction measured at $E_{\mathrm{p}} = 200$ MeV for $\theta_{\mathrm{Lab}} = 11^{\circ}$ into approximations and details.

4.8.2 Extraction of 2^+ level density in ^{40}Ca

Following on from the DWT analysis of the previous section, the upper part of Fig. 4.40 shows the measured excitation energy spectrum for ^{40}Ca(p,p′) at $\theta_{\mathrm{Lab}} = 11^\circ$ together with the assumed DWT background. The fluctuation analysis of Sect. 2.5.2 then requires the smoothed spectra $g(E_{\mathrm{x}})$ and $g_{>}(E_{\mathrm{x}})$, shown next superimposed on each other, the stationary spectrum $d\,(E_{\mathrm{x}})$ and in the bottom part of Fig. 4.40 the autocorrelation functions for both the theoretical model and the experimental data. Here, application of Eq. (2.57) to the experimental data results in the solid line displayed in the bottom part of Fig. 4.40. In addition, it can be seen from the stationary spectrum that the intensity of the fluctuations decreases with increasing excitation energy *i.e* level density increases, thus indicating a decreasing level spacing.

In order to extract the mean level spacing $\langle D \rangle$, the experimental $(C\,(\epsilon = 0) - 1)$ value is inserted into Eq. (2.59) with the values of the other parameters listed in Table 4.11 . The resulting mean level spacing $\langle D \rangle$ and level density ρ are given by

$$\langle D \rangle = (C\,(\epsilon = 0) - 1) \times 0.506024, \tag{4.1}$$

and

$$\rho = 1/\langle D \rangle. \tag{4.2}$$

It should be noted that 2^+ level density as a function of excitation energy can be determined by repeating the above procedure for smaller excitation energy intervals or energy bins of the spectrum. Finally, the level density in each energy bin can be calculated using Eq. (4.2) as the reciprocal of the mean level spacing.

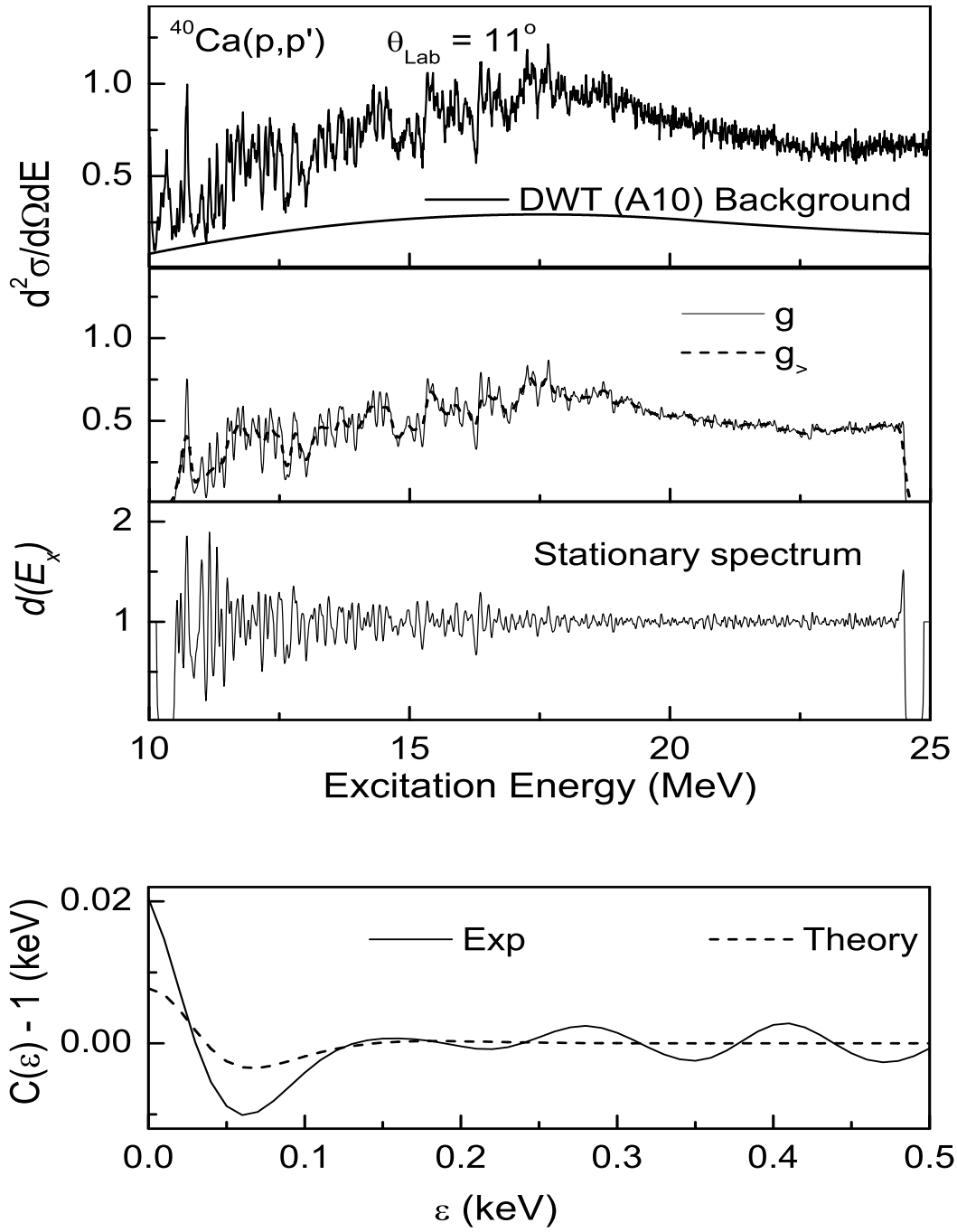

Figure 4.40: from top to bottom: Experimental ^{40}Ca(p,p′) spectrum including background obtained with the use of discrete wavelet transform, smoothed spectra $g(E_{\mathrm{x}})$ and $g_{>}(E_{\mathrm{x}})$, stationary fluctuating spectrum d(E_{x}) obtained by dividing the two smoothed spectra, autocorrelation functions from experimental (solid line) and theoretical (dashed line) method.

Table 4.11: List of parameters used in 2^+ level density extraction for ^{40}Ca.

Parameter	Value
Sum of normalised variances (α)	2.273
Experimental energy resolution ΔE	37 keV
σ	15 keV
$\sigma_>$	50 keV
$\frac{\sigma_>}{\sigma}$ (y)	1.5579

The results from the DWT background determination choosing A10 as the background and shifting the vertical axis below the spectrum is shown in Fig. 4.41. Figure 4.42 shows the comparison of the extracted experimental level density of 2^+ states in ^{40}Ca together with the theoretical model predictions. It should be noted that the excitation energy range shown is restricted to the region where $\langle\Gamma\rangle/\langle D\rangle \ll 1$, neglecting the Ericson fluctuation region at higher excitation energies. The dashed line indicates the result of the BSFG level density calculations using the parameterisations of [Rau97]. The spin- and parity-projected level densities from the HFB are shown as a dotted line in the figure. It can be seen that the HFB predicts well the experimental level densities with parity dependence. However, the BSFG approach which provides no parity information only gives the correspondence at certain excitation energy values. Uncertainties occur due to errors in the statistical-model input parameters.

The above procedures were then repeated for the measured ^{40}Ca(p,p$'$) excitation energy spectra at the scattering angles $\theta_{\rm Lab} = 15^\circ$ and $\theta_{\rm Lab} = 7^\circ$ being above and below the maximum of ISGQR, respectively. This was done in order to investigate the effect of the presence of the ISGQR in the spectra on extracted level densities. The corresponding results are shown for $\theta_{\rm Lab} = 15^\circ$ in Figs. 4.43 and 4.44 and for $\theta_{\rm Lab} = 7^\circ$ in Figs. 4.45 and 4.46.

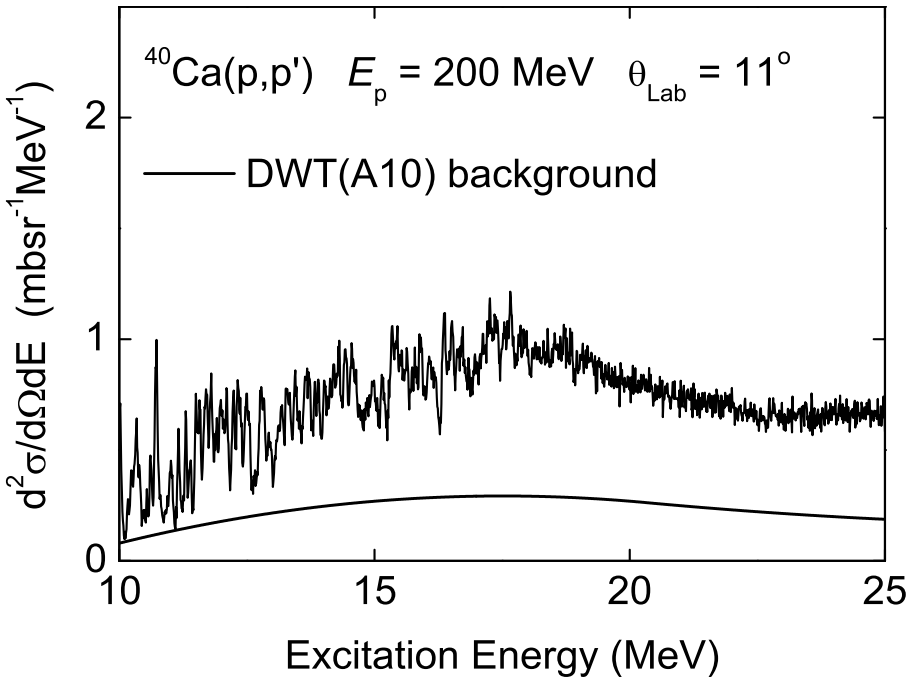

Figure 4.41: DWT (A10) background for ^{40}Ca(p,p′) at $\theta_{\mathrm{Lab}} = 11°$.

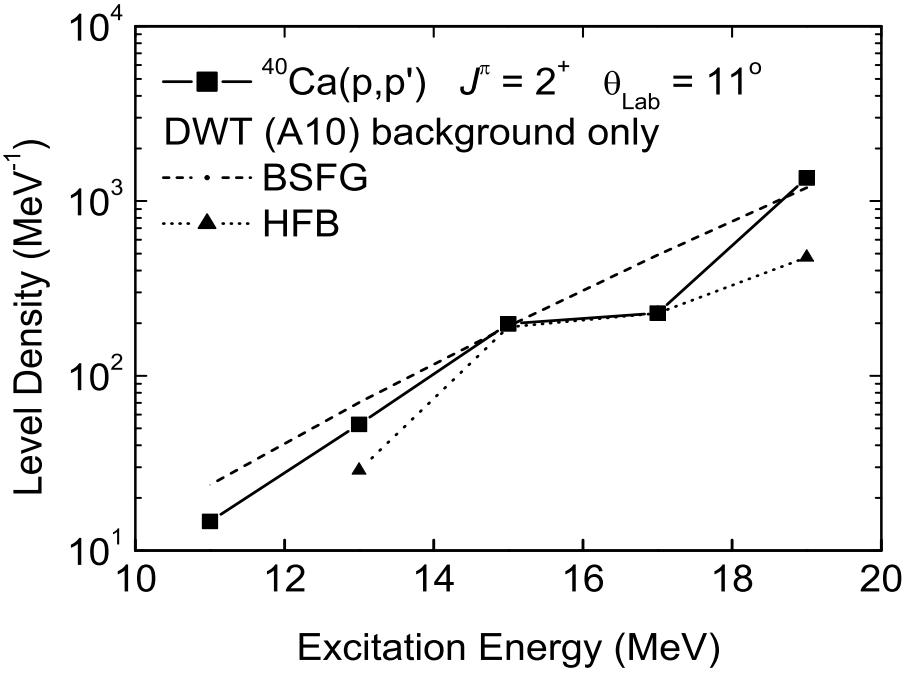

Figure 4.42: Extracted level density (solid line) of 2^+ states for ^{40}Ca(p,p′) at $\theta_{\mathrm{Lab}} = 11°$ compared to BSFG (dashed line) and HFB (dotted line) model predictions after using DWT (A10) background subtraction as shown in Figs. 4.39, 4.40 and 4.41.

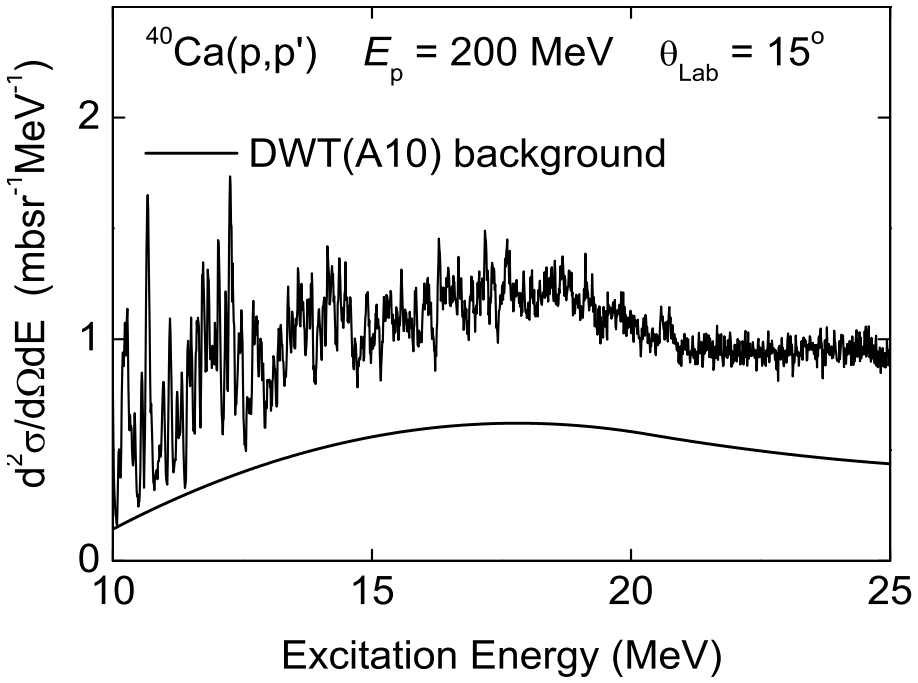

Figure 4.43: DWT (A10) background for ^{40}Ca(p,p′) at $\theta_{\mathrm{Lab}} = 15°$.

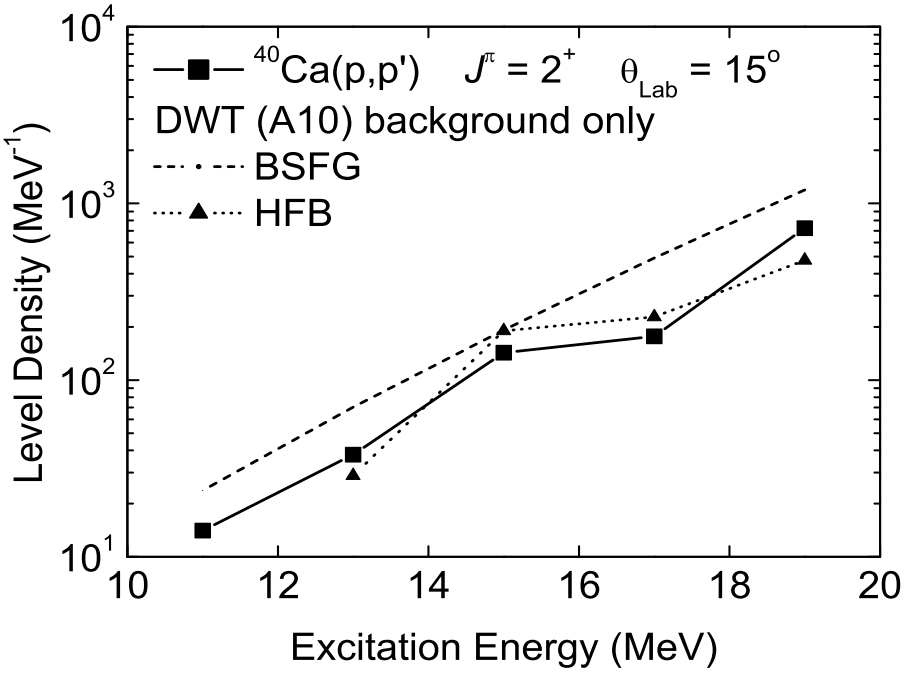

Figure 4.44: Extracted level density (solid line) of 2^+ states for ^{40}Ca(p,p′) at $\theta_{\mathrm{Lab}} = 15°$ compared to BSFG (dashed line) and HFB (dotted line) model predictions after using DWT (A10) background subtraction as shown in Fig. 4.43.

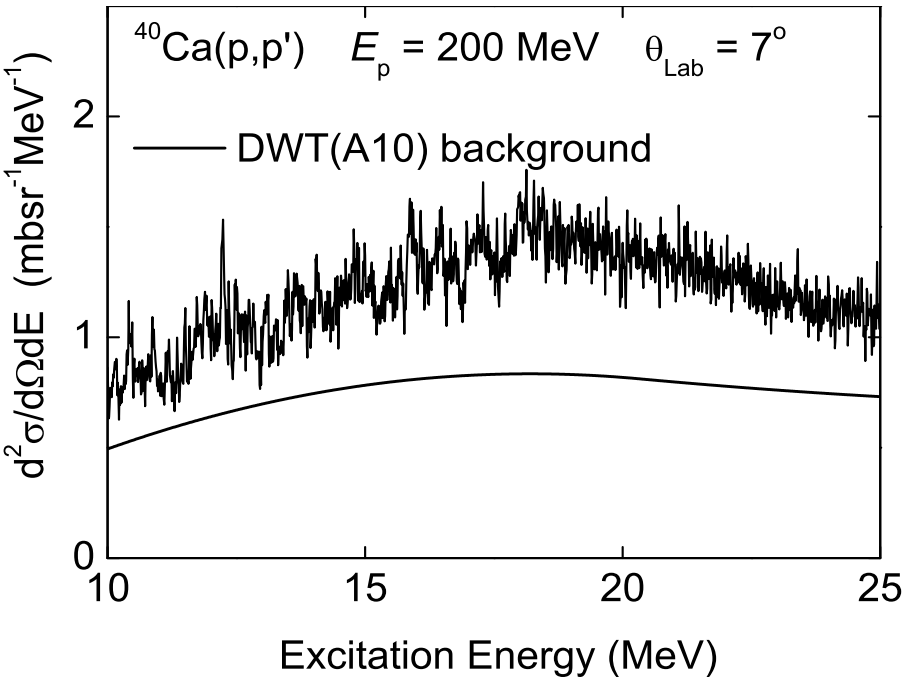

Figure 4.45: DWT (A10) background for ^{40}Ca(p,p′) at $\theta_{\mathrm{Lab}} = 7°$.

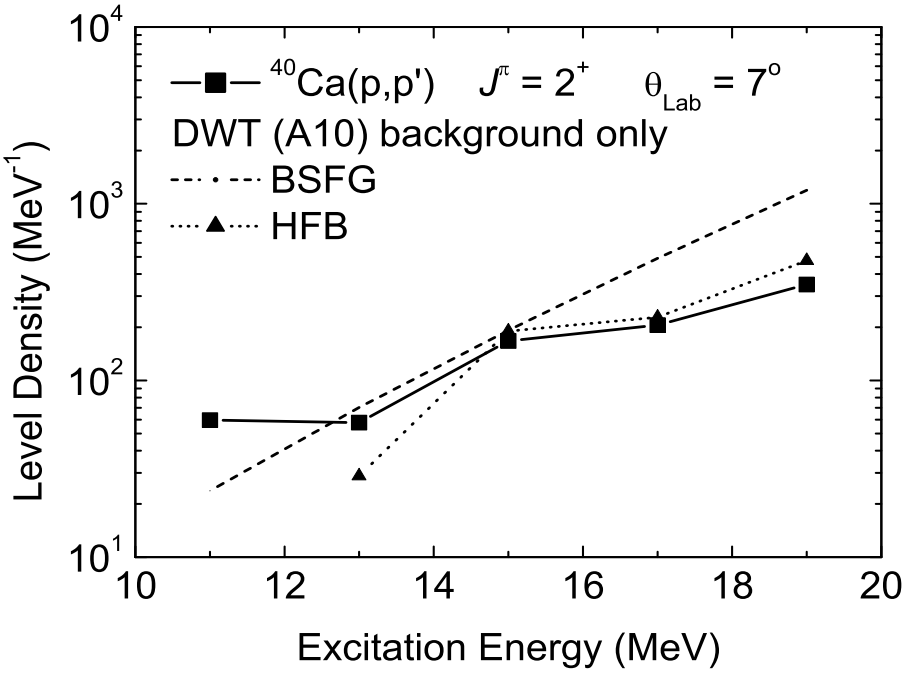

Figure 4.46: Extracted level density (solid line) of 2^+ states for ^{40}Ca(p,p′) at $\theta_{\mathrm{Lab}} = 7°$ compared to BSFG (dashed line) and HFB (dotted line) model predictions after using DWT (A10) background subtraction as shown in Fig. 4.45.

4.8.2.1 2^+ level density in ^{40}Ca via quasi-free background subtraction

The subtraction of the significant physical background produced by the quasi-free scattering reactions (p,2p) and (p,pn) from the measured ^{40}Ca(p,p$'$) energy spectra could, in principle, lead to a more reliable extraction of 2^+ level density in ^{40}Ca. Then, in order to remove other background contributions from the measured spectrum, DWT analysis can be performed on the quasi-free background-subtracted data. This two-step background subtraction is presented in Fig. 4.47 for ^{40}Ca(p,p$'$) at $\theta_{\rm Lab} = 11^\circ$ with the corresponding 2^+ level density result given in Fig. 4.48. The same procedures were repeated for the measured ^{40}Ca(p,p$'$) excitation energy spectra at the scattering angles $\theta_{\rm Lab} = 15^\circ$ (see Figs. 4.49 and 4.50) and $\theta_{\rm Lab} = 7^\circ$ (see Fig. 4.51 and 4.52), above and below the maximum of ISGQR, respectively. It should be noted, however, that in the case of $\theta_{\rm Lab} = 11^\circ$, the resulting DWT background shown in Fig. 4.47 is slightly negative for $E_{\rm x} > 22$ MeV but this does not affect the excitation energy region for which the 2^+ level density is extracted.

In order to see how good the ISGQR fine structure is preserved in ^{40}Ca at other scattering angles above and below the maximum of the ISGQR, semblance analysis were performed for $\theta_{\rm Lab} = 11^\circ$ / 15° and $\theta_{\rm Lab} = 11^\circ$ / 7°. It was found that very good correspondence exists between $\theta_{\rm Lab} = 11^\circ$ / 15° while there is little correspondence for $\theta_{\rm Lab} = 11^\circ$ / 7°. Therefore, the average level density was determined for $\theta_{\rm Lab} = 11^\circ$ and 15° and the results are shown in Fig. 4.53.

It is important to note that the uncertainty of 11% in the absolute cross section results in the uncertainty of the extraction of the level density $\leq 4\%$ due to background DWT compensating for the change. So the error on extracted level density is as big as data points shown for the experimental level density

in each of the figure. In addition, the relatively large background subtracted from $\theta_{\mathrm{Lab}} = 7^{\circ}$ data strongly influence the absolute 2^{+} level density extracted. The model independent procedure using the DWT analysis removes any large uncertainty associated with estimates of background contributions.

4.8.3 Discussion of extracted 2^{+} level densities for ^{40}Ca

Using DWT background determination, the 2^{+} level density results for ^{40}Ca at the different scattering angles $\theta_{\mathrm{Lab}} = 11^{\circ}$, 15° and 7° are presented in Figs. 4.42, 4.44 and 4.46, respectively. As can be seen, the BSFG parametrisation overestimates the extracted 2^{+} level densities at all scattering angles while the HFB model generally follows the pattern in reproducing the excitation energy dependence in all cases except at $\theta_{\mathrm{Lab}} = 7^{\circ}$ where the experimentally extracted level densities fall below the theoretical predictions. Also, at $\theta_{\mathrm{Lab}} = 11^{\circ}$, the maximum of the ISGQR, one can observe an almost constant level density between the excitation energy range 14 and 18 MeV which corresponds to the centroid of the ISGQR in ^{40}Ca but this feature diminishes at the scattering angles above and below the maximum of the ISGQR. This might indicate the dependence of level density on scattering angles where the ISGQR dominates.

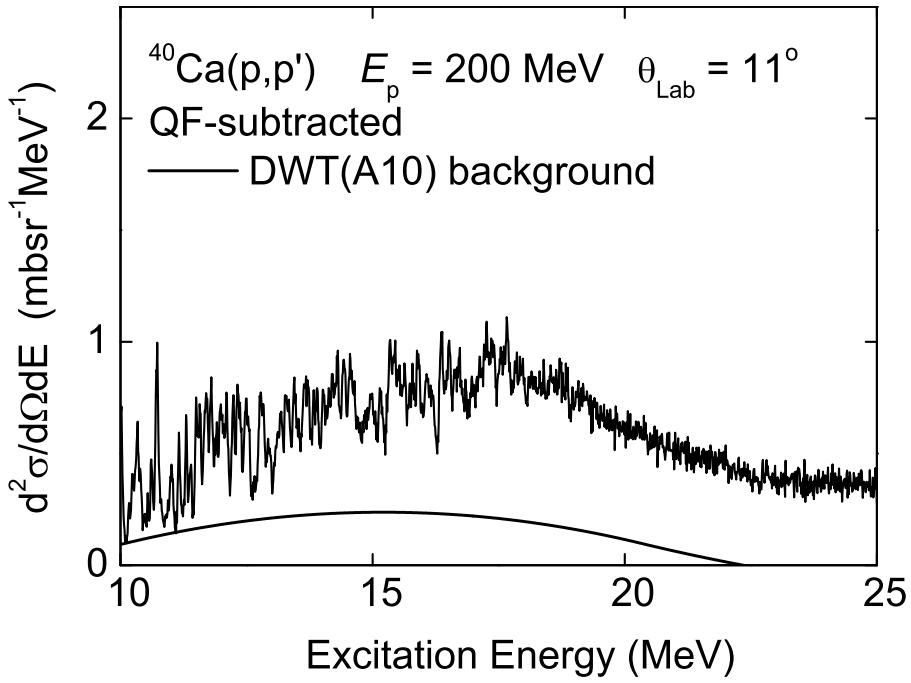

Figure 4.47: DWT (A10) background for the quasi-free subtracted spectrum ^{40}Ca(p,p′) at $\theta_{\rm Lab} = 11°$. See Fig. 4.36 for the quasi-free background.

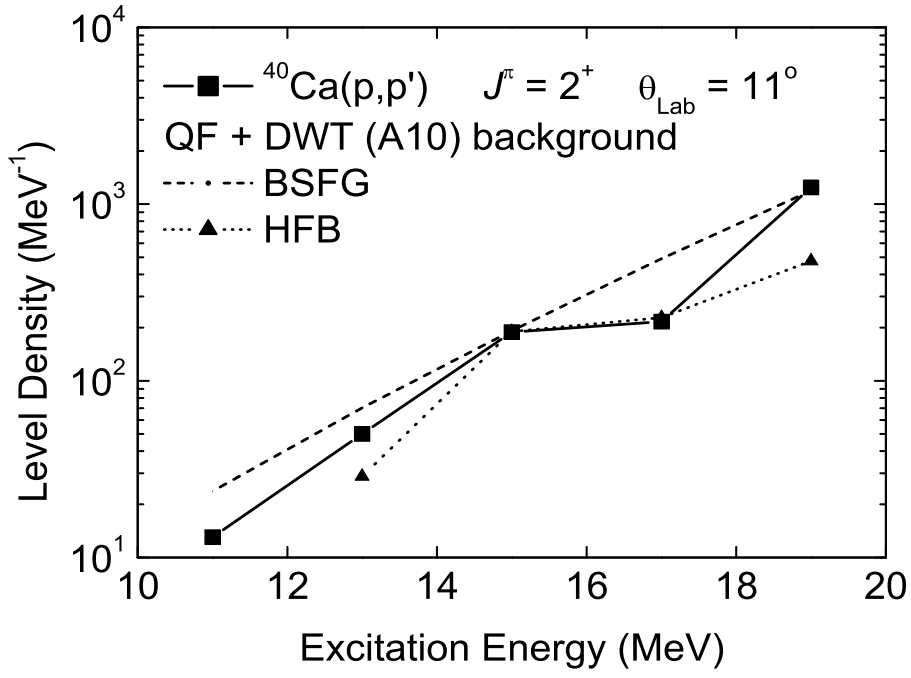

Figure 4.48: Extracted level density (solid line) of 2^+ states for ^{40}Ca(p,p′) at $\theta_{\rm Lab}$ =11° compared to BSFG (dashed line) and HFB (dotted line) model predictions after using quasi-free and DWT (A10) background subtraction as shown in Fig. 4.47.

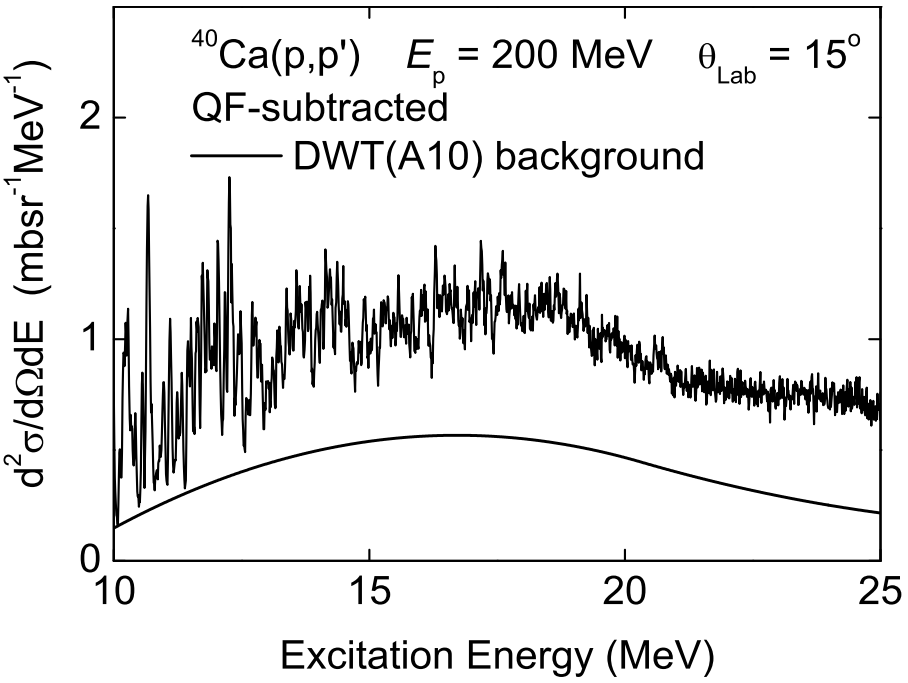

Figure 4.49: DWT (A10) background for the quasi-free subtracted spectrum ^{40}Ca(p,p′) at $\theta_{\rm Lab} = 15°$. See Fig. 4.37 for the quasi-free background.

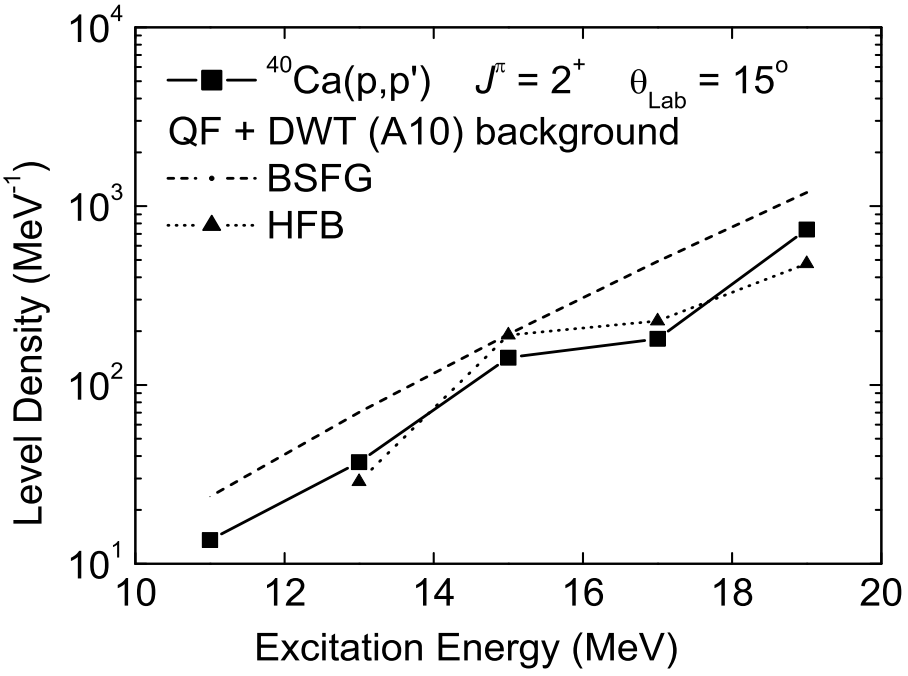

Figure 4.50: Extracted level density (solid line) of 2^+ states for ^{40}Ca(p,p′) at $\theta_{\rm Lab}$ =15° compared to BSFG (dashed line) and HFB (dotted line) model predictions after using quasi-free and DWT (A10) background subtraction as shown in Fig. 4.49.

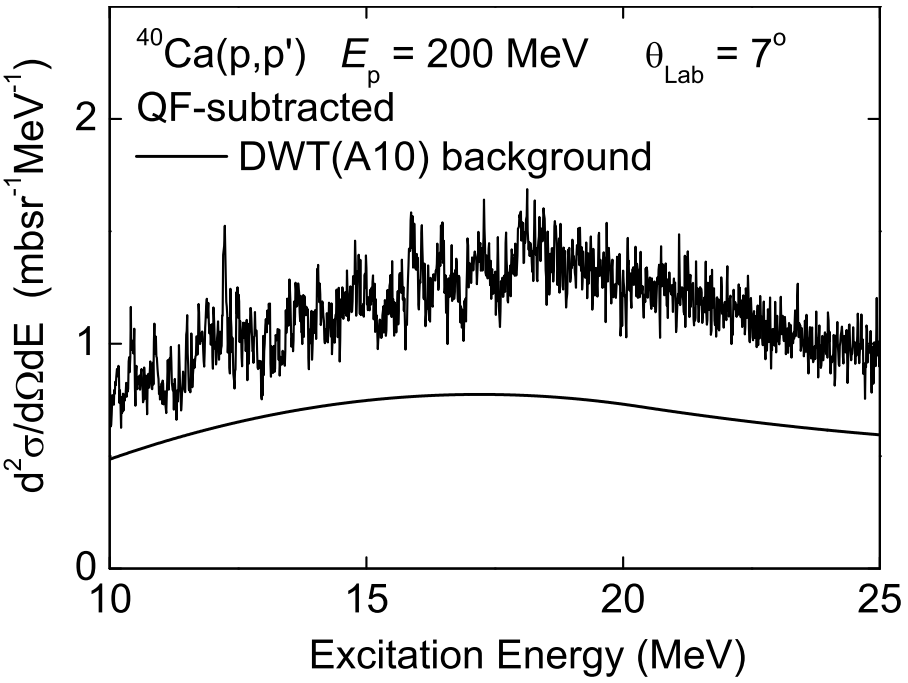

Figure 4.51: DWT (A10) background for the quasi-free subtracted spectrum ^{40}Ca(p,p′) at $\theta_{\rm Lab} = 7°$. See Fig. 4.38 for the quasi-free background.

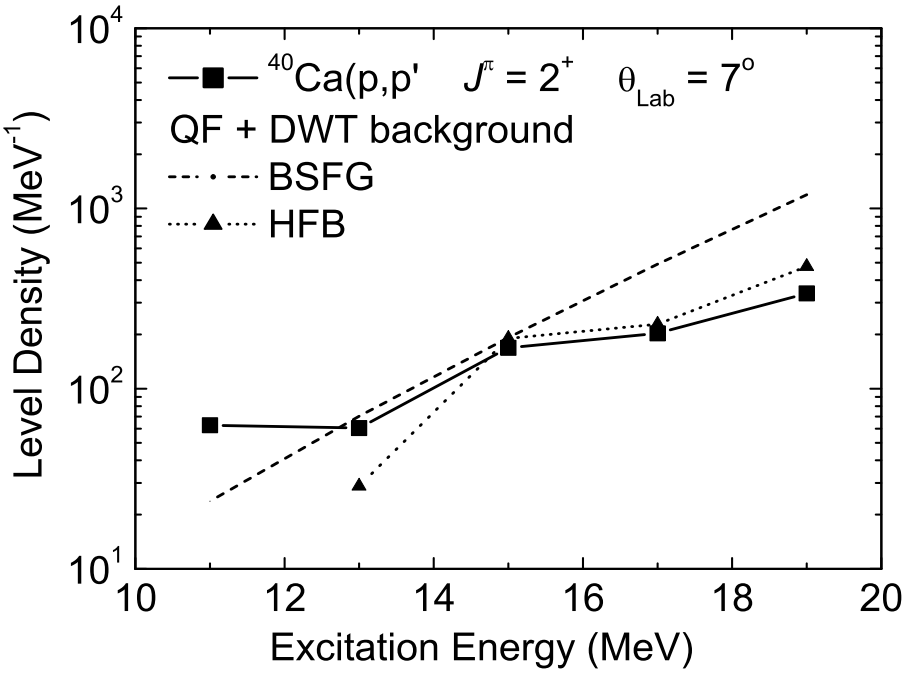

Figure 4.52: Extracted level density (solid line) of 2^+ states for ^{40}Ca(p,p′) at $\theta_{\rm Lab}$ =7° compared to BSFG (dashed line) and HFB (dotted line) model predictions after using quasi-free and DWT (A10) background subtraction as shown in Fig. 4.51.

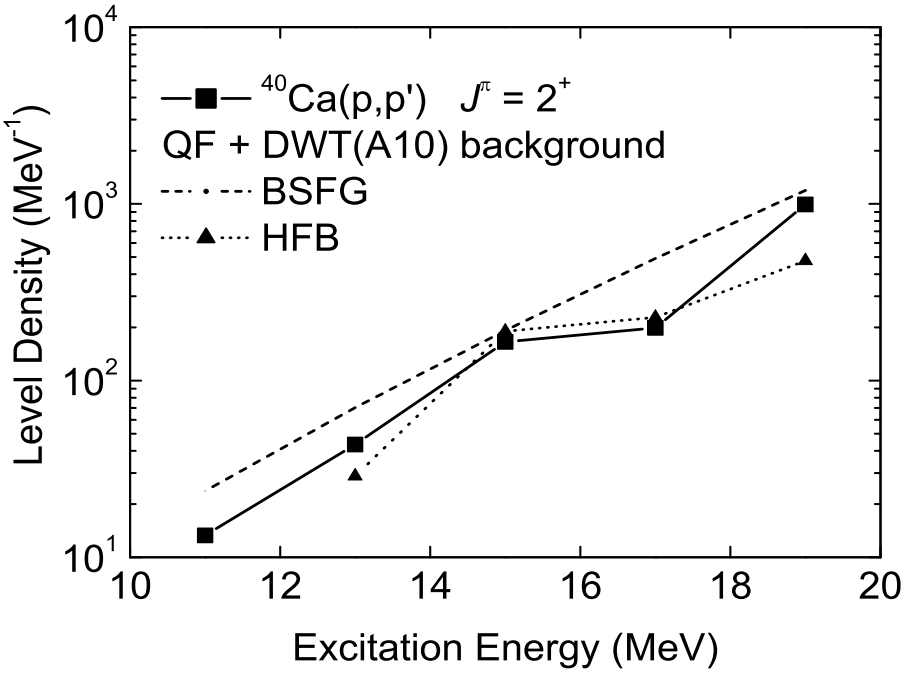

Figure 4.53: Extracted level density (solid line) of 2^+ states for ^{40}Ca(p,p′) averaged over $\theta_{\rm Lab} = 11^\circ$ and $\theta_{\rm Lab} = 15^\circ$ compared to BSFG (dashed line) and HFB (dotted line) model predictions.

In order to understand the importance of background determination on the extracted 2^+ level densities, the DWT analysis was applied to the quasi-free subtracted data at each scattering angle and the results of the extracted 2^+ level densities are presented in Figs. 4.48, 4.50 and 4.52 for $\theta_{\rm Lab} = 11^\circ$, 15° and 7°, respectively. As can be seen, these results are almost the same as when using only DWT background subtraction which suggests that DWT background determination encompasses correctly all background contributions including the knockout contributions as well. This indicates that DWT analysis can be relied upon as a model independent background determination for this type of level density extraction. In conclusion, the results of Fig. 4.53 indicate that experimentally extracted level densities are in better accord with the HFB microscopic model.

Chapter 5

Conclusions

The Isoscalar Giant Quadrupole Resonance (ISGQR) excited in the low-mass nuclei ^{40}Ca, ^{28}Si, ^{27}Al and ^{12}C has been investigated using inelastic proton scattering at 200 MeV. Characteristic energy scales have been extracted for all nuclei except ^{12}C by applying Wavelet Analysis techniques. There is no clear signal of fine structure in the ISGQR region of ^{12}C. A global analysis of the experimental data of nuclei from ^{27}Al to ^{208}Pb reveals three classes of scales; all nuclei studied so far (except ^{12}C) exhibit two or three scales below 300 keV (Class I scales), one or two scales between about 300 keV and 1000 keV strongly varying from nucleus to nucleus (Class II scales) and two or three scales of several MeV reflecting the total width of the resonance (Class III scales).

It should be noted that in the present analysis the newly developed Complex Lorentzian mother wavelet was used. Because of the nature of the mother wavelet (a series of Lorentzian functions with width Γ, separated by 2Γ and localised by a Gauss function), the extracted wavelet scale (also equivalent to the Fourier scale) when divided by two gives the FWHM of the feature. In comparison, the previously used Complex Morlet mother wavelet did not yield a simple scaling to the width of the feature. The real part of the resulting

complex coefficients when displayed on a two dimensional plot of wavelet energy scale *versus* excitation energy allows direct visualisation of the regions of importance of the various scales within the measured excitation energy spectra. As a result, it could be seen that energy scales identified at a scattering angle corresponding to the maximum of the ISGQR became less important at smaller and larger scattering angles where data were available for a particular nucleus.

In order to reveal the physical nature of observed scales, a comparison to the state-of-the-art Second Random Phase Approximation (SRPA) predictions was made for the cases of ^{40}Ca and ^{28}Si. The results serve as an important test of the UCOM interaction applied in the calculation of complex properties of nuclear excitations which works surprisingly well. These calculations confirmed the fragmented nature of the ISGQR seen in the experimental data. The application of Wavelet Analysis indicated good correspondence between experimental data and theoretical predictions at all classes of scales in ^{40}Ca while only intermediate (Class II) and large scale (Class III) correspondence was achieved for ^{28}Si.

Also, in order to gain further insight into the role of the different energy scales, reconstruction of the original experimental excitation energy spectrum in the region of the ISGQR was achieved using an algorithm applied to the coefficients produced by the Continuous Wavelet Transform (CWT). The advantage of the CWT is that specific scales showed regions of importance within the coefficient plots. On the other hand, spectrum reconstruction from the Discrete Wavelet Transform (DWT) has a severe limitation of powers of 2 within energy scales, obviously limiting the range of scales that can be selected for spectrum reconstruction.

Furthermore, the recently developed Semblance and Dot product analysis techniques were applied to the experimental data and theoretical predictions in the case of ^{40}Ca and ^{28}Si in order to show quantitatively the correspondence between experiment and theory. The level of positive correlation obtained in both cases shows that the SRPA theoretical calculations produce corresponding $E2$ strengths for the low-mass nuclei. A similar analysis was applied to compare the ^{28}Si(p,p$'$) data with other probes of different selectivity in the energy region where the fragmented ISGQR lies. In this study, it was established that high positive correlation exists for (p,p$'$) and (α, α') since both can be used to excite $E2$ resonances while the other probes ((e,e$'$), (α, γ_o), (p,γ_o)) excite other multipoles, in particular the IVGDR, besides exciting the ISGQR.

A comparison was also made between the experimental data obtained for one-proton different nuclei, ^{28}Si, ^{27}Al(p,p$'$) and ^{90}Zr, ^{89}Y(p,p$'$), again using the semblance analysis. For the medium-mass nuclei ^{90}Zr and ^{89}Y, high positive correlation was seen which can be related to a compact resonance and less fragmentation due to the nature of $1p$-$1h$ configuration existing in medium and heavy nuclei. In the case of the low-mass nuclei ^{28}Si and ^{27}Al, large negative correlation was seen especially in the Dot product spectrum which can also be related to the fragmentation effects present in low-mass nuclei.

Model calculations using the Distorted Wave Impulse Approximation (DWIA) were performed for ^{40}Ca in order to extract the quasi-free knockout contributions from the (p,2p) and (p,pn) reactions as a background underneath the measured (p,p$'$) excitation energy spectra. The integration over solid angle produced a smooth function below the excitation energy spectrum at each of the three scattering angles. The experimental 2^+ level density in ^{40}Ca was extracted using the model independent Discrete Wavelet Transform (DWT) both with and without the quasi-free knockout background determination. Here,

fluctuation analysis incorporating the autocorrelation function was applied to extract the experimental 2^+ level density and the results were compared to the Back-shifted Fermi Gas (BSFG) and Hartree-Fock Bogoluibov (HFB) theoretical models. In conclusion, it was found that experimentally extracted 2^+ level densities are in better accord with the HFB microscopic model predictions. It should be noted though that the use of the DWT for background determination was insensitive to the inclusion or not of the known quasi-free background and, therefore, can be relied upon as a model independent method of background determination.

Bibliography

[Abe96] Y. Abe, S. Ayik, P. G. Reinhard and E. Suraud, Phys. Rep. **275** (1996) 49.

[Ahm84] M. Ahmad, J. W. Watson, D. W. Devins, B. S. Flanders, D. L. Friesel, N. S. Chant, P. G. Roos and J. Wastell, Nucl. Phys. **A 424** (1984) 92.

[Aib99] H. Aiba and M. Matsuo, Phys. Rev. **C 60** (1999) 034307.

[Alh07] Y. Alhassid, S. Lui and H. Nakada, Phys. Rev. Lett. **99** (2007) 162594.

[Ant81] L. Antonuk, P. Kitching, C. A. Miller, D. A. Hutcheon, W. J. McDonald, G. C. Neilson, W. C. Olsen and A. W. Stetz, Nucl. Phys. **A 370** (1981) 389.

[Bad47] G. C. Baldwin and G. S. Klaiber, Phys. Rev. **71** (1947) 3.

[Bec69] F. D. Becchetti and G. W. Greenlees, Phys. Rev. **182** (1969) 1190.

[Bha83] *IAEA Advisory Group Meeting on Basic and Applied problems of Nuclear Level Densities*, M. R. Bhat, Brookhaven National laboratory, Long Island, New York (1983).

[Ber79] G. F. Bertsch, Nature **280** (1979) 23.

[Ber87] G. F. Bertsch, *Private communication* (1987).

[Ber83] G. F. Bertsch, P. F. Bortignon and R. A. Broglia, Rev. Mod. Phys. **55** (1983) 287.

[Ber81] F. E. Bertrand, Nucl. Phys. **A 354** (1981) 129c.

[Ber99] C. Bertulani and V. Ponomarev, Phys. Rev. **C 321** (1999) 139.

[Bet37] H. A. Bethe, Rev. Mod. Phys. **9** (1937) 69.

[Bor98] P. F. Bortignon, A. Bracco and R. A. Broglia, *Giant Resonances: Nuclear Structure at Finite Temperature*, Harwood Academic, Amsterdam (1998).

[Bor81] K. van der Borg, M. N. Harakeh and A. van der Woude, Nucl. Phys. **A 365** (1981) 243.

[Bot37] W. Bothe and W. Z. Gentner, Phys. **106** (1937) 236.

[Bro64] G. Brown, *Unified Theory of Nuclear Models*, North-Holland, Amsterdam (1964).

[Car98] J. Carter, A. A. Cowley, H. Diesener, R. W. Fearick, S. V. F*ö*rtsch, M. N. Harakeh, J. J. Lawrie, S. J. Mills, P. von Neumann-Cosel, R. T. Newman, J. V. Pilcher, A. Richter, K. Schweda, F. D. Smit, G. F. Steyn, S. Strauch and D. M, Whittal, Nucl. Phys. **A 630** (1998) 631.

[Car01] J. Carter, A. A. Cowley, H. Diesener, R. W. Fearick, S. V. F*ö*rtsch, J. J. Lawrie, P. von Neumann-Cosel, J. V. Pilcher, A. Richter, K. Schweda, F. D. Smit, G. F. Steyn and S. Strauch, Phys. Rev. **C 63** (2001) 057602.

[Cha98] N. S. Chant, THREEDEE, University of Maryland (1998) (unpublished).

[Cas90] W. Cassing and U. Mosel, Prog. Part. Nucl. Phys. **25** (1990) 235.

[Coo08] G. R. J. Cooper and D. R. Cowan, Computers and Geosciences **34** (2008) 95.

[Dau94] I. Daubechies, *Ten Lectures on Wavelets*, CBMS, SIAM, **61**, (1994) 76.

[Dem01] P. Demetriou and S. Goriely, Nucl. Phys. **A 695** (2001) 95.

[Dil73] W. Dilg, W. Schantl, H. Vonach and M. Uhl, Nucl. Phys. **A 217** (1973) 269.

[Dro86] S. Drozdz, V. Klent, J. Speth and J. Wambach, Nucl. Phys. **A 451** (1986) 11.

[Dro90] S. Drozdz, S. Nishizaki, J. Speth and J. Wambach, Phys. Rep. **C 197** (1990) 1.

[Egi05] T. von Egidy and D. Bucurescu, Phys. Rev. **C 72** (2005) 044311.

[Elt67] L. R. B. Elton and A. Swift, Nucl. Phys. **A 94** (1967) 52.

[End97] J. Enders, N. Huxel, P. von Neumann-Cosel and A. Richter, Phys. Rev. Lett. **79** (1997) 2010.

[Eri63] T. Ericson, Adv. Phys. **9** (1963) 425.

[For88] S. V. Förtsch, A. A. Cowley, J. V. Pilcher, D. H. Whittal, J. J. Lawrie, J. C. Van Staden and E. Friedland, Nucl. Phys. **A 485** (1988) 258.

[Fri81] A. Friebel, PhD Dissertation, T. U. Darmstadt, (1981).

[Fuj97] Y. Fujita, K. Hatanaka, G. P. A. Berg, K. Hosono, N. Matsuoka, S. Morinobu, T. Noro, M. Sato, K. Tamura and H. Ueno, Nucl. Instr. Methods **B 126** (1997) 274.

[Fuj02] H. Fujita, Y. Fujita, G. P. A. Berg, A. D. Bacher, C. C. Foster, K. Hara, K. Hatanaka, T. Kawabata, T. Noro, H. Sakaguchi, Y.

Shimbara, T. Shinada, E. J. Stephenson, H. Ueno and M. Yosoi, Nucl. Instr. Methods **A 484** (2002) 17.

[Fuj07] H. Fujita, *Private communication* (2007).

[Gad68] E. Gadioli and L. Zetta, Phys. Rev. **167** (1968) 1016.

[Gil65] A. Gilbert and A. G. W. Cameron, Can. J. Phys. **43** (1965) 1446.

[Gre04] J. P. Greene and P. Maier-Komor, *Proceedings of the 21st World Conference of the International Nuclear Target Development Society*, Argonne, USA Nov.4-8, (2002), Nucl. Instr. Methods **A 521** (2004) 1.

[Gol48] M. Goldhaber and E. Teller, Phys. Rev. **74** 1046 (1948).

[Gou81] C. Gould, L. G. Holzsweig, S. E. King, Y. C. Lau, R. V. Poore, N. R. Roberson and S. A. Wender, IEEE Trans. Nucl. Sci. **NS-28**, (1981) 3708.

[Gro84] A. Grossman and J. Morlet, SIAM J. Math. Anal. **15** (1984) 723.

[Han90] P. G. Hansen, B. Jonson and A. Richter, Nucl. Phys. **A 29** (1990) 13.

[Han79] P. G. Hansen, Ann. Rev. Nucl. Part. Sci. **29** (1979) 69.

[Har00] M. N. Harakeh and A. van der Woude, *Giant Resonances: Fundamental High-Frequency Modes of Nuclear Excitation*, Oxford University, Oxford (2000).

[Http] $http://www-astro.ulb.ac.be/html/nld_comb_ph.html$.

[Hil06] S. Hilaire and S. Goriely, Nucl. Phys. **A 779** (2006) 63.

[Hui69] J. R. Huizenga, H. K. Vonach, A. A. Katsanos, A. J. Gorski and C. J. Stephan, Phys. Rev. **182** (1969) 1149.

[Ito05] M. Itoh, *Private communication* (2005).

[Hux99] N. Huxel, P. von Brentano, J. Eberth, J. Enders, R. D. Herzberg, P. von Neumann-Cosel, N. Nicolay, N. Pietralla, H. Prade, C. Rangacharyulu, J. Reif, A. Richter, C. Schlegel, R. Schwengner, S. Skoda, H. G. Thomas, I. Wiedenhover, G. Winter and A. Zilges, Nucl. Phys. **A 645** (1999) 239.

[Jon76] B. Jonson, E. Hagberg, P. G. Hansen, P. Hornsöj and P. Tidemand-Petersson, *Proc. 3rd Int. Conf. on Nuclei far from Stability*, Cargèse, CERN **76 - 13** (1976) 277.

[Kal06] Y. Kalmykov, T. Adachi, G. P. A. Berg, H. Fujita, K. Fujita, Y. Fujita, K. Hatanaka, J. Kamiya, K. Nakanishi, P. von Neumann-Cosel, V. Yu. Ponomarev, A. Richter, N. Sakamoto, Y. Sakemi, A, Shevchenko, Y. Shimbara, Y. Shimizu, F. D. Smit, T. Wakasa, J. Wambach and M. Yosoi, Phys. Rev. Lett. **96** (2006) 012502.

[Kal07] Y. Kalmykov, C. Özen, K. Langanke, G. Martinez-Pinedo, P. von Neumann-Cosel and A. Richter, Phys. Rev. Lett. **99** (2007) 202502.

[Kam97] S. Kamerdzhiev, J. Lisantti, P. von Neumann-Cosel, A. Richter, G. Tertychny and J. Wambach, Phys. Rev. **C 55** (1997) 2101.

[Kat70] A. A. Katsanos, R. W. Shaw, R. van denbosch and D. Chamberlin, Phys. Rev. **C 1** (1970) 594.

[Kon08] A. J. Koning, S. Hilaire and S. Goriely, Nucl. Phys. **A 810** (2008) 13.

[Kuh83] E. Kuhlmann, K. A. Snover, G. Feldman and M. Hindi, Phys. Rev. **C 27** (1983) 948.

[Kuh81] G. Kühner, D. Meuer, S. Müller, A. Richter, E. Spamer, O. Titze and W. Knüpfer, Phys. Lett. **B 104** (1981) 189.

[Lac99] D. Lacroix and P. Chomaz, Phys. Rev. **C 60** (1999) 064307.

[Lac00] D. Lacroix, A. Mai, P. von Neumann-Cosel, A. Richter and J. Wambach, Phys. Lett. **B 479** (2000) 15.

[Lac01] D. Lacroix, S. Ayik and P. Chomaz, Phys. Rev. **C 63** (2001) 064305.

[Lew72] M. B. Lewis and F. E. Bertrand, Nucl. Phys. **A 196** (1972) 337.

[Lov81] W. G. Love and M. A. Franey, Phys. Rev. **C 24** (1981) 1073.

[Lu72] C. C. Lu, L. C. Vaz and J. R. Huizenga, Nucl. Phys. **A 190** (1972) 229.

[Lui85] Y. -W. Lui, J. D. Bronson, D. H. Youngblood and Y. Toba, Phys. Rev. **C 31** (1985) 1643.

[Mal92] S. Mallat and W. L. Hwang, IEEE Trans. Inf. Theory **38** (1992) 617.

[Mal98] S. G. Mallat, *A Wavelet tour of Signal Processing*, Academic Press, New York (1998).

[Mat06] The Mathworks, *Matlab, The Language of Technical Computing*, Version 7.2.0.232 (R2006a).

[Mar83] S. A. Martin, A. Hardt, J. Meissburger, G. P. A. Berg, U. Hacker, W. H*ü*rlimann, J. G. M. R*ö*mer, T. Sagefka, A. Retz, O. W. B. Schult, K. L. Brown and K. Halbach, Nucl. Instr. Methods **214** (1983) 281.

[Mey75] M. A. Meyer, I. Venter and D. Reitmann, Nucl. Phys. **A 250** (1975) 235.

[Mos76] J. M. Moss and D. H. Youngblood, Phys. Rev. Lett **37** (1976) 816.

[Mul83] S. M*ü*ller, PhD Dissertation D17, TH Darmstadt, (1983).

[Mul82] S. M*ü*ller, F. Beck, D. Meuer and A. Richter, Phys. Lett. **B 113** (1982) 362.

[Neu99] P. von Neumann-Cosel, F. Neumeyer, V. Yu. Ponomarev, C. Rangacharyulu, B. Reitz, A, Richter, G, Schrieder, D. I. Sober, T. Waindzoch and J. Wambach, Phys. Rev. Lett. **82** (1999) 1105.

[Nev08] R. Neveling, F. D. Smit, H. Fujita and R. T. Newman, *K600 user-manual*, iThemba LABS, Somerset West (2008), unpublished.

[New56] T. D. Newton, Can. J. Phys. **34** (1956) 804.

[Pap09] P. Papakonstantinou and R. Roth, Phys. Lett. **B 671** (2009) 356.

[Pet81] F. Petrovich and W. G. Love, Nucl. Phys. **A 354** (1981) 499c.

[Pit71] R. Pitthan and Th. Walcher, Phys. Lett. **B 36** (1971) 563.

[Por65] C. E. Porter and R. G. Thomas, Phys. Rev. **A 518** (1965) 13.

[Pil89] J. Pilcher, A. Cowley, D. Whittal and J. Lawrie, Phys. Rev. **C 40** (1989) 1937.

[Quasta] Three body kinematics computer code developed at iThemba LABS, South Africa.

[Rau97] T. Rauscher, F. K. Thielemann and K. L. Kratz, Phys. Rev. **C 58** (1997) 1613.

[Rei94] P. G. Reinhard and C. Toepffer, Int. J. Mod. Phys. **E 3** (1994) 435.

[Ric81] A. Richter, *Private communication* (1981).

[Rie78] H. Riedesel, K. T. Knopfle, H. Breuer, P. Doll, G. Mairle and G. J. Wagner, Phys. Rev. Lett. **41** (1978) 377.

[Ripl06] *Handbook for calculations of nuclear reaction data, (RIPL-2)* Reference Input Parameter Library-2, IAEA-TECDOC-1506, (2006).

[Rot05] R. Roth, H. Hergert, P. Papakonstatinou, T. Neff and H. Feldmeier, Phys. Rev. **C 72** (2005) 034002.

[Rot08] R. Roth, Nucl. Phys. **A 805** (2008) 416c. *Proceedings of the 23rd International Nuclear Physics Conference 2007.*

[Sat83] G. R. Satchler, *Direct Nuclear Reactions*, Oxford University Press, Oxford (1983).

[Sat72] G. R. Satchler, Nucl. Phys. **A 195** (1972) 1.

[Saw62] J. Sawicki, Phys. Rev. **126** (1962) 2231.

[Sch82] P. Schwandt, H. O. Meyer, W. W. Jacobs, A. D. Bacher, S. E. Vigdor and M. D. Kaitchuck, Phys. Rev. **C 26** (1982) 55.

[Sch01] K. Schweda, J. Carter, A. A. Cowley, H. Diesener, R. W. Fearick, S. V. Förtsch, J. J. Lawrie, P. von Neumann-Cosel, J. V. Pilcher, A. Richter, F. D. Smit, G. F. Steyn and S. Strauch, Phys. Lett. **B 506** (2001) 247.

[She03] A. Shevchenko, PhD Dissertation, T. U. Darmstadt, (2003).

[She04] A. Shevchenko, J. Carter, R. W. Fearick, S. V. Förtsch, H. Fujita, Y. Fujita, Y. Kalmykov, D. Lacroix, J. J. Lawrie, P. von Neumann-Cosel, R. Neveling, V. Yu. Ponomarev, A. Richter, E. Sideras-Haddad, F. D. Smit and J.Wambach, Phys. Rev. Lett. **93** (2004) 122501.

[She08] A. Shevchenko, G. R. J. Cooper, J. Carter, R. W. Fearick, S. V. Förtsch, Y. Kalmykov, P. von Neumann-Cosel, V. Yu. Ponomarev, A. Richter, I. Usman and J. Wambach, Phys. Rev. **C 77** (2008) 024302.

[Sin65] P. P. Singh, R. E. Segel, L. Meyer-scchutzmeister, S. S. Hanna and R. G. Allas, Nucl. Phys. **65** (1965) 577.

[Sol92] V. G. Solov'ev and V. I. Kisin, *Theory of Atomic Nuclei: Quasi-particles and Phonons*, Institute of Physics, Bristol and Philadephia, USA (1992).

[Spe91] J. Speth and J. Wambach, *Int. Review of Nuclear and Particle Physics*, Vol.7, World Scientific, Singapore (1991).

[Ste50] H. Steinwedel and J. H. D. Jensen, Z. Nature **5a** (1950) 413.

[Tor98] C. Torrence and G. P. Compo, Bull. Am. Meteorol. Soc. **79** (1998) 61.

[Usm06] I. Usman, MSc Research Report, University of the Witwatersrand (2006) (unpublished).

[Von69] H. Vonach and M. Hille, Nucl. Phys. **A 127** (1969) 289.

[Wat82] J. W. Watson, M. Ahmad, D. W. Devins, B. S. Flanders, D. L. Friesel, N. S. Chant, P. G. Roos and J. Wastell, Phys. Rev. **C 26** (1982) 961.

[Wel67] P. D. Welch, *The use of fast Fourier transform for the estimation of power spectra: A method based on time averaging over short, modified Periodograms*, IEEE Trans. Audio Electroacoustics, Vol. AU-**15** (1967) 70.

[Wig65] E. P. Wigner and C. E. Porter (Ed), *Statistical Theories of Spectra: Fluctuations*, Academic Press, New York (1965).

[Wil64] D. Wilmore and P. E. Hodgson, Nucl. Phys. **55** (1964) 673.

[Wir95] R. B. Wiringa, V. G. J. Stoks and R. Schiavilla, Phys. Rev. **C 51** (1995) 38.

[Won90] S. M. Wong, *Introductory Nuclear Physics*, Prentice Hall, New Jersey (1990).

[Wou87] A. van der Woude, *Giant resonances*, Prog. Part. Nucl. Phys. **18** (1987) 217.

[Yan83] C. Yannouleas, M. Dworzecka and J. Griffin, Nucl. Phys. **A 397** (1983) 239.

[Yan87] C. Yannouleas, Phys. Rev. **C 37** (1987) 1159.

[You78] D. H. Youngblood and C. M. Rozsa, Phys. Rev. **C 15** (1978) 1644.

[Zwa85] F. Zwarts, A. G. Drentje, M. N. Harakeh and A. van der Woude, Nucl. Phys. **A 439** (1985) 117.